

**INVESTIGATION OF INTERLAYER MAGNETIC
COUPLING IN MAGNETIC MULTILAYER FILMS
OF Al-Fe-Gd**

Ritthikrai Chai-ngam

**A Thesis Submitted in Partial Fulfillment of the Requirements for
the Degree of Doctor of Philosophy in Physics**

Suranaree University of Technology

Academic Year 2005

ISBN 974-533-431-6

การสืบสวนการค้ำวระหว่างชั้นแม่เหล็กในฟิล์มบางแม่เหล็ก
หลายชั้นของ Al-Fe-Gd

ฤทธิไกร ไชยงาม


วิทยานิพนธ์นี้เป็นส่วนหนึ่งของการศึกษาตามหลักสูตรปริญญาวิทยาศาสตรดุษฎีบัณฑิต
สาขาวิชาฟิสิกส์
มหาวิทยาลัยเทคโนโลยีสุรนารี
ปีการศึกษา 2548

ISBN 974-533-431-6

**INVESTIGATION OF INTERLAYER MAGNETIC COUPLING IN
MAGNETIC MULTILAYER FILMS OF Al-Fe-Gd**

Suranaree University of Technology has approved this thesis submitted in partial fulfillment of the requirements for the Degree of Doctor of Philosophy.

Thesis Examining Committee



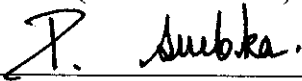
(Asst. Prof. Dr. Prapun Manyum)

Chairperson



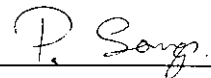
(Prof. Dr. Takehiko Ishii)

Member (Thesis Advisor)



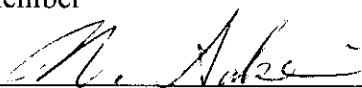
(Assoc. Prof. Dr. Prasart Suebka)

Member



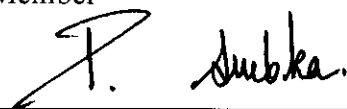
(Asst. Prof. Dr. Prayoon Songsiriritthigul)

Member

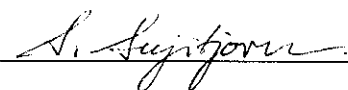


(Prof. Dr. Nobuhiko Sakai)

Member



(Assoc. Prof. Dr. Prasart Suebka)



(Assoc. Prof. Dr. Sarawut Sujitjorn)

Vice Rector for Academic Affairs

Dean of Institute of Science

ฤทธิ์ไกร ไชยงาม : การสืบสวนการคู่ควบระหว่างชั้นแม่เหล็กในฟิล์มบางแม่เหล็กหลายชั้นของ Al-Fe-Gd (INVESTIGATION OF INTERLAYER MAGNETIC COUPLING IN MAGNETIC MULTILAYER FILMS OF Al-Fe-Gd) อาจารย์ที่ปรึกษา : ศาสตราจารย์ ดร. ทาเคฮิโกะ อิชิอิ, 290 หน้า. ISBN 974-533-431-6

วิทยานิพนธ์ฉบับนี้ ได้นำเสนอรายงานผลการทดลองตลอดจนบทวิเคราะห์ผลการทดลอง ของการสืบสวนการคู่ควบระหว่างชั้นแม่เหล็กในฟิล์มบางแม่เหล็กหลายชั้นของ อะลูมิเนียม-เหล็ก-แกโดลิเนียม (Al-Fe-Gd) ฟิล์มบางแม่เหล็กหลายชั้น [Al(RÅ)/Gd(40Å)/Al(RÅ)/Fe(20Å)] ถูกเตรียมขึ้นด้วยวิธีแม็กนีตรอนสปัตเตอร์ริง โดยให้ค่าความหนาของอะลูมิเนียม (R) ที่ชั้นกลางระหว่างชั้นของเหล็กและแกโดลิเนียมเปลี่ยนเป็นค่าต่างๆ คือ 5 7 10 20 30 และ 100 อังสตรอม คุณสมบัติพื้นฐานทางด้านแม่เหล็กของฟิล์มบางแม่เหล็กหลายชั้นดังกล่าว ถูกตรวจสอบโดยการวัดฮิสเตอร์รีซิสและการเปลี่ยนแปลงกับอุณหภูมิของของค่าแม็กนีไคน์เซชันในสารตัวอย่าง ต่อจากนั้นสารตัวอย่างบางตัว ได้ถูกศึกษาโดยใช้เทคนิคแม็กเนติกคอมป์ตันโพรไฟล์ (Magnetic Compton profile, MCP) ซึ่งเหมาะสำหรับการตรวจสอบหาค่าแม็กนีไคน์เซชันซึ่งเกิดจากผลของสปินโมเมนต์ในชั้นของเหล็กและแกโดลิเนียมได้ นอกจากนี้แล้ว เทคนิคเอกซ์เรย์แม็กเนติกเซอร์คูล่าไดโครลิซึม (X-ray magnetic circular dichroism, XMCD) ยังถูกนำมาใช้ในการศึกษาทิศทางของแม็กนีไคน์เซชันในชั้นของแกโดลิเนียมเมื่อเปลี่ยนแปลงสนามแม่เหล็กภายนอก ผลการทดลองแสดงให้เห็นว่า การคู่ควบระหว่างชั้นแม่เหล็กของเหล็กและแกโดลิเนียมในฟิล์มบางแม่เหล็กหลายชั้นของ อะลูมิเนียม-เหล็ก-แกโดลิเนียม นั้นเป็นแบบตรงข้าม และเมื่อเพิ่มความหนาของอะลูมิเนียมขึ้น ปรากฏว่าความแรงของการคู่ควบระหว่างชั้นแม่เหล็กลดลงอย่างรวดเร็ว และหายไปเมื่อความหนาของชั้นอะลูมิเนียมมากกว่า 20 อังสตรอม

สาขาวิชาฟิสิกส์
ปีการศึกษา 2548

ลายมือชื่อนักศึกษา

ลายมือชื่ออาจารย์ที่ปรึกษา

RITTHIKRAI CHAI-NGAM : INVESTIGATION OF INTERLAYER
MAGNETIC COUPLING IN MAGNETIC MULTILAYER FILMS OF Al-
Fe-Gd. THESIS ADVISOR : PROF. TAKEHIKO ISHII, Ph.D. 290 PP.
ISBN 974-533-431-6

Fe-Al-Gd MULTILAYER/MAGNETIC COMPTON PROFILE/MAGNETIC
DICHROISM/ANTIFERROMAGNETIC



In this thesis, interlayer magnetic coupling (IMC) has been investigated in the magnetic multilayer films [Al($R\text{\AA}$)/Gd(40\AA)/Al($R\text{\AA}$)/Fe(20\AA)], where $R = 0, 5, 7, 10, 20, 30,$ and 100 . The samples are deposited by means of magnetron sputtering on polyimide and polyethylene films. Hysteresis and temperature dependence of magnetization of the samples are measured. X-ray magnetic circular dichroism (XMCD) technique has been used, in which the hystereses of the XMCD effect on the samples of $R = 0, 5, 10,$ and 100 have been measured. These hysteresis curves demonstrate orientating of Gd-spin moments with external field. Magnetic Compton-profile (MCP) technique has been used to determine the amounts and the signs of spin magnetizations of Fe and Gd layers for $R = 5$ and 20 . The experimental results show that the IMC in the multilayer films is antiferromagnetic coupling. The magnitude of IMC rapidly decreases with increasing thickness of Al spacer, and disappears when the Al thickness is above 20\AA .

School of Physics

Academic Year 2005

Student's Signature

Advisor's Signature

ACKNOWLEDGEMENTS

The work contained in this thesis has been implemented with assistance and guidance by many persons in various ways. It is my pleasure to express sincere gratitude to the following persons for their contribution:

- Professor Dr. Takehiko Ishii, my thesis advisor, for his enlightening guidance and encouragement throughout the course of this study over the past six years. I have learnt not only the relevant physics but also the spiritual attitude and the patience in performing careful professional investigations.
- Professor Dr. Nubohiko Sakai for all his encouragement, support and hospitality in both research and daily life for one and half years of my study in Himeji, Japan.
- Associate Professor Dr. Hisao Kobayashi and Associate Professor Dr. Akihisa Koizumi for their valuable guidance and teaching in experimental procedures.
- Associate Professor Dr. Prasart Suebka, the Dean of Institute of Science of Suranaree University of Technology, for his kind support and generous help.
- All of my friends in Quantum Magnetism Lab, especially Mr. Takahashi Takeshi and Tomiya Kawai, for their advice and help.
- My great brothers, Dr. Samred Kantee and Dr. Wiwat Wongkokua, for their help and support.

- The Royal Golden Jubilee (RGJ) for the scholarship which covered all of the expenses throughout my study at University of Hyogo and Suranaree University of Technology.
- The Association of International Education in Japan (AIEJ) and University of Hyogo for the scholarship which covered the expenses during my stay at University of Hyogo.
- My wife, my father- and mother-in-law, and my family members for their support and love throughout the years.

Ritthikrai Chai-ngam

CONTENTS

	Page
ABSTRACT IN THAI	I
ABSTRACT IN ENGLISH	II
ACKNOWLEDGEMENTS.....	III
CONTENTS	V
LIST OF TABLES.....	X
LIST OF FIGURES	XI
CHAPTER	
I INTRODUCTION.....	1
1.1 Overview of the Study	1
1.1.1 Introductory Remark.....	1
1.1.2 Magnetic Multilayer.....	5
1.1.3 Magnetic Compton Scattering	9
1.1.4 Magnetic Circular Dichroism	27
1.2 Basic Concept of Magnetism in Solid	73
1.2.1 Atomic Magnetism.....	74
1.2.2 Magnetizations	79
1.2.3 Diamagnetic and Paramagnetic in Solids	80
1.2.4 Magnetic Ordering in Solids I: Ferromagnetic	90
1.2.5 Magnetic Exchange Interactions.....	101

CONTENTS (Continued)

	Page
1.2.6 Magnetic Ordering in Solids II: Ferrimagnetism & Anti Ferromagnetism	111
1.2.7 Magnetic Domain and Hysteresis of Magnetization.....	120
1.3 Characteristic of Synchrotron Light.....	123
II PURPOSE OF THE STUDY.....	125
III INTERLAYER MAGNETIC COUPLING	126
3.1 Basic Concept of Interlayer Magnetic Coupling	126
3.2 Survey of Experimental Achievements.....	128
3.2.1 Bilinear Coupling.....	129
3.2.2 Oscillatory Interlayer Exchange Coupling.....	130
3.2.3 Biquadratic Coupling.....	132
3.3 Survey of Theoretical Models.....	134
3.3.1 Total energy calculation.....	134
3.3.2 Mean Field Theory.....	135
3.3.3 RKKY Model.....	143
3.3.4 Quantum Well Model.....	145
3.3.5 Biquadratic Coupling Model.....	148
3.4 Survey of Interlayer Magnetic Coupling Studies in Fe-Al-Gd Multilayer.....	151
3.4.1 Magnetic Coupling in Fe/Gd Ferrimagnetic Multilayer	151

CONTENTS (Continued)

	Page
3.4.2 Interlayer Magnetic Coupling in Fe/Al and Gd/Al Multilayers	152
IV EXPERIMENTAL METHODS	154
4.1 Experimental Techniques	154
4.1.1 DC+ RF Magnetron Sputtering.....	154
4.1.2 SQUID Magnetometry.....	160
4.1.3 Magnetic Compton Profile (MCP)	162
4.1.4 X-ray Magnetic Circular Dichroism (XMCD)	166
4.2 Experimental Apparatus.....	168
4.2.1 Sputtering Chamber	168
4.2.2 Superconducting Quantum Interference Device (SQUID).....	168
4.2.3 Beamline BL08W at SPring-8	175
4.2.4 Beamline BL39XU at SPring8.....	178
4.3 Experimental Procedures	181
4.3.1 Sample Preparation	182
4.3.2 Magnetometry	185
4.3.3 Magnetic Compton Profile (MCP)	189
4.3.4 X-ray Magnetic Circular Dichroism (XMCD)	192
V EXPERIMENTAL RESULTS.....	195

CONTENTS (Continued)

	Page
5.1 Magnetization Curves	195
5.1.1 Magnetization Curves of the Polyimide Film-Substrate Samples	195
5.1.2 Magnetization Curves of the Polyethylene Film- Substrate Samples	199
5.2 Magnetic Compton Profiles	202
5.3 Hysteresis of the XMCD Effect	205
VI DISCUSSION AND CONCLUSION	215
6.1 Discussion	215
6.1.1 IMC in Al/Fe/Al/Gd MLFs	215
6.1.2 Al-thickness Dependence of IMC Strength in Al/Fe/Al/Gd MLFs	217
6.1.3 Compensation Temperature	224
6.1.4 Coercive field (H_C) of Al/Fe/Al/Gd MLFs	226
6.1.5 Al(5)/Fe(20) and Al(5)/Gd(40) MLFs	228
6.1.6 Fe- and Gd- Spin Orientation in Al/Fe/Al/Gd MLFs	232
6.2 Conclusion	236
REFERENCES	239
APPENDICES	240
Appendix A Electromagnetic Radiation	250

CONTENTS (Continued)

	Page
Appendix B Quantization of Electromagnetic Field	260
Appendix C Hamiltonian of Electron Interacting with Electromagnetic Field	264
Appendix E Expected Compton Profile for free Electron	268
Appendix F Angular Momentum	270
CURRICULUM VITAE	290

LIST OF TABLES

Table	Page
1.1 Chart showing the sequence of work to be carried out in the investigation of magnetic layered materials.	7
1.2 Magnetic parameters of ferromagnetic substances [From C. Kittel., <i>Introduction to Solid State Physics</i> , John Wiley and Sons, Inc. 6 th ed., 1996].	100
4.1 Basic parameters of the materials, Fe, Gd, and Al [Kittel, Ed. 7th].	182
4.2 Sputtering conditions used in preparation of all the samples in this thesis.	184
4.3 Series of the samples deposited either on a polyimide film (POL) and a polyethylene film (PET).	185
4.4 Experimental conditions for MCP measurements.	191
4.5 List of XMCD's samples and of their experimental conditions.	194
6.1 Fe-spin, Gd-spin and unknown part magnetizations for $R = 5$ and 20 at the specified H and T . The samples were deposited on PET film.	229

LIST OF FIGURES

Figure	Page
1.1	Concept of the Compton scattering.....9
1.2	Schematic illustration of the concept of the Compton scattering. $\hbar k_F$: the momentum distribution on the Fermi level p : momentum of the electron to be scattered.....13
1.3	Compton profile of Li metal. [After Sakuri, 1995].....24
1.4	Compton profile of Heusler alloy, Ni ₂ MnSn. •••• : Calculated spectrum of the contribution of the Mn 3d moment (A). - - - - : Calculated spectrum of the contribution of the delocalized moment (B). - · - · - · - : Spectrum obtained by sum of A and B. ——— : Spectrum calculated by using the energy band. [After Deb, 2001]26
1.5	Electric field vectors of (a) elliptically polarized light and (b) circularly polarized light.32
1.6	Rotation of the electric vector circularly polarized light. (a) Changes of E_x and E_y in the $z = 0$ plane with time. (b) Change of \mathbf{E} with time in the $z = 0$ plane. This is the right rotation (clockwise) if it is viewed from the $z > 0$ side. It is the left rotation if viewed from the $z > 0$ side.....34
1.7	The rotation mode of the electric vector, \mathbf{E} , and the difference of

LIST OF FIGURES (Continued)

Figure	Page
phases, δ , between oscillation of the components, E_x , and E_y	35
1.8 Rotation of the electric vector as seen at different points of z	39
1.9 Linear dichroism. Upper panel: $\mu(\theta)$ vs θ , Lower panel: Direction of \mathbf{E} . \mathbf{r}_{fg} is directed toward the y axis	44
1.10 Classical electron motion in magnetic fields and the splitting of the spectral line. ω_0 is the angular frequency corresponding to the spectral line without the magnetic field. Light proceeds to the y direction in the case shown in the upper panel and to the z direction in the lower panel. $\mathbf{H} \parallel z$. \mathbf{E}_l : electric field of light. $\sigma : \mathbf{E}_l \perp \mathbf{H}, \pi : \mathbf{E}_l \parallel \mathbf{H}$	49
1.11 Zeeman splitting of atomic spectra in magnetic field. (a) The normal Zeeman triplet of Cd at 6438.47 Å ($^1P - ^1D$ transition). Upper panel: The location of the line without the magnetic field measured as light emitted with polarization in the directional parallel to the magnetic field. Lower panel: Components with the electric vector oscillating normal to the magnetic field. (b) The abnormal Zeeman splitting of the Na D lines at 5895.93 Å (D_1 line) and 5889.96 Å (D_2 line). The transition is $^2P - ^2P$. Upper panel: With magnetic field. Lower panel: Without a magnetic field. Both are not polarization resolved. (c) The	

LIST OF FIGURES (Continued)

Figure	Page
<p>abnormal Zeeman splitting of Zn $^3P_1 - ^3S_1$ lines at 4722.16 Å. The spectrum are not polarization analyzed.....</p>	56
<p>1.12 The normal Zeeman effect of the $J = 3 \rightarrow J = 2$ transition. The lines indicating transitions are the same for the $\Delta M = 1$ group, $\Delta M = 0$ group, and $\Delta M = -1$ group.</p>	57
<p>1.13 The abnormal Zeeman effect of Na D lines. ($^2S_{1/2} - ^2P_{1/2}$ and $^2S_{1/2} - ^2P_{3/2}$ transitions). Components σ correspond to transitions $\Delta M = 0$. The amounts of splitting are not the same between 2P lines and 2S lines. This gives rise to many observed lines.....</p>	58
<p>1.14 The abnormal Zeeman splitting of $^3P_1 - ^3S_1$ lines. The transition, $M = 0 \rightarrow M = 0$ with $\Delta J = 0$ is forbidden. In the figure it is shown with a broken line. This is applicable for Zn, shown in Figure 1.11.</p>	59
<p>1.15 Schematic illustration of XMCD experiments SR: synchrotron radiation. \mathbf{E}_l: Electric field vector of synchrotron radiation.....</p>	63
<p>1.16 The L_2 and L_3 absorption spectra of metallic Ni (upper panel) and the spectrum of magnetic circular dichroism (lower panel). In the upper panel, the full line is observed with right polarized light and the broken line with left polarized light. In the lower panel the difference spectrum is plotted.[After Chen, 1990]</p>	65

LIST OF FIGURES (Continued)

Figure	Page
1.17	Photo-excitation of a core electron into the empty conduction band.....71
1.18	Concept of the dipole allowed transition from the hole levels with a value of the principal quantum number of 2.....72
1.19	Transition from $2p_{1/2}$ level to the d level with various values of m . $ JM\rangle$ are indicated.73
1.20	The vector expression of the magnetic moments μ_l, μ_s and μ_j , and the angular momentums L, S and J in atoms.75
1.21	Plot of magnetic moment versus H/T (gauss/deg) for the samples of (I) potassium chromium alum, (II) ferric ammonium alum, and (III) gadolinium sulfate octahydrate. Over 99.5% magnetic saturation is achieved at a low temperature of 1.3 K and about 50,000 gauss. [After W.E. Henry, Phys. Rev. 88, 559 (1952)].....86
1.22	Density of states of the conduction electrons at absolute zero temperature ($T = 0$), (a) without magnetic field then there is no magnetic moment, (b) with applied field H , splitting of the band by magnetic energy $2\mu_B H$ occurs between the band for spins parallel (spin up) and that for spins opposite (spin down) to the field direction.....89
1.23	The alignments of magnetic moments at absolute zero temperature. (a) No alignment of adjacent magnetic moments is observed for

LIST OF FIGURES (Continued)

Figure	Page
<p>paramagnets. (b) Ferromagnets exhibit parallel alignment of adjacent magnetic moments. (c) Antiferromagnets exhibit antiparallel alignment of adjacent magnetic moments. (d) Ferrimagnets are composed of two magnetic spins of different strength and exhibit antiparallel alignment.....</p>	95
<p>1.24 Graphical determination of the spontaneous magnetization, M_{spont}. The intersection point leads to the value of M_{spont} which falls to zero at the Curie temperature T_C.....</p>	97
<p>1.25 Temperature dependence of M_{spont} of Ni for $J = 1/2$ in (1.173) (solid line) is compared with that of experimental data (open circles) [The experimental data by P. Weiss and R. Forrer].....</p>	97
<p>1.26 Two sublattices in the spinel structure. Each of these sublattices is repeated in diagonally opposite corners of the full cubic elementary cell. The two oxygen ions form a close-packed cubic lattice and the metal ions Fe^{3+} and M^{2+} are located in the interstices between the O^{2-}. The arrows indicate the up-spins and down-spin. [From D. H. Matin, <i>Magnetism in Solids</i>, London Iliffe Book LTD., 1967].....</p>	113
<p>1.27 The total spontaneous magnetization, M_{spont}, (broken lines) has various shapes depending on the combination of the sublattice magnetizations (full lines). If the saturation magnetization of sublattice A, M_{sA}, differs</p>	

LIST OF FIGURES (Continued)

Figure	Page	
<p>markedly from that of sublattice B, M_{sB}, M_{spon} show a gradual decrease falling more or less sharply to zero at T_C, and simplest ferrites show this behavior, as shown in fig (a). If M_{sA} and M_{sB} are comparable, anomalous variations occur. For example, M_{spon} may decrease to zero at an intermediate temperature, called the <i>compensation temperature</i>, T_{comp}, as shown in Fig (b). If $\lambda_{AA} \ll \lambda_{BB}$ the M_{spon} can rise to a maximum as shown in (c).</p>	117	
1.28	<p>Temperature dependence of the magnetic susceptibility in paramagnets, ferromagnets, and antiferromagnets. [From C. Kittel, <i>Introduction to Solid State Physics</i>, John Wiley and Sons, Inc. 6th ed., 1996].</p>	119
1.29	<p>The formation of domains in a single crystal of Fe. [From C. Kittel, <i>Introduction to Solid State Physics</i>, John Wiley and Sons, Inc. 6th ed., 1996]</p>	121
1.30	<p>Typical hysteresis of the magnetization curve versus the applied field.</p>	121
3.1	<p>Interlayer magnetic coupling (IMC) between magnetic films across the interlayer metallic spacer (dark shaded). The arrow in each circle indicates the magnetic moment of each monolayer sheet. These magnetic moments indicate (a) ferromagnetic coupling, (b) antiferromagnetic coupling, (c) biquadratic coupling where the</p>	

LIST OF FIGURES (Continued)

Figure	Page
magnetic moments in adjacent layers make an angle 90° to each other, and (d) the coupling between helical magnetic layers with different phase ϕ	127
3.2 Dependence of the saturation field on the spacer-layer thickness for families of (a) Co/V, (b) Co/Mo, and (c) Co/Rh multilayers. [after Parkin, December 1991].	131
3.3 Magnetization curves of the Fe(30Å)/Cr(38 Å)/Fe(30 Å) trilayer, demonstrate the biquadratic coupling between the magnetizations of Fe layers.[After Demokritov, 1998].	133
3.4 Magnetization configurations in the system of two magnetic layers separated by a non-magnetic layer.	140
3.5 Calculated magnetizations of the two magnetic layer system. The calculations are based on the mean-field theory. The magnetizations of both layers are assumed to be rotated independently with each other.	142
3.6 Oscillation of electron polarizations as a function of distance r around a single magnetic impurity. Alternatively, this figure can be viewed as the oscillatory RKKY coupling between two magnetic impurities separated by a distance r in three dimensions. Inset shows closed up the vertical axis view [After Jones, 1998].	145

LIST OF FIGURES (Continued)

Figure	Page
3.7	A schematic picture of a magnetic multilayer structure. An arrow points the direction of an electron spin, (a) possibilities of reflection and transmission of an electron in antiferromagnetic coupling system, and (b) the possibilities in ferromagnetic coupling system.147
3.8	Thickness variations in a trilayer, in which the thickness of the spacer layer varies periodically. The broken lines indicate the average magnetization direction. The heavy arrows exhibit the local variation in the magnetization direction [After Stiles, 2002].....149
3.9	Loose spin model of the biquadratic coupling. (a) the small solid arrow represents a loose spin located in the non-magnetic spacer, (b) the loose interfacial spins are locates at the two interfaces of the trilayer.....150
4.1	A schematic view of DC the diode sputtering. Dots denote electrons, solid circles denote Ar ions, and open circles denote atoms of deposited materials.....156
4.2	A schematic view of the magnetron configuration.158
4.3	A schematic view of the DC+RF magnetron sputtering.....159
4.4	Schematic diagrams showing (a) magnetic flux threading a superconducting ring, (b) Josephson junction, (c) rf-SQUID, and (d) rf-SQUID detector.....161
4.5	XMCD diagram167

LIST OF FIGURES (Continued)

Figure	Page
4.6 The DC+RF magnetron sputtering system.	169
4.7 A schematic drawing of the DC+RF magnetron sputtering system.....	170
4.8 A schematic diagram of the MPMS system.	171
4.9 MPMS magnetometer model in the Quantum Magnetism Lab.	172
4.10 Schematic diagram of the detection coils and the rf-SQUID. Upper panel: The tank circuit (detection coils). Lower panel: the output voltage curve (respond curve).....	174
4.11 A schematic diagram of the BL08W beamline.	176
4.12 Experimental equipments in the station A of the beamline BL08W	177
4.13 (a) The lay-out of Beamline BX39U and (b) the superconducting magnet system.....	180
4.14 Sample set up for magnetization measurements using SQUID.	187
4.15 M-H curve of vanish	188
4.16 SQUID sample taken by an optical microscope. The scale resolution is 0.05 cm.....	188
4.17 Preparation of MCP' sample	190
4.18 Experimental set up for MCP measurements.....	191
4.19 Sample preparation for XMCD measurements.....	193
4.20 Schematic diagram of the electric circuit for the XMCD measurement and along with the diagram of X-ray beam.	194

LIST OF FIGURES (Continued)

Figure	Page
5.1	Magnetization curves of Al/Fe/Al/Gd MLFs on POL film; a) at 5 K up to 50 kOe, b) ~h) at 5K in a low field region, and i) at 300 K.....196
5.2	Temperature dependence of magnetization ($M(T)$ curves) of the Al/Fe/Al/Gd MLFs measured at (a) 0.1 kOe and (b) 1 kOe.197
5.3	$M(H)$ curves of MLFs sputtered on PET substrates; (a) at 5K up to 50 kOe, (b)~(e) at 5 K in a low field region, and (f) at 300 K up to 50 kOe.200
5.4	$M(T)$ curves at 1 kOe of MLFs sputtered on PET substrates.201
5.5	MCPs of the sample of $R = 5$ on PET foil substrate at (a) 10 K under 1 kOe, and (b) 300 K under 1 kOe.....203
5.6	MCPs of the sample of $R = 20$ on PET foil substrate at (a) 10 K under 1 kOe, and (b) 300 K under 1 kOe.....204
5.7	XMCD and absorption spectra measured at (a) the Fe K edge (7.111 keV) at room temperature and 100 kOe, and (b) the Gd L_3 edge (7.243 keV), measured at 50 K and 100 kOe.207
5.8	Hysteresis loop of XMCD effect of the sample $R = 0$ at 280 K (solid circle) and 160 K (open circle); (a) covers a high field region, (b) a low field region. The solid lines are just for eye guide.....208
5.9	Magnetic hysteresis of XMCD effect of the sample of $R = 5$ at 5 K (open circles), 50 K (triangles), and 280 K (stars); (a) covers a high

LIST OF FIGURES (Continued)

Figure	Page
field region, (b) a low field region. The solid lines are just for eye guide.....	209
5.10 Magnetic hysteresis of XMCD effect of the sample of $R = 10$ at 5 K (open circles), 50 K (triangles), and 280 K (stars); (a) covers a high field region, (b) a low field region. The solid lines are just for eye guide.....	210
5.11 Magnetic hysteresis of XMCD effect of the sample of $R = 100$ at 5 K (open circles) and 280 K (solid circles); (a) covers a high field region, (b) a low field region. The solid lines are just for eye guide.	211
5.12 Magnetic hysteresis of XMCD effect at 5 K of the sample of $R = 5$ (open circles), $R = 10$ (triangles), and $R = 100$ (solid squares); (a) covers a high field region, (b) a low field region. The solid lines are just for eye guide.....	212
6.1 XCD effects in a low field region at 5 K for $R = 5, 10,$ and $100,$ where H is decreased from 50 kOe to -50 kOe.....	216
6.2 Hysteresis of Gd-XMCD effect of the samples of $R = 5, 10,$ and 100 at 280 K.....	218
6.3 $M(H)$ at 5 K and its derivative curves for the samples of $R = 0$ to 30 sputtered on POL film. H_f denotes an external field at the saddle-point of the derivative peaks.	220

LIST OF FIGURES (Continued)

Figure	Page
6.4	The end-point field of the kinks, H_f , versus the thickness of Al spacer at $T = 5$ K. The solid line shows a fit curve using an inverse 1 st exponential function.....221
6.5	$M(T)$ curves of MLFs on POL substrate and Al(200)/Fe MLF measured under $H = 100$ Oe. The Al thickness is denoted by R in units of Å.221
6.6	Hysteresis loops of magnetization of the samples R = 0 (POL substrate) and Al(20 Å)/Gd(40 Å) MLF (PET substrate) at 5 K.224
6.7	Coercive field (H_C) versus Al thickness. The solid line is just a simple eye guide.227
6.8	Hysteresis loops of Gd-XMCD at 5 K for the samples of R = 5 and 10 deposited on POL film.228
6.9	Fe-spin (M_{Fe}), Gd-spin (M_{Gd}), and total magnetic moments (M) in Al/Fe/Al/Gd MLFs.....234
6.10	XMCD effect and total magnetization of the sample R = 5 and 10 measured at 5 K235

CHAPTER I

INTRODUCTION

1.1 Overview of the Study

1.1.1 Introductory Remark

Since 1980, the study of magnetic layered films is one of the most popular topics in the research of magnetism. The progress of growth and deposition technologies allows scientists to be able to prepare a nearly ideal thin film and multilayer film without contamination. The new phenomena, which can be found only in films but not in bulk materials, are ones such as interlayer magnetic coupling (IMC) (Salamon et al., 1986), giant magnetoresistance (GMR) (Baibich et al., 1988), tunneling magnetoresistance (TMR), exchange bias (EB)(Meiklejohn and Bean, 1956, 1957) and interface anisotropy (Gradmann and Muller, 1968). These phenomena are completely changing the aspect of research of magnetism because of their vast applications. They have given scientists and engineers new tools for constructing remarkable new devices.

The products made by applications of magnetic layered films have been widely used in daily life. Those applications are very important commercially as found in magnetic storage media and magnetic sensors. Although, magnetic recording devices like tape and video recorders have been replaced by optical disks with much more capacity for computer memory disks, magnetic materials are still used in various

devices. For instance they are used for the data bit storage in hard disks. The semiconductor based dynamic random-access memories (DRAMs), the standard DRAMs now, will be replaced by magnetic random-access memories (MRAMs) in near the future, because MRAM is nonvolatile memory: the information is retained even the computer is switched off this leads to the higher storage density and the lower energy consumption. Another noticeable application is found in a magnetic optical disc, in which reading and writing can be achieved by the change of the magnetic state of a bit cell by laser heating. Moreover, the sophisticated magnetic sensors are widely used in industries as well as in our daily life. The noteworthy applications will be discussed in detail later.

The phenomenon chosen to study in this thesis is the interlayer magnetic coupling, which many authors call the interlayer exchange coupling. This coupling, in general, is an indirect exchange interaction between two magnetic layers through a non-magnetic metallic layer between them. In this thesis we call this layer the spacer layer. The majority of experimental achievements have been obtained using the systems that consist of the same magnetic layered materials separated by a non-magnetic metal. On the other hand, the system consisting of different magnetic materials is not many as the object materials. In the present study, experiments have been carried out on the interlayer magnetic coupling in the Fe/Al/Gd/Al multilayer film.

The thicknesses of Fe and Gd layers are fixed to be 20 Å and 40 Å respectively, while the Al thickness varies from zero to 100 Å. The interlayer coupling strength dependent on the Al thickness will be determined. The macroscopic properties of the samples are clarified by magnetization measurements. X-ray

magnetic circular dichroism (XMCD) measurements are performed on beamline BX39U at SPring-8. The results of the hysteresis of XMCD signals indicate the spin orientation of Gd. Moreover, magnetic Compton profile (MCP) technique is used to measure the ratio of the Fe magnetic moment versus to the Gd magnetic moment.

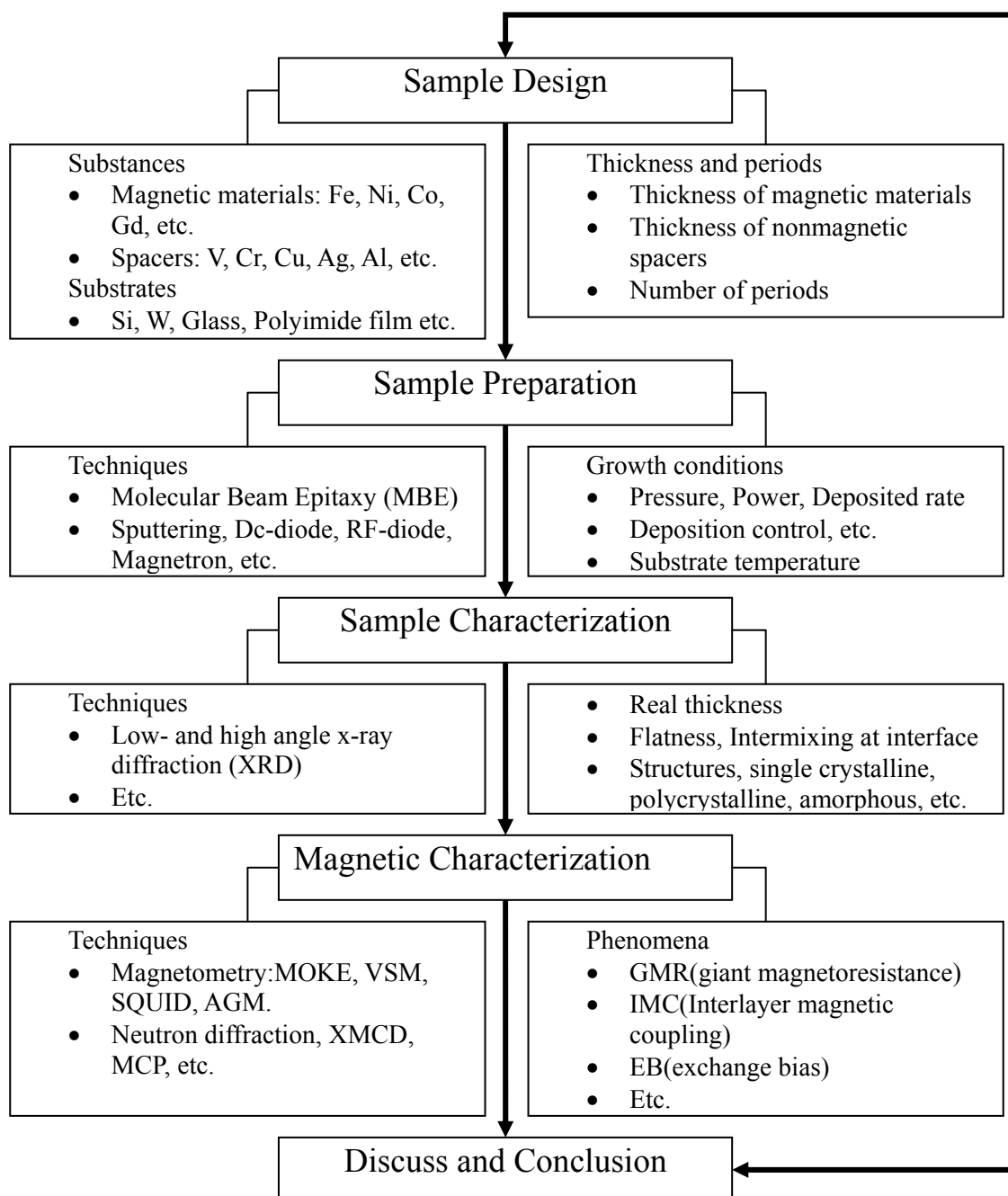
In this Chapter, the basic concept of magnetism will be overviewed, particularly for magnetism in metal. The definition and background of magnetic multilayers will be given including notable applications. In addition, the physics behind the experimental techniques used in this work, MCP, and XMCD will be briefly described.

In Chapter II, purposes of the study will be presented.

In Chapter III, the literature review on the interlayer magnetic coupling will be presented. The experimental achievements and theoretical models on interlayer exchange coupling will also be surveyed there. The key phenomena led by the interlayer exchange coupling between magnetic layers across the non-magnetic spacer such as the long-range or short-range oscillation of the bilinear coupling strength and biquadratic coupling will be reviewed. The twin model based on the mean field theory, the Ruderman-Kittel-Kasuya-Yoshida (RKKY) model and the quantum well model will be discussed in this chapter. Finally, some magnetic multilayer systems which are useful and related with the system of Fe/Al/Gd/Al will be mentioned.

In Chapter IV, experimental apparatus and experimental procedures used in the present work will be described. The experimental results will be presented in the Chapter V. Finally the discussion and conclusion will be described in the Chapter VI.

Table 1.1 Chart showing the sequence of work to be carried out in the investigation of magnetic layered materials.



1.1.2 Magnetic Multilayer

Artificially structured materials composed of layers of different phases are known generally as *heterostructures* materials. Heterostructure materials can be composed of only a few layers or of many layers. Multilayered materials have the heterostructure composed of many alternating layers that are generally stacked in a periodic manner. The multilayer structure is referred to the *superlattices*, if the layers are composed of single crystals that possess the same crystal structure and the interfaces are in the perfect atomic arrangement. Also, single crystals or large grained metallic multilayers whose component layers have different crystal structures but a well-defined epitaxial relationship at the interfaces are often referred to as superlattices.

Magnetic multilayers are usually composed of alternating layers of magnetic and non-magnetic metal spacers. Experimental researches on the magnetic multilayer may be summarized in Table 1.1. Substances and substrates are designed together with their thickness. The preparation technique and growth conditions affect to the quality of the sample considerably. The sample would be characterized basically by measuring thickness, flatness, the crystal structure, etc. Then, magnetic property of the sample can be studied by one or more techniques to observe for phenomena. Finally, discussion and conclusion of the research would be published, and new experiments can be designed systemically.

The magnetic materials, in general, are ferromagnetic transition metals (Fe, Co, Ni) and a rare-earth metal (Gd). The spacers may be *3d*-metals (V, noble metals Cu, Au, Ag), an *sp*-metal (Al), or a semi-conductor (Si). Currently, because of the applicable progress of sample preparation techniques, not only metal substrates (V,

Cr, Cu, etc.) are used, but also non-metals (Glass, Polyimide film), crystalline multilayers, the single-crystal substrates like Si, W, etc. have been used. Since magnetic property of magnetic multilayer films is significantly dependent not only on the kind of metals but also the thickness of layers. Thickness dependence of magnetic behavior has been widely studied.

Magnetic multilayer can be prepared by either chemical vapor deposition or just ordinary vacuum evaporation and deposition. It is known currently that there are two methods well suitable for preparing magnetic multilayers. They are molecular beam epitaxy (MBE) and sputtering. In both techniques, multilayer structures are fabricated by the sequential deposition onto a substrate by the alternate exposure to beams from elemental sources. In MBE, the sources may be either thermal by evaporated or evaporated by using an electron-gun. The constituent elements, the *molecular beam*, are deposited on to a heated crystalline substrate to form thin epitaxial layers. Specific growth axes, therefore, can be selected to form the crystalline multilayer (Farrow et al., 1990). On the other hand, the multilayer materials deposited by sputtering are usually polycrystalline but grown toward the direction normal to a crystallographic direction of the substrate which is usually the [111] direction in cubic metals.

There are many sputtering techniques in use today. They can be classified as the DC diode method, the RF diode method, the magnetron method, or ion beam sputtering method. All of these techniques have the same basic principle: a target is bombarded by energetic ions (usually inert gases), the atoms ejected from the target are deposited on substrates. However, the fluxes and energy of sputtered ions impacting the substrates are not the same among different sputtering methods. In

addition, the status of glow discharge causing sputter deposition is different according to the physical condition as gas pressure and the resulting growth condition is different. The magnetron sputtering is discussed in the Chapter V.

As the gas pressure is increased, the applied voltage falls, the number of working gas ions increases, but their energy decreases. Since the sputter yield increases with the number of ions and the ion energy, the total number of atoms ejected from the target depends on the gas pressure. Moreover, if the background pressure of the chamber is increased enough, the sputtered atoms can be prevented from reaching the substrate. However, even if the chamber is initially pumped down to a low pressure and the gas is of high purity, contamination may occur from outgassing, for example, of the chamber walls. Another factor is the power which is the key parameter controlling the process. The sputtering rate is proportional to the ion current incident on the target. For a constant voltage, it is therefore proportional to the input power. In the same way, the design of sputtering chamber, the distance between targets (in multi target system), the distance between the target and the cathode or the substrate, etc. can also affect the quality of the sample.

The magnetic properties of the sample, particularly the interlayer magnetic coupling, can be studied by measuring the field and temperature dependences of the direction and value of the magnetic moment of the sample. There are various techniques which provide this information. The macroscopic aspect of the magnetic moment can be measured by, such as magneto-optical Kerr effect (MOKE) magnetometry, vibrating sample magnetometry (VSM), superconducting quantum interference device (SQUID) etc.

The magnetic-optical Kerr effect (MOKE) is the change in the polarization plane and the ellipticity of light upon the reflection at the surface of magnetic materials. The difference is present only for a non-zero magnetization, and its magnitude is determined by the different magnetization components. There are three high-symmetry configurations used in MOKE measurements, which are called the polar, the longitudinal, and the transverse MOKE. For example, the polar MOKE is sensitive to the out-plane magnetization component, whereas the longitudinal one is sensitive to the in-plane magnetization component. Using all three configurations, it can in principle measure all three magnetization components.

The vibrating sample magnetometry (VSM) uses the Faraday induction effect for detecting the magnetic moment of the sample. During the measurements, the magnetic sample vibrates with a frequency ω between two pick-up coils. The coils are connected in such way that the induced voltages, which are proportional to the total magnetic moment of the sample, are added. The total voltage oscillating with the same frequency ω is measured by means of the lock-in technique, which is known to be very sensitive. As an option, one can use three pairs of pick-up coils, so that all three components of the magnetic moment can be measured simultaneously.

For the superconducting quantum interference device (SQUID), the description is made in the Chapter V. Magnetic structure in the sample can be determined by using x-rays. For example, the concomitant methods are resonant X-ray magnetic scattering (RXMS), magnetic Compton scattering (MCP), magnetic circular dichroism (XMCD). The MCP and the XMCD are discussed below.

1.1.3 Magnetic Compton Scattering

1.1.3.1 Compton Scattering in General

In this thesis, we are concerned with the magnetic Compton effects. Therefore it is useful for us to review the magnetic Compton scattering. We start with handling the simple Compton effect showing up in an elementary physics book. Suppose an X-ray photon collides with a free electron at rest. Incident X-ray photon is assumed to have energy ε_1 . By the collision, the electron is scattered toward the direction making the angle of ϕ from the incident direction. The photon loses energy and has energy ε_2 after the scattering. At the same time the electron is recoiled toward the direction making the angle ψ from the direction of the incidence of the photon. The electron is assumed to gain to E . The relation described above is presented in Figure 1.1. From the conservation of energy and momenta we have, energy conservation:

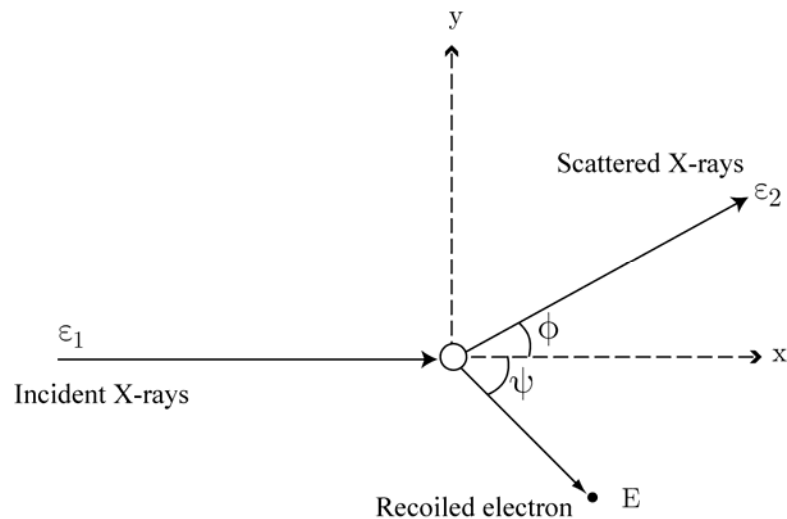


Figure 1.1 Concept of the Compton scattering

$$\varepsilon_1 = \varepsilon_2 + E - mc^2 \quad (1.1)$$

momentum conservation in x -direction:

$$p_{\lambda 1} = p_{\lambda 2} \cos \phi + p_E \cos \psi \quad (1.2)$$

momentum conservation in y -direction:

$$0 = p_{\lambda 2} \sin \phi - p_E \sin \psi \quad (1.3)$$

Here $p_{\lambda 2}$ and p_E are the momentum of the photon and the electron, respectively. $p_{\lambda 1}$ is the momentum of the incident photon. We use the relativistic relations,

$$\left. \begin{aligned} \varepsilon_2 &= cp_{\lambda 2} = \frac{hc}{\lambda_2} \\ \varepsilon_1 &= cp_{\lambda 1} = \frac{hc}{\lambda_1} \\ p_E &= \frac{mc\beta}{\sqrt{1-\beta^2}} \\ E &= mc^2\gamma \\ \gamma &= \frac{1}{\sqrt{1-\beta^2}} \\ \beta &= \frac{v}{c} \end{aligned} \right\} \quad (1.4)$$

Here m is the rest mass of the electron, v is the velocity of the electron, and λ_2 and λ_1 are X-ray wavelengths. Using relation (1.1) through (1.4), we obtain

$$\lambda_2 - \lambda_1 = \frac{h}{mc}(1 - \cos \phi) \quad (1.5)$$

This is the famous basic relation describing the wavelength shift by the Compton scattering.

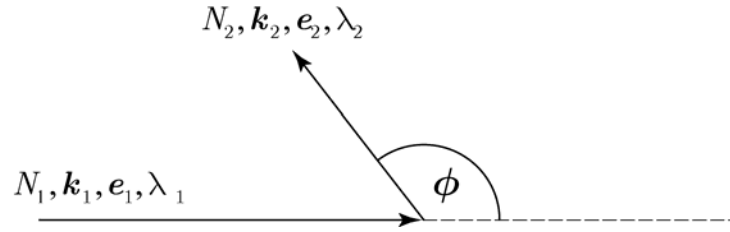
$$\lambda_C = \frac{h}{mc} \quad (1.6)$$

is called the Compton wavelength.

Inelastic X-ray scattering occurs as a result of the exchange of both energy and momentum. The spectrum of the scattered X-rays includes information on

the electronic structure that cannot be obtained by other methods. The applications of this method have been prevented by the weak intensity. The use of synchrotron radiation changed the situation very much. We will see the outline of the inelastic scattering, particularly the Compton scattering spectroscopy in what follows.

In the X-ray inelastic scattering spectroscopy, the scattering cross section is measured. Suppose incident X-rays have the intensity, N_1 ,



and X-rays scattered toward the direction making an angle of ϕ from the direction of the incidence having the intensity, N_2 . Then the cross section is defined as

$$\sigma = \frac{N_2}{N_1} \quad (1.7)$$

The intensities are dependent on the wave vector of the X-rays, k_1 and k_2 , the polarization vectors, e_1 and e_2 , and the wavelengths, λ_1 and λ_2 . The importance parameters are the energy loss and momentum transfer defined as

$$\Delta\varepsilon = h\nu_1 - h\nu_2 \quad (\text{energy loss}) \quad (1.8)$$

$$\hbar\mathbf{q} = \hbar\mathbf{k}_1 - \hbar\mathbf{k}_2 \quad (\text{momentum transfer}) \quad (1.9)$$

The scattering cross section is measured as a function of $\Delta\varepsilon$ and $\hbar\mathbf{q}$. In many cases, the momenta are described in the atomic unit; 1 a.u. is equivalent to 1.9928×10^{-19} cm·g/s. Since the wavelength is given as

$$\lambda = 2\pi / k = 2\pi \cdot \hbar / p = h / p,$$

We obtain

1 a.u. is equivalent to 3.325 \AA (wavelength)

or 1 a.u. is equivalent to 18.968 nm^{-1} (wave number, $2\pi/\lambda$)

In consideration of the basic Compton scattering phenomenon described above, we take the scattering electron to be a free electron. However, electrons in matter are bound in it. Therefore, in the Compton scattering, an X-ray photon gives a large amount of energy and momentum to the bound electron. Then the electron is excited to the state with energy high enough compare with that of the bound state. Thus, the excited electron is not affected by the potential to bound electron. Thus the excited electron, the recoiled electron in the example described above, behaves as a free electron. Therefore, the scattering spectrum, referred to as the Compton profile, reflects the momentum distribution of the ground state, the state of the electron before being ejected up to the high energy state.

The Compton profile is defined as a plot of the scattering cross section versus the momentum transfer defined in (1.9). The relation between the momentum transfer and the electron momentum in the initial state is shown in Figure 1.2. We define the electron momentum as \mathbf{p} . For simplicity, we assume that the distribution of \mathbf{p} is spherical and is given by a sphere with a radius of $\hbar k_F$ (the Fermi sphere).

Let us consider the case where the electron is at rest ($p = 0$), we obtain the result given in (1.5). The Compton wavelength given in (1.6) is 0.0243 \AA . Then, we consider the case, where p is not zero, ($p_{\max} = \hbar k_F$). We take z axis along the direction of the momentum transfer \mathbf{q} . Suppose that an X-ray photon collides with an electron moving with \mathbf{p} declined by θ from z . Then the momenta of the scattered X-rays, $\hbar \mathbf{k}_2$, has a width of the momentum transfer

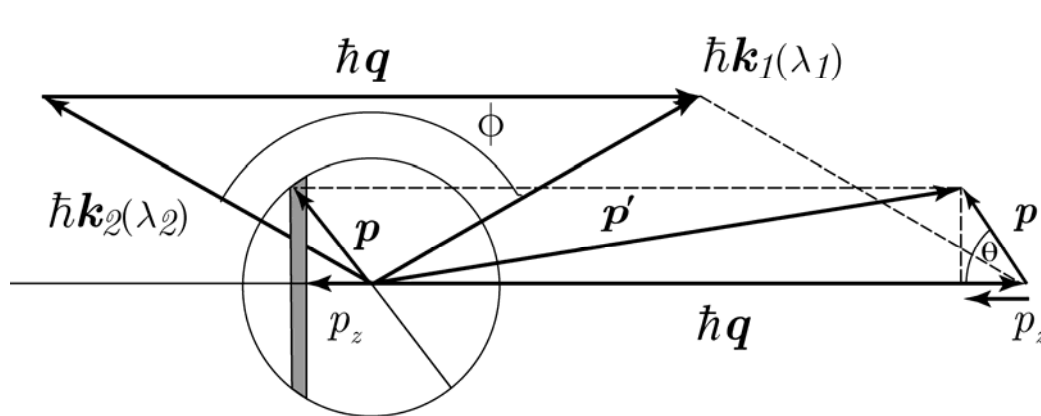


Figure 1.2 Schematic illustration of the concept of the Compton scattering. $\hbar k_F$: the momentum distribution on the Fermi level. \mathbf{p} : momentum of the electron to be scattered.

$$\hbar dq = \frac{\lambda_c}{\lambda_{20}} p \sin \phi \cos \theta \quad (1.10)$$

around $2\pi\hbar/\lambda_{20}$, where λ_{20} is equal to the value of λ_2 at $k_1 = 0$. Equation (1.10) is interpreted in the following way: First,

$$p_z = p \cos \theta \quad (1.11)$$

Then we assume the case where $k_1 = 0$. Then the distribution of q is given by δk_2 .

Then we have

$$\begin{aligned} \delta q = \delta k_2 &= \frac{2\pi}{\lambda_2^2} \delta \lambda_2 \\ &= \frac{1}{\lambda_2} 2\pi \frac{\delta \lambda_2}{\lambda_2} \\ &= \frac{\lambda_c}{\lambda_2} \sin \phi \cdot k_2 \delta \phi \end{aligned}$$

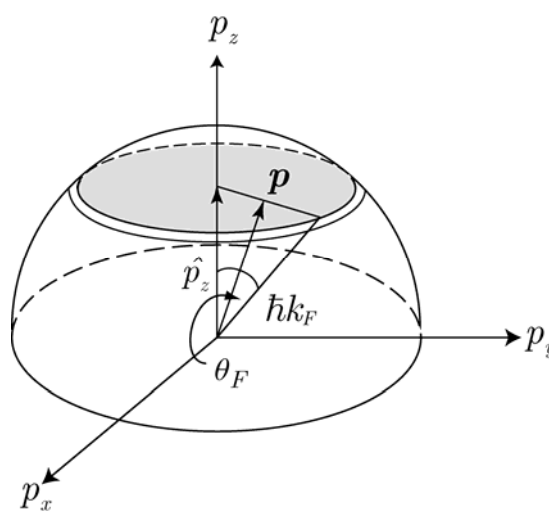
Then we have

$$\begin{aligned} \hbar \delta q &= \frac{\lambda_c}{\lambda_2} \sin \phi \cdot \hbar k_2 \delta \phi \\ &= \frac{\lambda_c}{\lambda_2} \sin \phi \cdot p_2 \delta \phi \end{aligned} \quad (1.12)$$

Figure 1.3 shows that we observed p' instead of the q because of the ambiguity caused by $p_2 \delta \phi$. The ambiguity of ϕ , $\delta \phi$, is caused by the direction of p' and the sized of p' due to p . The contribution of p to the magnitude of q is p_z . Thus we take $p_2 \delta \phi$ for p_z . Then we have (1.10) from (1.11) and (1.12).

From (1.10) we understand that the Compton profile is proportional to the density of states expressed in term of p . This is simply understood as follows: The Compton profile is given as the normalized intensity of scattered electron as a function of the momentum transfer in practice.

Equation (1.10) indicates that the momentum transfer is proportional to the electron momentum. The number of scattered electrons with a given momentum transfer is proportional to the production of the numbers of electrons, $N(p)$, with the pertinent momentum and the excitation cross section, σ , as



$$N(q) = \sigma N(p) \quad (1.13)$$

The rigorous definition is given later. The momentum distribution, $N(p)$, for the nearly-free electron is described in Appendix D.

From the consideration given above, the Compton profile is proportional to the momentum density for given p_z . It is proportional to the volume of the slice of the Fermi sphere to the surface of the slice. Thus the Compton profile is proportional to the cross section of the Fermi sphere normal to the z axis. The cross section is

$$\pi(\hat{p}_z \tan \theta_F)^2 = \pi \hbar^2 k_F^2 \cdot \sin^2 \theta_F \quad (1.14)$$

The Compton profile is proportional to p_z^2 . Thus the Compton profile has a shape of a parabola directing downward. If we consider the Compton effect as a process that an X-ray photon is first observed and subsequently it is emitted. However the emitter

electron is moving and the emitted wave has the broadening caused by the Doppler effect. Thus the Compton profile can also be understood as the Doppler broadening.

As will be shown later, the simple model described above works very well in a simple metal like alkali metals. However, the effect of the electron binding and correction cannot be ignored completely. The Compton profile of a simple metal deviated from the parabolic shape slightly. In transition metal, semiconductor and insulators, the deviation is considerable. By investigation we find the details of the Fermi sphere.

If the energy loss and the momentum transfer is not large, aspect of the inelastic scattering is different from that of the Compton scattering. In a case like this, the electronic states of the electrons are those of the whole crystal and the momentum transfer, $\hbar q$, is shared with all electrons in the crystal. The crystal potential affects the excited electrons and cannot be taken to be free. This situation is similar to the case of photoabsorption. The inelastic scattering like this is called the X-ray Raman scattering and reflects both ground state and excited state. If the ground state is one like that of $1s$ electron, the Raman spectrum reflects only the excited state.

It is decided by the relative magnitude of the electronic potential and the amount of scattering the Compton scattering. Or we can say that it is the Raman scattering or Compton scattering. Or we can say that it is decided by the relative size of the average radius of the electron orbit in the ground state versus the wavelength of the electron wave after gaining the energy from X-rays. In the limit of small q , the scattering by any electrons in matter, the inelastic X-ray scattering must be the X-ray Raman scattering. In the limit of small q , even the intermediate region, the intermediate inelastic scattering is observed. In this region, If the momentum transfer

is small, the scattering is Raman-scattering-like, and if the momentum transfer is large the scattering is Compton-scattering-like.

The distinctive aspect of the X-ray inelastic spectroscopy is that the interaction between X-rays and matter is weak. This results in the weakness of the signal to be detected. On the other hand, the contribution of multiple scattering is small and the data analysis can be carried out easily. The surface effect can be ignored; experiments can be carried out in air and this is impressive to be implemented in case of soft X-ray measurements or experiments with electron beams; these are advantages of the X-ray inelastic scattering spectroscopy. Until recently, the Compton scattering experiments have been the main stream of the X-ray inelastic scattering research. However, the inelastic X-ray scattering is invested recently from the view point that it provides us with information in the wider ranges of the excitation energy and the momentum transfer. For instance, the valence shell electronic structure can be analyzed using the dynamical structure factor, $S(\Delta\varepsilon, \mathbf{q})$ or dielectric function. The energy range of the absorption spectra to be estimated from the X-ray Raman scattering extends from the far infrared (about 1 MeV) to the soft X-ray (several 100 eV) region. In absorption measurements, the momentum distribution cannot be obtained. In order to investigate how the energy of X-ray photons or of charged particles propagates in matter, we should know the energy loss function as a function of the excitation energy, $\Delta\varepsilon$, and the momentum q . In the Compton scattering experiments in SPring-8, X-rays with energy at 115 keV from a multipole wiggler is used for primary radiation which is monochromatized with a double curved crystal monochromator. Since photon energy is high the available momentum transfer can be made large. Not only the absolute value of q but also the scattering angle is

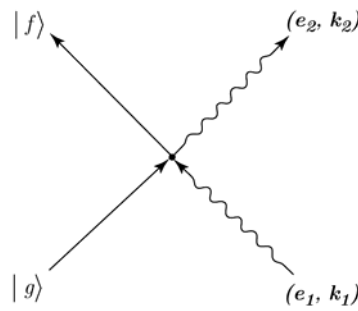
taken to be large. In NSLS, X-rays from a multipole wiggler are monochromatized with a four-crystal monochromator and the monochromatized light is focused with a toroidal mirror and used for the irradiation. In APS, eight crystals are used for monochromatization and focusing. In ESRF and SPring-8, a Bragg angle near 90° is employed and resolved band width of several milli electron volts is obtained

1.1.3.2 Cross Section

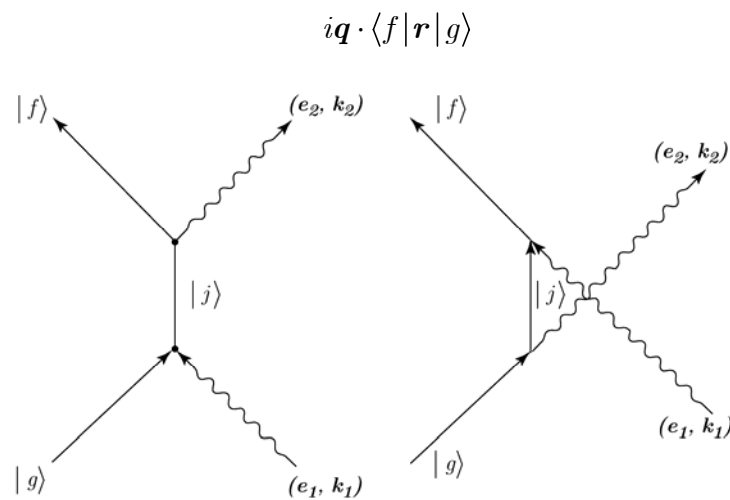
The cross section of the inelastic scattering is given by the formula called the Kramers-Heisenberg formula as

$$\frac{d^2\sigma}{d\Omega d\varepsilon_2} = r_0^2 \left(\frac{\nu_2}{\nu_1} \right) \delta(E_f - E_g + h\nu_2 - h\nu_1) \times \left| \begin{aligned} & \langle f | \exp(i\mathbf{q} \cdot \mathbf{r}) | g \rangle \mathbf{e}_1 \cdot \mathbf{e}_2 + \frac{i\hbar}{m} \sum_j \frac{\langle f | \mathbf{e}_2 \cdot \nabla | j \rangle \langle j | \mathbf{e}_1 \cdot \nabla | g \rangle}{E_f - E_g - h\nu_1 + iO^+} \\ & - \frac{i\hbar}{m} \sum_j \frac{\langle f | \mathbf{e}_1 \cdot \nabla | j \rangle \langle j | \mathbf{e}_2 \cdot \nabla | g \rangle}{E_i - E_g - h\nu_2 + iO^+} \end{aligned} \right|^2 \quad (1.15)$$

In (1.15), the differential cross section is given. σ is the cross section, Ω is the solid angle into which light is scattered, ε_2 the energy of scattered light, $\varepsilon_2 = h\nu_2$, ν_1 the frequency of incident light, E_f the final state energy of the electron system, E_g the ground state energy of the electron system, E_j the intermediate state energy of the electron system, \mathbf{e}_1 the polarization vector of incident light, \mathbf{e}_2 the polarization vector of scattered light, r_0 the classical electron radius, $|f\rangle$ the state of electron system, $|g\rangle$ the ground state of the electron system.



Equation (1.15) shows that there are three terms. The first term is zero if $\mathbf{q} \cdot \mathbf{r}$ is small and $|f\rangle$ is not equal to $|g\rangle$, since $\exp(i\mathbf{q} \cdot \mathbf{r}) = 1$ in this case. Then the delta function requires $h\nu_2 = h\nu_1$. In this case the scattering is elastic. If \mathbf{q} is large and we have to take a higher order terms in the expansion of $\exp(i\mathbf{q} \cdot \mathbf{r})$. The first order term of the expansion of $\exp(i\mathbf{q} \cdot \mathbf{r})$ is $i\mathbf{q} \cdot \mathbf{r}$. The corresponding matrix element is



and this is equal to the transition matrix element is equal to that of optical absorption. The first term of (1.15) arises from $\mathbf{A} \cdot \mathbf{A}$ term in the hamiltonian and is ignored in case of visible light, ultraviolet light, and soft X-rays, regarding inelastic scattering. The second and the third terms in (1.15) give rise to the Raman scattering. The terms arise from the perturbation $\mathbf{A} \cdot \nabla$ but in the second order.

In (1.15), the summation as to individual electron is omitted for simplicity, but we take ∇ and \mathbf{r} for expressing

$$\nabla \rightarrow \sum_n \nabla_n, \quad \mathbf{r} \rightarrow \sum_n \mathbf{r}_n,$$

respectively.

In practice, the first term in (1.15) is the leading one in the inelastic X-ray scattering. The second and the third terms are important in the resonance phenomena, but we disregard these terms here. Then the differential cross section for the inelastic scattering is given

$$\frac{d^2\sigma}{d\Omega d\varepsilon_2} = (\mathbf{e}_1 \cdot \mathbf{e}_2)^2 r_0^2 \left(\frac{\nu_2}{\nu_1} \right) \sum_f \left| \langle f | \sum_\gamma \exp(i\mathbf{q} \cdot \mathbf{r}_\gamma) | g \rangle \right|^2 \delta(E_f - E_g + h\nu_2 - h\nu_1) \quad (1.16)$$

$$\frac{d^2\sigma}{d\Omega d\varepsilon_2} = (\mathbf{e}_1 \cdot \mathbf{e}_2)^2 r_0^2 \left(\frac{\nu_2}{\nu_1} \right) \mathcal{S}(\Delta\nu, \mathbf{q}) \quad (1.17)$$

here $\Delta\nu = \nu_2 - \nu_1$, and $\mathcal{S}(\Delta\nu, \mathbf{q})$ is referred to as the dynamical structure factor.

If q is so large that the wavelength of the scattered electron wave is much smaller than the size of the valence electron location area, we have

$$q \gg \frac{1}{r}$$

and we can neglect the correlation among the valence electron positions. Then $\exp(i\mathbf{q} \cdot \mathbf{r}_\gamma)$ can be replaced with their average $\exp(i\mathbf{q} \cdot \mathbf{r})$. Then

$$\begin{aligned} \sum_f \left| \langle f | \sum_\gamma \exp(i\mathbf{p} \cdot \mathbf{r}_\gamma) | g \rangle \right|^2 &= \sum_f N \left| \langle f(\mathbf{r}) | \exp(i\mathbf{p} \cdot \mathbf{r}) | g(\mathbf{r}) \rangle \right|^2 \\ &= N \sum_f \langle g | \exp(-i\mathbf{p} \cdot \mathbf{r}) | f \rangle \langle f | \exp(i\mathbf{p} \cdot \mathbf{r}) | g \rangle \\ &= N \langle g | \exp(-i\mathbf{p} \cdot \mathbf{r}) \exp(i\mathbf{p} \cdot \mathbf{r}) | g \rangle \\ &= N \langle g | g \rangle \end{aligned}$$

$$\sum_f \left| \langle f | \sum_\gamma \exp(i\mathbf{p} \cdot \mathbf{r}_\gamma) | g \rangle \right|^2 = N \quad (1.18)$$

summation as shown in (1.18) cannot be applied to (1.16), because the δ -function restricts the selection of the state $|f\rangle$. In spite of this we remove this restriction and make the matrix part to be unity and take summation as to f for the function that satisfy the δ -function condition. In stead of total number N , we introduce the electron density that satisfy the δ -function condition. As we mentioned before, the final state of the excitation is the free electron state. By the transition the momentum of the electron changes from $\mathbf{p} = \hbar\mathbf{k}$ to $\mathbf{p} + \hbar\mathbf{q}$, then the energy of electron gained in the final state is

$$E_f = \frac{(\mathbf{p} + \hbar\mathbf{q})^2}{2m}$$

Letting the electron density ρ_p for electrons with momentum \mathbf{p} , we have

$$\mathbf{S}(\Delta h\nu, \mathbf{q}) = \int \rho_p \delta\left(\Delta h\nu - \frac{1}{2m}(\mathbf{p} + \hbar\mathbf{q})^2 + E_g(\mathbf{p})\right) d\mathbf{p} \quad (1.19)$$

Let z axis be on the direction \mathbf{q} . Then we have

$$\mathbf{S}(\Delta h\nu, \mathbf{q}) = \int \rho_p \delta\left(\Delta h\nu - \frac{\hbar^2 q^2}{2m} - \frac{\hbar q p_z}{2m} - \frac{p^2}{2m} + E_g(\mathbf{p})\right) d\mathbf{p} \quad (1.20)$$

$$\mathbf{S}(\Delta h\nu, \mathbf{q}) = \frac{m}{\hbar q} \int [\rho_p] dp_x dp_y \quad (1.21)$$

Here $[\rho_p]$ represent ρ_p that satisfy the δ -function condition. If the condition,

$$-\frac{p^2}{2m} + E_g(\mathbf{p}) \simeq 0$$

is satisfied, the δ -function condition gives us

$$p_z = \frac{m}{\hbar q} \Delta h\nu - \hbar q \quad (1.22)$$

Then \mathbf{q} can be converted to p_z . If we express $[\rho_p]$ in terms of the wave function $\chi(\mathbf{p})$, we have

$$S(\Delta h\nu, q) \propto \frac{J(p_z)}{q} \quad (1.23)$$

$$J(p_z) = \iint |\chi(\mathbf{p})|^2 dp_x dp_y \quad (1.24)$$

This is the Compton profile we measure.

In the data analyses $\chi(\mathbf{p})$ is theoretically calculated as (1.24) and obtained $J(p_z)$ is compared with experimentally observed $J(p_z)$.

1.1.3.3 Example

As already pointed out, the Compton profile reflects the electronic states of the ground state. In Figure 1.3, the Compton profile measured on a Li single crystal is shown. In the figure, the abscissa represents the momentum of the excited electron in the bound state as defined in (1.22). As mentioned already, z is the direction of the incident X-ray beam. In the measurements, the momentum transfer \mathbf{q} defined in (1.9) and the energy loss $\Delta\varepsilon = \Delta h\nu$ defined in (1.8) are obtained. The ordinate represents the dynamic structure factor, $S(\Delta h\nu, q)$, multiplied by q as defined in (1.23). The dynamic structure is given as the differential cross section defined in (1.17) and originally measured as (1.7).

We need a high technique to prepare a single crystal of Li. Since alkali metals are highly hygroscopic and cannot be exposed to air, the sample holder and its

container is specially designed. In the experiments, the crystal orientation is carefully determined.

Li metal has the electronic configuration, $1s^2 2s$. Two $1s$ electrons are core electrons and the valence electron has the $2s$ symmetry. The $2s$ electron is nearly-free electron. Thus, the Compton profile is formed by the two contributions, one from valence electrons and the other from the core electrons. In Figure 1.3, three $J(p_z)$ curves measured on three different crystallographic directions. In the figure, the experimental curves are compared with the curves theoretically calculated. The calculations were carried out by the local density functional method. The contributions of valence electrons appear in the range up to 0.5 atomic units, where the Compton profile has the upward parabolic shape. The edge of this parabola corresponds to the radius of the Fermi surface.

Careful inspection reveals the magnitude of the Fermi radius that is different slightly among the values for different crystal axes. The difference comes up to 4.6%. This indicates that even a metal like Li the energy band is not completely uniform. On the other hand, the $1s$ electron is localized. Then, it is much more delocalized in the reciprocal lattice and thus in the momentum space than the valence electrons. Thus p_z has a longer tail up to 3 atomic units.

Disagreement of the calculated data with the measured data is conspicuous in the area near $p_z = 0$. This is due to the situation that the electron correlation is not taken into account in the valence band calculation. In the Compton scattering phenomenon, the measured Compton profile is the quantity obtained by integrating non-symmetric $|\chi(\mathbf{p})|^2$ over p_x and p_y , and considerable information on

the three dimensions nature is lost. If we observe the Compton profile along various crystallographic axes, we obtain more three dimensional information. The coincident measurements of X-rays and recoiled electrons provide more direct information on $|\chi(\mathbf{p})|^2$.

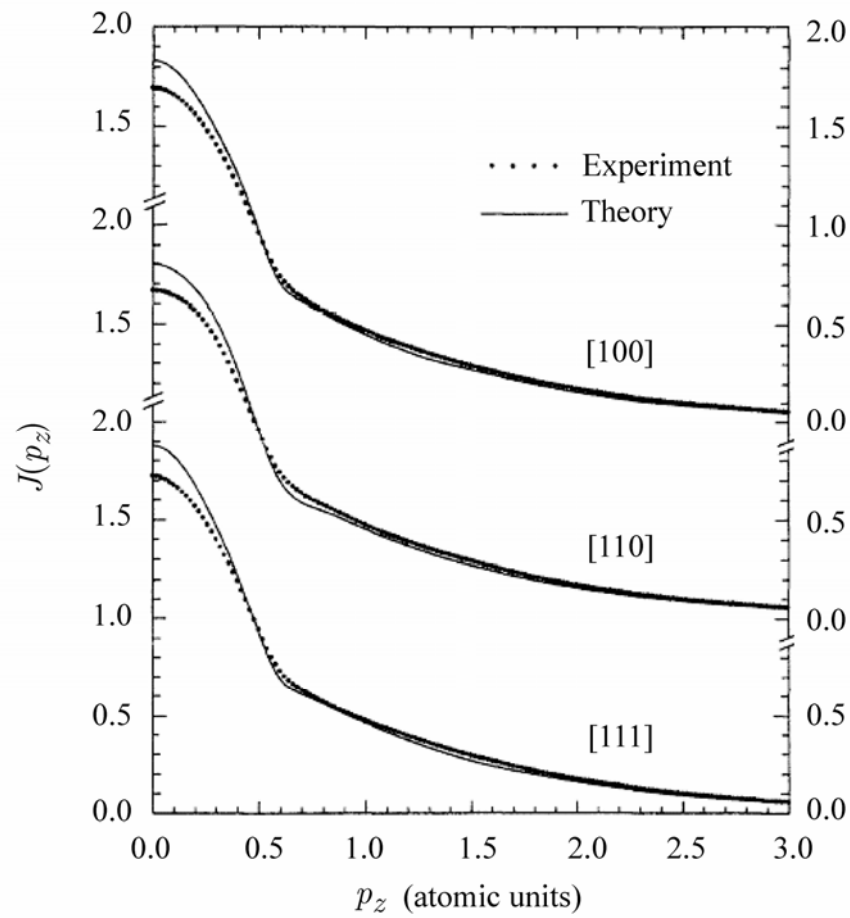


Figure 1.3 Compton profile of Li metal. [After Sakuri, 1995]

An example of the magnetic Compton scattering is shown in Figure 1.4. The figure shows the magnetic Compton profile of Ni_2MnSn . If we place a magnetic material in magnetic field and the Compton profile is measured with circularly polarized light, the difference of the Compton profiles measured with right and left polarized light gives us the Compton profile of the contribution of the orbitals only of magnetic electrons. The Compton effect in a case like this is called magnetic Compton scattering.

There are materials which are not magnetic but become magnetic if some other atoms are added to the materials. Alloys called the Heusler alloys are typical materials like this. The Heusler alloy has the composition of Cu_2MnAl . Cu can be replaced with Ni and Al can be replaced with one of Gd, In, Sn, and As. In this case, the enhancement of the magnetic moment is in $3d$ level on Mn atoms.

The sample used for the measurements illustrated in Figure 1.4, Ni_2MnSn , is a Heusler alloy. The magnetic Compton profile in Figure 1.4 is compared with the calculated data. One shown with a full line is by the energy band model. The profile calculated with localized Mn $3d$ moments and that calculated with delocalized free electrons are shown. The calculate results well reproduce the experimental data.

From the data shown in Figure 1.4, it is understood that the majority of the contribution of the spin moments to the magnetic moment of the Heusler alloy is from Mn $3d$ electrons that is widely spread in the momentum space. A small amount of the contribution from delocalized free electrons occurs near $p_z = 0$, but it gives the contribution of the negative sign. These show that the contribution of Mn $3d$ electrons localized in the real space to ferromagnetism is large but the non-vanishing

antiferromagnetic contribution from delocalized electrons also occurs. The contribution from Ni is almost zero.

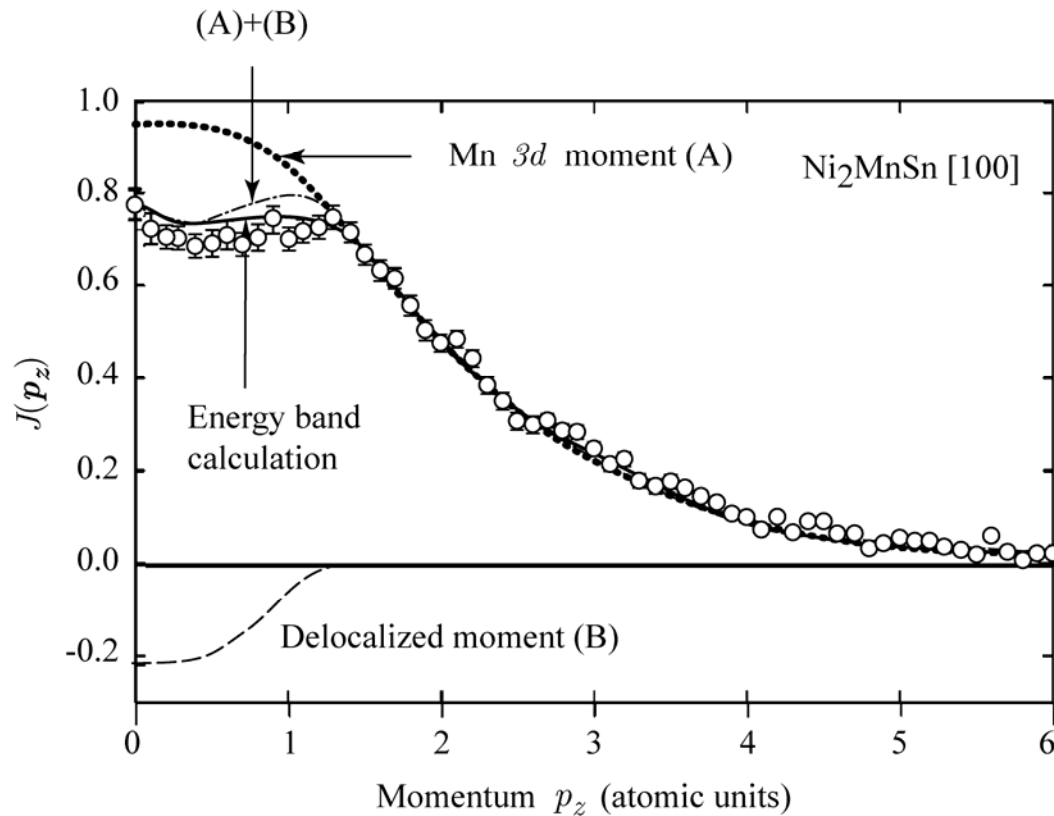


Figure 1.4 Compton profile of Heusler alloy, Ni_2MnSn . $\bullet\bullet\bullet\bullet$: Calculated spectrum of the contribution of the Mn $3d$ moment (A). $-----$: Calculated spectrum of the contribution of the delocalized moment (B). $- \cdot - \cdot - \cdot -$: Spectrum obtained by sum of A and B. $-----$: Spectrum calculated by using the energy band. [After Deb, 2001]

1.1.4 Magnetic Circular Dichroism

1.1.4.1 General Remark

In this thesis, experiments on magnetic circular dichroism are described. In this section, the related background knowledge is presented. There are two kinds of dichroism, linear dichroism and circular dichroism. The linear dichroism is the phenomena that physical quantities observed with two beams of light polarized linearly in two directions perpendicular to each other have different magnitudes. If physical quantities are measured with light polarized circularly in the left and right directions and resulting magnitudes are different, the phenomena are called the circular dichroism. The physical quantities to be measured are usually absorption coefficients, absorption rates, scattering cross section and fluorescent emission rates. In the present thesis, we restrict the quantities to ones associated with photoabsorption.

Magnetic circular X-ray dichroism (XMCD) is the difference between the absorption cross section of a ferromagnetic or ferrimagnetic compound measured with X-rays circularly polarized in the left and right directions. In this case, the dichroism is induced by a magnetic field. Thus a sample to be observed is placed in a magnetic field. Needless to say, X-rays are light with high photon energy of the short wavelength. Experimentally, this is equivalent to measuring the absorption cross section with light of fixed helicity and reversing the direction of the applied magnetic field along the direction of propagation of X-rays. Helicity is a quantity equal to the degree of polarization. We will discuss it later.

The advantage of the use of circularly polarized light arises from the fact that the absorption cross sections of magnetic materials in magnetic fields are directly proportional to the mean values of the macroscopic magnetic moments.

1.1.4.2 Polarization of Light

The polarization of light is the concept regarding the directions of the electric and magnetic vectors of the electromagnetic radiation. For example, if the electric vector is directed to the x direction. Since dichroism is the concept defined by the polarization of light, the polarization of light is dealt with in this subsection.

The wave field of light obeys Maxwell's electromagnetic equations. The solutions are given by the sum of many plane waves expressed as

$$\left. \begin{aligned} \mathbf{E} &= \mathbf{E}_0 \exp[i(\boldsymbol{\kappa} \cdot \mathbf{r} - \omega t)] \\ \mathbf{H} &= \mathbf{H}_0 \exp[i(\boldsymbol{\kappa} \cdot \mathbf{r} - \omega t)] \end{aligned} \right\} \quad (1.25)$$

Here $\boldsymbol{\kappa} \equiv 2\pi\mathbf{a}/\lambda$ is the wave vector and \mathbf{a} is the unit vector in the direction of light propagation. Maxwell's equations and their solutions are summarized in Appendix A. In many cases, it is sufficient for us to consider a single plane wave. It is the electric field of light that interacts with electrons, we consider only the electric vector in the single plane form in what follows.

In some cases, the vector potential, \mathbf{A} , of the electromagnetic field is considered. It is known that the following relations hold.

$$\left. \begin{aligned} \mathbf{H} &= \text{rot}\mathbf{A} \\ \mathbf{E} &= \frac{i\omega\mu}{c}\mathbf{A} \end{aligned} \right\} \quad (1.26)$$

Here μ is the magnetic permeability. Thus, if we find some rules concerning the polarization of \mathbf{E} , the same rules hold for \mathbf{A} . It is shown that

$$\boldsymbol{\kappa} \times \mathbf{E} = 0 \quad (1.27)$$

Thus we have

$$\boldsymbol{\kappa} \perp \mathbf{E}, \mathbf{H}, \mathbf{A} \quad (1.28)$$

This indicates that the light wave is a transversal wave. Without generality, we can choose the direction of light propagation as the z axis. Then the x and y component of the electric vector can be written as

$$\left. \begin{aligned} E_x &= E_{0x} \exp[i(\kappa z - \omega t + \delta_x)] \\ E_y &= E_{0y} \exp[i(\kappa z - \omega t + \delta_y)] \end{aligned} \right\} \quad (1.29)$$

Here, we assume that E_x and E_y have phase difference. We put

$$\tau \equiv \kappa z - \omega t \quad (1.30)$$

Then (1.29) is written as

$$\left. \begin{aligned} E_x &= E_{0x} \exp[i(\tau + \delta_x)] \\ E_y &= E_{0y} \exp[i(\tau + \delta_y)] \end{aligned} \right\} \quad (1.31)$$

In the argument of the polarization of light, we take (1.31) as expressing the light wave in general. In the consideration of the polarization of light, it is more convenient to express the light wave with the trigonometric functions as

$$\left. \begin{aligned} E_x &= E_{0x} \cos(\tau + \delta_x) \\ E_y &= E_{0y} \cos(\tau + \delta_y) \end{aligned} \right\} \quad (1.32)$$

If we eliminate τ in (1.32), we have

$$\left. \begin{aligned} \left(\frac{E_x}{E_{0x}} \right)^2 + \left(\frac{E_y}{E_{0y}} \right)^2 - 2 \left(\frac{E_x}{E_{0x}} \right) \left(\frac{E_y}{E_{0y}} \right) \cos \delta &= \sin^2 \delta \\ \delta &= \delta_y - \delta_x \end{aligned} \right\} \quad (1.33)$$

Equation (1.33) show that the components, E_x and E_y , of the vector \mathbf{E} change with time in the way that the terminal of \mathbf{E} is on an ellipse. In Figure 1.5, the ellipse is depicted. The light polarized in this manner is referred to as elliptically polarized light.

In case $\delta = 0$, (1.33) give us

$$\left(\frac{E_x}{E_{0x}} - \frac{E_y}{E_{0y}} \right) = 0 \quad (1.34)$$

This indicates that \mathbf{E} is on a straight line.

$$E_y = \frac{E_{0y}}{E_{0x}} \cdot E_x \quad (1.35)$$

The polarization like this is referred to the linear polarization. We can choose the direction of the polarization either in the x or y direction. In case $\delta = \pi$, (1.33) gives us

$$E_y = -\frac{E_{0y}}{E_{0x}} E_x \quad (1.36)$$

This is also the linearly polarized electric vector. Here we confined δ in the region

$$0 \leq \delta \leq 2\pi$$

From the periodicity, it is not necessary to consider the situation outside this region.

In case $\delta = \pi/2$ or $3\pi/2$, $\cos \delta = 0$ and $\sin^2 \delta = 1$. If

$E_{0x} = E_{0y} = E_0$ is satisfied in addition to this condition for δ , (1.33) gives us

$$E_x^2 + E_y^2 = E_0^2 \quad (1.37)$$

Thus, the end of electric vector is on a circle with a radius of E_0 when τ changes the end of \mathbf{E} moves on this circle. This is circularly polarized light. The electric vector of circularly polarized light is also shown in Figure 1.5.

Here we consider the propagation of light. The propagation of light is determined by the movement of the same phase as time passes on. Let the phase be τ_0 . Then we have from (1.30)

$$\begin{aligned} \tau_0 &= \kappa z_0 - \omega t_0 + \delta \\ &= \kappa(z_0 + \Delta z) - \omega(t_0 + \Delta t) + \delta \end{aligned} \quad (1.38)$$

Thus we have

$$\kappa\Delta z - \omega\Delta t = 0$$

Then,

$$\Delta z = \frac{\omega}{\kappa}\Delta t = c\Delta t \quad (1.39)$$

Since $\Delta t > 0$, $\Delta z > 0$. This means that light propagates from along the z axis from the minus to the plus direction. In other words, the definition of τ given by (1.30) is made as this propagation manner.

Consider the circularly polarized light. We take $\delta_x = 0$ for simplicity.

We put $\delta_y = 3\pi/2$ which is equivalent to $-\pi/2$. Then we have

$$\left. \begin{aligned} E_x &= \cos(\kappa z - \omega t) \\ E_y &= \sin(\kappa z - \omega t) \end{aligned} \right\} \quad (1.40)$$

We observe how E_x, E_y and \mathbf{E} move with time on the $z = 0$ plane. From (1.40) with $z = 0$, we have

$$\left. \begin{aligned} E_x &= \cos \omega t \\ E_y &= -\sin \omega t \end{aligned} \right\} \quad (1.41)$$

The changes of E_x and E_y with time are shown in the left panel of Figure 1.6. The corresponding change of \mathbf{E} is shown in the right panel. If we observe \mathbf{E} from the $z > 0$ side, \mathbf{E} rotates toward the right direction, namely the clockwise direction. If we observe \mathbf{E} from the $z < 0$ side, it rotates toward the left direction, the anticlockwise direction. Thus, the direction of the rotation of \mathbf{E} is opposite according to the direction of the observation. As the definition, we observe \mathbf{E} on the fixed plane from the direction from $z > 0$ to $z < 0$.

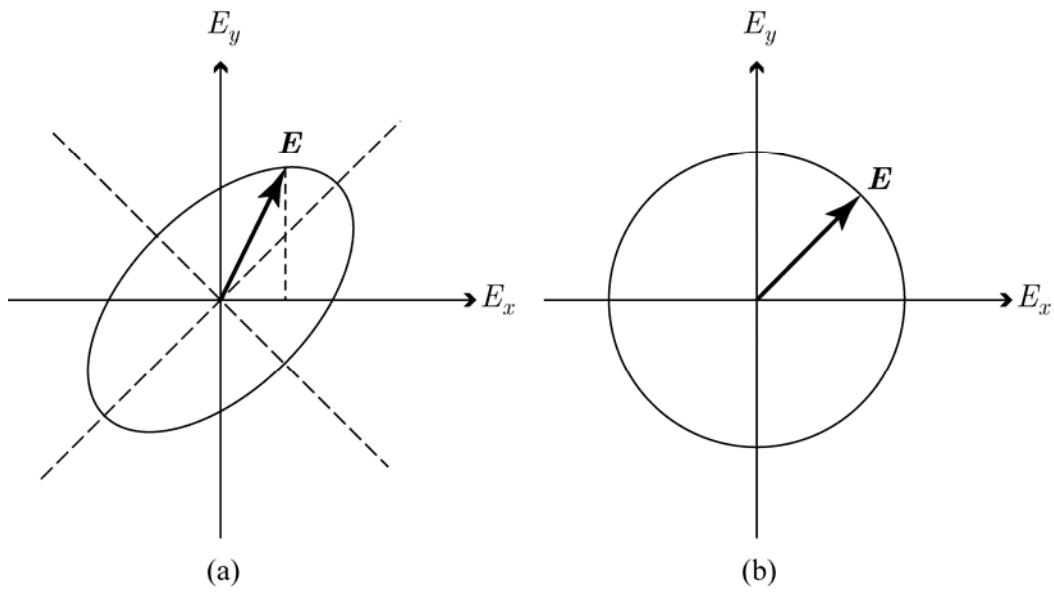


Figure 1.5 Electric field vectors of (a) elliptically polarized light and (b) circularly polarized light.

If we put $\delta = \pi/2$, we have

$$\left. \begin{aligned} E_x &= \cos \omega t \\ E_y &= \sin \omega t \end{aligned} \right\} \quad (1.42)$$

Then the rotation of \mathbf{E} is toward the left direction, i.e. the anticlockwise direction.

We put $E_{0x} = E_{0y} \equiv E_0$ as we did so far. Then we have from (1.33)

$$E_x^2 - 2E_x E_y \cos \delta + E_y^2 = E_0^2 \sin^2 \delta \quad (1.43)$$

In Figure 1.7, the mode of the rotation of the electric vector of light is shown along with the phase difference of component oscillation. In the figure, the circle and the ellipse are obtained from (1.43).

Next we see the spatial distribution of the electric vector at a fixed time.

For simplicity, we put $t = 0$. Then we have from (1.40)

$$\left. \begin{aligned} E_x &= \cos \kappa z \\ E_y &= \sin \kappa z \end{aligned} \right\} \quad (1.44)$$

This is depicted in Figure 1.8 along with \mathbf{E} . In the lower panel the trace of the terminal of \mathbf{E} is illustrated. It is spiral shaped. It should be emphasized that the spiral does not rotate with time but proceed to the $z > 0$ direction as it is.

We come back to the expression, (1.31). We put $E_{0x} = E_{0y} \equiv E_0$.

Then we have

$$\left. \begin{aligned} E_x &= E_0 e^{i\tau} \cdot e^{i\delta_x} \\ E_y &= E_0 e^{i\tau} \cdot e^{i\delta_y} \end{aligned} \right\} \quad (1.45)$$

Then we have

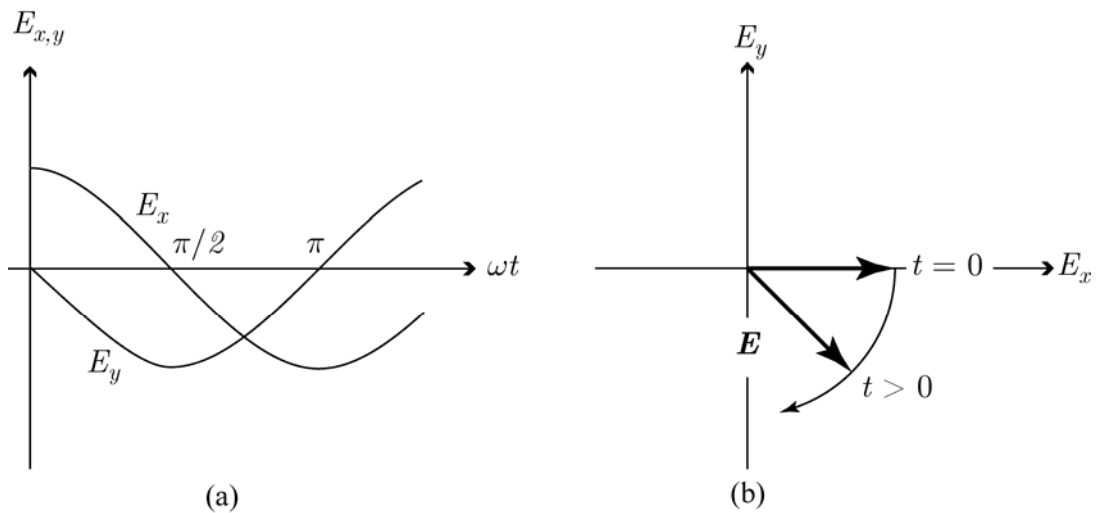


Figure 1.6 Rotation of the electric vector circularly polarized light. (a) Changes of E_x and E_y in the $z = 0$ plane with time. (b) Change of \mathbf{E} with time in the $z = 0$ plane. This is the right rotation (clockwise) if it is viewed from the $z > 0$ side. It is the left rotation if viewed from the $z < 0$ side.

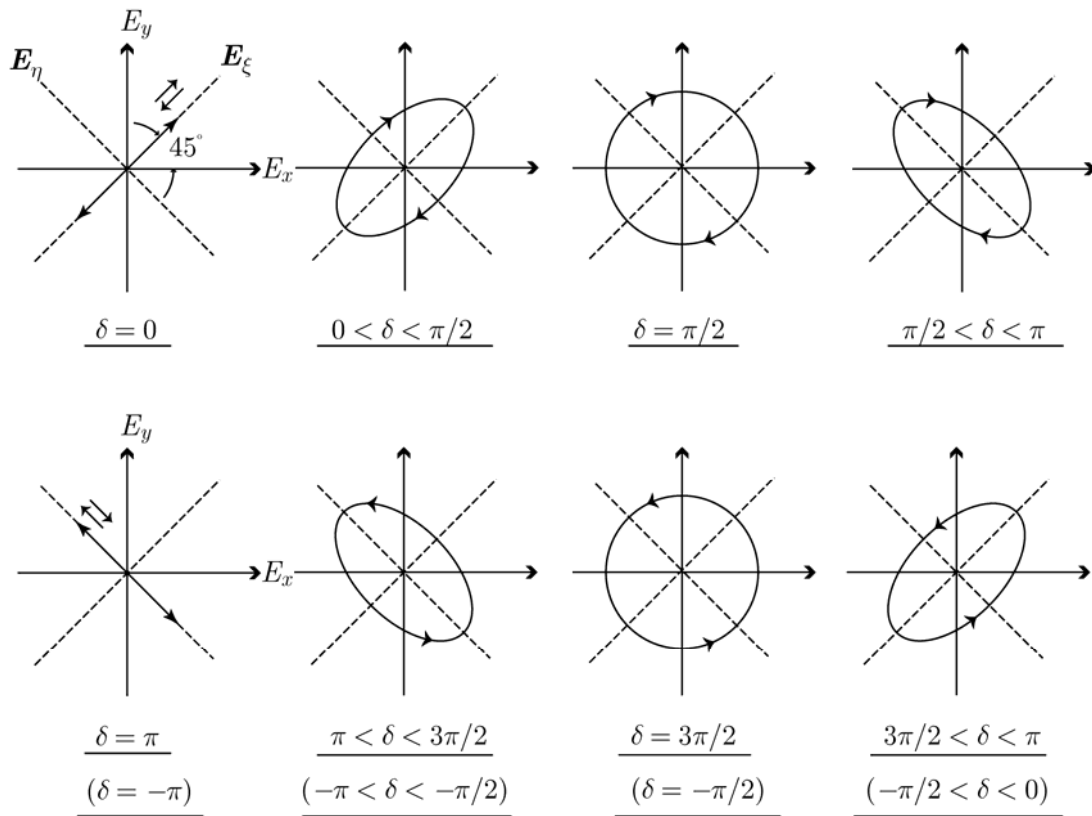


Figure 1.7 The rotation mode of the electric vector, \mathbf{E} , and the difference of phases, δ , between oscillation of the components, E_x , and E_y .

$$\frac{E_y}{E_x} = e^{i(\delta_y - \delta_x)} \equiv e^{i\delta} \quad (1.46)$$

As shown in Figure 1.7, the circularly polarized light is said to be right polarization if $\delta = \pi/2$. The circularly polarized light is said to be left polarization if $\delta = 3\pi/2$ or $-\pi/2$.

For the right polarization,

$$\frac{E_y}{E_x} = e^{i\frac{\pi}{2}} = -i \quad (1.47)$$

For the left polarization,

$$\frac{E_y}{E_x} = e^{-i\frac{\pi}{2}} = i \quad (1.48)$$

If light consists of left-and right-polarized light and the corresponding intensities are I_l and I_r , respectively. We define the degree of polarization which is equal to helicity in case of 100% polarization, as

$$h = \frac{I_l - I_r}{I_l + I_r} \quad (1.49)$$

Obviously, the helicity is equivalent to the degree of polarization.

Let us consider a wave propagating toward the z direction. According to (1.45) and (1.46), this wave can be written as

$$\mathbf{E} = \mathbf{e}_x E_x \exp i\tau + \mathbf{e}_y E_y \exp i(\tau + \delta) \quad (1.50)$$

Here \mathbf{e}_x and \mathbf{e}_y are unit vectors in the x and y axis, respectively. Now we take the regime in which E_x and E_y are given as

$$\left. \begin{aligned} E_x &= E_0 \cos \omega t \\ E_y &= E_0 \sin \omega t \\ \tau &= \kappa z \end{aligned} \right\} \quad (1.51)$$

Then (1.50) is written as

$$\mathbf{E} = E_0 \exp i\tau [\mathbf{e}_x \cos \omega t + \mathbf{e}_y \sin \omega t (\cos \delta + i \sin \delta)] \quad (1.52)$$

Now, we consider the circular polarization, then $\delta \pm \pi/2$. Then, (1.52) becomes

$$\begin{aligned} \mathbf{E} &= E_0 \exp i\tau [\mathbf{e}_x \cos \omega t + i\mathbf{e}_y \sin \omega t] \\ &= \exp i\tau [\mathbf{E}_x \pm i\mathbf{E}_y] \end{aligned} \quad (1.53)$$

Here we see that

$$\mathbf{E}_x + i\mathbf{E}_y : \text{left polarized light (anticlockwise)}$$

$$\mathbf{E}_x - i\mathbf{E}_y : \text{right polarized light (clockwise)}$$

Consider linearly polarized light proceeding toward the z direction. For simplicity, we take the direction of the polarization vector in the x axis. Then, we have

$$\begin{aligned} \mathbf{E} &= \mathbf{E}_x \exp(i\tau) \\ &= \mathbf{E}_x \exp(i\tau) + i\mathbf{E}_y \exp(i\tau) - i\mathbf{E}_y \exp(i\tau) \\ &= (\mathbf{E}_x + i\mathbf{E}_y) \exp(i\tau) + (\mathbf{E}_x - i\mathbf{E}_y) \exp(i\tau) \end{aligned} \quad (1.54)$$

This shows that the linearly polarized light consists of the left polarized light and the right polarized light. This is a very important fact. This fact is used in the explanation of the cause of the Faraday effect that the direction of the polarization vector of the linearly polarized light proceeding in a material in a magnetic field toward the direction of the magnetic field rotates in the material.

In the argument made above, we have implicitly assumed that phase δ_x generating the x component of the light vector and phase δ_y generating the y component of the light vector are constant and do not change in time. We have

assumed that, at least, difference of phases, δ , is constant. Apart from the special case of synchrotron radiation, electromagnetic radiation is emitted by atoms when they relax from the excited state to the ground state. Since this relaxation time spent to the transition is finite and short, the duration that δ is kept constant is short. The processes of the emission of photons by individual atoms are independent of each other. Thus, δ is random in ordinary light. Such light is called natural light and not polarized. We can use devices to collect only light of a given constant δ . The devices are referred to polarizers. Lasers are coherent light and polarized. The emission of light is not spontaneous but induced. Synchrotron radiation is polarized as mentioned later.

The wave field of light is quantized and form particles being referred to photons. The quantized vector potential is given by

$$\mathbf{A} = \sum_{\kappa, s} \mathbf{e}_s \frac{c}{\sqrt{\nu_s(\boldsymbol{\kappa})V}} [a_s \exp(i\boldsymbol{\kappa} \cdot \mathbf{r}) + a_s^+ \exp(-i\boldsymbol{\kappa} \cdot \mathbf{r})] \quad (1.55)$$

Here \mathbf{e}_s is a unit vector in the s direction and $s = x, y, z$. More detailed explanations are given in Appendix B. In circularly polarized light traveling toward the z direction the electric vector rotates in the xy plane. Then the vector made by \mathbf{e}_x and \mathbf{e}_y rotates in the xy plane. We consider this rotational motion as the angular motion of light generating the angular momentum. Then we consider the vector $\boldsymbol{\sigma}_{\pm}$, and define as the angular momentum of light. The circular motion occurs in the plane perpendicular to the direction of light propagation. Therefore $\boldsymbol{\sigma} \parallel z$ in this case. In general $\boldsymbol{\sigma} \parallel \boldsymbol{\kappa}$. There are two kinds of the circular motion, right and left, and so the value of $\boldsymbol{\sigma}$ takes ± 1 . We define this value $h = \pm 1$ as helicity. We do not consider helicity for linearly polarized light. In this case h may be zero.

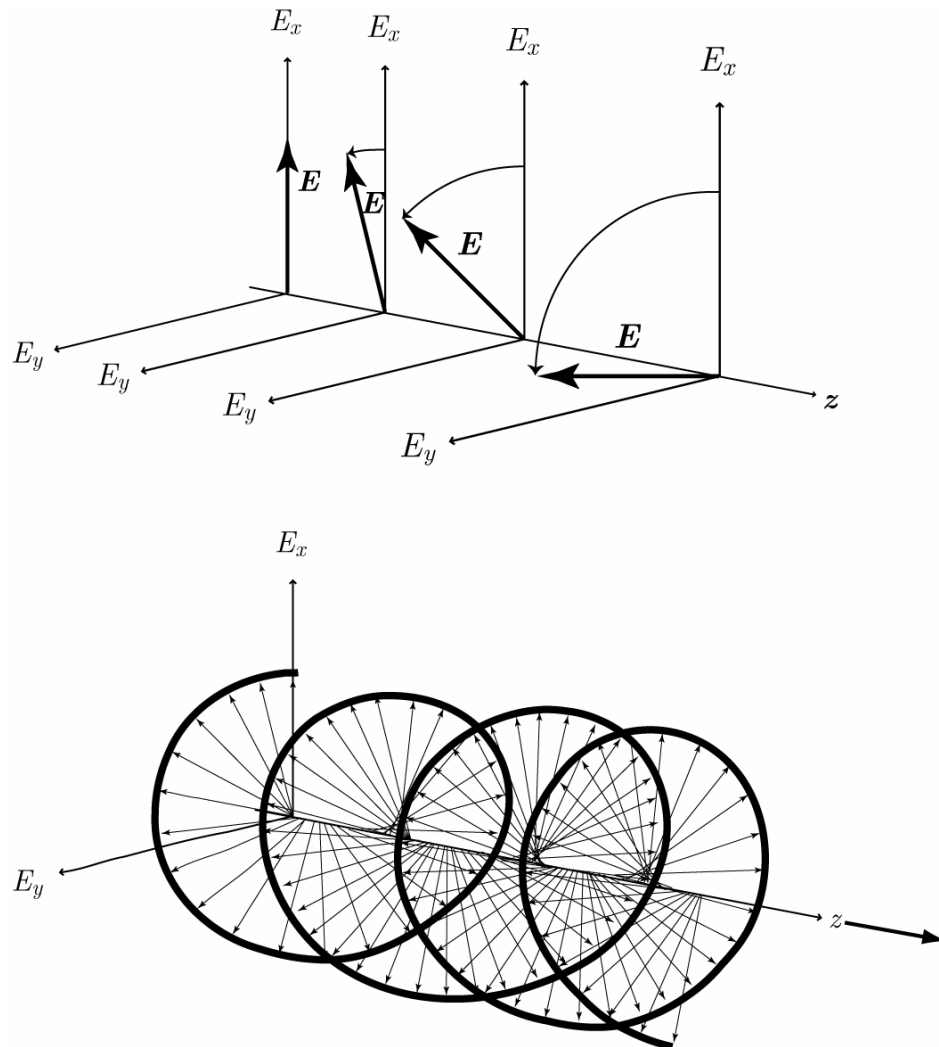


Figure 1.8 Rotation of the electric vector as seen at different points of z .

1.1.4.3 Magnetic Dichroism

We have already mentioned what dichroism is. Here in this subsection, we see the origin of the effect of the polarization of light on the optical transition. Obviously, this is inherent in the transition cross section. There are two cases of the origin of dichroism. One is that the dipole transition matrix elements or transition moments as expressed in the vector form are oriented along special crystallographic directions. Most of the causes of the linear dichroism are in this case. The other is the case that the transition moment is caused by the local orbital angular momentum. This is the case for magnetic circular dichroism (MCD).

Thus, we have to start with inspecting the transition matrix element. For doing this, we should know the form of the perturbation to give rise to the optical transition. This is described in a more detailed manner in Appendix C.

As mentioned above, the origin of the magnetic circular dichroism (MCD) has to be found in the photon-matter interaction. In the X-ray regime, MCD is not directly due to the interaction between the transverse field, \mathbf{B} , of the photon in matter and the electron spin but rather to the interaction between the orbital angular momentum of the electron and photons. The electron spin comes in the problem through the spin-orbit coupling.

The quantum field theory describes the electron-photon interaction quite well from the unified particle point of view. There, the electron waves and the electromagnetic wave are quantized and treated as corresponding particles. By this treatment, the photoabsorption and the photon-emission processes are explained naturally and smoothly. Before this method was found, the somewhat inconsistent method that leads to the same results as those of the quantum field theory had been

used. The method is called semi-classical treatment of radiation and still quite conveniently used. A semi-classical model where the atom is quantized and the electromagnetic field is described by Maxwell's equations may be used. The perturbation hamiltonian is simply written as

$$\Delta H = -\frac{e}{m} \sum_i \mathbf{A}(\mathbf{r}_i) \cdot \mathbf{p}_i + \frac{e^2}{2m} \sum_i \mathbf{A}^2(\mathbf{r}_i) - \sum_i g_i \frac{e}{m_i} \mathbf{S}_i \cdot \mathbf{B}(\mathbf{r}_i) \quad (1.56)$$

where the electrons are characterized by their mass m , their charge e , their momentum \mathbf{p} and their spin \mathbf{S} . Mathematically \mathbf{p} is given as an operator, $(\hbar/i)\nabla$. The perturbation source is described by an electromagnetic field (\mathbf{E} and \mathbf{B}) where both \mathbf{E} and \mathbf{B} are replaced with vector potential, \mathbf{A} . The number, i , distinguish electrons. The perturbation hamiltonian consists of three terms apart from the equivalent terms brought about by number i . The first is the one-photon term which gives rise to the absorption of photons. The second one is a two-photons term which does not take part in the absorption process and can thus be neglected in the present model. However this term is essential in the scattering and diffraction processes. The third term does not operate on the spatial part of the wave function. It cannot couple the ground and the excited states leading to absorption in the X-ray range. Finally only the first term:

$$\Delta H = -\frac{e}{m} \sum_i \mathbf{A}(\mathbf{r}_i) \cdot \mathbf{p}_i \quad (1.57)$$

is relevant perturbation causing X-ray absorption.

In the X-ray range of several ten kilo electron volts in which we are interested, the wavelength is not large compared with the spatial extension of the probed core level. However, we make the approximation $\exp(i\mathbf{k} \cdot \mathbf{r}) = 1$ for the

vector potential \mathbf{A} given by $\mathbf{A}_0 \exp(i\mathbf{k} \cdot \mathbf{r} - \omega t)$. This is the well-known dipolar electric approximation: $\mathbf{A} = \mathbf{A}_0 = A_0 \mathbf{a}$ where \mathbf{a} is the unit vector directing toward the electric field. We should remember that $\mathbf{E} \parallel \mathbf{A}$ as described in Appendix A. In practice, higher order terms causing the derivation from the dipolar approximation do not affect the MCD. This point will be explained later in the next section. Thus, the transition matrix element is given by

$$M_{fg} = -\frac{e}{m} \langle f | \sum_i \mathbf{A} \cdot \mathbf{p}_i | g \rangle = \alpha \langle f | \sum_i \mathbf{E} \cdot \mathbf{r}_i | g \rangle \quad (1.58)$$

Here, α is a constant factor including the X-ray frequency equal to the difference of energy between the ground and excited states. The equality of the second term to the third term is held only in the case where both $|f\rangle$ and $|g\rangle$ are the complete eigen functions of the hamiltonian.

The first order term of the exponential factor gives the electric quadrupolar contribution (15% of the total signal at the Ag K-edge: 25 keV). This quadrupolar effect may be neglected for the K-edge of $3d$ transition metals but starts to be important for $4d$ metals.

The dipolar magnetic contribution to X-ray MCD (XMCD) is negligible in the first approximation because the principal quantum number of the ground state is different from the final state. The wave functions of the ground state and final state remain orthogonal during the absorption process and the S matrix element is zero.

The transition probability from the ground state $|g\rangle$ to a final state $|f\rangle$ is given by

$$T = A \sum_f |\langle f | \mathbf{E} \cdot \mathbf{r} | g \rangle|^2 \delta(E_f - E_g - h\nu) \quad (1.59)$$

Here, E_f and E_g are the many electron energy of the final state and the ground state, respectively. $|f\rangle$ and $|g\rangle$ are the many electron final and ground states, respectively.

A is a constant. It may be simplified by using the one-electron approximation. Only one electron is excited changing its quantum number during the absorption process, while the other electrons remain spectators. Thus, we have

$$T_{fg} = \hat{A} |\langle \chi | \mathbf{E} \cdot \mathbf{r} | c \rangle|^2 \delta(E_f - E_g - h\nu) \quad (1.60)$$

where $|\chi\rangle$ is the excited state and $|c\rangle$ the core electron state electron state. The wave function associated to $|\chi\rangle$ and $|c\rangle$ are thus single electron eigen functions. \hat{A} is a constant.

The transition probability given by the equation (1.60) does not depend directly on the spin. This show that the spin is conserved in the absorption process: $\Delta S = 0$. Spin-dependent absorption will be induced in our case by the spin-orbit coupling. The spin-orbit coupling of the core hold produced by the optical excitation is larger than that of the valence electrons because the spin-orbit coupling amplitude is proportional to the potential gradient seen by the electron (or by hole).

If the transition moment is approximated as

$$\begin{aligned} \mathbf{M}_{fg} &= \langle f | \mathbf{E} \cdot \mathbf{r} | g \rangle \\ &= \mathbf{E} \cdot \langle f | \mathbf{r} | g \rangle \\ &= \mathbf{E} \cdot \mathbf{r}_{fg} \\ &= |E \cdot r| \cos \theta \end{aligned} \quad (1.61)$$

Here, θ is the angle between \mathbf{E} and \mathbf{r}_{fg} . Then the absorption coefficient is given by

$$\mu = \hat{A} M^2 \cos^2 \theta \quad (1.62)$$

Here, \hat{A} is a constant. The relation (1.62) presents the linear dichroism. Equation (1.62) shows that absorption coefficient varies as θ changes. This aspect is shown in Figure 1.9. If μ is measured for two different values of θ and the resulting μ 's are compared to each other, the orientation of the moment \mathbf{r}_{fg} in the crystal is found.

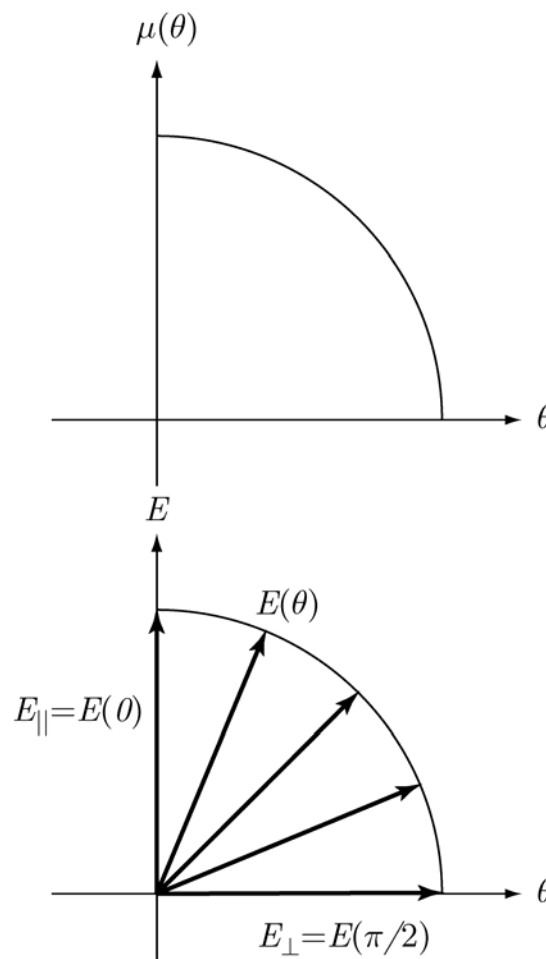


Figure 1.9 Linear dichroism. Upper panel: $\mu(\theta)$ vs θ , Lower panel: Direction of \mathbf{E} . \mathbf{r}_{fg} is directed toward the y axis.

When the moment is that for an isolated atom, the orientation relative to the external field direction is obtained. If the $\theta = 0$ direction is selected as that parallel to \mathbf{r}_{fg} and μ is measured for $\theta = 0$ and $\theta = 90^\circ$, $\mu(90^\circ)$ must be zero and we can inspect that

experimentally selected $\theta = 0$ is correct. In case $\mathbf{r}_{fg}(0^\circ) = \mathbf{r}_{fg}(90^\circ)$, we select $\theta = 0$ and $\theta = 45^\circ$. The MCD is described in the following sections.

1.1.4.4 Zeeman Effect

When we discuss MCD, we consider how the optical absorption coefficient changes in a magnetic field and how the change is related with circularly polarized light. It is well known that the spectral lines of light emitted by atoms are split when the atoms are brought into a magnetic field. This phenomenon is referred to the Zeeman effect. The emitted light is circularly polarized light. The transition moment for absorption or induced emission is different from that for spontaneous emission by a factor of $\pi^2 h \nu_{fg}^2$. Therefore it is useful to look into the Zeeman effect.

To understand the MCD transition, it is of great help to consider the classical model of a harmonic oscillator atom. The equation of motion is given by

$$n \frac{d^2 \mathbf{r}}{dt^2} + k \mathbf{r} = \mathbf{v} \times \mathbf{H} \quad (1.63)$$

Suppose the magnetic field is directed toward the z direction as

$$\mathbf{H} = (0, 0, H) \quad (1.64)$$

Setting parameter ω_0 as

$$\omega_0^2 = \frac{k}{m} \quad (1.65)$$

we have

$$\left. \begin{aligned} \frac{d^2 x}{dt^2} + \omega_0^2 x &= \frac{eH}{mc} \frac{dy}{dt} \\ \frac{d^2 y}{dt^2} + \omega_0^2 y &= \frac{eH}{mc} \frac{dx}{dt} \\ \frac{d^2 z}{dt^2} + \omega_0^2 z &= 0 \end{aligned} \right\} \quad (1.66)$$

Equation (1.66) can be reformed by setting the variables as

$$\left. \begin{aligned} \zeta_+ &= x + iy \\ \zeta_- &= x - iy \end{aligned} \right\} \quad (1.67)$$

we have

$$\left. \begin{aligned} \frac{d^2\zeta_+}{dt^2} + \omega_0^2\zeta_+ &= -2i\omega_L \frac{d\zeta_+}{dt} \\ \frac{d^2\zeta_-}{dt^2} + \omega_0^2\zeta_- &= 2i\omega_L \frac{d\zeta_-}{dt} \end{aligned} \right\} \quad (1.68)$$

Here

$$\omega_L = \frac{e\mathbf{H}}{2mc} \quad (1.69)$$

General solution of (1.68) can be written as

$$\left. \begin{aligned} \zeta_+ &= A \exp(i(-\omega_L + \sqrt{F})t) + B \exp(i(-\omega_L - \sqrt{F})t) \\ \zeta_- &= C \exp(i(\omega_L + \sqrt{F})t) + D \exp(i(\omega_L - \sqrt{F})t) \end{aligned} \right\} \quad (1.70)$$

Here parameter F is defined as

$$F = \omega_0^2 + \omega_L^2 \quad (1.71)$$

From (1.65) and (1.69), we see

$$\omega_0 \gg \omega_L \quad (1.72)$$

There we ignore ω_L in (1.71) and write (1.70) as

$$\left. \begin{aligned} \zeta_+ &= A \exp(i(-\omega_L + \omega_0)t) + B \exp(i(-\omega_L - \omega_0)t) \\ \zeta_- &= C \exp(i(\omega_L + \omega_0)t) + D \exp(i(\omega_L - \omega_0)t) \end{aligned} \right\} \quad (1.73)$$

Both ζ_+ and ζ_- can be the solutions of the original equations, (1.66). The constants

A through D are decided by the initial conditions. The solutions express the rotational motions and, therefore, we can select the conditions so that $B = D = 0$.

Putting $A = A_+, C = A_-$, we have

$$\left. \begin{aligned} \zeta_+ &= A_+ \exp(i\omega_0 t) \cdot \exp(-i\omega_L t) \\ \zeta_- &= A_- \exp(i\omega_0 t) \cdot \exp(i\omega_L t) \end{aligned} \right\} \quad (1.74)$$

From (1.66) we have

$$z = z_0 \exp(i\omega_0 t) \quad (1.75)$$

This indicates that the particle motion toward the z direction is not affected by the magnetic field directed toward the z direction. (1.74) indicates that both ζ_+ and ζ_- express circular motion. If we impose a magnetic field on the atomic system, the electron motion in the xy plane is such that extra rotational motions with frequencies, are added to the circular motion of frequency ω_0 .

We make the motion is circular by putting

$$A_+ = A_- \equiv A_0 \quad (1.76)$$

We have set

$$\omega_{\pm} \equiv \omega_0 \mp \omega_L \quad (1.77)$$

From (1.74), we have

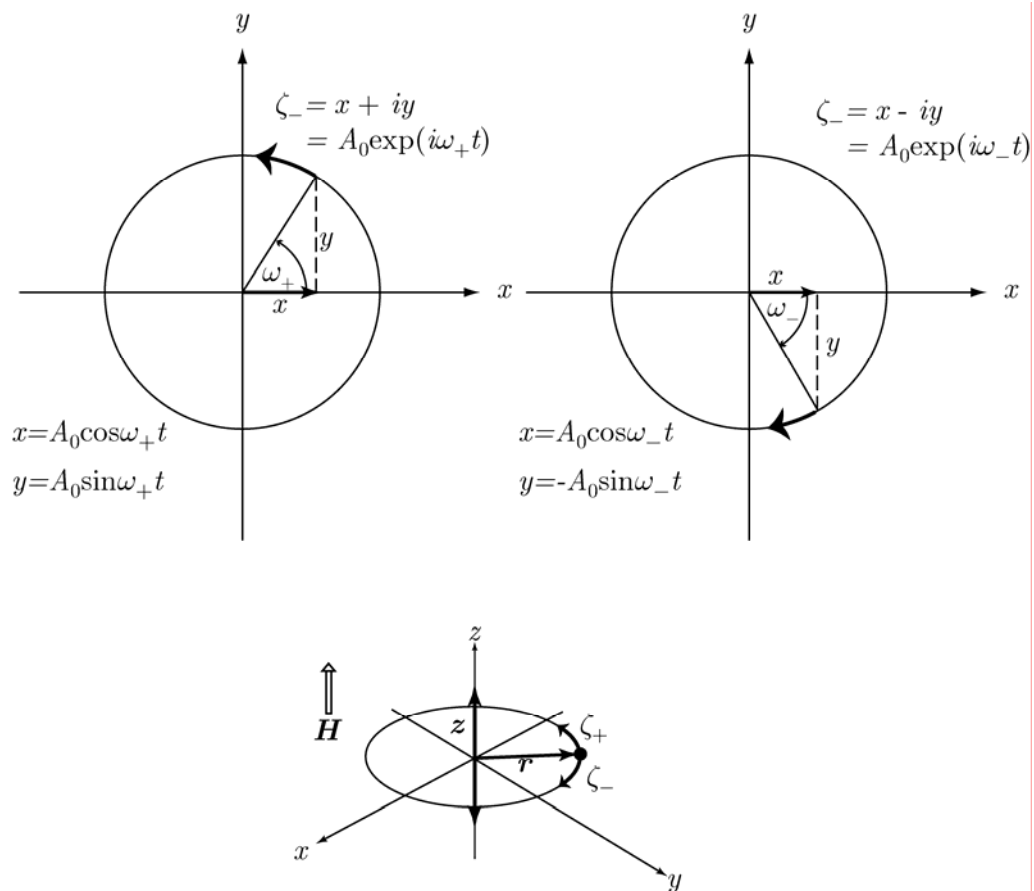
$$\zeta_{\pm} = x \pm iy \quad (1.78)$$

$$\begin{aligned} \zeta_{\pm} &= A_0 \exp(i\omega_{\pm} t) \\ &= A_0 [\cos(\omega_{\pm} t) + i \sin(\omega_{\pm} t)] \end{aligned} \quad (1.79)$$

Therefore we have

$$\left. \begin{aligned} x &= A_0 \cos(\omega_{\pm} t) \\ y &= \pm A_0 \sin(\omega_{\pm} t) \end{aligned} \right\} \quad (1.80)$$

Therefore the solutions are as depicted below.



In this way, the simple classical motions of an electron in a magnetic field are two circular motions directed opposite to each other. Classically, the circular motion of a dipole, er , reacts with circularly polarized light. The proof of this is lengthy and we understand the electron motion and the polarization of light intuitively. The corresponding splitting of the spectral line is shown in Figure 1.10 schematically.

Figure 1.10 shows that two a bound electron according to the direction of observation relative to the direction of the magnetic field. In the figure, σ represents that the direction is perpendicular to the magnetic field direction and π parallel to the magnetic field direction. As shown later, this is found in the spectral of divalent atoms. The Zeeman effect that can be explained by the classical theory is called the normal Zeeman effect.

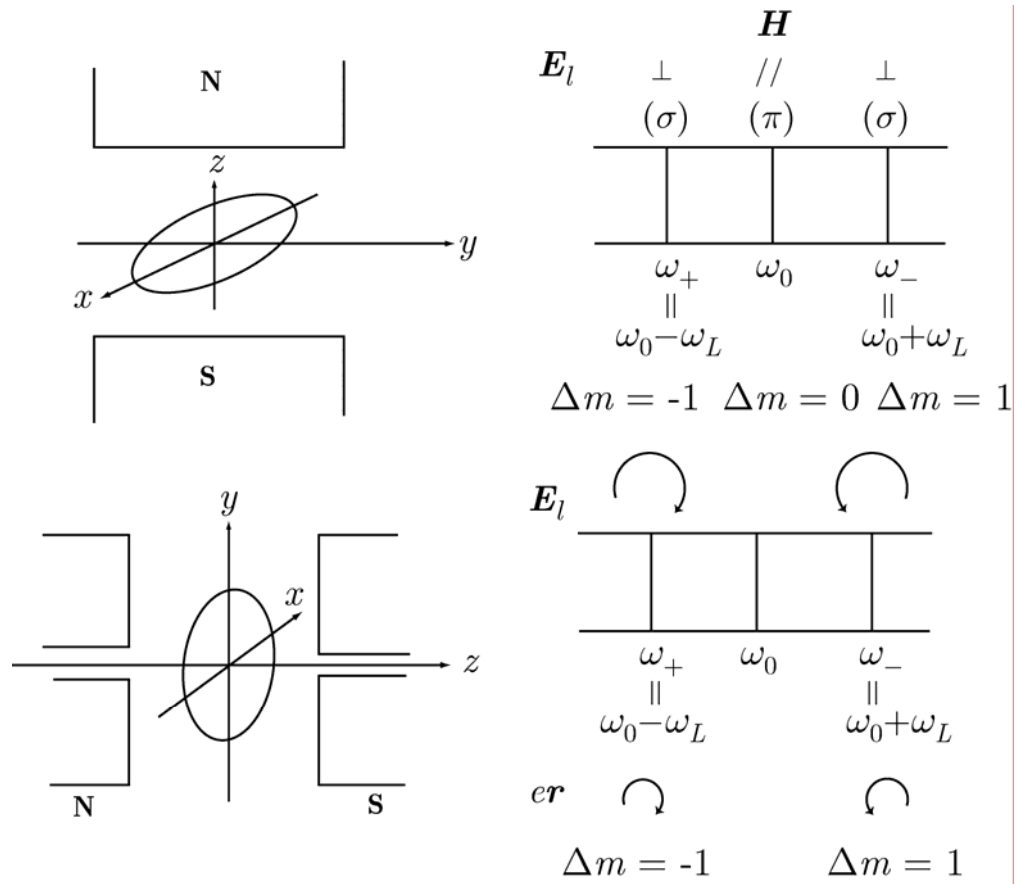


Figure 1.10 Classical electron motion in magnetic fields and the splitting of the spectral line. ω_0 is the angular frequency corresponding to the spectral line without the magnetic field. Light proceeds to the y direction in the case shown in the upper panel and to the z direction in the lower panel. $\mathbf{H} \parallel z$. \mathbf{E}_l : electric field of light. $\sigma : \mathbf{E}_l \perp \mathbf{H}, \pi : \mathbf{E}_l \parallel \mathbf{H}$.

The relation between the state of the circular polarization of excitation light and the transition probability can be found in the calculation of the transition matrix element of an isolated atom. The operator of the transition matrix element is

$$\begin{aligned}\mathbf{E} \cdot \mathbf{r} &= E_x x + E_y y + E_z z \\ &= E_x r \sin \theta \cos \phi + E_y r \sin \theta \sin \phi + E_z r \cos \theta\end{aligned}\quad (1.81)$$

Here, we use the spherical coordinate. Since

$$\cos \phi = \frac{1}{2}(e^{i\phi} + e^{-i\phi}) \quad (1.82)$$

$$\sin \phi = \frac{1}{2}(e^{i\phi} - e^{-i\phi}) \quad (1.83)$$

, we have

$$\mathbf{E} \cdot \mathbf{r} = \frac{1}{2}(E_x + iE_y)r \sin \theta \cdot e^{i\phi} + \frac{1}{2}(E_x - iE_y)r \sin \theta \cdot e^{-i\phi} + E_z r \cos \theta \quad (1.84)$$

Under the central field approximation, the eigen function of an electron of an electron is given by

$$\psi_{nlm}(r, \theta, \phi) = R_{nl}(r)Y_{lm}(\theta, \phi) \quad (1.85)$$

Thus, we have

$$\begin{aligned}\langle f | \mathbf{E} \cdot \mathbf{r} | g \rangle &= N \iiint R_{nl}^* Y_{lm}^* \mathbf{E} \cdot \mathbf{r} R_{n'l'} Y_{l'm'} r^2 \sin \theta dr d\theta d\phi \\ &= NG(l, l', m, m') \int r^3 R_{nl}^*(r) R_{n'l'}(r) dr\end{aligned}\quad (1.86)$$

$$\begin{aligned}G(l, l', m, m') &= \int d\theta P_l^{m*}(\cos \theta) P_l^m(\cos \theta) \sin^2 \theta \\ &\quad \times \left[\frac{1}{2}(E_x - iE_y) \int d\phi \exp[-i(m - m' - 1)\phi] \right. \\ &\quad \left. + \frac{1}{2}(E_x + iE_y) \int d\phi \exp[i(m - m' + 1)\phi] \right] \\ &\quad + E_z \int d\theta P_l^{m*}(\cos \theta) P_l^m(\cos \theta) \sin \theta \cos \theta \int d\phi \exp[i(m - m')\phi]\end{aligned}\quad (1.87)$$

In (1.87), the integral on r does not impose any restriction on n and n' . This means that no selection rule exists for the principal quantum number. On the other hand, $G(l, l', m, m')$ is not zero for special combinations of l, l', m , and m' . By practical calculations of (1.87), it is non-vanishing only for

$$\left. \begin{aligned} l &= l' \pm 1 \\ m &= m' \text{ or } m = m' + 1 \end{aligned} \right\} \quad (1.88)$$

These are the selection rules. They are also written as

$$\left. \begin{aligned} \Delta l &= \pm 1 \\ \Delta m &= 0, \pm 1 \end{aligned} \right\} \quad (1.89)$$

From (1.87) we find that the selection rule on l does not relate with the polarization condition of light. The selection rule on m is affected by the polarization condition.

From (1.87), we know that the transition moment satisfying the selection rule $\Delta m = 0$ vanishes if $E_z = 0$. This means that transition satisfying $\Delta m = 0$ is excited with linearly polarized light whose polarization direction is in the x axis.

The transition moment that satisfy the selection rule $\Delta m = +1$ vanishes for light having the electric vector components satisfying $E_x + iE_y = 0$. Namely it vanishes for left polarized light. ($E_x \neq E_y = i$). In the same way, the transition satisfying $\Delta m = -1$ does not occur for right polarized light. As described before, arbitrary linearly polarized light consists of right and left polarized light. Therefore we can summarize relation between the selection rules and the polarization of light as

$$\Delta m = 0 : \text{Linearly polarized light}$$

$\Delta m = +1$: Right circularly polarized light

$\Delta m = -1$: Left circularly polarized light

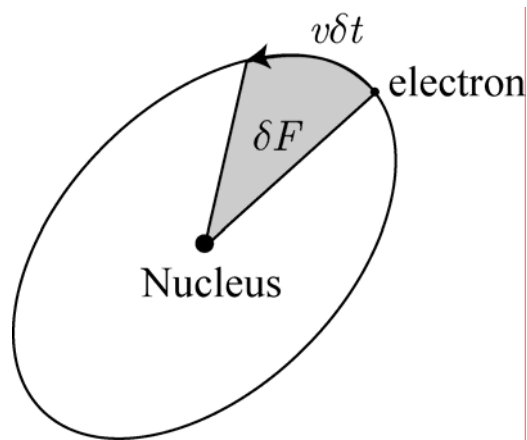
Here, we assume that light proceeds toward the z direction for the $\Delta m = \pm 1$ transition case and in the xy plane for $\Delta m = 0$ transition case.

In the practical application of the above mentioned issue of the interaction of polarized light and an electron in an atom, we have to define the coordinate system. This is equivalent to the assigning of the direction of the z axis. Since the selection of the z axis is arbitrary, in order to understand this problem, we have to define the angular momentum of the many electron system. We will discuss this problem later. However, we can understand the selection rule intuitively as follows: Unless the states specified by m are not separated, we cannot detect the states according to different values of m . In other word, the states are degenerate. If we intend to distinguish the direction of E according to the difference in m , it is equivalent to assign the coordinate system according to the difference in m . The states are degenerate regarding m . This means that the coordinate system, namely the direction in space, is degenerate.

If we apply a magnetic field to the atomic system, the degeneracy regarding m is lifted. This means the directional degeneracy is lifted. If the directional degeneracy is lifted, the direction is quantized. This is the famous concept of the directional quantization. Obviously the directional quantization is brought about by the external field. In the present case, it is convenient to select the z axis along the direction of the magnetic field. Even if we select the direction of the z axis other than that of the magnetic we rotate the coordinate mathematically so that the direction of the new z axis coincides with the direction of the magnetic field. This is

simply the problem of mathematical convenience. The directional quantization is experimentally proved by the Stern-Gerlach experiment, which shows that a beam of Ag is split into two in a non-uniform magnetic field.

Before we treat the normal Zeeman effect quantum mechanically, it is better for us to introduce two important parameters, gyro-magnetic ratio and the Bohr magneton. Let the angular momentum of an electron in an atom be \mathbf{l} . Then



$$|\mathbf{l}| = |\mathbf{r} \times \mathbf{p}| = mvr \quad (1.90)$$

Define F as $\delta F = \frac{v\delta t \cdot r}{2}$

Then, we have

$$vr = 2 \frac{dF}{dt} = 2 \frac{F}{\tau} \quad (1.91)$$

Here τ is the period of the rotation. Form (1.90) and (1.91) we have

$$|\mathbf{l}| = 2m \frac{F}{\tau} \quad (1.92)$$

The electric current generated by the electron is

$$j = \frac{e}{\tau}$$

Therefore the magnetic moment is given by

$$|\boldsymbol{\mu}| = \frac{j}{c} F = \frac{1}{c} \cdot \frac{e}{\tau} \cdot F \quad (1.93)$$

From (1.92) and (1.93), we define the gyro-magnetic ratio, γ , as

$$\gamma = \frac{|\boldsymbol{\mu}|}{|\boldsymbol{l}|} = \frac{e}{2mc} \quad (1.94)$$

If we use the general angular momentum, \boldsymbol{J} , γ is defined by

$$\boldsymbol{\mu} = -\gamma \boldsymbol{J} \quad (1.95)$$

Then averaging $\boldsymbol{\mu}$, we have

$$\langle |\boldsymbol{\mu}| \rangle = -\gamma \langle |\boldsymbol{J}| \rangle = -\gamma \hbar M \quad (1.96)$$

Here, $\langle |\boldsymbol{J}| \rangle = \hbar M$ will be discussed later. From (1.94) and (1.96) we have

$$\langle |\boldsymbol{\mu}| \rangle = -\frac{e\hbar}{2mc} \langle |\boldsymbol{J}| \rangle \equiv -\mu_B M \quad (1.97)$$

The constant $\mu_B = \frac{e\hbar}{2mc}$ is called the Bohr magneton. The general angular momentum will be explained in Appendix E .

The quantum theory of the normal Zeeman effect will be described below. First, the aspects of the Zeeman splitting of atomic spectra are shown in Figure 1.11. Examples of three elements , Cd, Na, and Zn, are illustrated. The spectra of Cd in panel (a) those for the normal Zeeman effect. The spectra of Na in panel (b) are those of the famous D lines and the abnormal Zeeman splitting. The upper panel illustrates the Zeeman split line and the lower panel the D_1 and D_2 lines without the magnetic field. The polarization analysis is not made. The Zeeman split lines of the triplet system of the Zn $^3P_1 - ^3S_1$ is shown in panel (c). This is the abnormal Zeeman

effect. The polarization analysis is not made. In this way, the spectra illustrated in Figure 1.11 show the splitting of lines under the magnetic field. The schematic energy diagram consideration is made later in Figure 1.12 through Figure 1.14. In magnetic field, the following extra term, W , is added to the hamiltonian without magnetic field.

$$\left. \begin{aligned} W &= -\boldsymbol{\mu} \cdot \mathbf{H} \\ &= \gamma \mathbf{J} \cdot \mathbf{H} \end{aligned} \right\} \quad (1.98)$$

Here we used (1.95). We select the z axis in the direction of the magnetic field. Then, as before, $\mathbf{H} = (0, 0, H)$. Then, (1.98) is

$$W = \gamma H J_z \quad (1.99)$$

In general angular momentum state $|JM\rangle$, where M is the quantum number distinguishing different J_z . In the $|JM\rangle$ system, J_z is diagonal. When $H = 0$, the energy of the angular momentum part of the hamiltonian is determined by J . The situation is explained in Appendix E.

The diagonal matrix elements of (1.99) with $|JM\rangle$ which diagonalize the hamiltonian are given by

$$\langle JM|W|JM\rangle = \gamma H \hbar M, \quad (M = J, J-1, \dots, -J) \quad (1.100)$$

This shows that the energy level assigned by the J without the magnetic field is split into equally spaced $(2J + 1)$ lines under the magnetic field. The mathematical proof of (1.100) is equivalent to the proof of

$$J_z |JM\rangle = M \hbar |JM\rangle \quad (1.101)$$

The proof of (1.101) is given in Appendix E. In the case where the central field approximation is held and electron spins can be ignored, we have

$$\mathbf{J} = \mathbf{L} \quad (1.102)$$

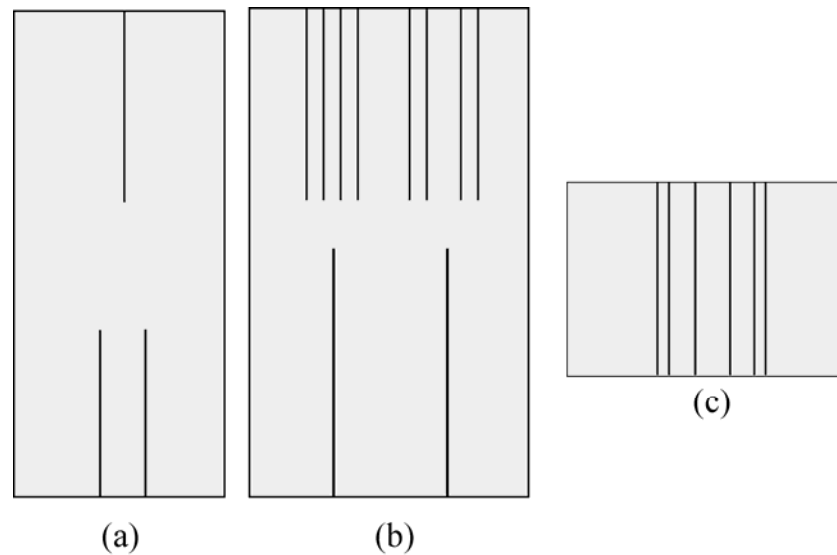


Figure 1.11 Zeeman splitting of atomic spectra in magnetic field. (a) The normal Zeeman triplet of Cd at 6438.47 \AA ($^1P - ^1D$ transition). Upper panel: The location of the line without the magnetic field measured as light emitted with polarization in the directional parallel to the magnetic field. Lower panel: Components with the electric vector oscillating normal to the magnetic field. (b) The abnormal Zeeman splitting of the Na D lines at 5895.93 \AA (D_1 line) and 5889.96 \AA (D_2 line). The transition is $^2P - ^2P$. Upper panel: With magnetic field. Lower panel: Without a magnetic field. Both are not polarization resolved. (c) The abnormal Zeeman splitting of Zn $^3P_1 - ^3S_1$ lines at 4722.16 \AA . The spectrum are not polarization analyzed.

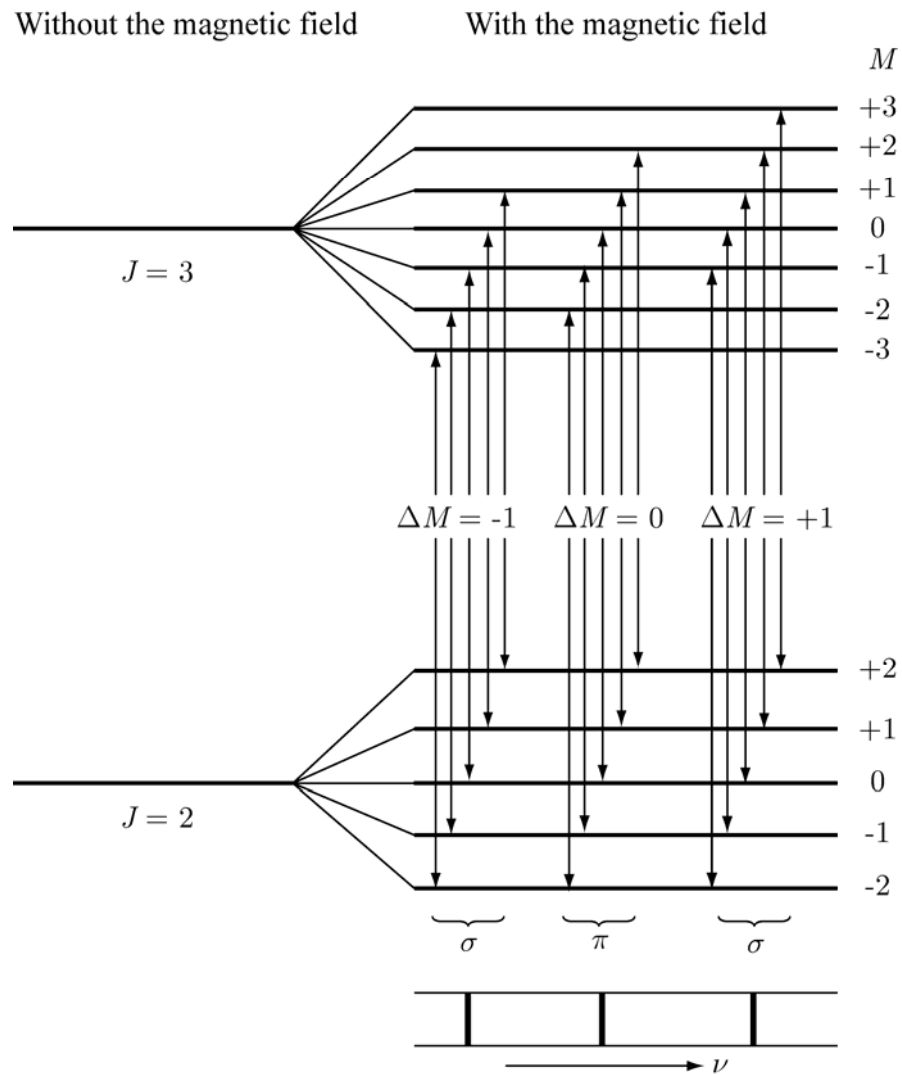


Figure 1.12 The normal Zeeman effect of the $J = 3 \rightarrow J = 2$ transition. The lines indicating transitions are the same for the $\Delta M = 1$ group, $\Delta M = 0$ group, and $\Delta M = -1$ group.

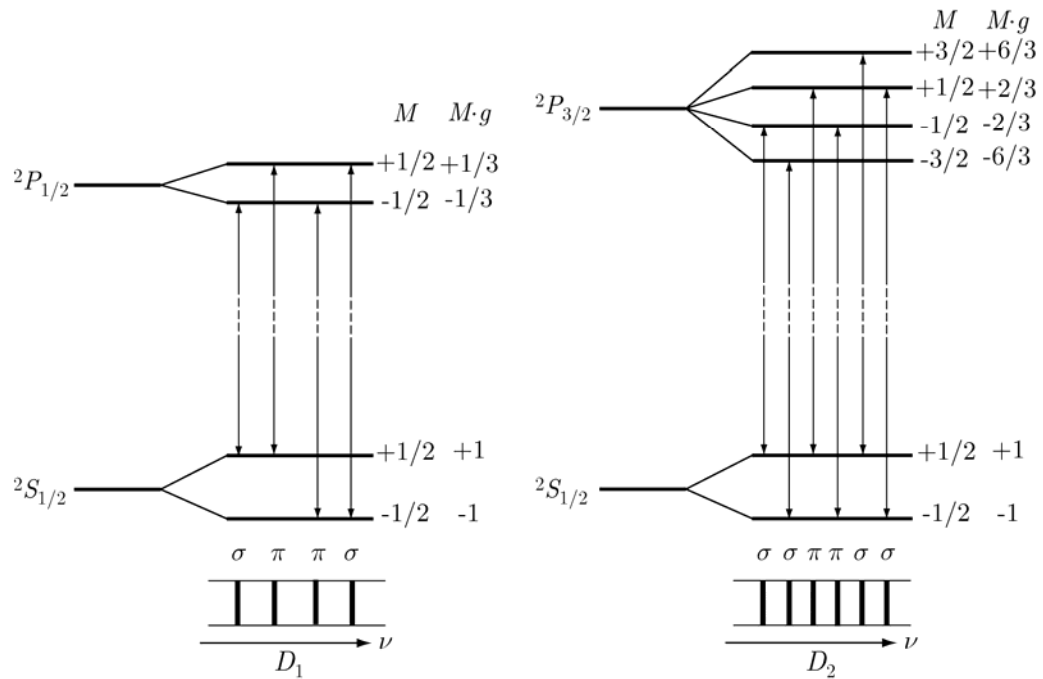


Figure 1.13 The abnormal Zeeman effect of Na D lines. ($^2S_{1/2} - ^2P_{1/2}$ and $^2S_{1/2} - ^2P_{3/2}$ transitions). Components σ correspond to transitions $\Delta M = 0$. The amounts of splitting are not the same between 2P lines and 2S lines. This gives rise to many observed lines.

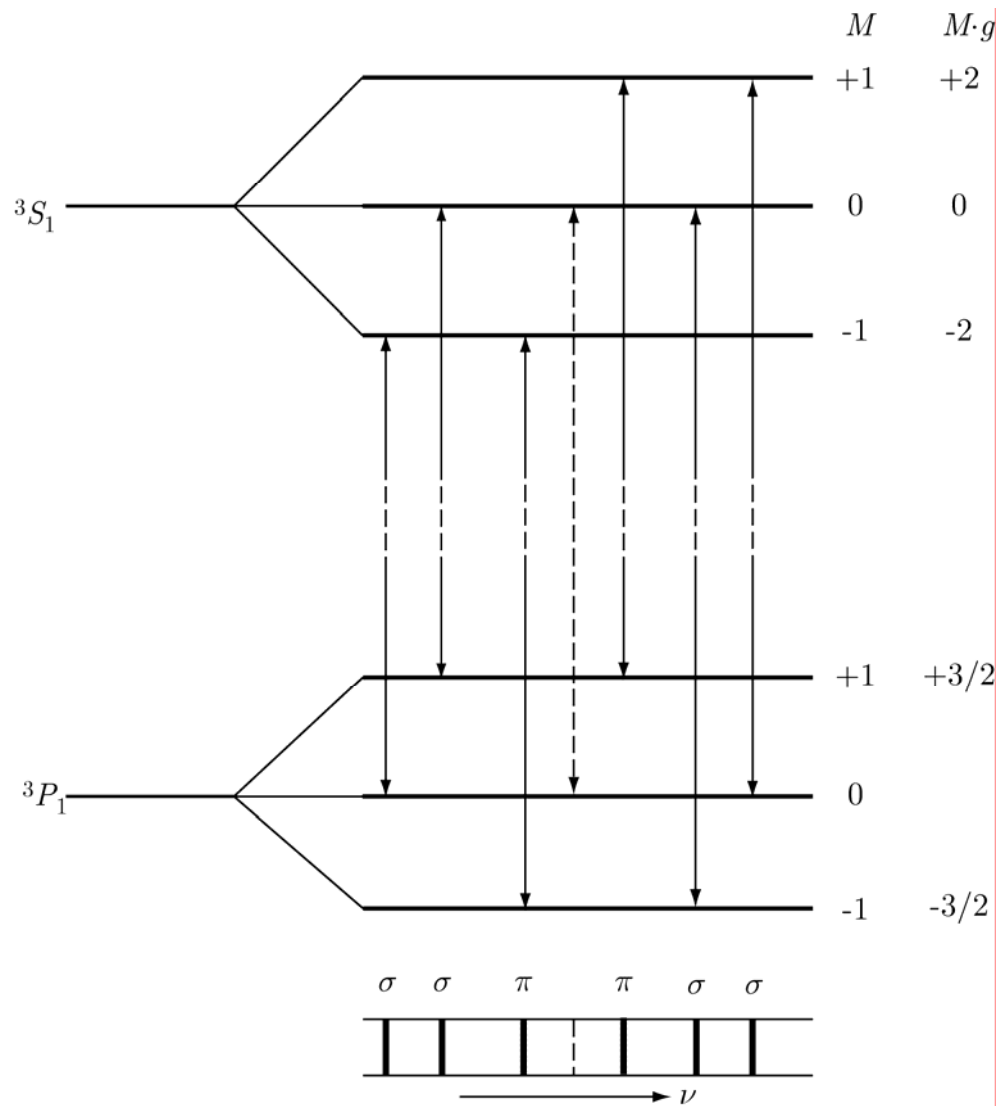


Figure 1.14 The abnormal Zeeman splitting of ${}^3P_1 - {}^3S_1$ lines. The transition, $M = 0 \rightarrow M = 0$ with $\Delta J = 0$ is forbidden. In the figure it is shown with a broken line. This is applicable for Zn, shown in Figure 1.11.

And L is obtained by simply summing up the angular momentum, l_j , of individual electrons. Then, the selection rule applicable for the state of each electron can be applied for the total electronic state. Thus, we have from (1.89)

$$\left. \begin{array}{l} \Delta L = \pm 1 \\ \Delta M = 0, \pm 1 \end{array} \right\} \quad (1.103)$$

The relation of the transition probability with the polarization of light is the same as those given already for an electron in an atom. For light proceeding toward the z direction, we have

$$\left. \begin{array}{l} \Delta M = 0 \quad : \text{Linearly polarized light} \\ \Delta M = +1 \quad : \text{Right circularly polarized light} \\ \Delta M = -1 \quad : \text{Left circularly polarized light} \end{array} \right\} \quad (1.104)$$

If the size of the level splitting for different J is equal, only the three kinds of the spectral lines can be observed. They are determined by (1.103), namely $\Delta M = 0, \pm 1$. The situation is shown in Figure 1.12. This is the normal Zeeman effect. The spectrum is brought about in the singlet system, where $S = 0$.

We have assumed that $S = 0$ for the normal Zeeman effect to be observed. However, the selection rules in (1.103) and (1.104) are valid even in case of $S \neq 0$. These rules are for the orbital part of the eigen functions and proved generally by the use of the group theory. This is out of scope in the present thesis and we use only its results.

If $S \neq 0$, the spectra are complicated. The spectral splitting observed in this case under the existence of the magnetic field is referred to as the abnormal Zeeman effect. The experimental facts are summarized as follows:

(1) The magnitude of splitting is a multiple of that of the normal Zeeman splitting by a factor of a rational number.

(2) The number of the component lines is larger than 3.

(3) The magnitude of the term splitting is different from term to term.

In other words, the size of the splitting is different if J and L are different.

Mathematically, the additional level energy is given by

$$\left. \begin{aligned} \langle W \rangle &= \hbar \omega_L M g \\ \omega_L &= \gamma H = \frac{\mu_B H}{\hbar} \end{aligned} \right\} \quad (1.105)$$

Here, ω_L is called the Larmor frequency. g is called Lande's g factor and given by

$$g = 1 + \frac{2J(J+1) + S(S+1) - L(L+1)}{2J(J+1)} \quad (1.106)$$

The proof of this is given in Appendix E. The splitting of the multiplet lines in the magnetic field and the possible transitions are shown in Figure 1.13 for the Na D lines. The selection rules are those shown in (1.103) and (1.104). That the magnitudes line splitting are different between the D_1 and the D_2 line indicates that the values of J are different between the D_1 and the D_2 lines. This can be explained by the following assumptions:

- 1) $\boldsymbol{\mu} = \boldsymbol{J}$
- 2) $\langle W \rangle = g \mu_B H \langle J_z \rangle$
- 3) $g = g(J, L)$

These lead to the conclusion that the multiplet is made by \boldsymbol{J} .

In Figure 1.14, the level splitting corresponding to abnormal Zeeman effect in the triplet system is illustrated. The corresponding energy levels are 3P_1 and 3S_1 . The element is Zn.

1.1.4.5 The use of synchrotron radiation

The Zeeman effect described so far is for emission of light in the visible region. From experimental restrictions, the absorption measurement using polarized light is not easy, particularly for X-rays. From the lack of an appropriate polarizer, the dichroism experiments have been almost impossible by use of ordinary X-rays from an X-ray tube. This situation is greatly changed by the use of synchrotron radiation.

The experimental setup is schematically illustrated in Figure 1.15. More detailed explanation of the experimental arrangement will be given later. Circularly polarized synchrotron radiation is generated with a helical wiggler installed in the storage ring. Polarized light is monochromatized by a double crystal monochromator and irradiates a sample placed in the magnetic field. The field direction is reversible.

With this arrangement, we can irradiate the sample with intense circularly polarized light and measure the absorbance. In Figure 1.15, we show a drawing of a magnet to emphasize that light proceeds toward the direction of the magnetic field. In the practical measurements a superconducting magnet was used. Then the magnet arrangement is much simpler. Synchrotron radiation from a helical wiggler is circularly polarized from the beginning. This is also simply the experimental procedure. The helical wiggler can produce both right and left polarized light by changing the relative locations of the vertical and horizontal magnet arrays.

When we use a superconducting magnet to give the magnetic field to the sample, the field direction is fixed and light helicity can be changed. The detail of the experimental arrangement will be described later. More detailed explanation on synchrotron radiation will be present later.

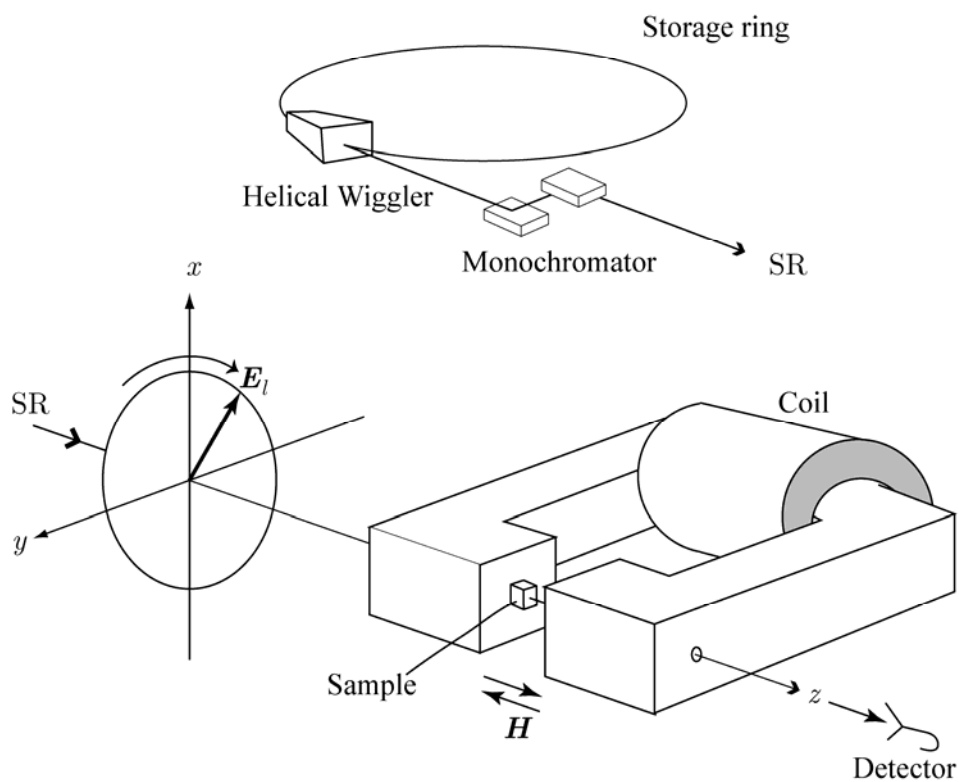


Figure 1.15 Schematic illustration of XMCD experiments SR: synchrotron radiation. E_l : Electric field vector of synchrotron radiation.

1.1.4.6 Magnetic circular dichroism

Even if we have all necessary experimental equipment and carry out the measurements the obtained data of magnetic circular dichroism cannot be interpreted easily. In the preceding subsection, we have learnt the Zeeman effect. There we learnt that we can see the interaction of matter with circularly polarized light as long as J and M are good quantum number to describe the system. In the visible to ultraviolet region the condition is fulfilled in many cases. However, this condition is not fulfilled for light in the X-ray region.

In spite of this situation, the experimental results came out first. In stead of illustrating the MCD data measured in the X-ray region, we show the MCD spectrum of metallic Ni measured in the L_2 , and L_3 spectral region. The region correspond the soft X-ray range and the $2p \rightarrow 3d$ transition observed there exhibits the angular momenta as describing the quantum state more definitely.

Since we can observe XMCD in some materials, we have to define what we observe in experiments. In the argument of XMCD, we use the helicity, σ , of measuring light which is defined in relation to (1.49) and (1.55). As we mentioned already, the helicity vector is considered to the angular momentum of light.

Another important difference of MCD from the Zeeman effect is that samples in MCD measurements are ferromagnetic or antiferromagnetic materials. Therefore we must use \mathbf{B} instead of \mathbf{H} as the magnetic field to cause the Zeeman splitting. The restricts the orientation of the sample in the magnetic field, the direction of the axis of the magnetization, the direction of the external field, and the direction of the light propagation cannot be selected independently.

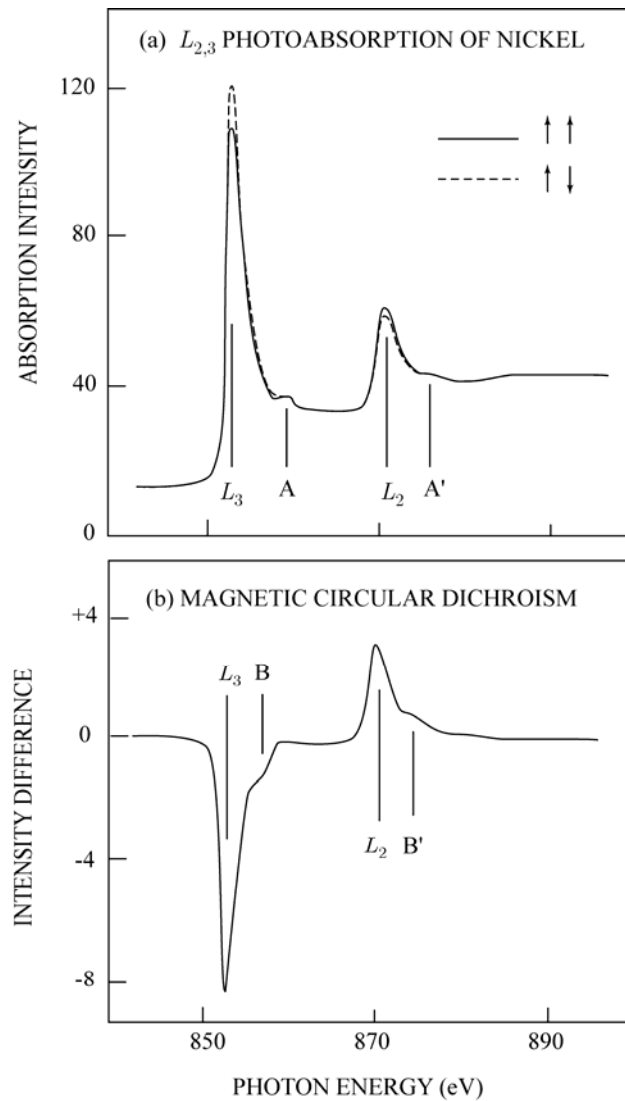
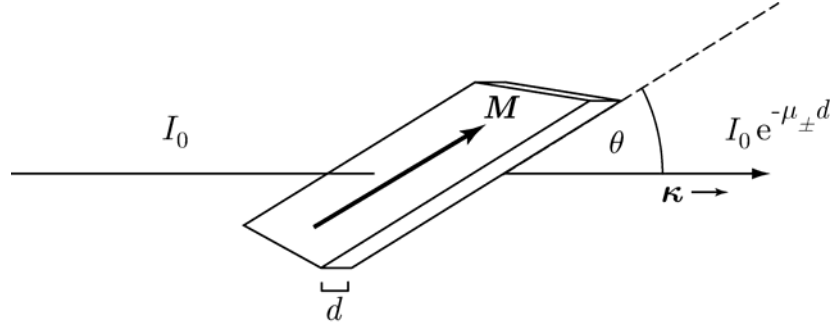


Figure 1.16 The L_2 and L_3 absorption spectra of metallic Ni (upper panel) and the spectrum of magnetic circular dichroism (lower panel). In the upper panel, the full line is observed with right polarized light and the broken line with left polarized light. In the lower panel the difference spectrum is plotted.[After Chen, 1990]



In the ideal case $M \parallel \kappa$ so that $\theta = 0$ and $B \parallel \kappa$. In the explanation of the Zeeman effect, we considered the transition probability for light with

$$E_{\pm} = E_x \pm iE_y$$

However, if we consider σ instead of E_{\pm} , the derivation of the transition moment is easier.

In magnetic circular dichroism measurements, the normalized value of the difference of absorption coefficients for light with opposite helicity are measured and analyzed.

$$\Delta I = I_+ - I_- = I_0(e^{-\mu_+ z} - e^{-\mu_- z}) = I_0 e^{-\mu_0} (\Delta\mu_+ - \Delta\mu_-) z$$

$$\Delta I = I_+ + I_- = I_0(e^{-\mu_+ z} + e^{-\mu_- z}) = I_0 e^{-\mu_0} (\Delta\mu_+ + \Delta\mu_-) z$$

$$P_c \equiv \frac{\Delta I}{I} = \frac{I_+ - I_-}{I_+ + I_-} = \frac{\Delta\mu_+ - \Delta\mu_-}{\Delta\mu_+ + \Delta\mu_-} \quad (1.107)$$

Here we assumed that

$$\mu_{\pm} = \mu_0 \pm \Delta\mu_{\pm} \quad (1.108)$$

Here, \pm corresponds to ± 1 helicity (left and right polarization). The large size of typical X-ray wavelengths in comparison with the dimensions of the orbitals of deep inner-shell electrons effectively ensures that electric dipole interactions dominate most photon-induced excitations in atoms. We consider $\exp(i\kappa \cdot r)$ being unity. This means that the transition rates are calculated by dipole matrix elements involving the

spatial wave functions of the initial and final states. However, the extension of the final state orbits and the intermediate state orbits are not small enough to satisfy

$$\boldsymbol{\kappa} \cdot \boldsymbol{r} = \frac{2\pi}{\lambda_x} \cdot r_e \ll 1 \quad (1.109)$$

Here λ_x is the X-ray wavelength and r_e is the average orbit radius. Therefore, the higher order correction as the quadrupole transition is necessary in some cases. In spite of this, we use only the dipole transition matrix elements even in the calculation of the second order perturbation calculation. This is understandable if we compare the dipole transition matrix element with the quadrupole transition matrix element. There is no explicit spin dependence and so the electronic spins remain unaltered by the transition unless they are coupled to the orbital angular momenta by a strong spin-orbit interaction.

In considering the relation of the polarization of light with the transition matrix element in case of the Zeeman effect, we have inspected the role of the electric field directly. However, we can treat this issue using a somewhat different formalism. It is conservation of angular momentum. Within the dipole approximation, one can consider the total angular momentum of the system before a photon is observed is $\boldsymbol{J} + \boldsymbol{\sigma}$. After the absorption it changes to \boldsymbol{J}' . The conservation of the angular momentum tells us

$$\boldsymbol{J}' = \boldsymbol{J} + \boldsymbol{\sigma} \quad (1.110)$$

Suppose that an atom is initially in a pure quantum state $|JM\rangle$, where M is the z component of \boldsymbol{J} . We take the z components and have

$$\begin{aligned} M' &= M + \sigma \\ \text{or } \Delta M &= \sigma = \pm 1 \end{aligned} \quad (1.111)$$

This is the selection rule for the transition with circularly polarized light. In case the core level is filled up in the ground state as is usually the case, $\mathbf{J} = 0$. Thus, the conservation of the angular momentum is written as

$$\sigma = \mathbf{J}_f \quad (1.112)$$

Where \mathbf{J}_f is the total angular momentum in the final state. In the final state, we have a hole in the core level and an excited electron above the Fermi level. If we write their angular momentum as $-\mathbf{J}$ and \mathbf{J}' , (1.112) is written as

$$\mathbf{J}' - \mathbf{J} = \sigma \quad (1.113)$$

This is the same as (1.110).

For the selection rule, (1.111), to be valid, we should have the system in which $|JM\rangle$ and $|J'M'\rangle$ are the good quantum states of the same hamiltonian. Theoretically, it appears to be difficult to establish such states. However, in formulating the selection rule, (1.103), in the Zeeman effect, we based on the selection rule, (1.89), for a single electron. We can postulate that a similar concept works in case of the inner-shell excitation. We treat the core-hole state in the final state as if the particle state exists in the initial state. Regarding the final state, we assume that the corresponding excited electron occupies the state for which the angular momentum has the well-defined quantum number. The validity of these basic assumptions arises from the experimental fact that the MCD is found in the spectra of core electron excitation. In this way, we treat the electron states involved in the inner-shell excitation by the one-electron approximation.

We have to remark the fact that a large lifetime broadening occurs in the inner shell excitation. This is caused by the cascade Auger transitions following the generation of a core hole. Thus the broadening function

$$W = \frac{Ah\nu + B}{(h\nu - h\nu_0)^2 + \Gamma^2} \quad (1.114)$$

Here $h\nu_0$ is the resonance energy near to the energy difference between the excited electron level and the core level. Γ is the interaction energy causing the lifetime broadening. A and B are constants arriving from the renormalization of various terms in the description of the interaction. In the case where A is small, (1.114) represents the well-known Lorentzian line shape function indicating the lifetime broadening. All constants occurring in (1.114) are renormalized ones and have weak energy dependence.

As mentioned already, the selection rule on the electron spin is

$$\Delta S = 0 \quad (1.115)$$

The apparent spin state change is brought about by the spin-orbit coupling. This indicates that the circular dichroism is the phenomenon caused by the orbital angular momentum. In spite of the fact we mention already, the possibility that the orbital angular momentum state in the energy band state. The schematic illustration of the electronic excitation in the energy band picture is presented in Figure 1.17. Electrons jump into the energy band. Since the electron orbits extend over the crystal, the localized angular momentum disappears. For X-rays, the dipole transition probability is low. Then, we have to take the second order effect like one we find in the scattering process into account. In this case, the absorption is the same as the resonant scattering.

The transition probability given in (1.59) must be decomposed for light of different helicity. As pointed out above, the single electron excitation picture is more convenient to understand the decomposed transition probability. In addition to this, there are sublevels in the ground state. Thus the decomposed transition probability is given by summing over the sublevels in the ground state. Then we have

$$T_{\pm} = A \sum_{f(M'),g(M)} |\langle f | \mathbf{E} \cdot \mathbf{r} | g \rangle|^2 \delta_{\pm}(\Delta M) \delta(h\nu - \varepsilon_f - \varepsilon_g) \quad (1.116)$$

$\delta_{\pm}(\Delta M)$ select the sub states satisfying the selection rule $\Delta M = \pm 1$. A is a proportionally constant. We assume that $\langle f | \mathbf{E} \cdot \mathbf{r} | g \rangle$ is a slow varying function and can be replaced with its average value M_{\pm} . Then we have

$$\begin{aligned} T_{\pm} &= M_{\pm}^2 \sum_{f(M'),g(M)} \delta(\Delta M) \delta(E_f - E_g - h\nu) \\ &= M_{\pm}^2 D_{\pm}(h\nu) \end{aligned} \quad (1.117)$$

Here $D_{\pm}(h\nu)$ represent partial joint density of states (DOS) that collect the levels of electron responding to circularly polarized light with ± 1 helicity. From (1.117) we have the MCD spectrum $P(h\nu)$ as

$$\begin{aligned} P(h\nu) &= \frac{T_+ - T_-}{T_+ + T_-} \\ &= \frac{M_+^2 D_+(h\nu) - M_-^2 D_-(h\nu)}{M_+^2 D_+(h\nu) + M_-^2 D_-(h\nu)} \end{aligned} \quad (1.118)$$

If $M_+^2 \simeq M_-^2$, we have

$$P(h\nu) = \frac{D_+(h\nu) - D_-(h\nu)}{D_+(h\nu) + D_-(h\nu)} \quad (1.119)$$

In the discussion made above, we have assumed perfect polarization of excitation light. In practice, this is not the case. Therefore, the dichroism observed is reduced by a factor p_c . Then we have

$$P(h\nu) = \frac{D_+(h\nu) - D_-(h\nu)}{D_+(h\nu) + D_-(h\nu)} \quad (1.120)$$

In Figure 1.18 and Figure 1.19, two additional explanations are presented. We have assumed that the concepts depicted there are obvious.

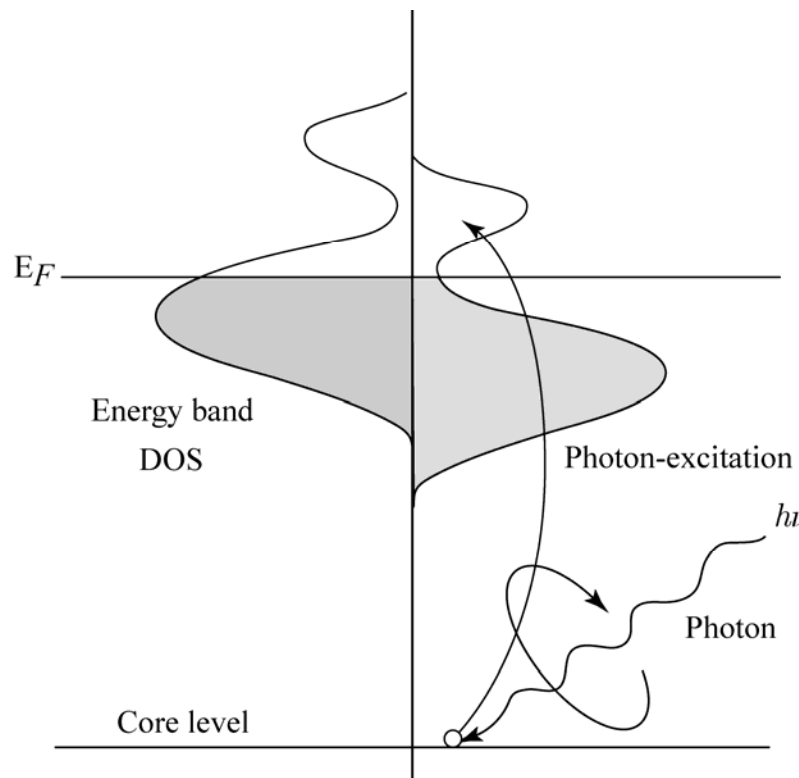


Figure 1.17 Photo-excitation of a core electron into the empty conduction band.

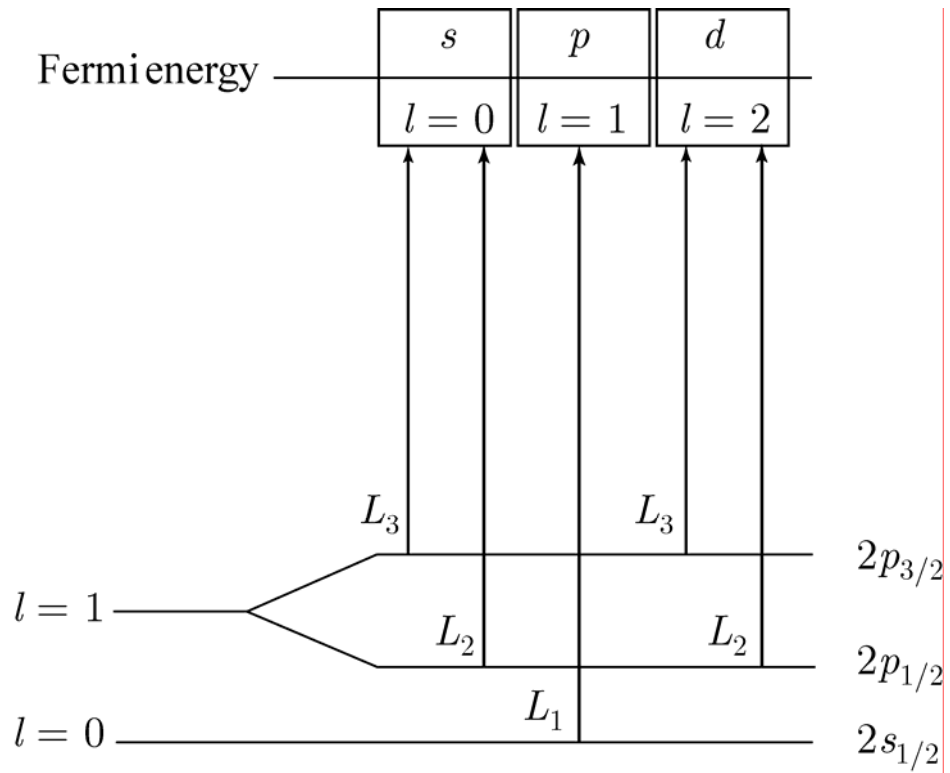


Figure 1.18 Concept of the dipole allowed transition from the hole levels with a value of the principal quantum number of 2.

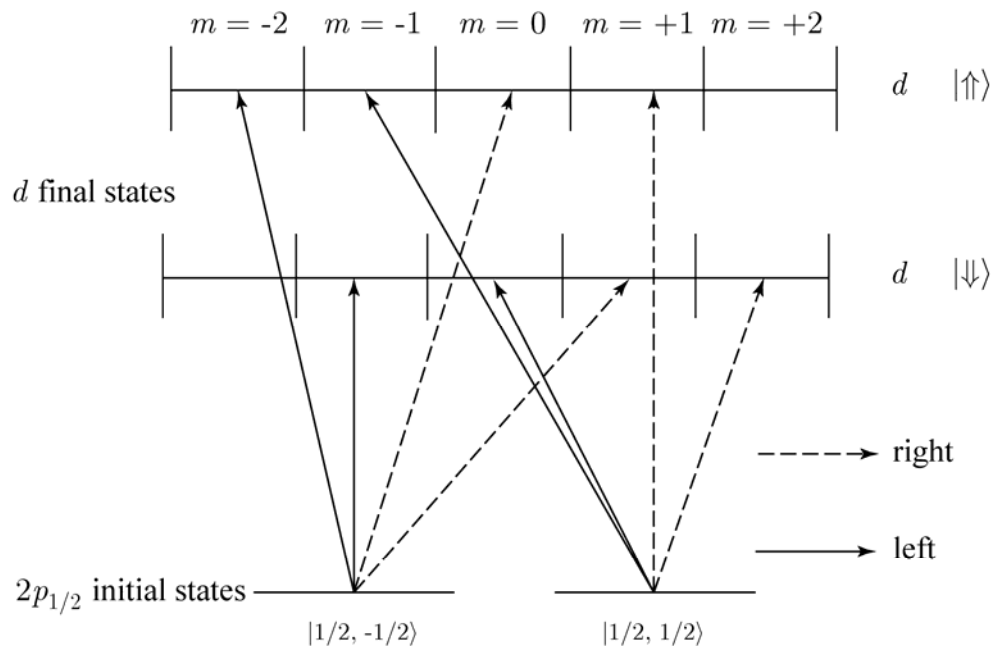


Figure 1.19 Transition from $2p_{1/2}$ level to the d level with various values of m . $|JM\rangle$ are indicated.

1.2 Basic Concept of Magnetism in Solid

Before going to understanding the concept of magnetism in solids, It is better for us to see some of the fundamentals relevant to it. In this thesis we will do it. These fundamental theories are summarized in the standard books, e.g. *Kittel (1996), Introduction to Solid State Physics*, and *Martin (1967), Magnetism in Solids*.

1.2.1 Atomic Magnetism

Discovery of the quantum mechanics in beginning of 20th century made it possible to understand the fundamental properties of magnetism in matter. In quantum mechanics, an electron in an isolated atom occupies a state which is described by a set of quantum numbers: the principal quantum number, n , the azimuthal quantum number, l , the magnetic quantum number, m , and the spin, s . In many electrons system, electrons interact with each other to form the whole electron state. If the one electron approximation is valid, the individual electron state forms the whole electron state by filling up the single electron levels in accordance with the Pauli exclusion principle. If the electronic state is localized at lattice site, the atomic state can be that to describing magnetic moment. For the system in which the spin-orbit coupling is dominant the good quantum numbers describing the system are that of the total angular momentum, j , and its z component m_j as already mentioned. Each electron gives rise to the magnetic moment with which both the orbital angular momentum and the spin angular momentum are associated. In the following, the essences of the explanation of the magnetic moment presented in Appendix E are described.

The magnetic moment associated with the orbital momentum \mathbf{L} is expressed as

$$\boldsymbol{\mu}_l = -\frac{e}{2mc} \mathbf{L} \quad (1.121)$$

, and also that associated with the spin angular momentum \mathbf{S} is expressed as

$$\boldsymbol{\mu}_s = -2\frac{e}{2mc} \mathbf{S} \quad (1.122)$$

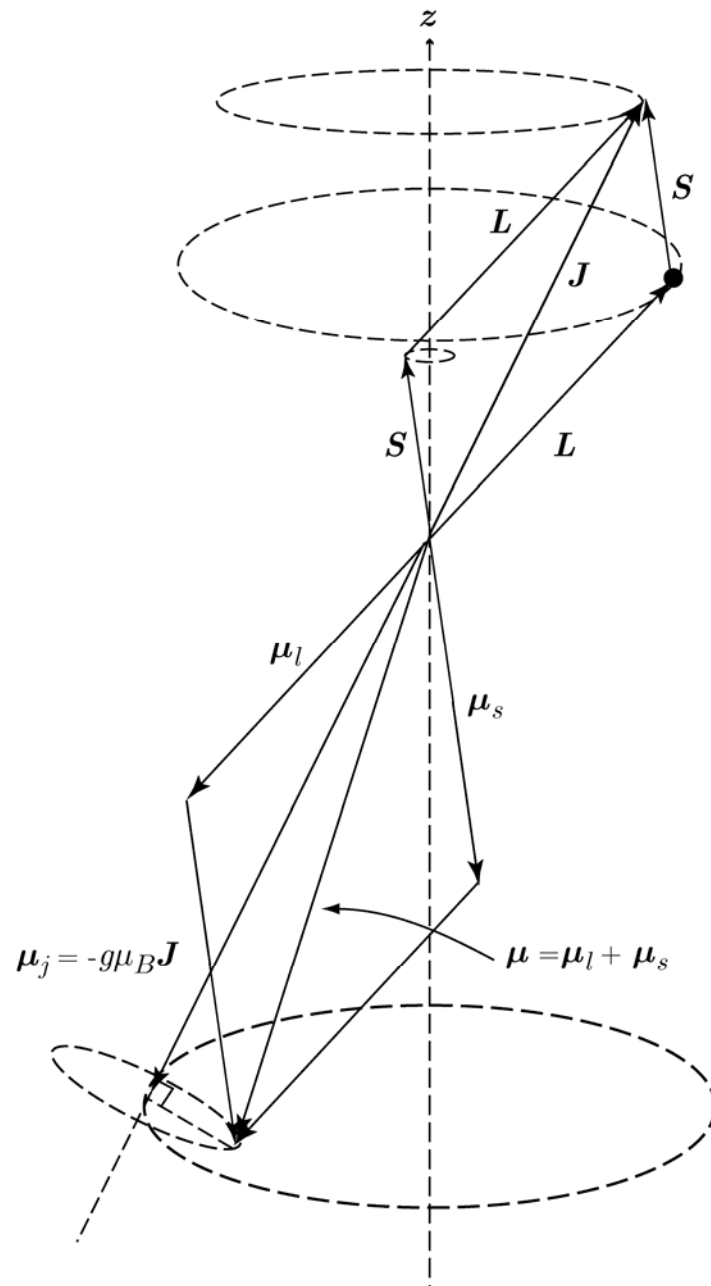


Figure 1.20 The vector expression of the magnetic moments μ_l , μ_s and μ_j , and the angular momentums L , S and J in atoms.

The spin magnetic moment, μ_s , is a permanent magnetic moment; it occurs regardless of the existence of an external magnetic field. On the other hand, the orbital magnetic moment, μ_l , is proportional to the applied magnetic field and is called *induced moment*. The angular momentum of an electron in an atom is quantized in unit of the *Bohr magneton* μ_B .

$$\mu_B = \frac{e\hbar}{2mc} = 9.27410 \times 10^{-21} \text{ erg / gauss} \quad (1.123)$$

In general, the magnetic moment of free electrons is expressed as

$$\boldsymbol{\mu} = \boldsymbol{\mu}_l + \boldsymbol{\mu}_s = -\frac{e}{2mc}(\mathbf{L} + 2\mathbf{S}) = -\frac{\mu_B}{\hbar}(\mathbf{J} + \mathbf{S}) \quad (1.124)$$

Here the total angular momentum, \mathbf{J} , is given by

$$\mathbf{J} = \mathbf{L} + \mathbf{S} \quad (1.125)$$

The relation among the angular momenta and magnetic moments are in Figure 1.20.

The magnetic moment, $\boldsymbol{\mu}$, is in the direction along \mathbf{J} . Thus, we obtain

$$\boldsymbol{\mu}_j = \gamma\hbar\mathbf{J} = -g\mu_B\mathbf{J} \quad (1.126)$$

where γ is the ratio of the magnetic moment to the angular momentum, called the *gyromagnetic ratio* or the *magnetogyric ratio*. The factor g is referred to as Lendé's g -factor as already described in other section and in Appendix E in detail. It is given by

$$g = 1 + \frac{J(J+1) + S(S+1) - L(L+1)}{2J(J+1)} \quad (1.106)$$

Figure 1.20 shows that both \mathbf{L} and \mathbf{S} are precessing around \mathbf{J} . This is considered as follows: The equation of motion of $\boldsymbol{\mu}$ in a magnetic field is written as

$$\frac{d\boldsymbol{\mu}}{dt} = \gamma[\boldsymbol{\mu} \times \mathbf{H}] \quad (1.127)$$

Here γ is the gyromagnetic ratio. Since $\boldsymbol{\mu} = -\gamma\hbar\mathbf{J}$ from (1.95), we can convert (1.127) to the equation of motion of the corresponding angular momentum \mathbf{J} .

$$\frac{d\mathbf{J}}{dt} = \gamma[\mathbf{J} \times \mathbf{H}] \quad (1.128)$$

If we take the direction of \mathbf{H} as being along the z axis, (1.127) and (1.128) can be solved easily to give the solution that \mathbf{J} and $\boldsymbol{\mu}$ is precessing around the direction of \mathbf{H} . This motion is called the Larmor precession.

An electron making an orbit motion is considered to be in the magnetic field arising from the electron spin. The magnetic field is given by $\lambda\mathbf{S}/\mu_B$. λ is the spin-orbit coupling constant. If we replace \mathbf{H} in (1.128) with $\lambda\mathbf{S}/\mu_B$ and \mathbf{J} with \mathbf{L} , we have

$$\frac{d\mathbf{L}}{dt} = \frac{\gamma\lambda}{\mu_B}[\mathbf{L} \times \mathbf{S}] \quad (1.129)$$

Note that

$$\mathbf{J} \times \mathbf{L} = (\mathbf{L} + \mathbf{S}) \times \mathbf{L} = \mathbf{S} \times \mathbf{L} \quad (1.130)$$

Since $\mu_B/\gamma = -\hbar$, we have from (1.129) and (1.130)

$$\hbar \frac{d\mathbf{L}}{dt} = \gamma[\mathbf{J} \times \mathbf{L}] \quad (1.131)$$

If \mathbf{J} is constant, (1.131) shows that \mathbf{L} makes precession around \mathbf{J} .

Similarly the magnetic field caused by \mathbf{L} and acting on \mathbf{S} is given by $\gamma\mathbf{L}/\mu_B$. Then we have the relation to (1.131) as

$$\hbar \frac{d\mathbf{S}}{dt} = \lambda[\mathbf{J} \times \mathbf{S}] \quad (1.132)$$

This shows that \mathbf{S} also makes precession around \mathbf{J} .

In the discussion described above, we postulate the spin orbit coupling given by (1.126). This leads ultimately to the spin-orbit coupling energy, $\lambda \mathbf{L} \cdot \mathbf{S}$. This is the hamiltonian for many electrons given by

$$\begin{aligned} H_{SL} &= \sum \zeta_i \mathbf{l}_i \cdot \mathbf{s}_i \\ &= \lambda \mathbf{L} \cdot \mathbf{S} \end{aligned} \quad (1.133)$$

This is inherent in the intrinsic nature of electron and derived in quantum electrodynamics by solving Dirac's relativistic hamiltonian as already mentioned. However, it is understandable qualitatively as follows: If we observe the orbital motion of an electron from the electron, the nucleus appears to be rotating around the electron. This causes a closed current I . According to the Biot-Savart law, the magnetic field generated by this current is given by

$$\frac{1}{r^3} [\mathbf{r} \times \mathbf{I}]$$

Here, $[\mathbf{r} \times \mathbf{I}]$ is proportional to the orbital angular momentum, \mathbf{l} , of the electron. Then, the magnetic field acting on the electron spin is proportional to \mathbf{l} . Then from (1.133). the energy regarding to this is

$$h_{ls} = \zeta \mathbf{l} \cdot \mathbf{s} \quad (1.134)$$

Here, ζ is given by

$$\zeta = \frac{1}{2} Z \left(\frac{e\hbar}{mc} \right)^2 \left\langle \frac{1}{r^3} \right\rangle_{av.} \quad (1.135)$$

Z is the atomic number. In practice, (1.135) must be changed to

$$\zeta = \frac{1}{2} Z \left(\frac{e\hbar}{mc} \right)^2 \left\langle \frac{1}{r} \frac{\partial V_0}{\partial r} \right\rangle_{av.} \quad (1.136)$$

V_0 is the potential acting on the electron. From (1.134), (1.133) is obtained. Then we have the spin-orbit interaction hamiltonian as

$$H = \lambda \mathbf{L} \cdot \mathbf{S} \quad (1.133)$$

This is the source to make the precession of \mathbf{L} and \mathbf{S} around \mathbf{J} . For obtaining (1.133) from the theory, we have to use the relativistic theory. However, the agreement with experimental results is not always good. So, we use (1.133) as empirical formula and λ is obtained experimentally.

1.2.2 Magnetizations

The magnetic properties of solids are described quantitatively in terms of the magnetization, \mathbf{M} , which is defined as the magnetic moment per unit volume. When the external field, \mathbf{H} , is applied to a solid, the amount of \mathbf{M} is related to the magnitude of \mathbf{H} through a factor called the *magnetic susceptibility*, χ , it is defined by

$$\mathbf{M} = \chi \cdot \mathbf{H} \quad (1.137)$$

In a crystalline solid the susceptibility χ is generally a tensor. In Gaussian units (cgs), χ is dimensionless because the units of \mathbf{M} usually indicated with gauss (G) and the unit of \mathbf{H} indicated with Oersted (Oe) are equivalent to each other. Materials with negative susceptibilities are called *diamagnetic* materials. Materials with positive susceptibilities less than one are called *paramagnetic* materials. Materials with large positive susceptibilities are called either *ferromagnetic*, *antiferromagnetic*, or *ferrimagnetic* materials. Without the external applied field, materials in these three kinds exhibit the magnetization $\mathbf{M}_{\text{spont}}$ which is called *spontaneous magnetization*. \mathbf{M} and \mathbf{H} , are related to the magnetic induction, \mathbf{B} , through the *permeability* μ_r ,

$$\begin{aligned}
\mathbf{B} &= \mu_r \mathbf{H} \\
\mathbf{B} &= \mathbf{H} + 4\pi \mathbf{M} \\
&= \mathbf{H} + 4\pi \chi \cdot \mathbf{H} \\
&= (1 + 4\pi \chi) \cdot \mathbf{H}
\end{aligned} \tag{1.138}$$

where, the permeability, μ_r , is a tensor in a crystalline solid, and 1 is a unit tensor having elements of unity along the main diagonal and zero elsewhere. This is given in Appendix A, [(A.8) and (A.9)]. \mathbf{B} is also referred to as the magnetic flux density.

1.2.3 Diamagnetism and Paramagnetism in Solids

As mentioned in the preceding section that the magnetization can be developed when atoms are in an applied field. In this section, the effect of the magnetic field on free atoms or ions is discussed. The hamiltonian, \hat{H} , of ions in a solid under an applied uniform magnetic field, \mathbf{H} , is given by

$$\hat{H} = \left[\sum_i \left(\frac{\mathbf{p}_i^2}{2m} - e\phi_i \right) + \sum_{ij} \frac{e^2}{r_{ij}} + \lambda \mathbf{L} \cdot \mathbf{S} \right] + \frac{\mu_B}{\hbar} (\mathbf{L} + 2\mathbf{S}) \cdot \mathbf{H} + \sum_i \frac{e^2}{8mc^2} (\mathbf{H} \times \mathbf{r}_i)^2 \tag{1.139}$$

where the summations are made over several bound electrons in the ion. The terms enclosed in the square brackets are the hamiltonians for the ion in the absence of the magnetic field. The scalar potential ϕ_i , for instance, includes the electric field due to the nucleus and the neighboring ions (crystal field). The coulomb interactions between electrons, e^2/r_{ij} , and the spin-orbit coupling term $\lambda \mathbf{L} \cdot \mathbf{S}$ are also included in this part, where λ is spin-orbit coefficient. The remaining two terms in (1.139) are the perturbations due to \mathbf{H} . The first interaction term gives rise to a paramagnetic contribution to the susceptibility, while the second term causes a diamagnetic contribution.

We consider only the magnetic perturb terms. The perturbation energy generated by the magnetic field which is postulated to be directed to the z -direction is considered.

$$E' = \frac{\mu_B}{\hbar} H \langle (L_z + 2S_z) \rangle + \frac{e^2}{8mc^2} H^2 \left\langle \sum_i (x_i^2 + y_i^2) \right\rangle \quad (1.140)$$

The magnetic moment of the ion can be derived directly by differentiating the hamiltonian H with respect to \mathbf{H} .

$$\boldsymbol{\mu} = -\frac{\partial \hat{H}}{\partial \mathbf{H}} = -\frac{\mu_B}{\hbar} (\mathbf{L} + 2\mathbf{S}) - \frac{e^2}{4mc^2} \sum_i [r_i^2 \mathbf{H} - (\mathbf{r}_i \cdot \mathbf{H}) \mathbf{r}_i] \quad (1.141)$$

If the magnetic field \mathbf{H} is in z -direction we obtain

$$\boldsymbol{\mu} = -\frac{\mu_B}{\hbar} (\mathbf{L} + 2\mathbf{S}) - \frac{e^2}{4mc^2} \sum_i [(x_i^2 + y_i^2 + z_i^2) \mathbf{H} - z_i \mathbf{H} \mathbf{r}_i] \quad (1.142)$$

and the z component magnetic moment is

$$\mu_z = -\frac{\mu_B}{\hbar} (L_z + 2S_z) - \frac{e^2}{4mc^2} \sum_i (x_i^2 + y_i^2) H \quad (1.143)$$

$$\mu_z \equiv \mu_z^{para} + \mu_z^{dia} \quad (1.144)$$

where μ_z^{para} and μ_z^{dia} denote the magnetic moments of the paramagnetic contribution and the diamagnetic contribution, respectively.

The diamagnetic term may be interpreted in the form of

$$\langle \mu_z \rangle_{dia} = -\frac{e^2}{4mc^2} \left\langle \sum_i \rho_i^2 \right\rangle H \quad (1.145)$$

where $\rho_i^2 = x_i^2 + y_i^2$ interprets the square of perpendicular distance of the electron from the field axis. This equation can also be derived in classical electrodynamics by assuming that the electrons have spherically symmetric orbits of motion without magnetic field. In magnetic field, it is only the motion perpendicular to the field that

is relevant to the magnetic properties of an atom. In this plane the motion of electrons is characterized the well known *Larmor precession*. It is described in Appendix F and here in Figure 1.20. However, $\langle \sum_i \rho_i^2 \rangle$ can be obtained only by quantum mechanics, where the expectation value is calculated. If r_i is the distance of electrons from the nucleus, $\langle r_i^2 \rangle = \langle x_i^2 \rangle + \langle y_i^2 \rangle + \langle z_i^2 \rangle$, and if the system is spherically symmetric, $\langle x_i^2 \rangle = \langle y_i^2 \rangle = \langle z_i^2 \rangle$, so that $\langle \sum_i \rho_i^2 \rangle = \frac{2}{3} \langle \sum_i r_i^2 \rangle$. From (1.137) χ is given by $\chi = \partial M / \partial H$ and $M = N \langle \mu_z^{dia} \rangle$ where N is number of atoms per unit volume. Eq. (1.145) indicates that the diamagnetic susceptibility per unit volume is

$$\chi^{dia} = -\frac{Ne^2}{6mc^2} \left\langle \sum_i r_i^2 \right\rangle \quad (1.146)$$

The result in equation (1.146) is identical to the *Langevin diamagnetic susceptibility* which can also be obtained in the classical electrodynamics. In quantum mechanics, $\langle \sum_i r_i^2 \rangle$ means that the mean square distance of the i^{th} electron from the nucleus averaged. The diamagnetism is, therefore, a universal property of materials though many of materials are generally dominated by paramagnetism. It is independent of temperature and induced by an external field. The Langevin diamagnetic susceptibility is applicable for monatomic gas (inert gas). However, it is not in good agreement for the heavy atoms. Since the diamagnetic susceptibility has the negative sign, the induced magnetization is directed opposite to the external field.

The paramagnetic contribution is not universal property which is found in all materials. For the local electrons in atoms, the paramagnetic moment operator is written as.

$$\boldsymbol{\mu}^{para} = -\frac{\mu_B}{\hbar} (\mathbf{L} + 2\mathbf{S}) \quad (1.147)$$

Since both \mathbf{L} and \mathbf{S} vanish in a closed shell, the paramagnetic moment of the atom without unpaired electrons vanishes. On the other hand, the unpaired electrons in transition metals ($3d, 4d, 5d$) and rare-earth metals ($4f$) contribute to paramagnetism. For those localized electrons, each state of atoms or ions (neglecting the interaction between atoms or ions) is characterized by quantum number J . Therefore, the magnetic moment operator is follow equation (1.126), and the expectation value of the magnetic moment is obtained as

$$\langle \mu^{para} \rangle = -g\mu_B m_J \quad (1.148)$$

Where m_J is magnetic quantum number and has the values $J, J-1, \dots, -J$. The Lendé g -factor is given by (1.106). Thus, the perturbation energy due to the magnetic field \mathbf{H} , in z -direction, is obtained as

$$W = -\langle \boldsymbol{\mu}^{para} \cdot \mathbf{H} \rangle = -g\mu_B m_J H \quad (1.149)$$

This is equivalent to (1.105). Now magnetic energy of a single atom or ion is identified. Next problem is the statistical calculation for whole atoms in solids. Suppose the case where the atoms are free from each other and localized. Their states at temperature T obey the Maxwell-Boltzman distribution. The paramagnetic magnitude of the magnetization, M , can be obtained as

$$M = \frac{\sum_i M_i e^{-E_i/k_B T}}{\sum_i e^{-E_i/k_B T}} \quad (1.150)$$

where k_B is the Boltzman's constant (1.38062×10^{-16} erg·K⁻¹). By substituting the magnetic energy, (1.149), we obtain

$$M = \frac{Ng\mu_B \sum_{m_j=-J}^J m_j e^{g\mu_B m_j H / k_B T}}{\sum_{m_j=-J}^J e^{g\mu_B m_j H / k_B T}} \quad (1.151)$$

Here, N is number of atoms per unit volume. Let x be $g\mu_B JH / k_B T$, where J is maximum value which m_j . Physically, x is the ratio between the magnetic energy and thermal energy. The magnetization can be derived as follows:

$$\begin{aligned} M &= \frac{Ng\mu_B \sum_{m_j=-J}^J m_j e^{m_j \frac{x}{J}}}{\sum_{m_j=-J}^J e^{m_j \frac{x}{J}}} \\ &= Ng\mu_B J \frac{\partial}{\partial x} \left(\ln \sum_{m_j=-J}^J e^{m_j \frac{x}{J}} \right) \\ &= Ng\mu_B J \frac{\partial}{\partial x} \left(\ln \left[\frac{e^{(J+\frac{1}{2})\frac{x}{J}} - e^{-J\frac{x}{J}}}{e^{\frac{x}{J}} - 1} \right] \right) \\ &= Ng\mu_B J \frac{\partial}{\partial x} \left(\ln \left[\frac{e^{(J+\frac{1}{2})\frac{x}{J}} - e^{-(J+\frac{1}{2})\frac{x}{J}}}{e^{\frac{x}{2J}} - e^{-\frac{x}{2J}}} \right] \right) \\ &= Ng\mu_B J \frac{\partial}{\partial x} \left(\ln \left[\frac{\sinh \left[\left(\frac{2J+1}{2J} \right) x \right]}{\sinh \left[\frac{x}{2J} \right]} \right] \right) \\ &= Ng\mu_B J \left(\frac{2J+1}{2J} \coth \frac{2J+1}{2J} x - \frac{1}{2J} \coth \frac{x}{2J} \right) \end{aligned}$$

$$M = M_s B_J(x) \quad (1.152)$$

$$\left. \begin{aligned} x &= \frac{g\mu_B JH}{k_B T} \\ M_s &= Ng\mu_B J \end{aligned} \right\} \quad (1.153)$$

where $M_s = Ng\mu_B J$ is a saturate magnetization, and

$$B_J(x) = \frac{2J+1}{2J} \coth \frac{2J+1}{2J} x - \frac{1}{2J} \coth \frac{x}{2J} \quad (1.154)$$

is known as *Brillouin function*. Equation (1.152) is known as *Langevin paramagnetic formula*. In the limit case of small x , $\mu_B H \ll k_B T$,

$$B_J(x) \simeq \left(\frac{J+1}{3J} \right)$$

The magnetization becomes

$$\begin{aligned} M &= \frac{N\mu_B^2 H}{3k_B T} g^2 J(J+1) \\ &= \frac{N\mu_B^2 p^2 H}{3k_B T} \end{aligned}$$

\therefore

$$\chi = \frac{N\mu_B^2 p^2}{3k_B T} \equiv \frac{C}{T} \quad (1.155)$$

where

$$C = \frac{N\mu_B^2}{3k_B} g^2 J(J+1) \quad (1.156)$$

and $p = g(J(J+1))^{\frac{1}{2}}$ is the *paramagnetic effective number of Bohr magnetic moment*. Equation (1.155) is called *Curie's law*. Comparison between experimental results and the magnetization calculated by equation (1.152) is shown in Figure 1.21. At a normal field is and room temperature, magnetic energy (μH) is much smaller

than the thermal energy, ($x \ll 1$), the magnetization is proportional to H/T , giving the constant susceptibility involved in the Curie's law. Only when the energy due to the magnetic field is larger or comparable to the thermal energy as $\mu H \geq k_B T$, the magnetization can be saturated by the applied field.

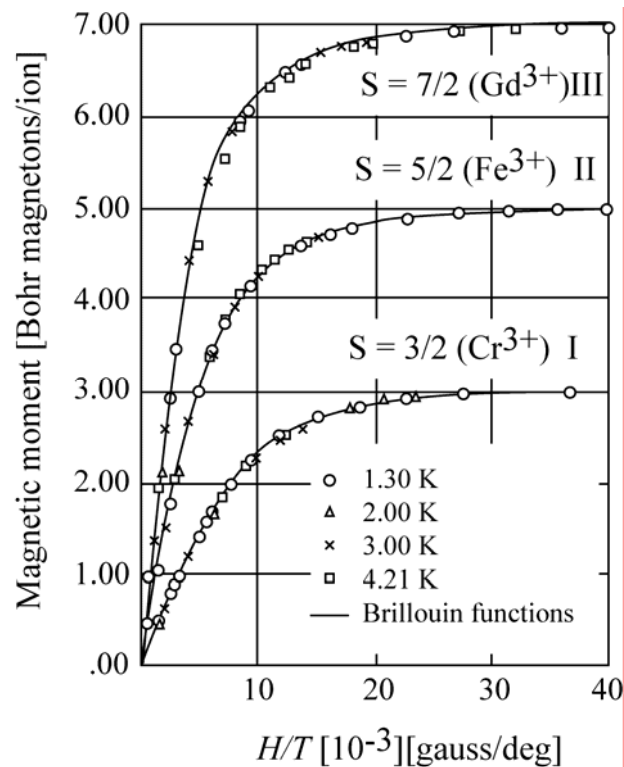


Figure 1.21 Plot of magnetic moment versus H/T (gauss/deg) for the samples of (I) potassium chromium alum, (II) ferric ammonium alum, and (III) gadolinium sulfate octahydrate. Over 99.5% magnetic saturation is achieved at a low temperature of 1.3 K and about 50,000 gauss. [After W.E. Henry 1952, Physical Review 88, 559]

In the Langevin paramagnetic formula and the Curie's law, the total angular momentum J is assumed to be maximum value of m_j . According to the Hund's rule, this assumption is that every atom is assumed to be in the ground state. In fact, the atomic wave function is distorted by the external field. In the perturbation theory, the wave function is written in the form of admixtures of wave functions of other states of the system. In the case that an energy separation between the excited state and the ground state is much larger than the thermal energy as $E_s - E_g \gg k_B T$, the susceptibility due to the perturbation is known as *Van Vleck paramagnetic susceptibility*. It is expressed by

$$\chi^{VanVleck} = \frac{2N \sum_s |\langle \psi_s | \mu^{para} | \psi_g \rangle|^2}{E_s - E_g} \quad (1.157)$$

where the subscripts s and g denote the excited state and the ground state, respectively. The summation is over all excited states s . Note that the Van Vleck susceptibility is temperature independent and positive because $E_s > E_g$. In other cases, in which $E_s - E_g \simeq k_B T$ or $E_s - E_g \ll k_B T$, the susceptibility is not independent of temperature.

Up to now we have discussed only the response of bound electrons to external magnetic field. In metals, another type of paramagnetism is caused by the contribution from conduction electrons. These itinerant electrons lose their strong affinity for a particular nucleus and become more or less free to move throughout metals. The number of states in which electrons have energy E is expressed by the concept of "*Density of States*", $D(E)$. The density of states in three dimensions is expressed as

$$D(E) = \frac{dN}{dE} = \frac{V}{2\pi\hbar^2} (2m)^{3/2} E^{1/2} \quad (1.158)$$

The maximum value of the energy of the level that electrons can occupy, at the absolute zero of temperature $T = 0$ K, is defined as *Fermi energy* E_F . In the absence of the external field, the electrons with up and down spin fill the levels below the E_F in balance generating zero net magnetic moment, as shown in Figure 1.22 (a). Under the field \mathbf{H} , the magnetic energy, $\mu_B \mathbf{H}$, causes a downward shift of the energy levels for the electrons with spin up and upward shift for spin down electrons, as shown in the Figure 1.22 (b).

The associated susceptibility can be computed by subtracting the number of states of the conduction electrons in the spin down state from that in the spin up states.

$$\Delta n = \frac{\Delta n}{\Delta E} \Delta E = \frac{D(E_F)}{2} \mu_B \mathbf{H} \quad (1.159)$$

The induced magnetization per unit volume (from both spin up and spin down) is, therefore,

$$M = \frac{2\Delta n \mu_B}{V} = \frac{D(E_F) \mu_B^2 H}{V}$$

$$\chi^{Pauli} = \frac{D(E_F) \mu_B^2}{V} \quad (1.160)$$

It is easy to evaluate that the density of states $D(E_F) = (3/2)N/E_F$ where N is a number of electrons per volume [C. Kittel, Introduction to Solid state physics, 7th Ed. 1996. page 151]. Then the susceptibility $\chi = M/H$ can be obtained as

$$\chi^{Pauli} = \frac{3}{2} \frac{N \mu_B^2}{E_F} \quad (1.161)$$

This is known as *Pauli paramagnetic susceptibility*. In addition, since the electrons are moving in a periodic potential, the applied field couples to the motion of the conduction electrons, causing a *Landau diamagnetic susceptibility* that is $-\frac{1}{3}$ of the Pauli paramagnetic susceptibility. The magnetic energy level associated with this diamagnetism is called *Landau level*. The mathematical derivation of the Landau diamagnetism is very long and is not presented in this thesis.

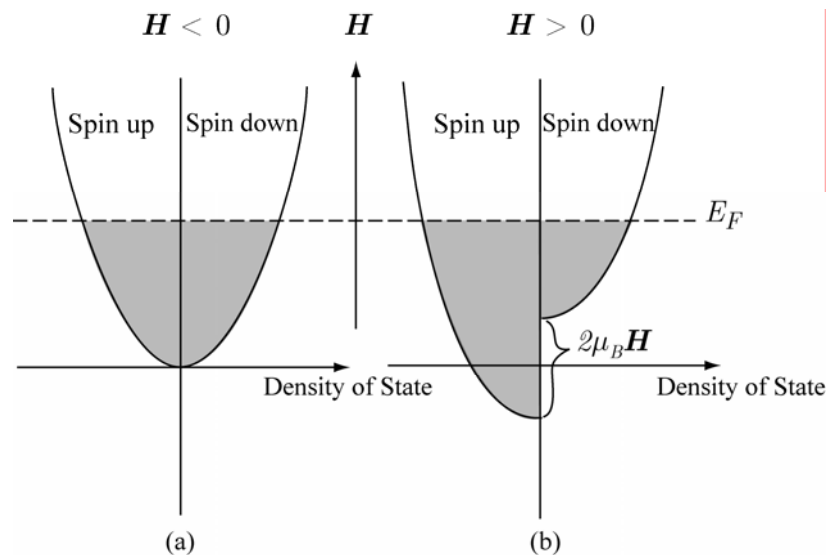


Figure 1.22 Density of states of the conduction electrons at absolute zero temperature ($T = 0$), (a) without magnetic field then there is no magnetic moment, (b) with applied field H , splitting of the band by magnetic energy $2\mu_B H$ occurs between the band for spins parallel (spin up) and that for spins opposite (spin down) to the field direction.

1.2.4 Magnetic Ordering in Solids I: Ferromagnetism

The magnetism in diamagnetic and paramagnetic materials can be explained without considering the affect from weak magnetic interactions between atoms. On the other hand, if the magnetic interactions between neighboring atoms are strong, the orientation of their elementary magnetic moments is spontaneously ordered. The cause that the magnetic moments align parallel to each other is not obvious.

The interacting on potential between two magnetic moments μ_1 , and μ_2 , separated by a distance of r_{12} is given by

$$V_{12} = \frac{(\mu_1 \cdot \mu_2)}{r_{12}} - \frac{3(\mu_1 \cdot r_{12})(\mu_2 \cdot r_{12})}{r_{12}^5} \quad (1.162)$$

Suppose that μ_1 and μ_2 take values of a few Bohr magneton and are separated by 2 Å, then energy given by (1.162) is less than 8.6×10^{-5} eV. The Curie temperature or the Neel temperature of a ferromagnetic material or antiferromagnetic material, respectively, gives the rough size of the energy difference between the ordered state and the disordered state. In some materials they take values larger than 0.1 eV. This indicates that the magnetic dipole-dipole interaction cannot cause the ferromagnetic or antiferromagnetic state.

There are either showing magnetic ordering materials *ferromagnets*, *antiferromagnets*, or *ferrimagnets*, depending on the aspect of the alignment of their magnetic moments, as shown in Figure 1.23. All of the magnetically ordered materials become paramagnets above the *Curie temperature*, T_C . The entropy of the system, S , is large if magnetic moments are distributed randomly. At height

temperature, the amount of the lowering of the free energy, F , of the system defined as

$$F = E - ST \quad (1.163)$$

is larger than the increase of the internal energy caused by the random distribution. Then gives rise to the random distribution of the moments at high temperature. At the Curie temperature, both pieces energy are equal.

For convenience, we study the simplest case of the magnetic ordering, the ferromagnetism. In ferromagnetic materials, electrostatic interaction (called exchange interaction) of electrons in atoms with those in their neighbors makes the spin align parallel. In order to describe the electrostatic interaction, we need to consider localized electrons and itinerant electrons separately. For the localized electrons the *Weiss model* works well, while the *Stoner model* takes explains the magnetism of the itinerant electrons.

Here, we see a few important issues that give rise to the magnetic ordered state. First, we know that the electrons on adjacent atoms interact electrostatically. The overlap of the electron orbits between adjacent atoms is assumed to be negligibly small. Let each atom have one electron. If we calculate the total energy of the system base on the Heitler-London approximation, we find two electron-electron interaction terms in addition to the single electron energy. One is that brought about by the electrostatic interaction between electrons in the orbitals belonging to each atom. The energy integral is called the coulomb energy and the supposed interaction leading to this energy is called coulomb interaction. The other is the energy integral in which the orbitals of the coulomb integral is interchanged. This energy integral is called the exchange energy and the supposed interaction is called

the exchange interaction. The more detailed explanation of the coulomb and exchange energy will be given later.

The theoretical treatments of the spin dependent electrostatic interactions are very complicated and out of scope in the present thesis. The rough conclusion is that the coulomb interaction shifts the total energy but does not change the total energy according to the relative orientation of the spin of each electron. In the system, there are two relative orientation of each electron spin. One is the parallel orientation and the other is antiparallel orientation. The contribution of exchange energy to the total energy changes its sign according to the relative spin orientation, parallel or antiparallel. Hereafter we refer to the exchange energy as J_{ij} . i and j distinguish atoms. If $J_{ij} > 0$, the contribution is negative for parallel spins and the total energy is lower. If $J_{ij} < 0$, the total energy is lower for antiparallel spins. This indicates that the ordered state is more stable and the source of the ferromagnetism and antiferromagnetism is the exchange interaction.

As mentioned already, the situation is not so simple. However, we can postulate that the interaction has the following form:

$$\hat{H} = \sum_{i>j} 2J_{ij} \mathbf{S}_i \cdot \mathbf{S}_j \quad (1.164)$$

This is the energy corresponding to that of the spin state in the hamiltonian. (1.164) is determined by the selection of the quantization axis. The method to deal the magnetic ordering according to (1.164) is referred to as the Heisenberg model. It must be emphasized that the improvement of the approximation method does not necessarily lead to the better agreement of the theoretical results with the experimental results.

We have discussed the formation of \mathbf{J} from \mathbf{L} and \mathbf{S} . There, we considered the magnetic field generated by one of the angular momenta acts on the magnetic moment formed by the other angular momentum. Here we consider a similar effect. The i^{th} electron spin is in the magnetic field formed by other electrons. The field is

$$\mathbf{H}_{\text{eff}}(i) = -\frac{1}{g\mu_B} \sum_j 2J_{ij} \mathbf{S}_{ij} \quad (1.165)$$

This effective field is not constant in time but fluctuating owing to the thermal agitation. If we average this fluctuation caused by the temperature effect, we have

$$\mathbf{H}_m(i) = -\frac{1}{g\mu_B} \sum_j 2J_{ij} \langle \mathbf{S}_{ij} \rangle_{\text{av.}} \quad (1.166)$$

We regard that the i^{th} electron is in this average field. This field is referred to as the molecular field. For various calculations related with the magnetic order and disorder using the molecular field are employed in the system in which relevant electrons are localized.

On the other hand, electrons in metals form the energy bands as is the case of the $3d$ electrons in the transition metals. In a case like this, it is not practical to consider the system as the assembly of electrons localized on atoms. Therefore, we assume that the total magnetization, M , does existence that the energy bands are given by

$$\varepsilon_{\pm}(\mathbf{k}) = \varepsilon(\mathbf{k}) \pm \alpha M \quad (1.167)$$

\pm corresponds to up and down spins. Namely, we assume there are up-spin band and down-spin band separated by the magnetization. α is a constant. The magnetization, M , is calculated as

$$M = \mu_B \left[\int_{-\infty}^{\infty} d\varepsilon \frac{D(\varepsilon)}{\exp[(\varepsilon - \alpha M - \varepsilon_F)/k_B T] + 1} - \int_{-\infty}^{\infty} d\varepsilon \frac{D(\varepsilon)}{\exp[(\varepsilon + \alpha M - \varepsilon_F)/k_B T] + 1} \right] \quad (1.168)$$

This calculation is made self-consistently. First, M is calculated appropriately. Using calculated M , we calculated new M . $D(\varepsilon)$ is the density of states and ε_F is the Fermi energy. This model of calculation of the magnetization is called the Stoner model.

In Weiss Model, each atom of ferromagnetic materials form a magnetic dipole due to the exchange interaction of the localized electrons ($3d$ or $4f$) within the atom. The exchange field (\mathbf{H}_{ex}) is represented as the internal field called *molecular field* which is proportional to the magnetization of the material. So that, the total magnetic field (called the *mean field*) acting on atoms is assumed to be

$$\begin{aligned} \mathbf{H}_{total} &= \mathbf{H} + \mathbf{H}_{ex} \\ &= \mathbf{H} + \lambda_m \mathbf{M} \end{aligned} \quad (1.169)$$

where λ_m is called *molecular field constant*.

If we apply $\mathbf{H}_{total} = \mathbf{H} + \lambda_m \mathbf{M}$ to the Langevin paramagnetic magnetization in equation (1.152), we obtain

$$\frac{M_{spont}}{M_s} = B_J \left(\frac{g\mu_B J \lambda_m M_{spont}}{k_B T} \right) \quad (1.170)$$

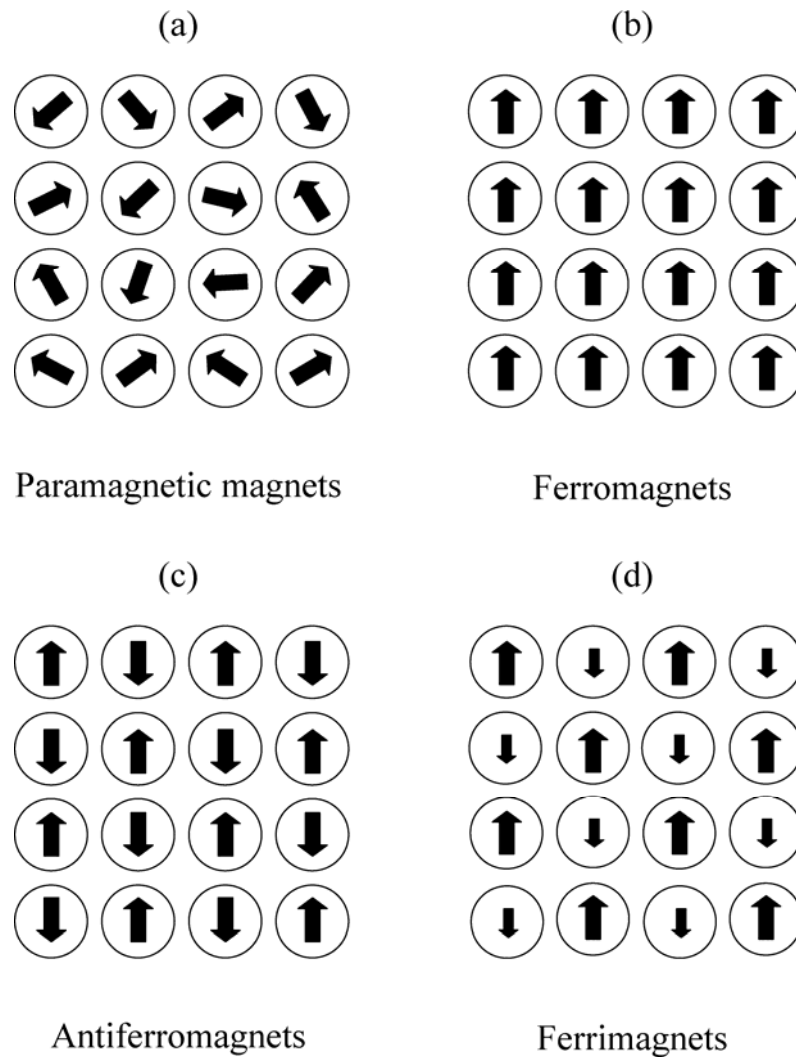


Figure 1.23 The alignments of magnetic moments at absolute zero temperature. (a) No alignment of adjacent magnetic moments is observed for paramagnets. (b) Ferromagnets exhibit parallel alignment of adjacent magnetic moments. (c) Antiferromagnets exhibit antiparallel alignment of adjacent magnetic moments. (d) Ferrimagnets are composed of two magnetic spins of different strength and exhibit antiparallel alignment.

where M_s is the saturation magnetization, and M_{spont} is called the *spontaneous magnetization*. M_{spont} is the magnetization of materials in the absence of an external field, ($H = 0$). This equation can be solved graphically as shown in Figure 1.24. We plot the following function for various temperatures.

$$\left. \begin{aligned} y &= M_s B_J [a(T)\xi] \\ a(T) &= \frac{g\mu_B J \lambda_B}{k_B T} \end{aligned} \right\} \quad (1.171)$$

The intersection of the curve (1.171) and

$$y = \xi$$

give the spontaneous magnetization, M_{spont} . If the slope of the function (1.171) is lower than 45° , the only solution is $\xi = 0$. This means $M_{spont} = 0$. So, at corresponding temperatures, the spontaneous magnetization does not exist. If the slope is larger than 45° , the intersection occurs at $\xi \neq 0$. At these temperatures the magnetization is spontaneous magnetization. The temperature at which the slope is 45° is the Curie temperature.

When the spontaneous magnetization, M_{spont} , falls to zero the ferromagnetic materials turn to paramagnetic ones. We make the derivative of (1.171) regarding ξ , $dy/d\xi$, using (1.154). Let the value of $dy/d\xi$ at $\xi = 0$ equal to 1. From this we obtain the Curie temperature as

$$\begin{aligned} T_C &= \frac{Ng^2\mu_B^2}{3k_B} J(J+1)\lambda_m \\ &= C\lambda_m \end{aligned} \quad (1.172)$$

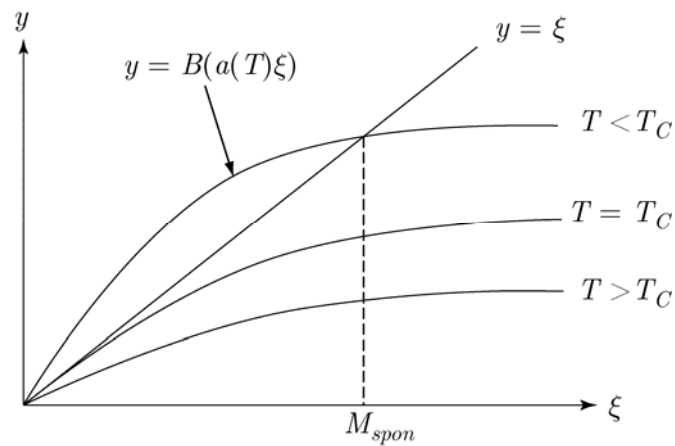


Figure 1.24 Graphical determination of the spontaneous magnetization, M_{spon} . The intersection point leads to the value of M_{spon} which falls to zero at the Curie temperature T_C .

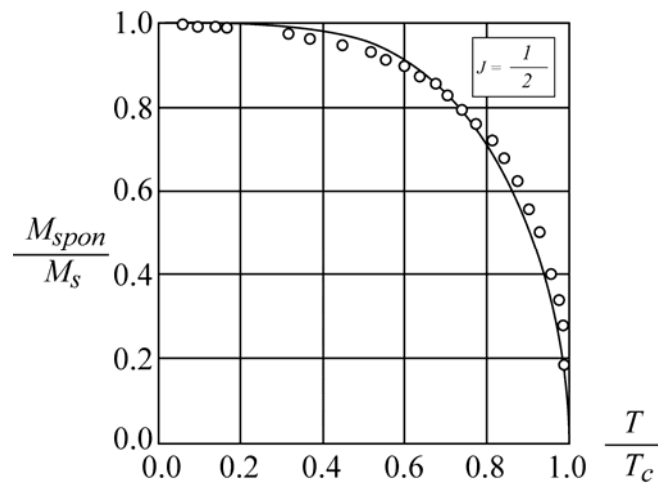


Figure 1.25 Temperature dependence of M_{spon} of Ni for $J = 1/2$ in (1.173) (solid line) is compared with that of experimental data (open circles) [The experimental data by P. Weiss and R. Forrer].

where N is a number of atoms per unit volume. This equation indicates that the Curie temperature is proportional to the mean field constant λ_m . By substituting the $\lambda_m = T_C / C$ into (1.170), we obtain that

$$\frac{M_{\text{spont}}}{M_s} = B_J\left(\frac{3J}{J+1} \frac{T_C}{T} \frac{M_{\text{spont}}}{M_s}\right) \quad (1.173)$$

This equation indicates that how the spontaneous magnetization depends on temperature. The experimental result on Ni, for example, is compared with the plot of the equation (1.173) for $J = 1/2$. In Figure 1.25, the theoretical curve is the best fit.

The Weiss model may be applied for paramagnetic materials. By substituting the molecular field $\mathbf{H}_{\text{total}} = \mathbf{H} + \lambda_m \mathbf{M}$ to the Curie law in (1.155), we obtain the magnetization as

$$\begin{aligned} \mathbf{M} &= \frac{C}{T} (\mathbf{H} + \lambda_m \mathbf{M}) \\ \chi &= \frac{C}{T - \lambda_m C} = \frac{C}{T - T_C} \end{aligned} \quad (1.174)$$

where C is Curies constant, and $T_C \equiv \lambda_m C$ is defined as Curie temperature. This equation is known as *Curie-Weiss law*. It is not valid for $T = T_C$ and is valid only for $T \gg T_C$.

According to the Weiss model, at the absolute zero temperature, the magnetization becomes saturated. Then we have

$$M_s = Ng\mu_B J = n_B N \mu_B \quad (1.175)$$

where $n_B = gJ$ is a number of Bohr magneton per atom (formula unit), called *effective magneton number*, N is number of atoms per unit volume. The effective

magneton number, n_B , of some ferromagnetic substances are shown in Table 1.2, together with others basic parameters.

As shown in the Table 1.2, values of the effective magneton numbers are not integer. These observed values cannot be explained by of the Weiss model. For example, in transition metals, the magnetic moment due to orbital angular momenta are largely quenched ($L = 0, J = S$). The z component of the orbital motion of an electron in a transition metal cannot be a good quantum number. Thus their effective magneton numbers should be integral values ($n_B = 2S$). This discrepancy would be the result of the itinerant electrons existing in transition metals. It is need another model to give a description of those electrons which are moving through the metals.

Stoner model is successful to explain the ferromagnetic in transition metals (Fe, Co, Ni). The Pauli paramagnetism described above has already shown that how collective electrons magnetic moments are induced by an external applied field. In the same sense, ferromagnetic magnetic moment can be generated by the molecular field ($\lambda_m M$). Stoner applied the Weiss's molecular field idea to the nearly free electron model as follow. The Pauli susceptibility, therefore, is modified to

$$\chi^{Pauli} = \frac{M}{H + \lambda_m M} \quad (1.176)$$

$$\therefore \chi^{Stoner} = \frac{\chi^{Pauli}}{1 - \lambda_m \chi^{Pauli}} \quad (1.177)$$

Table 1.2 Magnetic parameters of ferromagnetic substances [From C. Kittel., *Introduction to Solid State Physics*, John Wiley and Sons, Inc. 6th ed., 1996].

Substances	Saturation magnetization M_s ,		n_B (0 K) Per formula unit	Curie temperature (K)
	in gauss (G)			
	300 K	0 K		
Fe	1707	1740	2.22	1043
Co	1400	1446	1.72	1388
Ni	485	510	0.606	627
Gd	-	2060	7.63	292
Dy	-	2920	10.2	88

and from (1.160), the Stoner susceptibility is written as

$$\chi^{Stoner} = \chi^{Pauli} \frac{1}{1 - I_s D(E_F)} \quad (1.178)$$

where

$$I_s = \frac{\lambda_m \mu_B^2}{V} \quad (1.179)$$

Here $D(E_F)$ is the density of states at Fermi level, and λ_m is the molecular field constant. Hence the susceptibility diverges when

$$I_s D(E_F) = 1$$

Thus,

$$I_s D(E_F) > 1 \quad (1.180)$$

This is known as the Stoner criterion. Only metals with large $D(E_F)$ can order ferromagnetically. This is why the late 3d elements, Fe, Co, Ni, are ferromagnetic, but the early 3d or 4d elements, Ti, V, Cr, are not. Elements in the middle of the series, Cr, V, are antiferromagnetic because the 3d band is approximately half-filled.

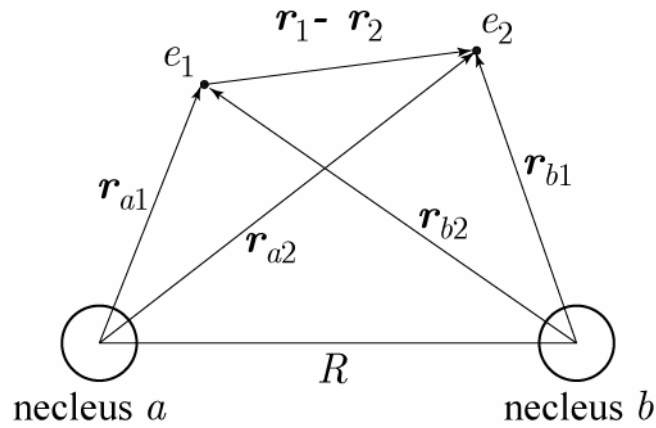
1.2.5 Exchange Interactions

The molecular field theory in the preceding section gives a good qualitative explanation for the magnetic ordering. However, it does not reveal the origin of the magnetic interactions. As mentioned above, the interaction is of the electrostatic origin. To understand the origin of the interaction, the interaction between two electrons in a hydrogen molecule is considered.

To evaluate total energy of the system, Schrödinger equation

$$\hat{H}\Psi = E\Psi$$

must be solved. We consider electrons e_1 and e_2 in the coulomb field of nuclei a and b . hamiltonian of the system can be expressed as



$$\hat{H} = \frac{p_1^2}{2m} + \frac{p_2^2}{2m} - e^2 \left(\frac{1}{r_{a1}} + \frac{1}{r_{a2}} \right) - e^2 \left(\frac{1}{r_{b1}} + \frac{1}{r_{b2}} \right) + \frac{e^2}{|\mathbf{r}_1 - \mathbf{r}_2|} \quad (1.181)$$

where, the coulomb force between nuclei is neglected. According to *atomic-orbital approximation*, the repulsive force between electrons is assumed to be perturbation term. The hamiltonian, therefore, is separated to be unperturbed terms, (\hat{H}_1, \hat{H}_2) , and perturbation term, \hat{H}_{12} . Then we have

$$\left. \begin{aligned} \hat{H}_1 &= \frac{p_1^2}{2m} - e^2 \left(\frac{1}{r_{a1}} + \frac{1}{r_{b1}} \right) \\ \hat{H}_2 &= \frac{p_2^2}{2m} - e^2 \left(\frac{1}{r_{a2}} + \frac{1}{r_{b2}} \right) \\ \hat{H}_{12} &= \frac{e^2}{|\mathbf{r}_1 - \mathbf{r}_2|} \end{aligned} \right\} \quad (1.182)$$

These hamiltonians indicate that, for unperturbed terms, the wave functions of the system cannot be separated to that for nucleus a , $\psi_a(\mathbf{r}_1, \boldsymbol{\sigma}_1)$, and for that nucleus b , $\psi_b(\mathbf{r}_1, \boldsymbol{\sigma}_1)$. This implies that the electrons are moving around both nuclei equally. However, the wave function of each electron retains $\psi_i(\mathbf{r}_1, \boldsymbol{\sigma}_1)$ and $\psi_j(\mathbf{r}_2, \boldsymbol{\sigma}_2)$ for the

electrons e_1 and e_2 , respectively. Electron e_1 is in a state i and electron e_2 is in a state j . When the spin-orbit coupling is not large, reversal of spin does not change the orbital. The wave functions can be separated to the spatial and spin parts.

$$\left. \begin{aligned} \psi_i(\mathbf{r}_1, \sigma_1) &= \phi_i(\mathbf{r}_1)\chi(\sigma_1) \\ \psi_j(\mathbf{r}_2, \sigma_2) &= \phi_j(\mathbf{r}_2)\chi(\sigma_2) \end{aligned} \right\} \quad (1.183)$$

Then we write the one-electron wave function of the unperturbed state that satisfies the Schrödinger equation $(\hat{H}_1 + \hat{H}_2)\Psi = (E_i + E_j)\Psi$ as

$$\left. \begin{aligned} \Psi &= \psi_i(\mathbf{r}_1, \sigma_1)\psi_j(\mathbf{r}_2, \sigma_2) \\ &= \phi_i(\mathbf{r}_1)\phi_j(\mathbf{r}_2)\chi(\sigma_1)\chi(\sigma_2) \\ &= \Phi(\mathbf{r}_1, \mathbf{r}_2)\chi(\sigma_1, \sigma_2) \end{aligned} \right\} \quad (1.184)$$

For simplicity, consider only the spatial part. We have to construct the wave functions in terms of the linear combination of the function of the type of (1.183). This is necessary because $\phi_j(\mathbf{r}_1)\phi_i(\mathbf{r}_2)$ can also be the solution. Thus the energy state is degenerate. The perturbation removes the degeneracy. It is well known in quantum mechanics that the new wave functions are well approximated by the linear combination of the degenerate component functions. The method to obtain the coefficients is simple. From the normalization and the symmetry consideration, we obtain the coefficients as $\pm 1/\sqrt{2}$. As a conclusion, there are two ways to construct the two- electrons wave functions, i.e.

$$\begin{aligned} \Phi_S(\mathbf{r}_1, \mathbf{r}_2) &= \frac{1}{\sqrt{2}}[\phi_i(\mathbf{r}_1)\phi_j(\mathbf{r}_2) + \phi_j(\mathbf{r}_1)\phi_i(\mathbf{r}_2)] \\ \Phi_A(\mathbf{r}_1, \mathbf{r}_2) &= \frac{1}{\sqrt{2}}[\phi_i(\mathbf{r}_1)\phi_j(\mathbf{r}_2) - \phi_j(\mathbf{r}_1)\phi_i(\mathbf{r}_2)] \end{aligned} \quad (1.185)$$

Here the subscripts S and A denote the symmetric and the anti-symmetric functions, respectively. Now the total energy E can be evaluated from

$$E = \iint \Phi^* \hat{H} \Phi d\tau_1 d\tau_2 \quad (1.186)$$

where the integration is carried out over volume elements $d\tau_1 d\tau_2$. By using (1.185), we obtain

$$E = E_i + E_j + Q_{ij} \pm J_{ij} \quad (1.187)$$

where

$$\left. \begin{aligned} E_i &= \int \phi_i^*(\vec{r}_1) \hat{H}_1 \phi_i(\vec{r}_1) d\tau_1 \\ E_j &= \int \phi_j^*(\vec{r}_2) \hat{H}_1 \phi_j(\vec{r}_2) d\tau_2 \\ Q_{ij} &= \int \phi_i^*(\vec{r}_1) \phi_j^*(\vec{r}_2) \hat{H}_{12} \phi_i(\vec{r}_1) \phi_j(\vec{r}_2) d\tau_1 d\tau_2 \\ J_{ij} &= \int \phi_i^*(\vec{r}_1) \phi_j^*(\vec{r}_2) \hat{H}_{12} \phi_i(\vec{r}_2) \phi_j(\vec{r}_1) d\tau_1 d\tau_2 \end{aligned} \right\} \quad (1.188)$$

The J_{ij} term of positive sign in (1.187) arises from the symmetric function of (1.186) and that of negative sign from the antisymmetric function. The E_i and E_j are the unperturbed energies of the electrons in states i and j , respectively. The perturbed terms Q_{ij} is coulomb energy, and the J_{ij} is known as *exchange energy*. We see that the symmetric wave function gives the total energy different from that the anti-symmetric wave function gives. Since the Pauli exclusion principle states that the total wave function of the two electrons, $\Psi = \Phi(\mathbf{r}_1, \mathbf{r}_2) \chi(\boldsymbol{\sigma}_1, \boldsymbol{\sigma}_2)$, must be anti-symmetric, the symmetry and anti-symmetry of the spatial wave function is related to the spin wave functions.

Now, we consider the spin part of the total wave function. Each electron can take either the up-spin state or the down-spin state, denoted by $\chi_\alpha(\sigma)$,

and $\chi_\beta(\sigma)$, respectively. σ is the spin coordinate taking values of $\pm 1/2$. It corresponds to the z component of the spin vector, s . $\chi_\alpha(\sigma)$ is defined as

$$\chi_\alpha\left(\frac{1}{2}\right) = 1 \text{ and } \chi_\alpha\left(-\frac{1}{2}\right) = 0$$

$\chi_\beta(\sigma)$ is defined as

$$\chi_\beta\left(\frac{1}{2}\right) = 0 \text{ and } \chi_\beta\left(-\frac{1}{2}\right) = 1$$

Then, the spin wave functions of two electrons system can be constructed from one-electron spin wave functions $\chi_\alpha(\sigma_1)$, $\chi_\beta(\sigma_1)$, and $\chi_\alpha(\sigma_2)$, $\chi_\beta(\sigma_2)$. If the spin-orbital interaction is not taken into account, the spin part of the wave function is independent of the spatial part of the wave function. In other words, the spin wave functions are separable from the orbital part.

The addition of two angular momenta is explained in Appendix E. According to Appendix E, there are four z components of the total angular momentum composed of $j_1 = 1/2$ and $j_2 = 1/2$. They are

$$\left. \begin{array}{l} J = 1, M = 1, 0, -1 \\ J = 0, M = 0 \end{array} \right\} \quad (1.189)$$

If we put $j_1 = s_1$ and $j_2 = s_2$, there are four z components of composed total spin.

The corresponding wave function are given by

$$\left. \begin{array}{l} \chi_S^I(\sigma_1, \sigma_2) = \chi_\alpha(\sigma_1)\chi_\alpha(\sigma_2) \\ \chi_S^{II}(\sigma_1, \sigma_2) = \chi_\beta(\sigma_1)\chi_\beta(\sigma_2) \\ \chi_S^{III}(\sigma_1, \sigma_2) = \frac{1}{\sqrt{2}}[\chi_\alpha(\sigma_1)\chi_\beta(\sigma_2) + \chi_\beta(\sigma_1)\chi_\alpha(\sigma_2)] \\ \chi_A(\sigma_1, \sigma_2) = \frac{1}{\sqrt{2}}[\chi_\alpha(\sigma_1)\chi_\beta(\sigma_2) - \chi_\beta(\sigma_1)\chi_\alpha(\sigma_2)] \end{array} \right\} \quad (1.190)$$

where the $1/\sqrt{2}$ is a normalization factor. The subscripts, S and A , denote the symmetric and the anti-symmetric states, respectively. The symmetric states are called the *triplet state*, for which the total spin moment is unity ($S = 1$). The antisymmetric state is called the *singlet state*. The total spin moment is zero ($S = 0$). The way to make the total spin function is summarized below.

$S(=J)$	M	m_1	m_2	direction	function
1	1	1/2	1/2	$\uparrow\uparrow$	$\chi_\uparrow\chi_\uparrow$
1	0	1/2	-1/2	$\left. \begin{array}{l} \uparrow\downarrow \\ \downarrow\uparrow \end{array} \right\}$	$\chi_\uparrow\chi_\downarrow + \chi_\downarrow\chi_\uparrow$
		-1/2	1/2		
1	-1	-1/2	-1/2	$\downarrow\downarrow$	$\chi_\downarrow\chi_\downarrow$
0	0	1/2	-1/2	$\left. \begin{array}{l} \uparrow\downarrow \\ \downarrow\uparrow \end{array} \right\}$	$\chi_\uparrow\chi_\downarrow - \chi_\downarrow\chi_\uparrow$
		-1/2	1/2		

The way to make the linear combination for the two degenerate states of $M = 0$ is the same as for the case of the orbital wave functions.

The energy of unperturbed state is just the sum of two pieces of the unperturbed energy of electrons in two atoms. Thus we do not consider this part, but we consider only the perturbed part of the total energy, ΔE . For the symmetric spatial wave functions, we have

$$\Delta E = Q_{ij} + J_{ij} \quad (1.191)$$

Because the total wave function of the system must be anti-symmetric, the spin part must be antisymmetric. Then the spin state is singlet. For the anti-symmetric spatial wave function, we have

$$\Delta E = Q_{ij} - J_{ij} \quad (1.192)$$

Then the spin part must be symmetric and it produces the triplet state. If the exchange energy is positive, ($J_{ij} > 0$), the energy of the triplet state is lower than that of the singlet state. In the ground state spins are parallel. If the exchange energy is negative, ($J_{ij} < 0$), the lower energy state is singlet where the spins are anti-parallel.

Now we have found that the spin states affect to the total energy of the two-electron system indirectly through the exchange interaction. As we mentioned already, the situation that the exchange interaction align spins is treated the Heisenberg model and the resulting molecular field. In what follows, we handle this problem mathematically, although treatment is very much simplified. We start with the vector model.

Consider the total spin angular momentum operator of the system of two electrons which are in the states i and j .

$$\begin{aligned} S^2 &= (\mathbf{s}_i + \mathbf{s}_j)^2 \\ &= s_i^2 + s_j^2 + 2\mathbf{s}_i \cdot \mathbf{s}_j \end{aligned} \quad (1.193)$$

We may assume

$$\begin{aligned} \left. \begin{aligned} 2\langle \mathbf{s}_i \cdot \mathbf{s}_j \rangle &= \langle S^2 \rangle - \langle s_i^2 \rangle - \langle s_j^2 \rangle \\ 2\langle \mathbf{s}_i \cdot \mathbf{s}_j \rangle &= \hbar^2 [S(S+1) - s_i(s_i+1) - s_j(s_j+1)] \\ \therefore &= \hbar^2 \left[S(S+1) - \frac{1}{2} \left(\frac{1}{2} + 1 \right) - \frac{1}{2} \left(\frac{1}{2} + 1 \right) \right] \\ &= \hbar^2 \left[S(S+1) - \frac{3}{2} \right] \end{aligned} \right\} \quad (1.194) \end{aligned}$$

For the triplet state ($S = 1$)

$$2\langle \mathbf{s}_i \cdot \mathbf{s}_j \rangle = \frac{\hbar^2}{2} \quad (1.195)$$

For this state we have

$$\frac{1}{2} + \frac{2}{\hbar^2} \langle \mathbf{s}_i \cdot \mathbf{s}_j \rangle = 1 \quad (1.196)$$

For the singlet state ($S = 0$), we have from (1.194)

$$2 \langle \mathbf{s}_i \cdot \mathbf{s}_j \rangle = -\frac{3}{2} \hbar^2 \quad (1.197)$$

For this state we have

$$\frac{1}{2} + \frac{2}{\hbar^2} \langle \mathbf{s}_i \cdot \mathbf{s}_j \rangle = -1 \quad (1.198)$$

By using the equations (1.196) and (1.198), the exchange energy can be written in the form of

$$\pm J_{ij} = -J_{ij} \left[\frac{1}{2} + \frac{2}{\hbar^2} \langle \mathbf{s}_i \cdot \mathbf{s}_j \rangle \right]$$

Eventually, the full energy of the two electrons system becomes

$$E = E_i + E_j + Q - \frac{J_{ij}}{2} - \frac{2J_{ij}}{\hbar^2} \langle \mathbf{s}_i \cdot \mathbf{s}_j \rangle \quad (1.199)$$

The term, $-\frac{2J_{ij}}{\hbar^2} \langle \mathbf{s}_i \cdot \mathbf{s}_j \rangle$, which depends on the spin states is known as the *Heisenberg exchange energy*, and the *Heisenberg hamiltonian* is written as

$$\hat{H}_{ex} = -\frac{2J_{ij}}{\hbar^2} \mathbf{s}_i \cdot \mathbf{s}_j \quad (1.200)$$

Here, $\mathbf{s}_i \cdot \mathbf{s}_j$ is the operator form by the scalar product of spin vectors of the electrons.

For N electrons system, the anti-symmetric wave function is given by the *Slater determinant*.

$$\Psi(\mathbf{r}_1, \mathbf{r}_2, \dots, \mathbf{r}_N, \sigma_1, \sigma_2, \dots, \sigma_N) = \begin{vmatrix} \psi_1(\mathbf{r}_1, \sigma_1) & \psi_1(\mathbf{r}_2, \sigma_2) & \dots & \psi_1(\mathbf{r}_N, \sigma_N) \\ \psi_2(\mathbf{r}_1, \sigma_1) & \psi_2(\mathbf{r}_2, \sigma_2) & \dots & \psi_2(\mathbf{r}_N, \sigma_N) \\ \vdots & \vdots & \ddots & \vdots \\ \psi_N(\mathbf{r}_1, \sigma_1) & \psi_N(\mathbf{r}_2, \sigma_2) & \dots & \psi_N(\mathbf{r}_N, \sigma_N) \end{vmatrix} \quad (1.201)$$

This form guarantees that two electrons are not in the same quantum state, because two electrons in the same state result in two identical rows in the determinant and the determinant is zero. The Heisenberg hamiltonian for the N -electrons system may be approximated by

$$\hat{H}_{ex} = -\frac{2}{\hbar^2} \sum_{i'j'} J_{i'j'} \mathbf{s}_{i'} \cdot \mathbf{s}_{j'} \quad (1.202)$$

where the summation is over pairs of electrons in which the states i' and j' . We postulate

$$\sum_{i'j'} J_{i'j'} \mathbf{s}_{i'} \cdot \mathbf{s}_{j'} = \sum_{ij} J_{ij} \mathbf{S}_i \cdot \mathbf{S}_j \quad (1.203)$$

where i' and j' represent electrons and i and j atoms. As mentioned before, the analytical proof of the relation, (1.203), base on the wave function, (1.201), is too complicated to be made rigorously. Instead, we take (1.203) as the assumption at the start point. Then, we can write (1.202) as

$$\hat{H}_{ex} = \sum_{ij} J_{ij} \mathbf{S}_i \cdot \mathbf{S}_j \quad (1.204)$$

The Heisenberg hamiltonian can be applied for the Weiss model in the mean field theory in which each atom has a magnetic moment. Suppose that the j^{th} atom has the total spin operator \mathbf{S}_j / \hbar . Then the magnetic moment operator is given by

$$\boldsymbol{\mu}_j = -\frac{g\mu_B}{\hbar} \mathbf{S}_j \quad (1.205)$$

This equation is equivalent to (1.122) except that it expresses the state of an atom instead of an electron. The second assumption is that, the Heisenberg hamiltonian in (1.200) can be written as

$$\begin{aligned}\hat{H}_{ex} &= -\frac{2}{g\mu_B\hbar} \sum_{ij} J_{ij} \mathbf{S}_i \cdot \boldsymbol{\mu}_j \\ &= -\sum_j \mathbf{H}_{exj} \cdot \boldsymbol{\mu}_j\end{aligned}\quad (1.206)$$

where

$$\mathbf{H}_{exj} = \frac{2}{g\mu_B\hbar} \sum_i J_{ij} \mathbf{S}_i \quad (1.207)$$

Here, If the assumptions made above are good approximations, the magnetic moment of the j^{th} atom sees the exchange field operator \mathbf{H}_{exj} . Suppose that only nearest neighbors are considered and the entire nearest are identical. Then, at absolute zero temperature ($T = 0$), the exchange field can be written as

$$\left. \begin{aligned}\mathbf{H}_{exj} &= \frac{2Z}{g\mu_B\hbar} J_{ij} \mathbf{S}_i \\ \mathbf{H}_{exj} &= \frac{2ZJ_{ij} \mathbf{M}_{spont}}{Ng^2\mu_B^2}\end{aligned}\right\} \quad (1.208)$$

where the spontaneous magnetization $\mathbf{M}_{spont} = Ng\mu_B \mathbf{S}_j$, N is a number of atom per unit volume and Z is the number of nearest neighbor atoms. From the assumption of the Weiss model, ($\mathbf{H}_{ex} = \lambda_m \mathbf{M}$), the mean field constant is obtained as

$$\lambda_m = \frac{2ZJ_{ij}}{Ng^2\mu_B^2} \quad (1.209)$$

, and from Curie law (1.155) and (1.156) we obtain

$$\begin{aligned}T_C &= \frac{Ng^2\mu_B^2}{3k_B} J(J+1)\lambda_m \\ &= C\lambda_m\end{aligned}\quad (1.172)$$

Thus, we have

$$J_{ij} = \frac{3}{2} \frac{k_B T_C}{ZJ(J+1)} \quad (1.210)$$

This shows that the exchange energy, J_{ij} , can be estimated from Curie temperature T_C .

1.2.6 Magnetic Ordering in Solids II: Ferrimagnetism & Anti Ferromagnetism

Because the samples used in this thesis are artificial ferrimagnetic materials, it is better to discuss the physical concept of ferrimagnetic materials. In ferromagnetic materials, the exchange energy is positive, $J_{ij} > 0$. Spins align parallel to each other. On the other hand, in antiferromagnetic and ferrimagnetic materials, the exchange energy is negative, $J_{ij} < 0$. Spins align antiparallel to each other in ground state. To discuss this antiparallel alignment, it is convenient to introduce the simplest structure of ferrite. Ferrite is compounds having the atomic composition of the form of MFe_2O_4 in which M is a divalent metal of Cu, Pb, Mg, Mn, Co, Ni, and Fe. Ferrite is known to have the *spinel structure* shown in Figure 1.26. Spinel is $MgAl_2O_3$ and the crystal structure of ferrite is almost the same as that of spinel. The crystal structure is cubic. In a unit cell there are 8 molecules, namely, $16Fe^{3+}$, $8M^{2+}$ and $32O^{2-}$. O^{2-} ions approximately form the face centered cubic structure. In the interstitial position of this oxygen sublattice, M^{2+} ions and Fe^{3+} ions are located.

There are two kinds of interstice for the metals ions in the spinel structure. One is tetrahedral site, called *A* site, and the other is octahedral site, called *B* site. An *A* site is surrounded by O^{2-} ions in the tetrahedral arrangement. An *B* is surrounded by O^{2-} ions in the octahedral arrangement. In ferrite of normal spinel, all the Fe^{3+} ions occupy site *B*, and the M^{2+} ions occupy site *A*. There is another type of spinel called reverse spinel. In ferrite of reverse spinel, Fe^{3+} ions occupy *A* sites and

the half B sites. M^{2+} ions occupy the remaining B sites. A magnetic ion in an A site makes strong exchange interaction with 12 magnetic ions in the B sites through 12 O^{2-} ions. The exchange energy is negative and the interaction is antiferromagnetic. On the other hand, a magnetic ion in a B site interacts with 6 ions in A sites.

We represent the interactions between the ions in the same site the exchange integrals J_{AA} for site A and J_{BB} for site B . The pertinent interactions are called AA and BB interactions. The interaction between ions in different site is designated by the J_{AB} and the AB interactions, which are usually stronger than those J_{AA} and J_{BB} . The different pieces of exchange energy are estimated in the molecular field theory as follows:

The physical situation of the spinel magnetic structure in Figure 1.26 can be analyzed in terms of the molecular fields \mathbf{H}_A and \mathbf{H}_B . They depend on the magnetizations, \mathbf{M}_A , of sites A and \mathbf{M}_B of sites B .

$$\begin{aligned}\mathbf{H}_A &= \lambda_{AA}\mathbf{M}_A - \lambda_{AB}\mathbf{M}_B \\ \mathbf{H}_B &= -\lambda_{AB}\mathbf{M}_A + \lambda_{BB}\mathbf{M}_B\end{aligned}\tag{1.211}$$

Here, \mathbf{H}_A and \mathbf{H}_B are the molecular fields that act on the ions in sites A and B , respectively. The interpretation of the relations, (1.211), is that molecular field \mathbf{H}_A is determined both by the nearest neighbor interaction with sublattice B and by the nearest neighbor interaction with sublattice A . Usually λ_{AB} is much larger than λ_{AA} though the distance between atoms in different sites is longer. The minus signs indicate that the molecular fields are antiparallel to the applied field. The molecular field constant for the AB interaction, λ_{AB} , must be positive since this interaction favors an antiparallel alignment of the moments of A and B ions.

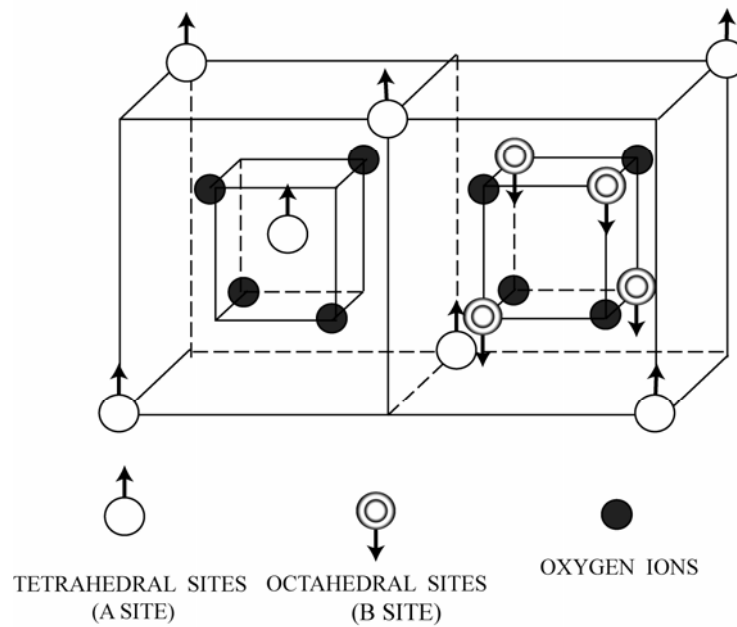


Figure 1.26 Two sublattices in the spinel structure. Each of these sublattices is repeated in diagonally opposite corners of the full cubic elementary cell. The two oxygen ions form a close-packed cubic lattice and the metal ions Fe^{3+} and M^{2+} are located in the interstices between the O^{2-} . The arrows indicate the up-spins and down-spin. [From D. H. Martin, *Magnetism in Solids*, London Iliffe Book LTD., 1967]

Similarly to that we proceeded for ferromagnetic materials, by applying the mean fields \mathbf{H}_A and \mathbf{H}_B , (1.211), to the Langevin formula, (1.152), we obtain

$$\begin{aligned}\frac{M_A}{M_{sA}} &= B_J \left(\frac{g\mu_B J}{k_B T} (\lambda_{AA} M_A - \lambda_{AB} M_B) \right) \\ \frac{M_B}{M_{sB}} &= B_J \left(\frac{g\mu_B J}{k_B T} (-\lambda_{AB} M_A + \lambda_{BB} M_B) \right)\end{aligned}\quad (1.212)$$

where M_{sA} and M_{sB} are the saturation magnetizations for the A and B sublattices, and the Brillouin function is given by (1.154)

$$B_J(x) = \frac{2J+1}{2J} \coth \frac{2J+1}{2J} x - \frac{1}{2J} \coth \frac{x}{2J} \quad (1.154)$$

To solve for the magnetizations M_A and M_B , graphical methods must be used, as shown in Figure 1.24. L. Néel first made calculation of this kind for ferrimagnetic crystals and found that magnetizations M_A and M_B are antiparallel if $\lambda_{AB} \gg \lambda_{AA}, \lambda_{BB}$ and decreases monotonically with increasing temperature, from M_{sA} and M_{sB} at $T = 0$ to zero at a critical temperature, the Curie temperature, T_C .

Below T_C , the total spontaneous magnetization is

$$\mathbf{M}_{spon} = \mathbf{M}_A + \mathbf{M}_B \quad (1.213)$$

Because of the antiferromagnetic situation, we have

$$M_{spon} = M_A - M_B \quad (1.214)$$

The form of the M_{spon} versus T curve can vary widely with the relative magnitudes of the parameters in the theory because M_{spon} is a difference between two varying terms. Some possibilities are shown in Figure 1.27.

Above T_C the molecular field calculation can also be applied. By substituting the molecular fields \mathbf{H}_A and \mathbf{H}_B , (1.211), into the Curie's law ($M = CH/T$), we obtain the magnetization in the individual sublattice as

$$\begin{aligned} M_A &= \frac{C_A}{T} (\mathbf{H} + \lambda_{AA} \mathbf{M}_A - \lambda_{AB} \mathbf{M}_B) \\ M_B &= \frac{C_B}{T} (\mathbf{H} - \lambda_{AB} \mathbf{M}_A + \lambda_{BB} \mathbf{M}_B) \end{aligned} \quad (1.215)$$

where

$$C_A = \frac{N_A g^2 \mu_B^2 J(J+1)}{3k_B} \quad (1.216)$$

The similar relation is held for C_B . Here \mathbf{H} is external applied field; C_A and C_B are the Curie constants for sublattices A and B , respectively. For simplicity, the interactions between ions in the same site are neglected, $\lambda_{AB} \gg \lambda_{AA}, \lambda_{BB} \simeq 0$. The ferrimagnetic susceptibility in zero applied fields can be obtained from (1.215).

$$\chi = \frac{M_A + M_B}{H} = \frac{(C_A + C_B)T - 2\lambda_{AB}C_A C_B}{T^2 - \lambda_{AB}^2 C_A C_B} \quad (1.217)$$

The Curie temperature in this model is given as the temperature at which the susceptibility becomes infinity, i.e. $1/\chi = 0$. Thus, from (1.217)

$$T_C = \lambda_{AB} \sqrt{C_A C_B} \quad (1.218)$$

Thus, the susceptibility at $T > T_C$ is obtained as

$$\chi = \frac{(C_A + C_B)T - 2\lambda_{AB}C_A C_B}{T^2 - T_C^2} \quad (1.219)$$

The result is more complicated than the Curie-Weiss law in (1.174).

For the antiferromagnetic materials, however, the result is simpler. In the antiferromagnetic case, the nearest neighbors of an A ion are all on the B sublattice,

and vice versa. Therefore, the molecular field acting on ions, say, A and B , can be given by

$$\begin{aligned} \mathbf{H}_A &= -\Lambda \mathbf{M}_A - \lambda_{AB} \mathbf{M}_B \\ \mathbf{H}_B &= -\lambda_{AB} \mathbf{M}_A - \Lambda \mathbf{M}_B \end{aligned} \quad (1.220)$$

where the mean field constants λ_{AB} and Λ measure the interactions between the nearest neighbor ions and next nearest neighbor ions, respectively. λ_{AB} must be positive because it favors antiparallel coupling. Since A and B ions are equivalent, $\mathbf{M}_A = -\mathbf{M}_B$, and $\mathbf{M}_{sA} = \mathbf{M}_{sB} \equiv \mathbf{M}_0$. Thus, similar to that we have proceeded for (1.212), the temperature dependence of antiferromagnetic magnetizations are obtained as

$$\begin{aligned} \frac{M_A}{M_0} &= B_J \left(\frac{g\mu_B J}{k_B T} (\lambda_{AB} - \Lambda) M_A \right) \\ \frac{M_B}{M_0} &= B_J \left(\frac{g\mu_B J}{k_B T} (\lambda_{AB} - \Lambda) M_B \right) \end{aligned} \quad (1.221)$$

where M_0 is saturation magnetization. It is equal for site A and site B . This equation is identical to (1.173) with $(\lambda_{AB} - \Lambda)$ serving as the resultant molecular field constant in place of λ_m . At absolute zero, M_A and M_B are equal to M_0 , that is $\frac{1}{2} N g \mu_B J$ if N is the total number of magnetic ions per unit volume. With increasing temperature the spontaneous magnetization falls, reaching zero at the temperature known as the *Néel temperature*, T_N . From (1.172),

$$\begin{aligned} T_N &= \frac{\frac{1}{2} N g^2 \mu_B^2}{3k_B} J(J+1)(\lambda_{AB} - \Lambda) \\ &= \frac{C}{2} (\lambda_{AB} - \Lambda) \end{aligned} \quad (1.222)$$

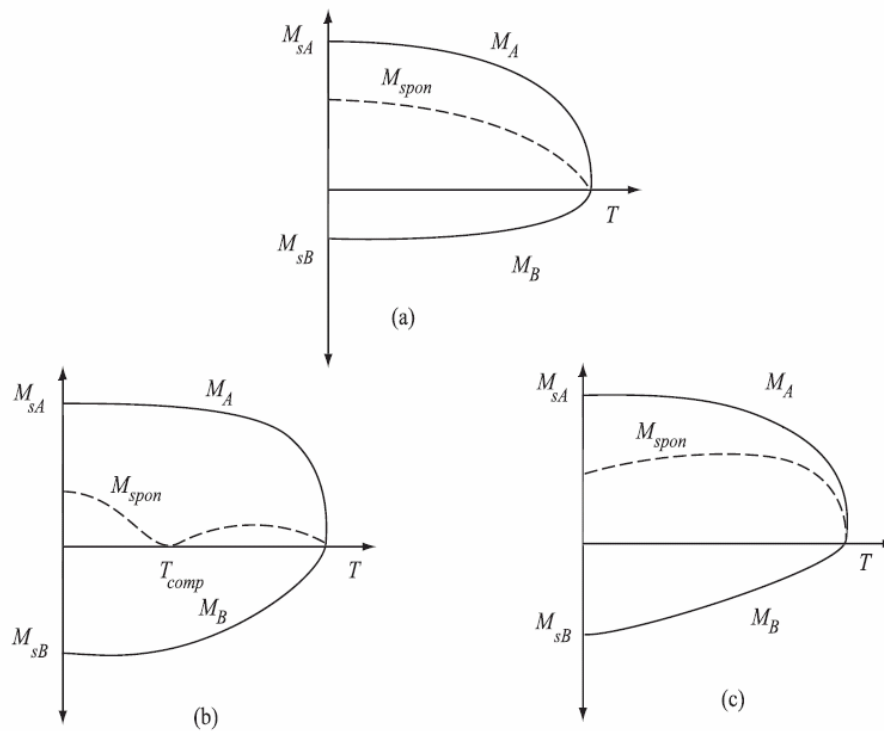


Figure 1.27 The total spontaneous magnetization, M_{spon} , (broken lines) has various shapes depending on the combination of the sublattice magnetizations (full lines). If the saturation magnetization of sublattice A , M_{sA} , differs markedly from that of sublattice B , M_{sB} , M_{spon} show a gradual decrease falling more or less sharply to zero at T_C , and simplest ferrites show this behavior, as shown in fig (a). If M_{sA} and M_{sB} are comparable, anomalous variations occur. For example, M_{spon} may decrease to zero at an intermediate temperature, called the *compensation temperature*, T_{comp} , as shown in Fig. (b). If $\lambda_{AA} \ll \lambda_{BB}$ the M_{spon} can rise to a maximum as shown in (c).

Above Néel temperature, $T > T_N$, it is assumed that M_A and M_B are both parallel to the applied field. Thus, the mean field constant, $\lambda_{AB} - \Lambda$, is replaced by $\lambda_{AB} + \Lambda$. The antiferromagnetic susceptibility can be derived easily to be

$$\chi = \frac{M_A + M_B}{H} = \frac{C}{T + \frac{1}{2}(\lambda_{AB} + \Lambda)C} = \frac{C}{T + \theta} \quad (1.223)$$

where

$$C = \frac{Ng^2\mu_B^2 J(J+1)}{3k_B}$$

and

$$\theta = \frac{1}{2}(\lambda_{AB} + \Lambda)C \quad (1.224)$$

Equation (1.223) is in the form of Curie-Weiss law. However, the Curie-Weiss constant is not equal to the Néel temperature, T_N , at which the long-range order disappears. From (1.222),

$$\frac{\theta}{T_N} = \frac{(\lambda_{AB} + \Lambda)}{(\lambda_{AB} - \Lambda)} \quad (1.267)$$

Now, we compare the temperature dependence of magnetic susceptibility among paramagnets, ferromagnets, and antiferromagnets at temperatures above the Curie temperature, as shown in Figure 1.28. In the figure, below the Néel temperature of an antiferromagnets the spins have antiparallel orientations; the susceptibility attains its maximum value at T_N where there is a well-defined kink in the curve of χ versus T . The transition is also marked by peaks in the heat capacity and the thermal expansion coefficient.

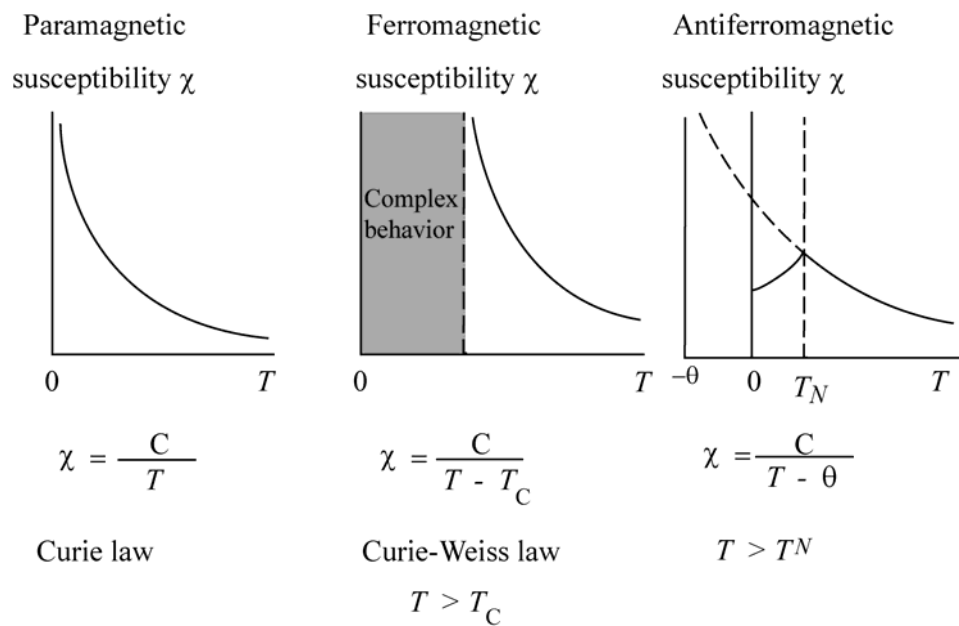


Figure 1.28 Temperature dependence of the magnetic susceptibility in paramagnets, ferromagnets, and antiferromagnets. [From C. Kittel, *Introduction to Solid State Physics*, John Wiley and Sons, Inc. 6th ed., 1996].

1.2.7 Magnetic Domain and Hysteresis of Magnetization

In a lump of ferromagnets, iron for example, all the spins do not align in the same direction as shown in Figure 1.29 (a). In order to produce a single magnetized domain through a crystal the single direction of spontaneous a very strong external magnetic field is necessary. For the domain alignment a lot of energy is needed. This energy can be reduced by arranging one side of the crystal block to be magnetized *up* and the other side to be magnetized *down*, which are divided by a wall, as illustrated in Figure 1.29 (b). If the number of such blocks is increased as shown in (c), the energy is further reduced. However, the energy can be enhanced at the wall because of antiparallel alignment of spins. This energy is sometimes called the *wall energy*. A region having only one direction of magnetization is called the *domain*, and the wall is called the *domain wall*.

Actually nature has discovered the ways to arrange domains so as for the fields do not go outside the materials, as shown in Figure 1.29 (d)-(e). When a magnetic field is applied, the domain walls begin to move into regions which are magnetized opposite to the field. The magnetization of the sample increases according to the increase of the domain area. If the applied field is increased, all of the magnetic spins are eventually aligned along the direction of applied field, giving the saturated magnetization. The relation curve between magnetization and applied field, therefore, can tell something about the spin structure. The curve of magnetization versus applied field is known as *magnetization curve*. The irreversible aspect of the magnetization curve, as shown in Figure 1.30, is known as *hysteresis*.

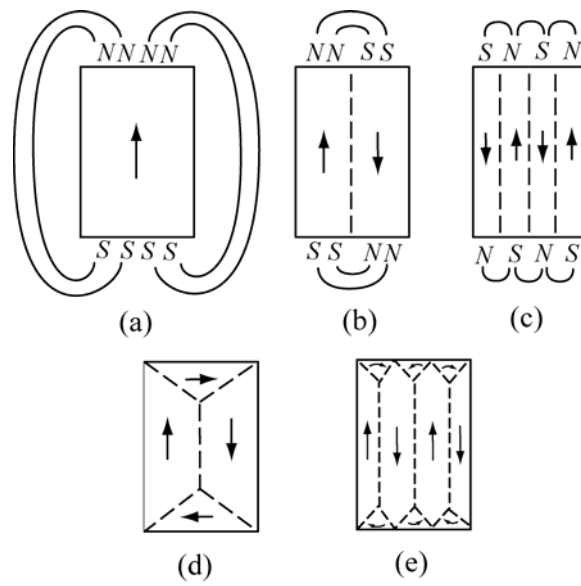


Figure 1.29 The formation of domains in a single crystal of Fe. [From C. Kittel, *Introduction to Solid State Physics*, John Wiley and Sons, Inc. 6th ed., 1996]

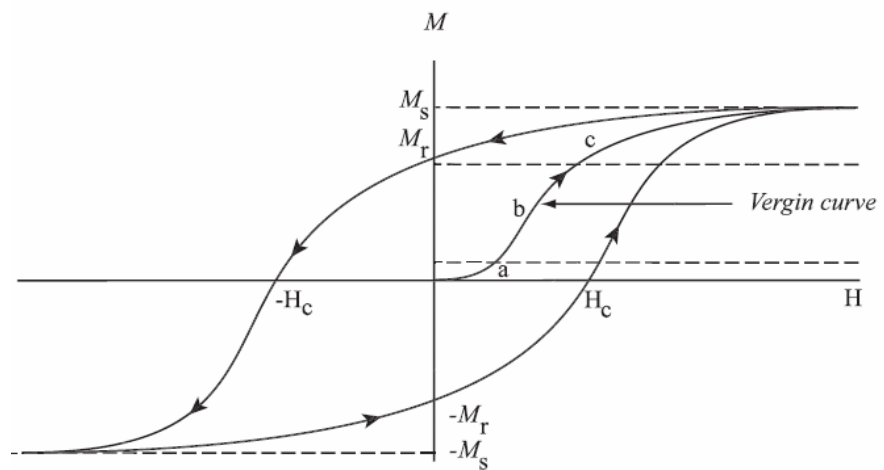


Figure 1.30 Typical hysteresis of the magnetization curve versus the applied field.

In sputtered materials, usually they have a polycrystalline structure. Inside such materials there are many different little crystals with axes at different orientations. When a magnetic field is applied the domain walls in each crystal begin to move, and the domains which have a favorable direction of easy magnetization grow larger. This growth is reversible. If the magnetic field is turned off the magnetization will return to zero. This part of the magnetization curve is marked “a” in Figure 1.30. As the applied field is increased, the domain walls can be stuck at various defects as grain boundaries and dislocations. When the applied field is large enough, the wall suddenly snap the past cause of the rapid increase of magnetization, as shown in part “b” in Figure 1.30. Since there is an energy loss in the interaction between the domain walls and the grain boundaries, this part of magnetization is irreversible. Even though all the spin moments align parallel to each other, they may not be aligned with the applied field but along some preferred crystallographic direction. This is due to *magnetic anisotropy*.

As the applied field is further increased, the magnetization gradually reaches a maximum value, it is the *saturation magnetization* (M_s). The saturation magnetization is an intrinsic property of materials. It has the same value no matter what the proceeding history has been. If the field is decreased back to zero, the magnetization follows a different curve on the way down and the magnetization does not go to zero. The magnetization at zero applied field is called *remanent magnetization* (M_r). Materials with large remanent magnetization are called *hard ferromagnets*, and those with small remanent magnetization are called *soft ferromagnets*. The magnetization is brought to zero by applying the external field in the opposite direction. The field required to return the magnetization to zero is called

coercive field denoted by H_c as shown in Figure 1.30. The remanent magnetization and coercive field are not intrinsic properties of materials.

1.3 Characteristic of Synchrotron Light

Synchrotron light has a number of unique properties:

(1) Wide energy range and continuous spectrum: Synchrotron radiation is emitted with a wide range of energy from the far infrared to X-ray region. This tunable light is useful to study electronic structure of materials. Incident photon energy is sufficient to excite core electrons in atoms. Moreover, the continuous spectrum allows one to study atomic construction in materials using EXAFS (Extended X-ray Absorption Fine Structure: EXAFS), for which the continuous incident x-rays are required.

(2) High flux: Synchrotron radiation has much higher photon flux than those of radiation from a conventional source. It has very high intensity. This reduces measurement time and increases resolution and accuracy in experiments.

(3) High brilliance: Synchrotron radiation is extremely intense (hundreds of thousands of times higher than conventional X-ray sources) and highly collimated. The size of the source point is small. These increases the brilliance of radiation and the radiation intensity available at the sample site is quite high.

(4) Synchrotron radiation is highly polarized light: Synchrotron radiation emitted from a bending magnet is linearly polarized and elliptically polarized in the directions in-plane and off-plane of the electrons orbit, respectively. A more high circularly polarized can be generated by insertion devices such as an helical multipole wiggler and a specially designed undulator. The polarization of incident photon is

utilized to investigate magnetic properties of materials. It is used to study spin orientation of an electron in a magnetic sample.

(5) Synchrotron light is emitted in very short pulses: Typically, the pulse length is less than a billionth of a second. Because of the fact that the electron beam in a storage ring consists of a series of electron bunches, synchrotron light is generated as very short repeating pulses. Pulsed light makes it possible to study time-dependent phenomena.

CHAPTER II

PURPOSE OF THE STUDY

The present study aims at investigating the interlayer magnetic coupling (IMC) in Al/Fe/Al/Gd magnetic multilayer films. The following manners will be described and discussed:

- 1) A series of Al/Fe/Al/Gd multilayer films are deposited by means of magnetron sputtering. The detail of the sample preparation is described.
- 2) The hysteresis and the temperature dependence of the magnetization are measured by SQUID. The selective element studies by means of X-ray magnetic dichroism (XMCD) is used to measure the hysteresis of the XMCD effect at Gd L_3 -edge. The magnetic Compton profile (MCP) measurements are used to study the ratio of spin-moments in Fe and Gd layers.
- 3) Comparison of IMC between Fe/Gd and Fe/Al/Gd/Al multilayer films is made.
- 4) The Al thickness dependence of IMC in Al/Fe/Al/Gd multilayer film is studied.

CHAPTER III

INTERLAYER MAGNETIC COUPLING

3.1 Basic Concept of Interlayer Magnetic Coupling

Interlayer magnetic coupling (IMC) typically means the exchange interaction between magnetic layers through a non-magnetic spacer. The possible lowest energy states of the system led by the IMC are shown in Figure 3.1. In the figure, the magnetic moments of a layer couples to those of nearby layers through the non-magnetic-metal spacer. In many cases the spacer is made of metal. This is because it is believed that the conduction electrons in the spacer are the key of IMC between the magnetic layers. The IMC is significantly affected by the thickness of the spacer, denoted by R , which is the main subject of the present thesis and will be discussed later. IMC is either *antiferromagnetic coupling* or *ferromagnetic coupling*. The phase difference, ϕ , between two magnetic layers is 0° for the ferromagnetic coupling and 180° for the antiferromagnetic coupling as seen in Figure 3.1(a) and (b), respectively.

The antiferromagnetic and ferromagnetic interlayer couplings are referred to as *bilinear coupling*. Another case is that the magnetization of each layer couples at an angle of 90° to an adjacent layer as shown in Figure 3.1 (c). This is often called *biquadratic coupling*. In other case, for films with the helical magnetic structure like a Dy film (see Figure 3.1 (d)) the interlayer coupling leads to an angle ϕ between the magnetic moments on both sides of the spacer (Majkrzak, 1986 June).

Discussion on the multilayer consisted of helical magnetic layers is out of the scope of this thesis and will not be included in this thesis. The good review of the interlayer coupling for rare-earth magnetic multilayers was written by Majkrzak (1991).

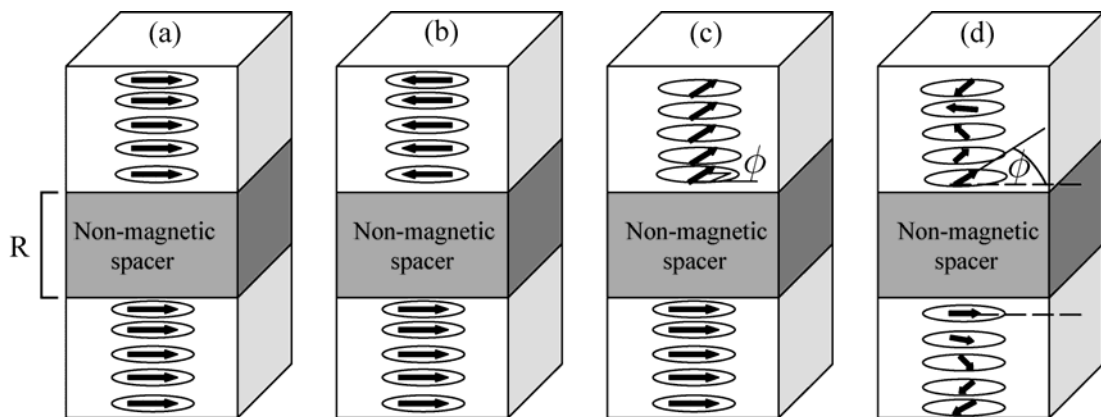


Figure 3.1 Interlayer magnetic coupling (IMC) between magnetic films across the interlayer metallic spacer (dark shaded). The arrow in each circle indicates the magnetic moment of each monolayer sheet. These magnetic moments indicate (a) ferromagnetic coupling, (b) antiferromagnetic coupling, (c) biquadratic coupling where the magnetic moments in adjacent layers make an angle 90° to each other, and (d) the coupling between helical magnetic layers with different phase ϕ .

3.2 Survey of Experimental Achievements

The interlayer magnetic coupling (IMC) was first observed in Dy/Y by Salamon, et al. (January 1986), Gd/Y by Majkrzak, et al. (June 1986), and in Fe/Cr by Grünberg, Schreiber, Pang, Brodsky, and Sowers (November 1986). Shortly after those, Baibich et al. (1988) and Binasch, Grünberg, Saurenbach, and Zinn (1989) discovered a huge magnetoresistance led by the antiferromagnetic IMC in Fe/Cr multilayer known as a giant magnetoresistance (GMR). A year later, Parkin, More, and Roche (1990 May) reported the discovery of the oscillatory coupling strength as a function of the spacer thickness, in Co/Ru, Co/Cr and Fe/Cr. After that a number of investigations of IMC in various films have been reported. Particularly studies on multilayers consisting of magnetic transition materials (Fe, Ni, Co) separated by non-magnetic transition or noble metals are remarked; they are either paramagnetic (Cu, Ag, Au, Al, Ru, Pd, V, etc.) or antiferromagnetic (Cr, Mn). In case the spacer layer is a transition metal, the oscillation of IMC is found to be a general phenomenon (Parkin, December 1991). The oscillatory coupling behavior has been described with several models. For example, with The RKKY-like model, the quantum well model, etc. These models will be mentioned below. In the same year that Parkin et al. discovered the oscillatory IMC, Grünberg, Demokritov, Fuss, Vohl, and Wolf (1991) have observed the biquadratic exchange in a Fe/Cr/Fe trilayer. This coupling is believed to be due to the imperfection of the interface between layers which will be discussed later.

Since 1990, a great number of work on IMC in various materials has been reported. Only the key phenomena are reviewed here. They are led by IMC between magnetic layers through a non-magnetic spacer. Experimental achievements

concerning the bilinear coupling, oscillatory IMC, and the biquadratic coupling are surveyed in this section.

The review articles about IMC have been reported by a number of authors. Fert et al. (1995) gave a critical review of the research on the interlayer coupling. Slonczewski (1995) overviewed theories of the interlayer exchange. In particular, he described the fluctuations of spacer thickness and loose spin theory which is to explain the biquadratic coupling phenomena. Moreover, for the biquadratic coupling, both the observations of phenomena and theoretical explanations were reviewed by Demokritov (1998). Jones (1998) gave an excellent review of the developments of theoretical models on IMC. He classified the theoretical models according to groups of authors. Himpsel, Jung, and Seidler (1998) provided a survey of the quantum well states model and the experimental confirmation of the model. Stiles (1999) emphasized the bilinear coupling, particularly on oscillatory IMC and compared the theory and the experimental results. A more general theoretical model, the quantum interference model, is given by Bruno (1999).

3.2.1 Bilinear Coupling

The discovery of antiferromagnetic IMC by Grünberg et al. (1986) in Fe/Cr/Fe layers, demonstrated that the antiferromagnetic interlayer interaction, decaying regularly with increasing Cr spacer thickness. Phenomenologically, the exchange coupling energy per area can be expressed as

$$E_{exc} = -2JM_1 \cdot M_2 \quad (3.1)$$

where J is called the coupling constant. M_1 and M_2 are the magnetizations of two ferromagnetic layers. Since equation (3.1) bilinear with respect to M_1 and M_2 , it is so called the bilinear coupling. This exchange energy is, in fact, in the form of the

Hiesenberg exchange energy, (1.202), in which the coupling constant J includes the exchange integral. Thus, the interlayer coupling constant is positive for ferromagnetic coupling and is negative for antiferromagnetic coupling.

3.2.2 Oscillatory Interlayer Exchange Coupling

The discovery, by Parkin (1990), that the magnitude of the interlayer coupling constant in (3.1) oscillates with as the thickness of the spacer layer is varied. He found that IMC oscillates with a long period ranging in 12 Å in Co/Ru to 18-21 Å in Fr/Cr and Co/Cr. After that, systematic studies of the multilayer grown by sputtering with Co as ferromagnetic layer (Parkin , December 1991) revealed that the oscillatory behavior is observed in spacer layers consisting of almost any transition or noble metals. He reported that the oscillation periods were in the range of 9 Å to 12 Å for V, Cu, Mo, Ru, Th, Re, and Ir spacer layers and 18 Å for Cr spacer layer. These results were confirmed later by several reported e.g. Grünberg et al. (1991, April), Petroff et al. (1991), Ounadjela et al. (1992), Huai and Cochrane (1992). Oscillatory IMC is expressed as the spacer thickness dependence of the saturation filed as shown in Figure 3.2. The generic behavior of oscillatory IMC is understood as an interaction which varies periodically in the sign and the magnitude decaying as $1/R^2$, where R is the spacer thickness. The strength of IMC depends both on the characteristics of the spacer and of the magnetic layers. The oscillation period, on the other hand, depends on the nature and the crystalline orientation of the spacer metal, but not on the nature or the thickness of the magnetic layers.

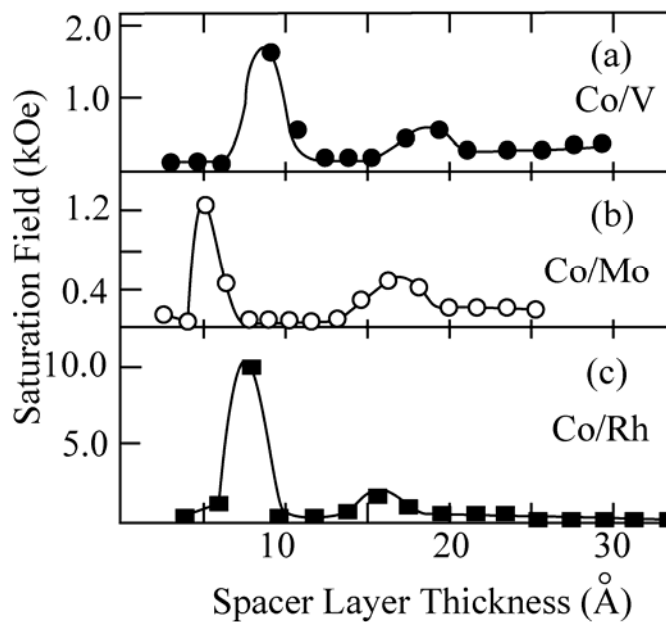


Figure 3.2 Dependence of the saturation field on the spacer-layer thickness for families of (a) Co/V, (b) Co/Mo, and (c) Co/Rh multilayers. [After Parkin, December 1991].

In multilayer films grown by means of sputtering, and having the polycrystalline structure, only long periods (10-18 Å) have been observed. The calculation of the oscillatory IMC periods by using several models revealed also a short period (2-3 Å) which will be discussed below. On the other hand, for the multilayer grown epitaxially, it has been found experimentally that multi-periodic (both short period and long period) oscillatory IMC exists. Usually, this epitaxially grown film consists of two magnetic layers separated by a layer of spacer, three layers in total. It is so called *trilayer film*. Examples, the short periods oscillatory IMC has been observed in the trilayer systems of Fe/Cr/Fe (Demokritov et al., 1991), Fe/Au(001)/Fe and Fe/Al/Fe (Fuß, 1992), Fe/Ag/Fe(100) (Unguris, 1993), Fe/Au/Fe(100) (Unguris, 1994), etc. The excellent review on the oscillatory magnetic properties is given by Allenspach and Weber (1998).

3.2.3 Biquadratic Coupling

The biquadratic coupling phenomenon was first observed in Fe/Cr/Fe(001) trilayer (Grünberg et al., April 1991). The magnetization curves of the Fe/Cr/Fe(001) layered system, measured for relatively thick Cr spacers, demonstrate a well-defined phase, existing in a finite interval of the applied field. In this phase, the total of magnetization of the trilayer equals to one-half of the saturation magnetization, found, for example, in Figure 3.3. Detailed investigation of the Fe/Cr/Fe with a wedge shaped Cr interlayer was reported by Rühlig et al. (1991). They measured the domain pattern by MOKE magnetometry and the magnetization curves of the Fe(100Å)/Cr(5 Å)/Fe(100 Å) trilayer. Their results successfully evidence that the two layers of Fe exhibit the biquadratic coupling to each other.

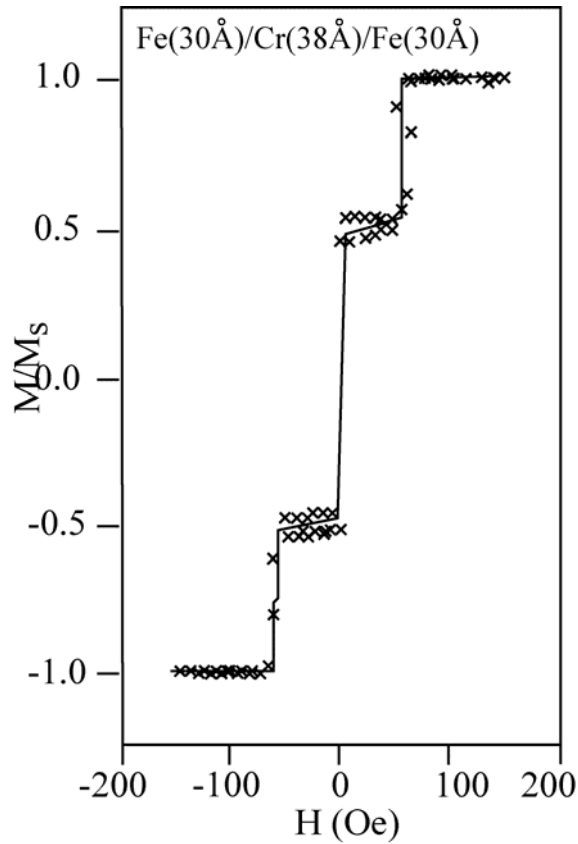


Figure 3.3 Magnetization curves of the $\text{Fe}(30\text{\AA})/\text{Cr}(38\text{\AA})/\text{Fe}(30\text{\AA})$ trilayer, demonstrate the biquadratic coupling between the magnetizations of Fe layers.[After Demokritov, 1998].

The phenomenological description of the exchange energy per surface area is, therefore, obtained as an expression of the form:

$$E_{\text{exch}} = -2J_1 \mathbf{M}_1 \cdot \mathbf{M}_2 - J_2 (\mathbf{M}_1 \cdot \mathbf{M}_2)^2 \quad (3.2)$$

The first term represents the bilinear coupling and the second term represents the biquadratic coupling. J_1 and J_2 are the bilinear and biquadratic exchange coupling constants, respectively.

The experimental evidences for the biquadratic coupling have also been found in a number of trilayer films. They are reviewed by Demokritov (1998),

i.e. Fe/Al/Fe, Fe/Cu/Fe, Fe/Ag/Fe, Fe/Au/Fe, NiFe/Ag/NiFe, Co/Ru/Co, NiFe/Cu/Co, NiFe/Cu/NiFe, Fe/FeSi/Fe, and Fe/AuSn/FeNiB.

3.3 Survey of Theoretical Models

3.3.1 Total energy calculation

In a bilinear coupling system, the strength of IMC for a certain spacer thickness (R) is calculated from

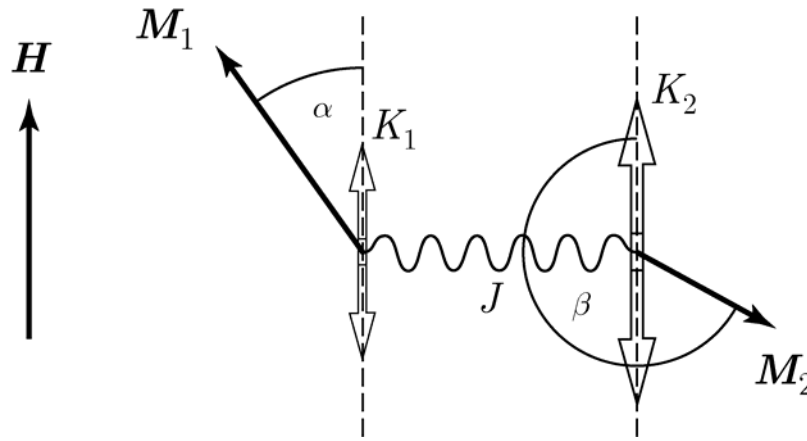
$$J = \frac{E_{total}^{\uparrow\downarrow} - E_{total}^{\uparrow\uparrow}}{2} \quad (3.3)$$

where $E_{total}^{\uparrow\downarrow}$ is the total energy of the system in the case of antiferromagnetic coupling between the magnetic layers and $E_{total}^{\uparrow\uparrow}$ is the total energy in the case of ferromagnetic coupling. If J takes a positive value, the system has antiferromagnetic coupling, if J is negative ferromagnetic system occurs.

Advance in the computer performance made it possible to calculate the total energy although the value is extremely larger than that of the difference. The first-principle calculations have been performed by numerous authors to calculate the total energy for the realistic systems. Herman and his group calculated the IMC in Fe/X, where $X = \text{Cr}$ and Cu (1991) and later V , Mn (1995), by means of self-consistent spin-polarized linearized muffin-tin orbital/atomic sphere approximation (LMTO/ASA) and linearized augmented spherical wave methods/atomic sphere approximation (LASW/ASA). Krompiewski and coworkers (1993) calculated IMC in Fe/Cu by tight-binding LMTO/ASA method. The results of the total energy calculations present both the coupling strength and periods of oscillation of IMC. Unfortunately, no such calculation has been reported on Fe/Al or Gd/Al multilayers.

3.3.2 Mean Field Theory

We consider the simplest case of a exchange energy in a multilayer consisting of two different magnetic layers separated by a non-magnetic layer having thickness R . We assume that the magnetic layers have magnetic moments M_1 and M_2 making angle α and β to the direction of external field H which is aligned to the z - direction. The magnetic anisotropy energy of the magnetic layers is assumed to be uniaxial. The magnetic anisotropy constants of the layers 1 and 2 are given by K_1 and K_2 , respectively.



The hamiltonian can be written as

$$H = -(M_1 + M_2) \cdot H - 2J_{12}(M_1 \cdot M_2) - K_1 \cos^2 \alpha - K_2 \cos^2 \beta \quad (3.4)$$

The first term expresses the energy due to the external field H , the Zeeman energy. The second term represents the interlayer coupling between the magnetic layers 1 and 2 through the spacer layer. J_{12} is known as the *coupling constant*. The coupling constant is positive or negative for the ferromagnetic or antiferromagnetic coupling modes, respectively. Then, the total energy of the system is given by

$$E = -M_1 H \cos \alpha - M_2 H \cos \beta - 2J_{12} M_1 M_2 \cos(\alpha - \beta) - K_1 \cos^2 \alpha - K_2 \cos^2 \beta \quad (3.5)$$

For simplicity, we consider the case where either the magnetization of layer 1 or that of layer 2 rotates independently. Then, the equilibrium angles can be determined from the energy minimum conditions, namely,

$$\begin{aligned}\frac{\partial E}{\partial \alpha} &= M_1 H \sin \alpha + 2J_{12}M_1M_2 \sin(\alpha - \beta) + K_1 \sin 2\alpha = 0 \\ \frac{\partial E}{\partial \beta} &= M_2 H \sin \beta - 2J_{12}M_1M_2 \sin(\alpha - \beta) + K_2 \sin 2\beta = 0\end{aligned}\quad (3.6)$$

and

$$\begin{aligned}\frac{\partial^2 E}{\partial \alpha^2} &= M_1 H \cos \alpha + 2J_{12}M_1M_2 \cos(\alpha - \beta) + 2K_1 \cos 2\alpha > 0 \\ \frac{\partial^2 E}{\partial \beta^2} &= M_2 H \cos \beta + 2J_{12}M_1M_2 \cos(\alpha - \beta) + 2K_2 \cos 2\beta > 0\end{aligned}\quad (3.7)$$

Obviously (3.6) and (3.7) are satisfied if α and β take the following pairs of values:

$$\begin{aligned}(1) \quad & \alpha = 0, \beta = 0 \\ (2) \quad & \alpha = 0, \beta = \pi \\ (3) \quad & \alpha = \pi, \beta = 0 \\ (4) \quad & \alpha = \pi, \beta = \pi\end{aligned}\quad (3.8)$$

The magnetization configurations of the system are stable if α and β takes one of the pairs in (3.8). It depends on the quantities H, K_1, K_2 and the interlayer coupling term, $J_{12}M_1M_2$. The possible states in (3.7) are shown in Figure 3.4. In the figure, the four possible states in (3.8) are shown. There are several possible switching among these states, e.g. (1) \rightarrow (2), (2) \rightarrow (4), (4) \rightarrow (3), etc. The switching field required for changing states is dependent on the factors M_1, M_2, K_1, K_2 and $J_{12}M_1M_2$, as mentioned above.

For simplicity, we consider only the case of antiferromagnetic coupling system. This is the case $J_{12} < 0$. Thus, if we change the external field from $-\infty$ to ∞ , the state changes as follows:

$$(1) \rightarrow (2) \rightarrow (3) \rightarrow (4)$$

Now, a problem arises. What is the magnitude of the applied field that is required for changing between the states? We first consider the state switching from state (1) to state (2). In switching from the state (1) to state (2), only the layer 2 flops. Then, the switching field can be obtained from

$$\frac{\partial^2 E}{\partial \beta^2} = 0, \quad \alpha = \beta = 0 \quad (3.9)$$

Using (3.9) and (3.7), we obtain

$$H^{12} = -2J_{12}M_1 - \frac{2K_2}{M_2} \quad (3.10)$$

Calculating in the similar way, we have

$$H^{34} = 2J_{12}M_1 - \frac{2K_2}{M_2} \quad (3.11)$$

$$H^{43} = 2J_{12}M_1 + \frac{2K_2}{M_2} \quad (3.12)$$

$$H^{21} = -2J_{12}M_1 + \frac{2K_2}{M_2} \quad (3.13)$$

The calculation of the switching field H^{23} is slightly different, because the magnetizations in both layers rotate simultaneously. We assume that $\theta = \alpha = \beta + \pi$. Then, from (3.5) we obtain

$$E = -M_1 H \cos \theta + M_2 H \cos \theta + 2J_{12}M_1M_2 - K_1 \cos^2 \theta - K_2 \cos^2 \theta \quad (3.14)$$

The equilibrium angles is determined from

$$\left. \begin{aligned} \frac{\partial E}{\partial \theta} &= M_1 H \sin \theta - M_2 H \sin \theta + K_1 \sin 2\theta + K_2 \sin 2\theta = 0 \\ \frac{\partial^2 E}{\partial \theta^2} &= M_1 H \cos \theta - M_2 H \cos \theta + 2K_1 \cos 2\theta + 2K_2 \cos 2\theta > 0 \end{aligned} \right\} (3.15)$$

The switching field required to change the states between the states (2) and (3) can be determined from

$$\frac{\partial^2 E}{\partial \theta^2} = 0 \quad (3.16)$$

Therefore,

$$\theta = 0, \pi \quad (3.17)$$

We are considering the changing of the magnetization states from state (2) to state (3). So that we use $\theta = 0$. Therefore the switching field is

$$H^{23} = -\frac{2(K_2 + K_1)}{M_1 - M_2} \quad (3.18)$$

Similarly,

$$H^{32} = \frac{2(K_2 + K_1)}{M_1 - M_2} = -H^{23} \quad (3.19)$$

From (3.4) through (3.19) we have considered the magnetic anisotropy in the total energy of the system. In order to calculate the coercive field, H_c , we consider in total energy of the system with the coercivity energy. We assume that the switching field, H^{mn} , is given by the field at which the free energy difference, $E_m - E_n$, exceeds the coercivity energy. The coercivity energy is the energy required for the irreversible magnetization reversal. In a single layer film with the magnetization M , the coercivity energy is equal to $2MH_c$. Then, we have

$$E_m - E_n = 2MH_c \quad (3.20)$$

When the system transition from state (1) to state (2), we have

$$\left. \begin{aligned} E_1 &= -M_1H - M_2H - 2J_{12}M_1M_2 \\ E_2 &= -M_1H + M_2H + 2J_{12}M_1M_2 \end{aligned} \right\} \quad (3.21)$$

Here, the magnetization reversal takes place only in the layer 2. From (3.10) and (3.21) we obtain

$$E_1 - E_2 = -2M_2H_{12} - 4J_{12}M_1M_2 = 2M_2H_{c2} \quad (3.22)$$

$$\therefore H^{12} = -2J_{12}M_1 - H_{c2} \quad (3.23)$$

Similarly,
$$H^{34} = 2J_{12}M_1 - H_{c2} \quad (3.24)$$

$$H^{43} = 2J_{12}M_1 + H_{c2} \quad (3.25)$$

$$H^{21} = -2J_{12}M_1 + H_{c2} \quad (3.26)$$

Here, H_{c2} denotes the field at which the reversal of M_2 occur. Comparing (3.23) with (3.11), we obtain the physical meaning of H_{c2} as

$$H_{c2} = \frac{2K_2}{M_2} \quad (3.27)$$

Thus, equation (3.23) means that the field required for changing the state (1) to the state (2) depends on the interlayer coupling strength, J_{12} , the magnitude of the magnetizations, M_1, M_2 , and the magnetic anisotropy constant, K_2 .

In the similar way, we can calculate switching field H_{23} . By carrying this, we obtain

$$E_2 - E_3 = -2M_1H^{23} + 2M_2H^{23} = 2(M_1H_{c1} + M_2H_{c2}) \quad (3.28)$$

$$H^{23} = \frac{2(M_1H_{c1} + M_2H_{c2})}{M_2 - M_1} \quad (3.29)$$

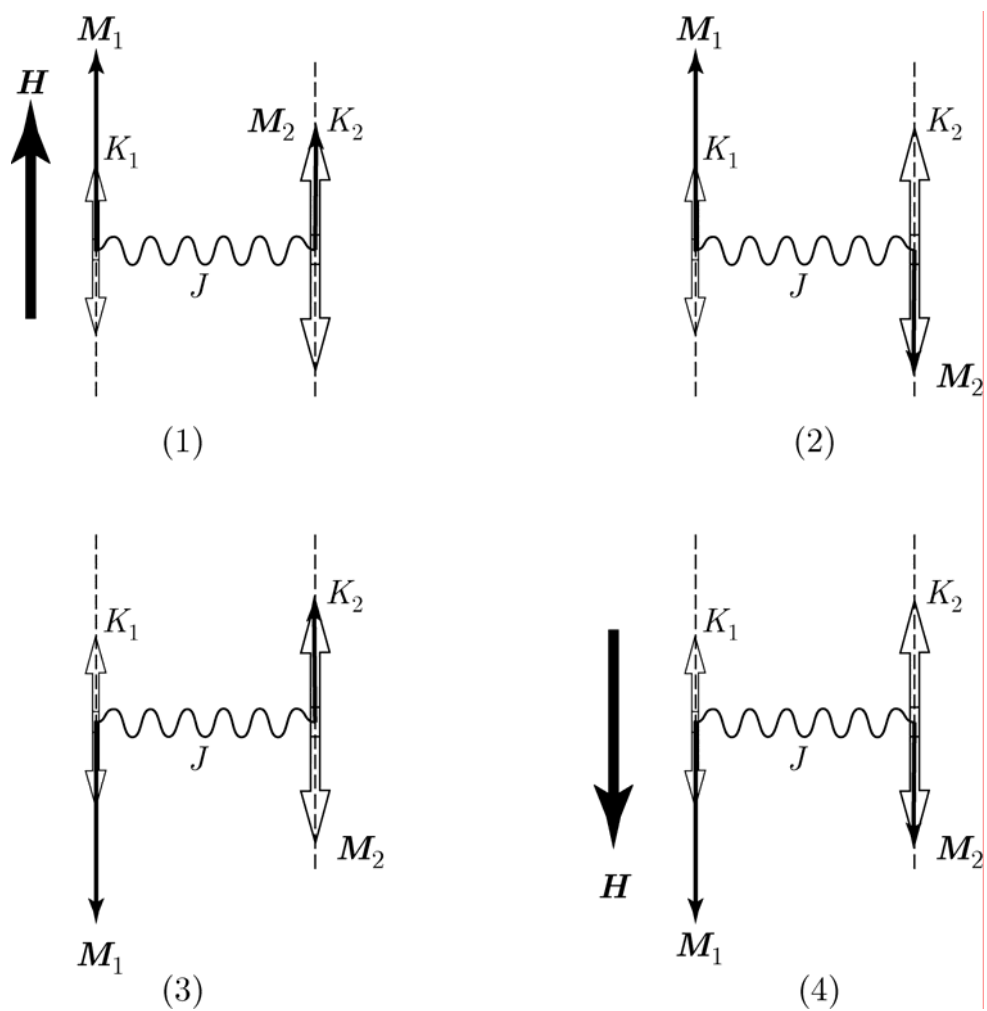


Figure 3.4 Magnetization configurations in the system of two magnetic layers separated by a non-magnetic layer.

Comparing (3.29) with (3.18), we obtain

$$H_{c1} = \frac{2K_1}{M_1} \quad (3.30)$$

Now, we can inspect the switching of the states (1) \rightleftharpoons (2) \rightleftharpoons (3) \rightleftharpoons (4).

For doing this we show the example of hysteresis of magnetizations, as seen Figure 3.5. In the figure, the magnitude of magnetization M_1 is assumed to be larger than that of M_2 .

If the external field is applied from $-\infty$ to ∞ the magnetization configurations change from states (1) \rightarrow (2) \rightarrow (3) \rightarrow (4). When the field is sufficiently high, the state (1) is the most stable state. In this state, the magnetizations in both layers are aligned parallel to the direction of the external field. Then, the total magnetizations are

$$M = M_1 + M_2; \quad H > H^{12} \quad (3.31)$$

When the external field is decreased to H^{12} , the most stable state is changed to be state (2). In this state, M_1 directs to the direction of H while M_2 opposes the direction of H . When the reverse field is applied, the magnetizations, in state (2), cannot easily rotate due to the presence of a magnetic anisotropy. However, when the field increases to H^{23} the states (2) changes to (3). Finally, the state (4) becomes the most stable state when the reverse field is sufficiently high. If we applied the external field from $-\infty$ to ∞ we obtain the hysteresis of magnetization, as shown in Figure 3.5.

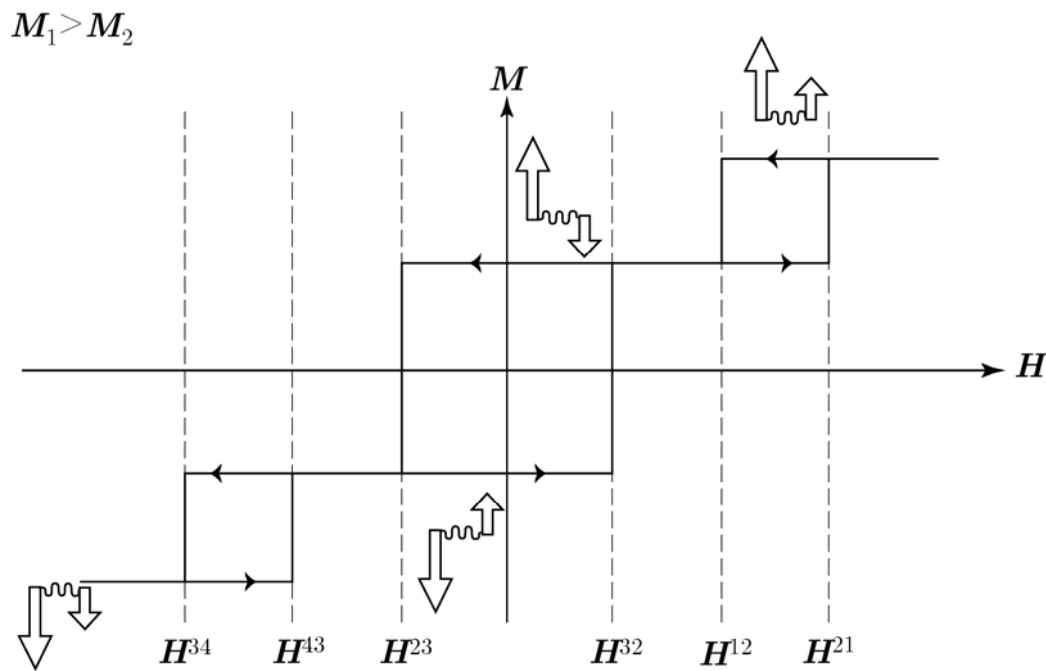


Figure 3.5 Calculated magnetizations of the two magnetic layer system. The calculations are based on the mean-field theory. The magnetizations of both layers are assumed to be rotated independently with each other.

In conclusion of this section, we have applied the mean-field theory to calculate the possible magnetization configurations of the two magnetic layers system. We have assumed that the magnetic anisotropy in both layers is uniaxial type, and the magnetization in one layer is larger than that in the other. The significant assumption of the consideration is that the magnetizations in both layers rotate independently with each other. This means calculation results may not be able to explain the complicated system of magnetic multilayers such as the Al/Fe/Al/Gd films. This is the sample used in experiments for this thesis.

In the system of Al/Fe/Al/Gd multilayer films, the magnitude of the magnetization of the Fe layer is larger than that of Gd layer. So that, we give the magnetization of Fe and Gd layers in equation (3.19) as M_1 and M_2 , respectively. Let us consider the magnetizations are in state (2). Then, the total magnetization is $M_0 = M_1 - M_2$. Since, the magnetic anisotropy of the Fe layers is very small compared with that of the Gd layer, we give $K_1 \simeq 0$ for Fe layer and $K_2 = K$ for the Gd layer. From equation (3.18), we have

$$H^{23} = \frac{2K}{M_0} = H_c \quad (3.32)$$

This is the coercive field of the system. This equation will be adopted in Chapter VI.

3.3.3 RKKY Model

The RKKY was named according to Ruderman and Kittel (1954), Kasuya (1956), and Yosida (1957). Ruderman and Kittel proposed the indirect exchange coupling between nuclear spins by the hyperfine contact interaction with conduction electrons. Kasuya and Yoshida proposed the similar indirect coupling between localized (d or f) electrons through their exchange interactions with the conduction electrons. They considered that a magnetic impurity embedded in a non-magnetic spacer produces the polarization of the conduction electrons in its near environment. The spin of the conduction electrons oscillates up and down as a function of the distance away from the magnetic impurity with the characteristic wavelength $\lambda_F = \pi / k_F$, where k_F is the wave vector on the Fermi surface. When two impurities are close enough to each other, interactions between the through the polarizations of conduction electrons occur. If a second impurity is within the positive polarization region of the conduction electron polarization due to the first impurity,

the second impurity couples ferromagnetically to the first impurity. On the other hand, if the second impurity is within the negative polarization, it makes the antiferromagnetic coupling to the first impurity. The RKKY interaction takes the form of the exchange coupling,

$$E_{RKKY} = -2J(r)\mathbf{S}_i \cdot \mathbf{S}_j \quad (3.33)$$

where \mathbf{S}_i and \mathbf{S}_j are spins of the two magnetic impurities and r is the distance between them. For bulk materials (3 dimensions), the exchange coupling $J(r)$ oscillates and decays as r^{-3} , as shown in Figure 3.6.

For magnetic multilayers, the RKKY interaction was first extended to explain the interaction between magnetic layers through a non-magnetic spacer layer by Yafet (1987). He derived that the strength of the interaction between two sheets of magnetic impurities separated by a distance, r , decays as $1/r^{-2}$. Bruno and Chappert (1991 - 1992) extended the two sheets impurities to arbitrary crystal structure. They derived the periods of the oscillatory coupling in terms of the Fermi surface of the spacer. The Fermi surface information by experiments has been used in the calculation and gives both short- and long- periods of the oscillations.

The long-period oscillation that is found in sputtered multilayers is known to be due to the *arising effect* (or *Vernier effect*). It has been reported by several authors (Coehoorn, 1991; Deaven, Rokhsar, and Johnson, 1991). Bruno (1995) extended the theory of the oscillation to the more general form. Although the periods of the oscillation that predicted by the models based on the RKKY interaction are in good agreement with experiments, the RKKY based models did not enable us to present the quantitative description of the amplitude of the oscillatory coupling.

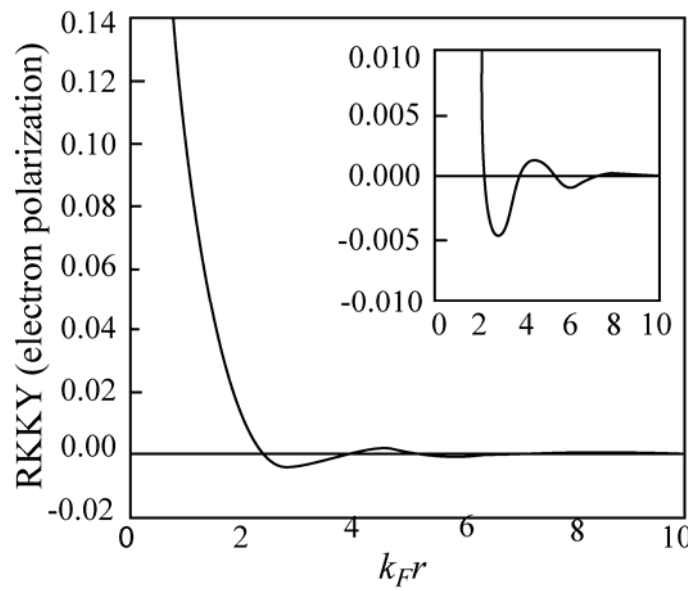


Figure 3.6 Oscillation of electron polarizations as a function of distance r around a single magnetic impurity. Alternatively, this figure can be viewed as the oscillatory RKKY coupling between two magnetic impurities separated by a distance r in three dimensions. Inset shows closed up the vertical axis view [After Jones, 1998].

3.3.4 Quantum Well Model

The quantum well model was first proposed by Edwards and Mathon and collaborators (Edwards et al., 1991; Edwards et al., 1992; Mathon et al., 1995; Mathon et al., 1997) and other authors (Barnas et al., 1992; Erickson et al., 1993). This model predicts not only periods of the oscillations but also the strength or the amplitude of the exchange coupling. Only the basic idea is presented briefly as follow.

In this approach the coupling is ascribed to the change of density of states resulting from the spin-dependent confinement of the electrons (or holes) in the quantum well provided by the spacer layer. Figure 3.7 shows a schematic picture of the bulk band structure of a multilayer film. The figures demonstrate the electron confinement for antiferromagnetic IMC (Antiparallel coupling) and for ferromagnetic IMC (Parallel coupling). In the magnetic layers, the bands are completely spin polarized so that the minority band is unoccupied above the Fermi level (E_F). The total magnetization of the layers point along the direction of the electron spins which occupy in the majority band. In the spacer layer, non-magnetic material, there is no polarization of spin so that the up-spin and down-spin bands are degenerated.

In the case of antiferromagnetic IMC, the magnetizations of the magnetic layers are aligned antiparallel to each other. The propagating state in the spacer reaching an interface is reflected if the state in the magnetic layer is not of the same symmetry as that of the spacer. If the symmetry is the same, the propagating state is allowed to transmit into the magnetic material. This is just caused by the Pauli exclusion principle. Then the up-spin electrons in the spacer cannot jump into up-spin states in the magnetic layer, since the corresponding empty state is located well above the E_F , see the right hand side in Figure 3.7(a).

The situation is different on the left hand side that the spin-up electrons will escape into the magnetic layer. The same situation occurs for a spin-down electron which can escape to the right.

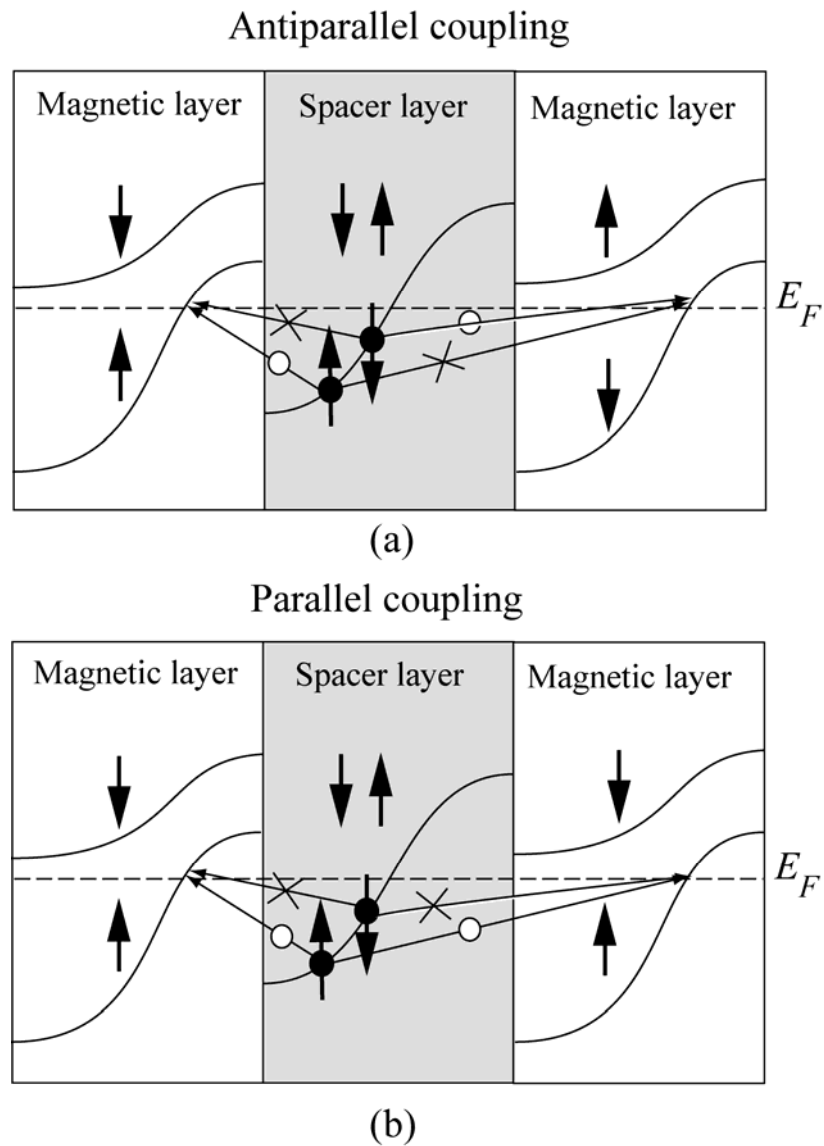


Figure 3.7 A schematic picture of a magnetic multilayer structure. An arrow points the direction of an electron spin, (a) possibilities of reflection and transmission of an electron in antiferromagnetic coupling system, and (b) the possibilities in ferromagnetic coupling system.

In the case of ferromagnetic IMC, the magnetizations of the magnetic layers are aligned parallel to each other. The situation is identical on both sides for up-spin electrons. They may escape into either the left or the right side (see Figure 3.7(b)). On the other hand, the down-spin electrons are trapped inside the spacer layer. This is similar to the quantum well problem in quantum mechanics. The states of the spin-down electrons are, therefore, quantized.

Remarkably, the quantum well model yields exactly the same oscillatory behavior and decays as the RKKY model does (Edwards et al., 1991-2; Mathon et al., 1995-7). In addition, this method also obtains the amplitude.

Quantum well states in a multilayer were observed experimentally by Ortega and Himpsel (1992) and later the concept was extended to study to more systems (Ortega, Himpsel, Mankey, and Willis, 1993). They have investigated multilayer films of Co/Cu/Co, Fe/Ag/Fe, and Fe/Cu/Fe using inverse photoemission and photoemission spectroscopy. They found the long period and the short period that are equivalent to the periods from RKKY theory.

3.3.5 Biquadratic Coupling Model

Slonczeski (1991, 1993, 1995) has introduced two possible sources of the biquadratic exchange coupling. The first one is the fluctuation mechanism of the bilinear exchange coupling (Slonczeski, 1991). According to this interpretation, the biquadratic coupling is an effective coupling due to fluctuation of magnetizations in the layer around their average direction (see Figure 3.8).

The different thickness regions of a multilayer have different coupling strengths. Each region has well-defined average magnetization due to the intralayer exchange coupling. However, the intralayer exchange coupling is not strong enough

to align the magnetizations in the average direction. The fluctuation of the magnetizations in each the region turns out to give an effective interaction between the average magnetization direction. This effective interaction favors perpendicular alignment of the average direction (Slonczewski, 1991).

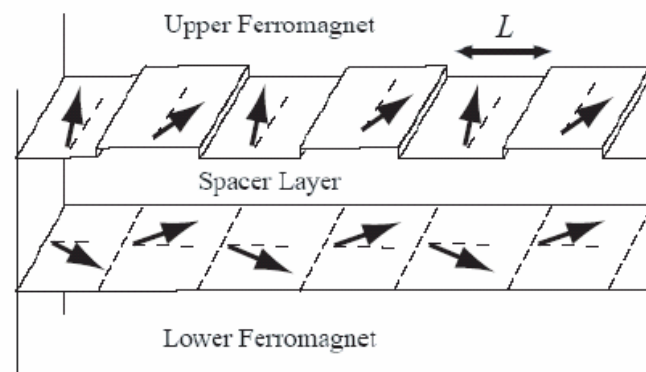


Figure 3.8 Thickness variations in a trilayer, in which the thickness of the spacer layer varies periodically. The broken lines indicate the average magnetization direction. The heavy arrows exhibit the local variation in the magnetization direction [After Stiles, 2002].

The second one is the loose spin model (Slonczewski, 1993). In order to account for the strong temperature dependence in the trilayer composed of Fe layers separated by Au and Al spacers. He proposed that the indirect IMC such as the RKKY coupling is weak owing to the existence of magnetic moments that are only weakly coupled to the magnetic layers. He called this magnetic moment (spin) as the *loose spin*. The loose spins exist within the spacer or neighbor to its interfaces which he called *loose interfacial spins*. The basic idea of the loose spin model is shown in Figure 3.9(a).

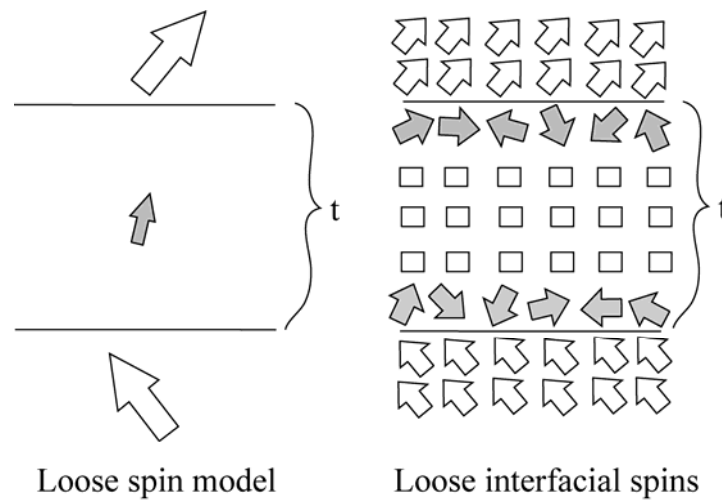


Figure 3.9 Loose spin model of the biquadratic coupling. (a) the small solid arrow represents a loose spin located in the non-magnetic spacer, (b) the loose interfacial spins are located at the two interfaces of the trilayer.

The edges of two ferromagnets have the magnetization at the interfaces. The loose spins are subjected to the exchange coupling that is induced by the two ferromagnets through a non-local spin polarization of an electron gas. He assumed the spacer layer to be composed of the free electron gas. Strength of the exchange coupling is a function of spacer thickness t and temperature (Slonczeski, 1995). Similarly, the loose interfacial spins, they see the potential due to their coupling to the magnetic layers, although they are paramagnetic.

The loose spin model turns out to be consistent with experimental results, both the sign and the temperature dependence in the systems of Fe/Al/Fe trilayer (Gutierrez, Krebs, Filipkowski, and Prinz, 1992) and Fe/Au/Fe (Fuss et al., 1992). However, no confirmation has been reported on sputtered multilayers which are studied in this thesis.

3.4 Survey of Interlayer Magnetic Coupling Studies in Fe-Al-Gd Multilayer

The present work is the first one to investigate IMC experimentally in the system of Fe/Al/Gd/Al multilayer film. It is interesting to compare the experimental results with that on the system of Fe/Gd multilayer film. The interlayer magnetic coupling in Fe/Al and Gd/Al will also be discussed in this section.

3.4.1 Magnetic Coupling in the Fe/Gd Ferrimagnetic Multilayer

Fe/Gd multilayer films are well known to be artificial ferromagnets in which the interlayer exchange coupling between Fe and Gd layers is strong antiferromagnetic. Magnetic phase diagram of the field versus temperature has been predicted theoretically by Camley (Camley, 1987-1993) and coworkers (LePage and Camley, 1990). Hereafter we report to it as Camley's model. They predicted, on the basis of molecular field model, that there are basically four possible states in Fe/Gd multilayer films, namely,

1) *Gd-aligned* state in which all the Gd magnetic moments are aligned with the magnetic field and all Fe magnetic moments are antiparallel to the field.

2) *Fe-aligned* state in which all Fe magnetic moments are aligned with the magnetic field and all Gd ones are antiparallel to the field.

3) *Twist* state in which both Gd and Fe magnetic moments are at varying angles with respect to the external field. The occurrence of this state depends on the distance from the interface.

4) A state in which the behavior of some of Gd magnetic moments is paramagnetic while Fe ones are still in the ferromagnetic order.

This prediction has been accepted by several experiments, e.g., magnetization measurements (Takanashi et al., 1992), neutron diffraction (Dufour et al., 1993), magnetoresistance measurements (Vaezzadeh et al., 1994), Mössbauer spectroscopy (Sajieddine et al., 1994), resonant x-ray magnetic scattering (Ishimatsu et al., 1999; Hosoi et al., 2002), and XMCD (Koizumi et al., 2000; Takagaki et al., 2003). Although the experimental results seem to be consistent with the Camley's model, the occurrence of the interlayer coupling between Fe and Gd layers is not clear since validity of the assumption of the molecular field model and the approximation that anisotropy is negligible are not evident.

3.4.2 Interlayer Magnetic Coupling in Fe/Al and Gd/Al Multilayers

There are only a few groups who study the interlayer coupling in the system of sputtered Fe/Al multilayers and no report has yet been appeared on that in Gd/Al multilayer film. Magnetic properties of Fe/Al multilayer films depend on the thickness of both Fe and Al layers. Moreover, the phenomena are also found to be sensitive to the sputtering conditions (Haeiwa et al., 1991). Nagakubo, Yamamoto, and Naoe (1988) have reported their studies on Fe/Al multilayer films prepared by ion-beam sputtering. They measured the saturation fields and coercive fields of the samples Fe layer thickness of which is fixed to be 100 Å. The Al thickness is varied up to 100 Å. They concluded that the magnetic properties changed significantly with the change of the Al thickness around 15 Å. Wang and coworkers (1990) studies the structure of the Fe/Al multilayers, prepared by planar magnetron sputtering, by means of x-ray diffraction. They reported that the structure of the Fe(R)/Al(22Å) multilayers is amorphous when R is less than 19 Å. They also claimed that this change into the amorphous state together with alloying between Fe and Al atoms at the interfaces, is

the reasons why the saturation magnetizations of their samples are lower than that of bulk Fe. Temperature dependence of magnetization of Fe/Al films is studied by the group of Abdul-Razzaq (Wu et al., 1992; Lee and Abdul-Razzaq, 2000). They reported that the Curie temperature of the Fe($R\text{\AA}$)/Al($R\text{\AA}$) multilayer films decreases with decreasing of thickness R . They also remarked that the alloying at the interfaces affects the magnetization to be reduced. This effect becomes important as layer thickness R becomes small.

CHAPTER IV

EXPERIMENTAL METHODS

4.1 Experimental Techniques

4.1.1 DC+ RF Magnetron Sputtering

The technique for growing multilayer films are grouped into two: the chemical vapour deposition (CVD) and the physical vapour deposition (PVD). The difference arises from the situation whether the gaseous or the solid source is used (du Tremolet de Lacheisserie, Gignoux, and Schenker, 2002). PVD processes are divided into sputtering, evaporation, or ion planting. The sputtering deposition technique is separated into the DC diode sputtering, RF diode sputtering, and magnetron sputtering. These techniques can be combined together. For example, DC diode sputtering and RF diode sputtering are combined with magnetron sputtering. We refer to this as DC+RF magnetron sputtering in this thesis.

A DC sputtering system consists of a pair of planar electrodes e.g. cathode and anode, as shown geometrically in Figure 4.1. A cathode is attached to the material to be sputtered we call the material to be deposited the target. The substrate where deposition occurs is attached to the anode. A static voltage, usually 0.5-5 kV, is applied to the electrodes to create a plasma discharge. Atoms of inert gas used in the sputtering system, mostly argon (Ar) and Krypton (Kr), are partially ionized by primary electrons. The positive ions, Ar^+ , are accelerated toward the target by the

electric field. These highly energetic ions sputter the target resulting in the emission of sputtered atoms. This is ascribed to the momentum exchange between Ar^+ ions and the sputtered atoms. Some of the Ar^+ are reflected and some of them may be implanted in the target which will be sputtered later. Secondary electrons are also emitted from the target in the sputtering process. Since these electrons are accelerated toward the substrate, collision with Ar atoms occurs, and Ar^+ ions are replenished. The secondary electrons together with the Ar^+ ions eventually form sustaining plasma in front of the substrate. The sputtered atoms emitted from the target travel to the substrate suffering collisions with Ar gas along the way and deposited on the substrate. The deposited atoms are denoted as adatoms in the Figure 4.1.

To sustain the sputtering glow discharge, a secondary electron must produce sufficient Ar^+ ions to release one further secondary electron from the target. Therefore, the applied voltage must be high in order that the electrons acquire adequate energy to ionize the Ar gas. Moreover, the pressure in the sputter chamber must not be too low during sputtering and the distance between electrodes must be appropriately long, so that enough for the collision events between electrons and Ar gas sustained. In usual the pressure used in the DC sputtering is in a range of 50 - 100 mtorr. The bombardment of an insulator with the positive Ar^+ ions leads to a charging of the surface and subsequently to shielding of the electric field. If this occurs the sputtering glow discharge can not be sustained. Therefore, the use of the DC diode sputtering is restricted to conducting materials like metal or doped semiconductors. This problem can be solved by applying an RF (radio frequency) AC-voltage to the target.

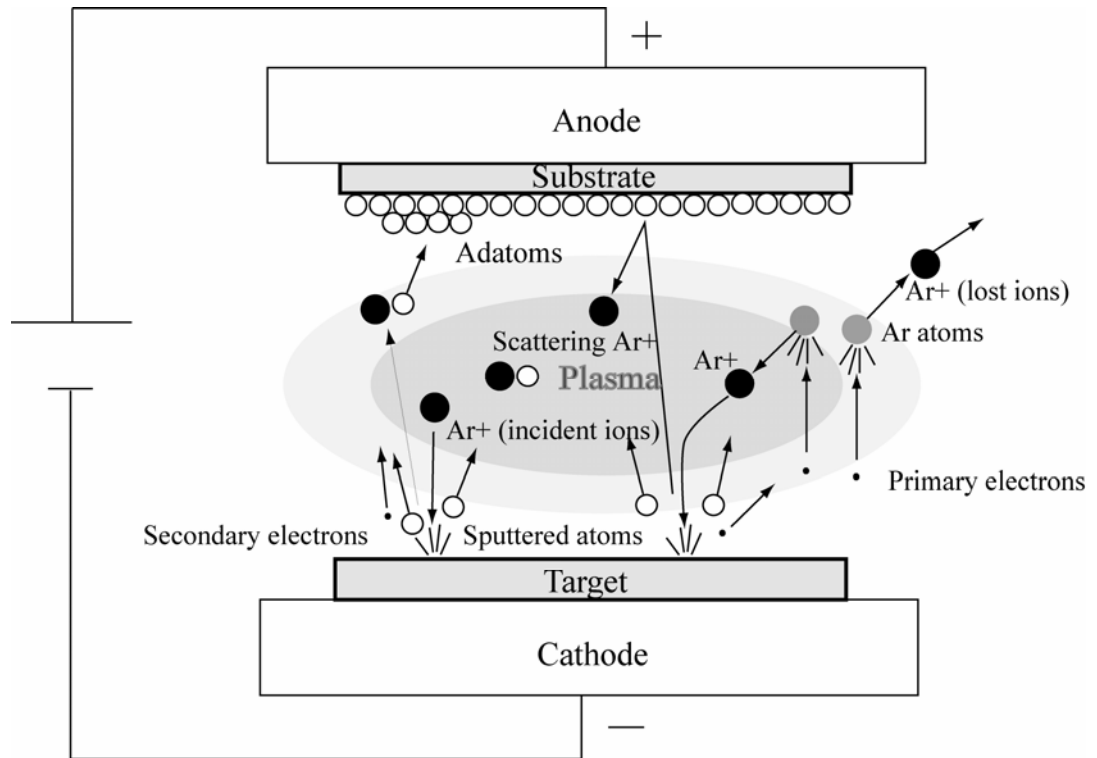


Figure 4.1 A schematic view of DC the diode sputtering. Dots denote electrons, solid circles denote Ar ions, and open circles denote atoms of deposited materials.

In RF sputtering, the RF field is supplied by coupling to the input cathode (target) through a capacitor. The difference in mobility of the Ar^+ ions and electrons gives rise to a negative self bias of the cathode, which in turn gives the necessary potential for sputtering. These plasma-sheath potentials are maintained by the RF power source. In general the RF field accelerated the Ar^+ ions across these plasma sheaths to strike both target and substrate. However, the density of the Ar^+ ions hitting the substrate is made low by selecting an appropriate apparatus design.

In the RF sputtering system, electrons oscillate inside the plasma and the loss of electrons from the plasma is reduced. Subsequently high collision frequency works. The high voltage in used in DC sputtering is, therefore, no longer necessary. Moreover, the working pressure in the RF sputtering chamber (usually 5-15 mtorr) is lower than that for the DC sputtering (usually 50-100 mtorr). Since the electron mean free path is proportional to the reciprocal of the pressure in the chamber, higher pressure can enhance interactions (collisions) in the plasma. These collisions can prevent the traveling of sputtered atoms to the substrate, so that the sputtering rate decreases. The lower working pressure can be new in magnetron sputtering.

In magnetron sputtering, a magnetic field is applied to the target, as shown in Figure 4.3, which represents the simplest case of the planar magnetron sputtering. The target is magnetized by permanent magnets fixed to the reverse side. The magnets provide a toroidal confinement field with the field lines forming a closed tunnel on the target surface as exhibited in Figure 4.2. Since sputtering heats the target, the magnetron incorporates blocks for water cooling during operation. The field strength is so chosen as to provide effective confinement for electrons. However it does not confine heavier ions. The transverse field component is typically > 0.1 kOe.

The secondary electrons that are accelerated from the target to the substrate due to the electric field, are forced into a spiral path owing to the Lorentz force. One component of the motion is a helical path about the magnetic field lines. The electrons traveling along these helical lines toward the center of the target are reflected because of the higher density of field lines in this region and the repulsive electric field encountered. After reflection the electrons eventually reach the perimeter of the target where the field lines again intersect the surface. The electrons are, therefore, trapped by the magnetic field close to the target. Another component of the electrons motions is a drift from one field line to another resulting in a race track orbit about the toroidal tunnel on the target surface. The combined motion let their path length be long in the plasma and increase the possibility of collisions with the Ar gas. This results the enhancement of the sputtering rate. This means the magnetron sputtering can operate at a lower pressure than that in the DC- and the RF- diodes sputtering (usually 0.1-10 mtorr).

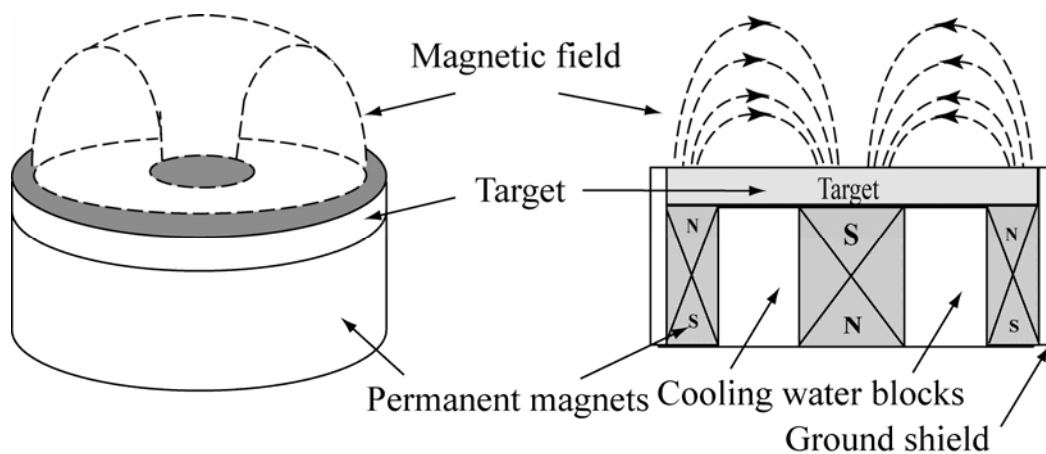


Figure 4.2 A schematic view of the magnetron configuration.

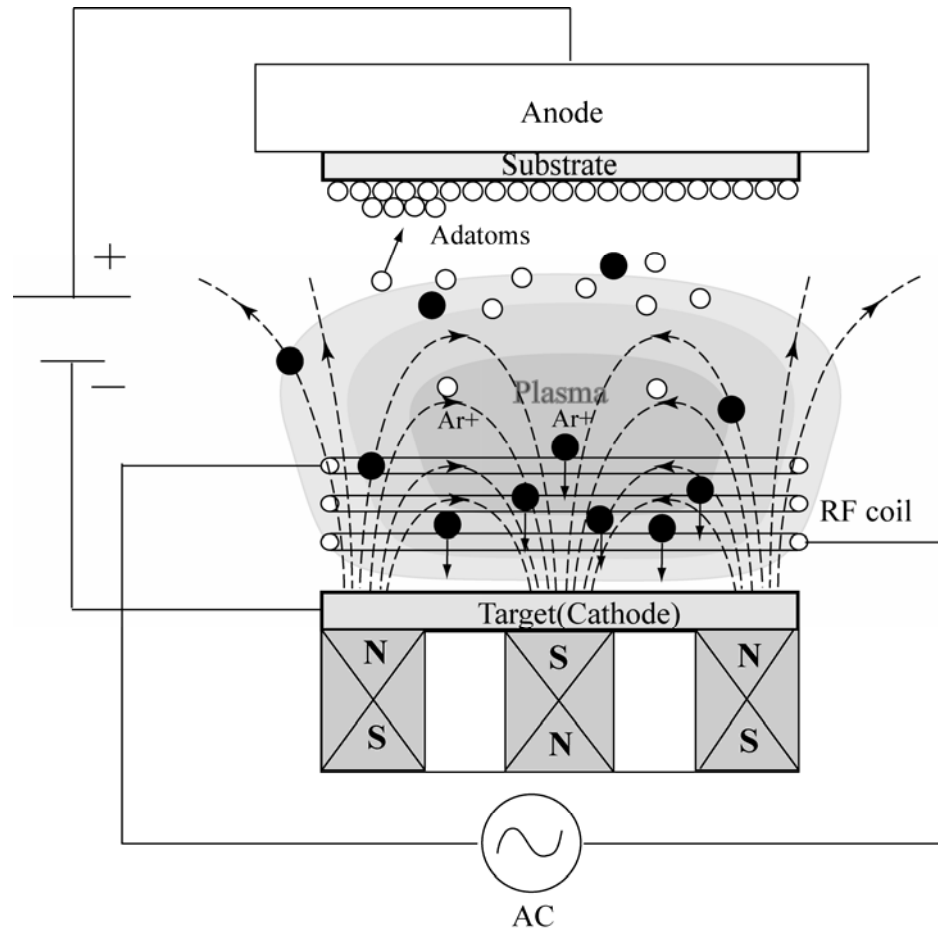


Figure 4.3 A schematic view of the DC+RF magnetron sputtering.

4.1.2 SQUID Magnetometry

SQUID (Superconducting Quantum Interference Device) is the most sensitive device for measuring the magnetic field. SQUID combines two physical phenomena: Flux quantization in a superconducting ring and the *Josephson effect*. There are two types of SQUID. They are dc-SQUID (direct current) involving two Josephson junctions and the rf-SQUID (resonant frequency) which has only one junction. The SQUID-magnetometry model employed in this work is rf-SQUID.

Suppose a current flows in a superconducting ring as shown in Figure 4.4(a) , then a magnetic flux threading in a superconducting ring can only be an integral number times the flux quantum $\Phi_0 = 2.07 \times 10^{-7} \text{ G} \cdot \text{cm}^2$. If an external field is applied, the flux enclosed by the ring is the sum of the external flux and that due to the current in the ring. Because the external flux is not quantized, the current adjusts so that flux quantization is always satisfied.

If two superconductors are separated by an insulator, as shown in Figure 4.4(b), this junction separates two superconducting regions. The waves of cooper-pair electrons in the superconducting regions have a different phase. Josephson showed that the electron-pairs are tunnel across the junction and the electron-pair waves between the two regions are coupled. This phenomenon is called the *Josephson effect* and the junction between the two superconducting regions is called the *Josephson junction*. The critical current, at which a superconductor changes its state to a normal conductor, is significantly reduced at the junction.

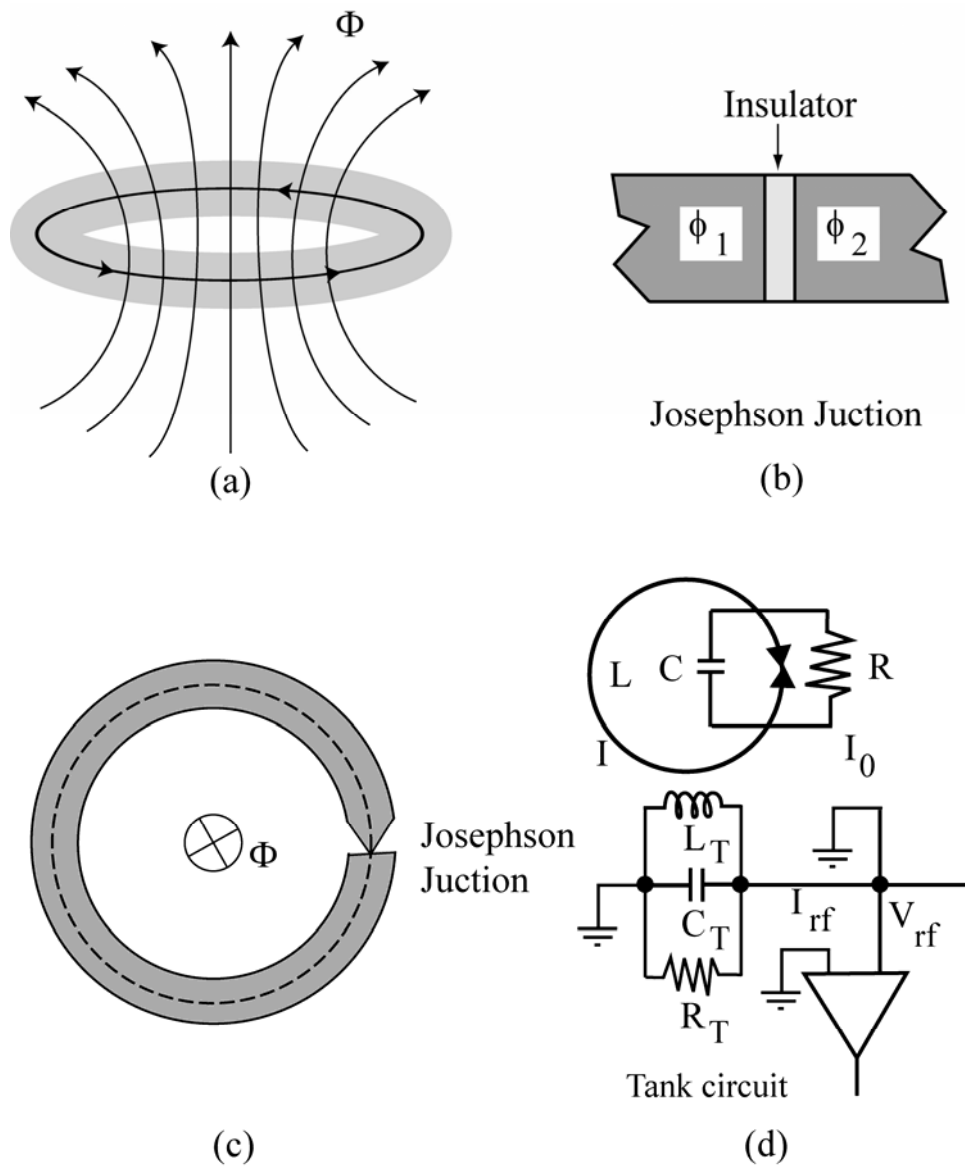


Figure 4.4 Schematic diagrams showing (a) magnetic flux threading a superconducting ring, (b) Josephson junction, (c) rf-SQUID, and (d) rf-SQUID detector.

The rf-SQUID consists of a ring involving a Josephson junction, seen in Figure 4.4 (c). Figure (d) schematically shows a typical rf-SQUID with a tank circuit. Assuming that the SQUID having a magnetic flux Φ_a to be measured. The tank circuit is driven by a current oscillating at or near a resonant frequency. The rf-SQUID inductance L is coupled to the inductor L_T of the tank circuit, which is connected to a preamplifier. The magnetic flux thus includes the resonant-frequency flux Φ_a to be measured. The loss in the tank circuit is represented by the resistance R_T . This loss is periodic function of the flux Φ_a with the period, Φ_0 . This means that the rf-voltage V_{rf} is related to the flux, Φ_a . Therefore, by detecting the magnitude of the rf-voltage the magnetic flux Φ_a can be measured.

4.1.3 Magnetic Compton Profile (MCP)

In the Compton scattering measurements, the total cross section of the scattering, $\left(\frac{d^2\sigma}{d\Omega dE_2}\right)_T$, contains the terms of charge-induced cross section, $\left(\frac{d^2\sigma}{d\Omega dE_2}\right)_0$, and the spin-dependent cross section, $\left(\frac{d^2\sigma}{d\Omega dE_2}\right)_{spin}$, as expressed by (Cooper et al., 2004)

$$\left(\frac{d^2\sigma}{d\Omega dE_2}\right)_T = \left[\left(\frac{d^2\sigma}{d\Omega dE_2}\right)_0 + \left(\frac{d^2\sigma}{d\Omega dE_2}\right)_{spin}\right] J(\hat{n}_{spin}, p_z) \quad (4.1)$$

where $J(\hat{n}_{spin}, p_z)$ is the Compton profile of up-spin or down-spin electrons, and

$$\left(\frac{d^2\sigma}{d\Omega dE_2}\right)_0 = \left(\frac{e^2}{mc^2}\right)^2 m \left(\frac{E_2}{E_1}\right) \Phi_0 \quad (4.2)$$

$$\left(\frac{d^2\sigma}{d\Omega dE_2}\right)_{spin} = \left(\frac{e^2}{mc^2}\right)^2 m \left(\frac{E_2}{E_1}\right) \Phi_{spin} \quad (4.3)$$

Here,

$$\Phi_0 = 1 + \cos^2 \phi + P_L \cos^2 \phi + \frac{E_1 - E_2}{mc^2} (1 - \cos \phi) \quad (4.4)$$

$$\Phi_{spin} = -(1 - \cos \phi) P_C \frac{\hbar}{mc} [\hat{n}_{spin} \cdot (\mathbf{k}_1 \cos \phi + \mathbf{k}_2)] \quad (4.5)$$

The spin-dependent Compton scattering cross section is proportional to the scalar product of between the electron spin direction (\hat{n}_{spin}) and the wave vectors of incident and scattered X-rays (\mathbf{k}_1 and \mathbf{k}_2 , respectively, $q = |\mathbf{k}_1 - \mathbf{k}_2|$), as expressed by (Sakai, 1996), here ϕ is the scattering angle ($\mathbf{k}_1 \angle \mathbf{k}_2$) and the Stoke parameters P_C and P_L represents the degree of circular and linear polarizations, respectively. Then, the subtraction of up-spin and down-spin Compton profiles can be represented by subtracting a Compton profile of a sample that is magnetized in one direction from the Compton profile of the same sample that is magnetized in the opposite direction. The result gives the magnetic Compton profile (J_{mag}), which is defined as a double integral of the momentum-spin density ($n_{spin}(\mathbf{p})$) (Sakai, 1997),

$$J_{mag}(p_z) = \iint n_{spin}(p) dp_x dp_y \quad (4.6)$$

$$n_{spin}(p_x, p_y, p_z) = n^\uparrow(p_x, p_y, p_z) - n^\downarrow(p_x, p_y, p_z) \quad (4.7)$$

here $n_{spin}(p_x, p_y, p_z)$ is the momentum density of the up-spin ($n^\uparrow(p_x, p_y, p_z)$) or down-spin ($n^\downarrow(p_x, p_y, p_z)$) electron state. The integration is performed on all occupied electron states. The z axis is taken to be parallel to the scattering vector of X-rays. A theoretical momentum density of electrons in crystal is expressed as,

$$n^{\uparrow\downarrow}(\mathbf{p}) = \sum_n \sum_G \int \delta_{p, \hbar(\mathbf{k}+G)} (2\pi)^{-3/2} \left| \int \psi_{n,\mathbf{k}}^{\uparrow\downarrow}(\mathbf{r}) \exp\left(\frac{i\mathbf{p} \cdot \mathbf{r}}{\hbar}\right) d\mathbf{r} \right|^2 d\mathbf{k} \quad (4.8)$$

Here $\psi_{n,\mathbf{k}}^{\uparrow,\downarrow}$ is a real-space electron wavefunction of the wave vector \mathbf{k} and n is the band index. \mathbf{G} is the reciprocal lattice vector. It should be noted that the intensity of MCP depends only on the spin and does not on the orbital angular momenta. Since the orbital magnetic moments of Fe and Gd MLFs are negligible, we can directly evaluate the ratio between the magnetizations of Fe and Gd layers by a line-shape fitting of MCPs mentioned below.

After a measurement of the momentum distribution spectra $n^{\uparrow}(\mathbf{p})$ for J_{mag}^{\uparrow} and $n^{\downarrow}(\mathbf{p})$ for J_{mag}^{\downarrow} , it is necessary to normalize each profile to the number of incident photons so that the spin-independent scattering intensity is completely cancelled out by the subtraction as (4.7). A simultaneous measurement of the elastic scattering peak intensity in $n^{\uparrow}(\mathbf{p})$ and $n^{\downarrow}(\mathbf{p})$ is adequate for this purpose because its spin dependence is negligibly small. Under the experimental conditions of large scattering vectors, as is the case of Compton scattering experiments, the spin-dependent scattering form factors are very small in comparison with the scattering factor of the core electrons since the spin dependence is induced by unfilled outer atomic orbitals such as 3d or 4f. In addition, the elastic scattering intensity is proportional to the number of incident photons and influenced by the same P_L -dependence as the charge-induced Compton-scattering cross-section. When a sample consists of light elements and the incident X-ray energy is high, the intensity of the elastic peak is insufficient for the normalization. In such a case, one must measure the incident flux intensity of X-rays by using an ionization chamber or some other instruments.

After $n^\perp(\mathbf{p})$ has been subtracted from $n^\uparrow(\mathbf{p})$, the same procedure is applied to the ordinary Compton profiles. The results can also be used to convert the resultant spectrum to the MCP. The momentum is determined by the relation,

$$p_z = mc \frac{E_2 - E_0 + E_1 E_2 (1 - \cos \theta) / mc^2}{\sqrt{E_1^2 + E_2^2 - 2E_1 E_2 \cos \theta}} \quad (4.9)$$

The total momentum resolution is determined by the relation,

$$\Delta p_z = \sqrt{\left(\frac{\partial p_z}{\partial E_1} \Delta E_1\right)^2 + \left(\frac{\partial p_z}{\partial E_2} \Delta E_2\right)^2 + \left(\frac{\partial p_z}{\partial \theta} \Delta \theta\right)^2} \quad (4.10)$$

In the arrangements of the beamline BL08W station A, where MCP's were measured for the present thesis, the parameters to be put in (4.10) are as follows: $\Delta E_1 = 0.2$ keV, $\Delta E_2 = 0.5$ keV, $\theta = 178^\circ$, and $\Delta \theta = 5.6$ mrad. A ^{133}Ba radioisotope was used to determine the SSD energy resolution, E_1 (Kakutani et al., 2003). The incident X-ray energy is $E_1 = 175$ keV. The scattering energy at the Compton peak can be calculated from

$$E_C = \frac{E_1}{1 + \frac{E_1}{mc^2}(1 - \cos \theta)} = 104 \text{ keV}. \quad (4.11)$$

Here $E_2 = E_C$ and $p_z = 0$ a.u.. The other terms are calculated by the formulas

$$\left(\frac{\partial p_z}{\partial E_1}\right)_{p_z=0} = \frac{137.036}{E_1 \sqrt{1 + (E_1 / E_C)^2 - 2(E_1 / E_C) \cos \theta}} = 0.29 \text{ a.u./keV} \quad (4.12)$$

$$\left(\frac{\partial p_z}{\partial E_2}\right)_{p_z=0} = \frac{137.036}{E_C \sqrt{1 + (E_C / E_1)^2 - 2(E_C / E_1) \cos \theta}} = 0.82 \text{ a.u./keV} \quad (4.13)$$

$$\frac{\partial p_z}{\partial \theta} = \left(\frac{\partial p_z}{\partial E_2} \frac{\partial E_2}{\partial \theta}\right)_{p_z=0} = \frac{\partial p_z}{\partial E_2} \frac{E_C^2}{mc^2} \sin \theta = 2.32 \text{ a.u./rad} \quad (4.14)$$

Using these parameters the total momentum resolution for the MCP measurements in these thesis is 0.42 a.u..

The total spin-dependent Compton scattering intensity is related to the magnitude spin magnetization of a sample and is insensitive to the orbital momentum magnetization. This means the following: When a sample, commonly a ferromagnet, is magnetized by an external field along the z -direction, the area of its MCP is proportional to S_z , the projection of the total spin on the z -direction. The constituents of spin-magnetic moments have momentum contributions from free electrons, relatively localized $3d$ or $4f$ electrons. They are evaluated by the line-shape analysis. For rare-earth elements, the Compton profiles of $4f$ electrons are broader than those of $3d$ electrons. The $4f$ electrons are represented satisfactorily by free-atom wave functions except in the case of light rare-earth atoms. Compton profiles of $3d$ electrons, on the other hand, cannot be approximated by corresponding atomic Compton profiles, because they usually hybridize strongly with itinerant s , p or $5d$ electrons.

However, it is empirically recognized that apart from the fine structure due to crystalline potentials, all $3d$ elements have almost the same Compton profile in the momentum region above 2 a.u., and that these profiles can be reasonably approximated by a flat or slightly round distribution above 2 a.u. For diffuse electrons such as free electrons, a Gaussian-shaped distribution with an adequate line width is usually adopted.

4.1.4 X-ray Magnetic Circular Dichroism (XMCD)

When circularly polarized X-rays penetrate a magnetized sample, the X-ray flux through the sample changes its intensity depending on the direction of the

magnetization of the sample as shown in the diagram in Figure 4.5. The difference of absorptions, $\Delta\mu$, is induced by the conservation of angular momentum in the dipole absorption process as mentioned in Chapter I. The values of $\Delta\mu$ are measured directly from the XMCD experiments in this thesis.

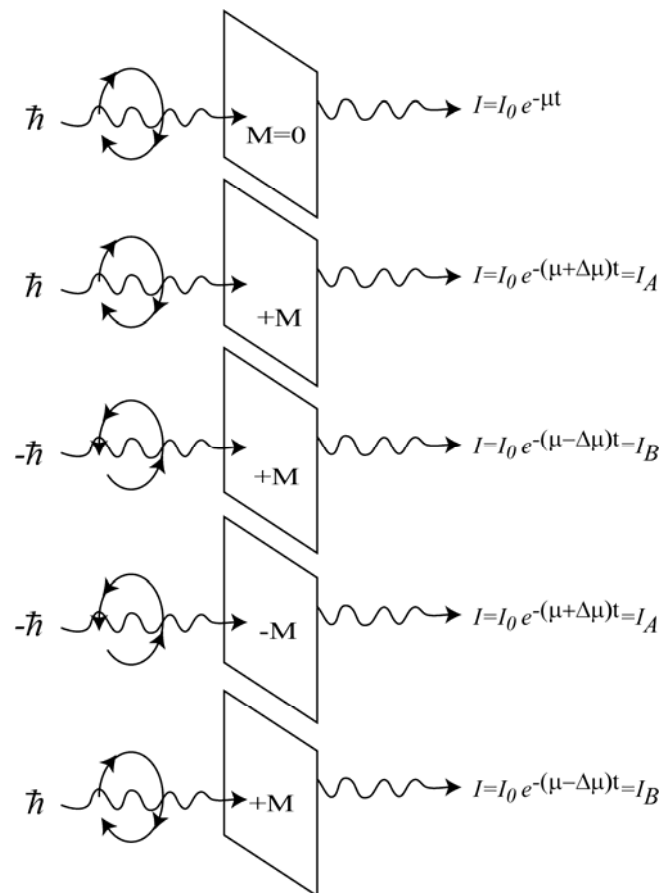


Figure 4.5 XMCD diagram

4.2 Experimental Apparatus

4.2.1 Sputtering Chamber

The DC+RF magnetron sputtering facility employed in this thesis work is the product of ULVAC Inc shown in Figure 4.6. The sample chamber is connected with the sample rotator system. A turbo molecular pump is used for evacuation. A separately designed magnetron source is installed. The targets mounted on the magnetron sources are Fe, Gd, and Al. The purities are 99.999% for Al and 99.9% for Fe and Gd. The substrate is mounted on the substrate holder which is positioned symmetrically among the magnetron sources as shown in Figure 4.7. The substrate and each target source are covered by a shutter to start and stop sputtering rapidly. The shutters are controlled by a computer. The program was developed by Dr. Masafumi Takagaki.

4.2.2 Superconducting Quantum Interference Device (SQUID)

A SQUID system used in this research was from Quantum Design MPMS (Magnetic Properties Measurement System). The MPMS model is currently used in research laboratories worldwide. The components are shown schematically in Figure 4.8 and photographically in Figure 4.9

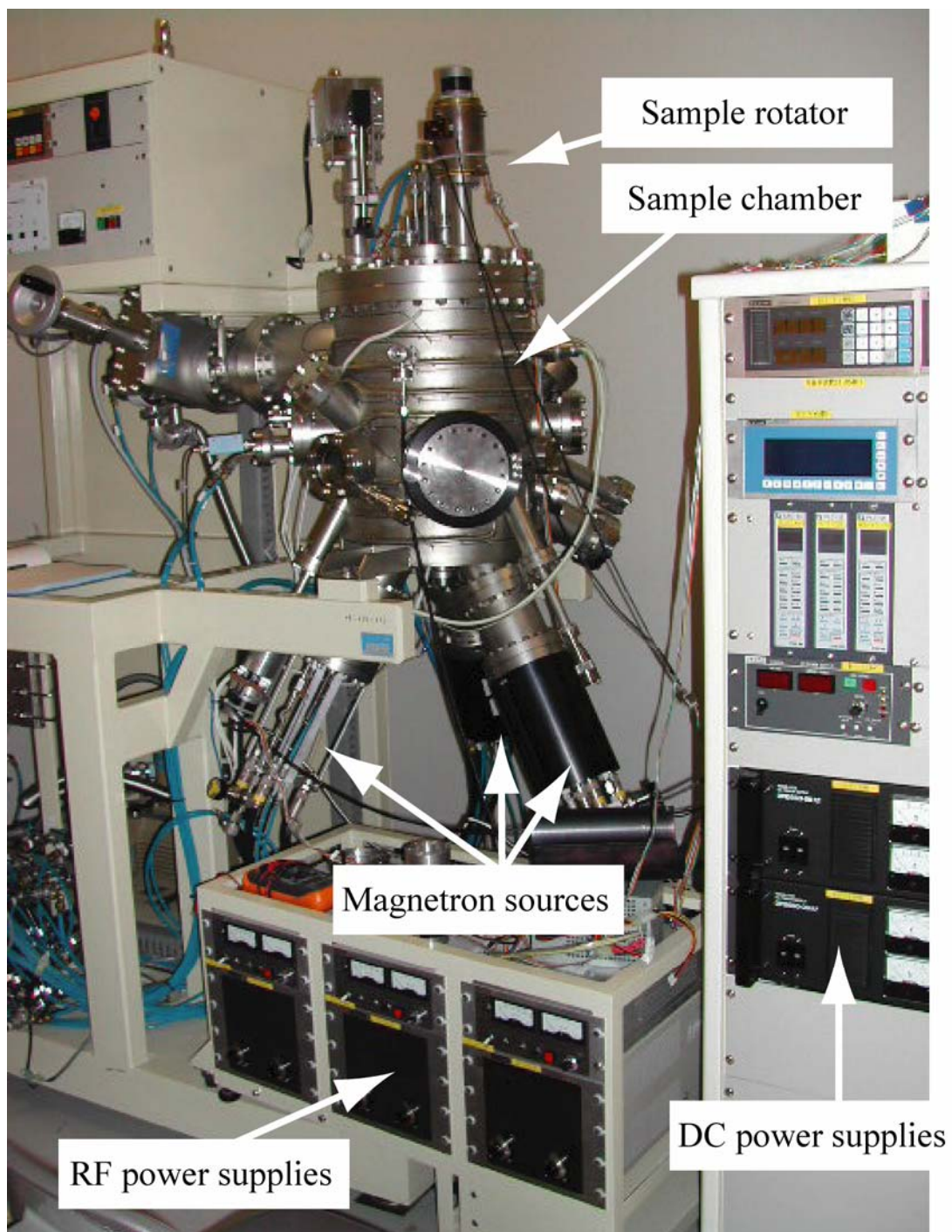


Figure 4.6 The DC+RF magnetron sputtering system.

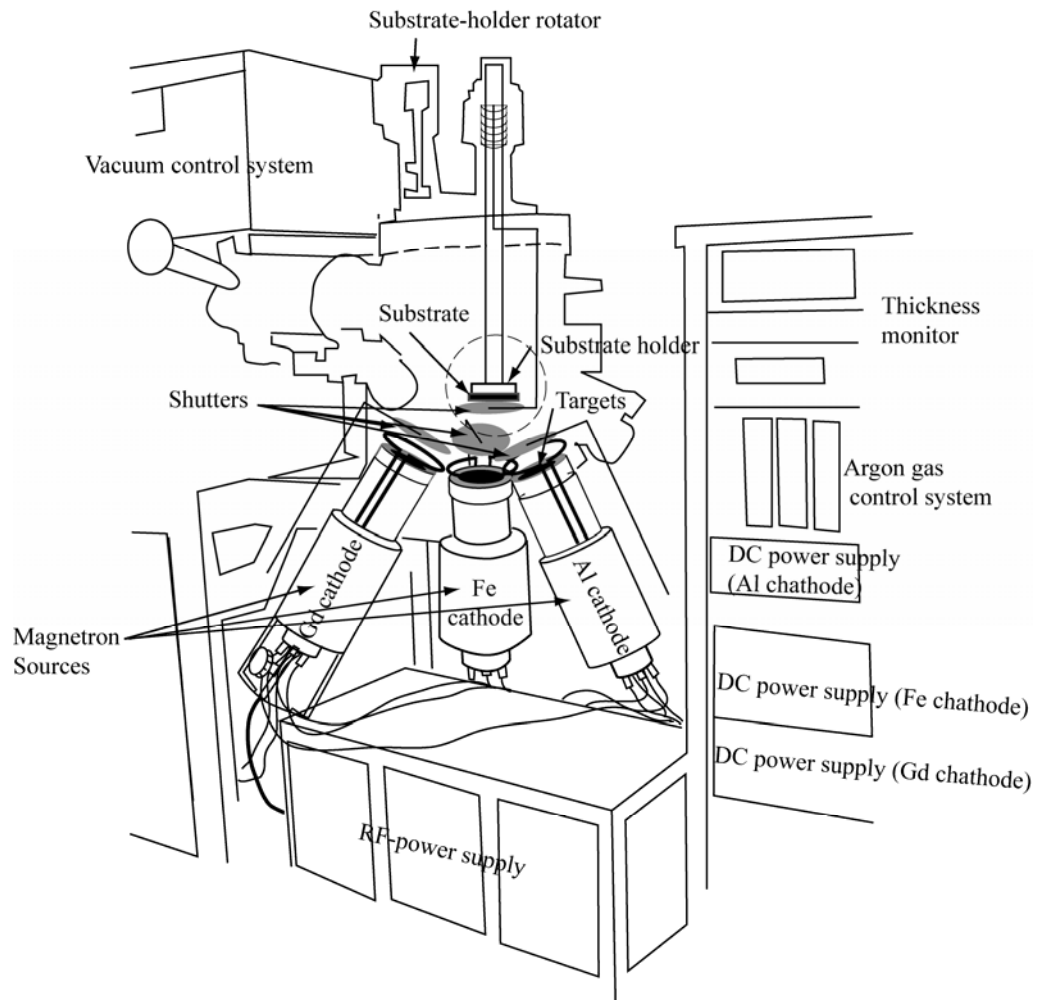
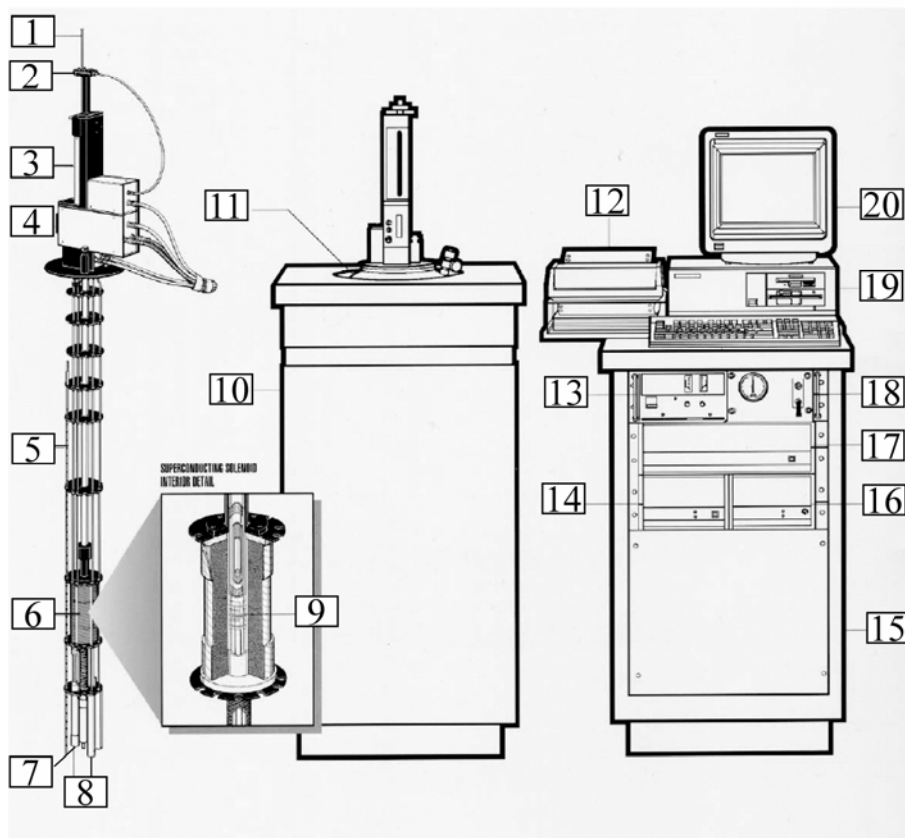


Figure 4.7 A schematic drawing of the DC+RF magnetron sputtering system.

MPMS system components



- | | |
|---------------------------------------|---------------------------------------|
| 1. Sample rod | 11. Dewar |
| 2. Sample rotator | 12. HP printer |
| 3. Sample transport | 13. Magnet power supply |
| 4. Probe assembly | 14. Model 1802 temperature controller |
| 5. Helium level sensor | 15. Console cabinet |
| 6. Superconducting solenoid | 16. Power distribution unit |
| 7. Flow impedance | 17. Model 1882 MPMS controller |
| 8. SQUID capsule with magnetic Shield | 18. Gas/Magnet control unit |
| 9. Superconducting pick-up coil | 19. HP vectra computer |
| 10. Dewar isolation cabinet | 20. monitor |

Figure 4.8 A schematic diagram of the MPMS system.



Figure 4.9 MPMS magnetometer model in the Quantum Magnetism Lab.

The principal components comprise the temperature control system, the magnetic control system, the sample handling system, the superconducting SQUID and amplifier circuit, and the computer control system. The temperature control system is basically a liquid helium (^4He) cryostat with superconducting magnet. The sample temperature, in a range 1.7 – 400 K, can be controlled by a ^4He gas flow control system. The superconducting magnet can produce an external field for the sample up to ± 50 kOe. A sample can be moved stepwise and rotated smoothly through the detection coils without transmitting undue mechanical vibration to the RF-SQUID. The RF-SQUID locates approximately 11 cm below the detection coils. All operating features are under computer control.

Magnetization curves can be measured by moving a sample through the superconducting coils, which are located at the center of the superconducting magnet (see Figure 4.10). As the sample moves through the coils, the magnetic moment of the sample induces an electric current in the detection coils. Because the detection coils, the connecting wires, and the SQUID input coil form a closed superconducting loop, any change of magnetic flux in the detection coils produces a change in the persistent current in the detection circuit (tank circuit). The current variation is proportional to the change in the magnetic flux. Since the SQUID functions as a highly linear current-to-voltage convertor, the variations in the current in the detection coils produce corresponding variations in the SQUID output voltage which are proportional to the magnetic moment of the sample. In a fully calibrated system, measurements of the voltage variations from the SQUID detector as a sample is moving through the detection coils provide a highly accurate magnitude of the

magnetic moment. The system can be accurately calibrated using a small piece of the material having a known mass and magnetic susceptibility.

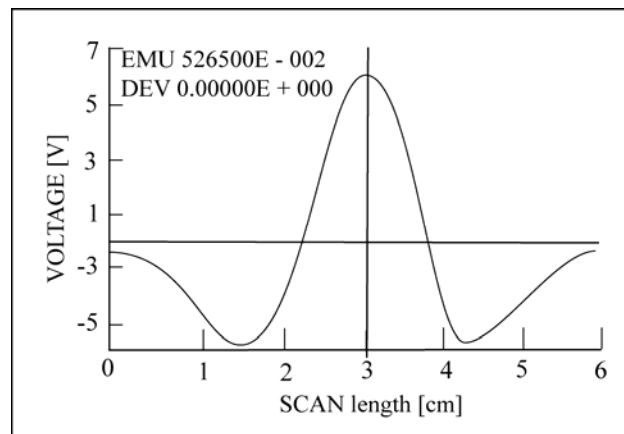
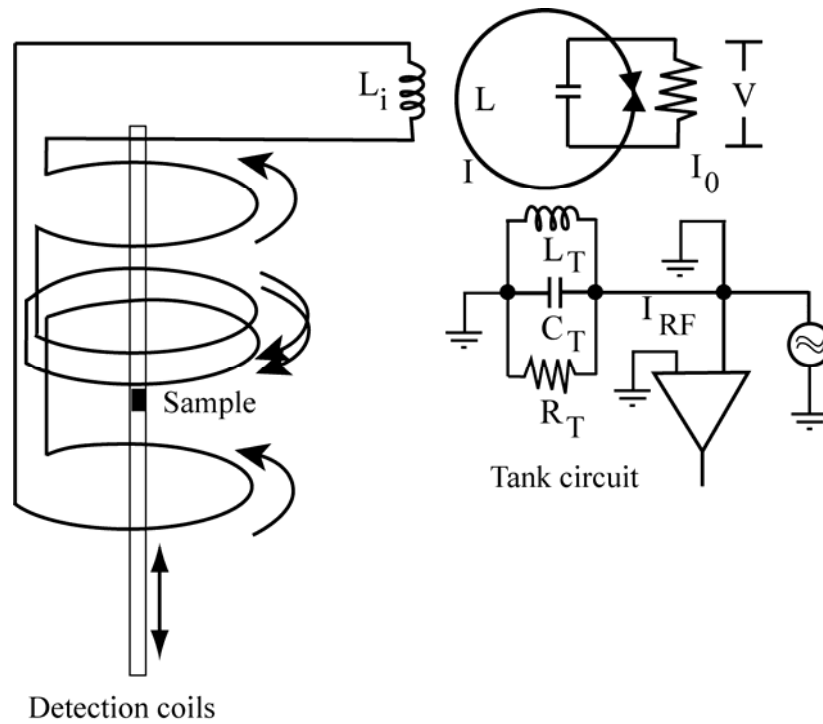


Figure 4.10 Schematic diagram of the detection coils and the rf-SQUID. Upper panel: The tank circuit (detection coils). Lower panel: the output voltage curve (respond curve).

4.2.3 Beamline BL08W at SPring-8

The magnetic Compton profiles (MCP) measurements were carried out at the beam line BL08W of SPring-8. The radiation source of this beamline is the *elliptical multipole wiggler* (EMPW). This beamline is designed for Compton scattering spectroscopy with linearly or elliptically polarized X-rays in the energy ranges of 100 ~ 120 keV and 170 ~ 300 keV. The experimental stations consist of station A for Compton scattering measurements and station B for high momentum-resolution experiments, respectively. Magnetic Compton spectrometer is located in station A.

The beamline BL08W (station A) is shown schematically in Figure 4.11. It contains two monochromators and other optical components, e.g. beam shutters, slits, fluorescence screens. White X-rays emitted from the EMPW are brought into the optics hutch after passing through some filters which protect the monochromators from heat loads, and then monochromatized with either of the two monochromators (Yamaoka et al., 1998, 2000). One of them horizontally reflects X-rays of 270 keV – 300 keV into station A, and the other vertically reflects 90 keV – 120 keV into station B. The former is equipped with a single bent Si 771 crystal. The crystal is asymmetrically cut for getting an optimum focal spot on a sample and an optimum resolution.

In station A, equipment is composed of a superconducting magnet, a 10-Kelvin refrigerator for cooling a sample, and a 10-segmented Ge solid-state detector (SSD) shown in Figure 4.12. A magnetic field up to ± 30 kOe can be generated with a current of ± 79 A. The sign of the magnetic field can be altered within 5 seconds from + 30 kOe to -30 kOe vice versa.

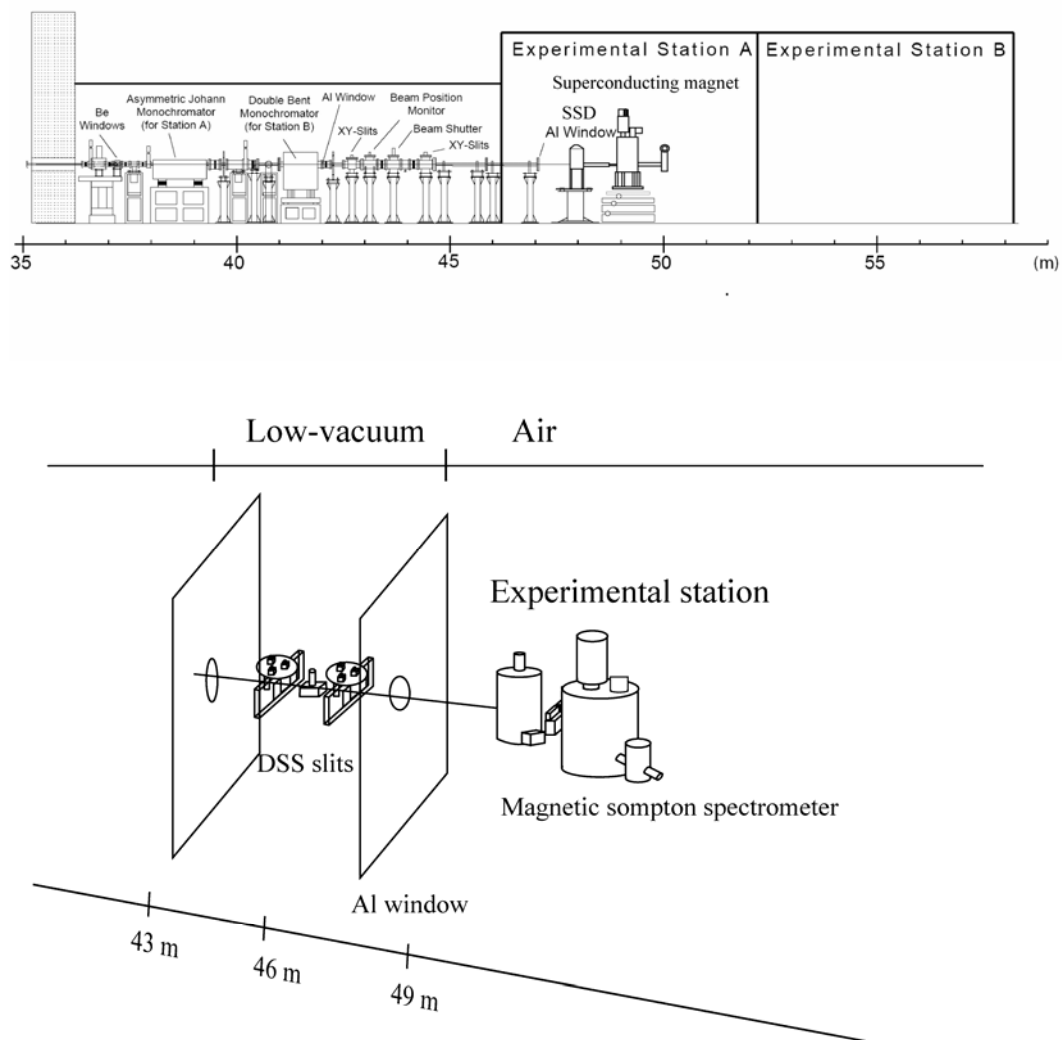


Figure 4.11 A schematic diagram of the BL08W beamline.

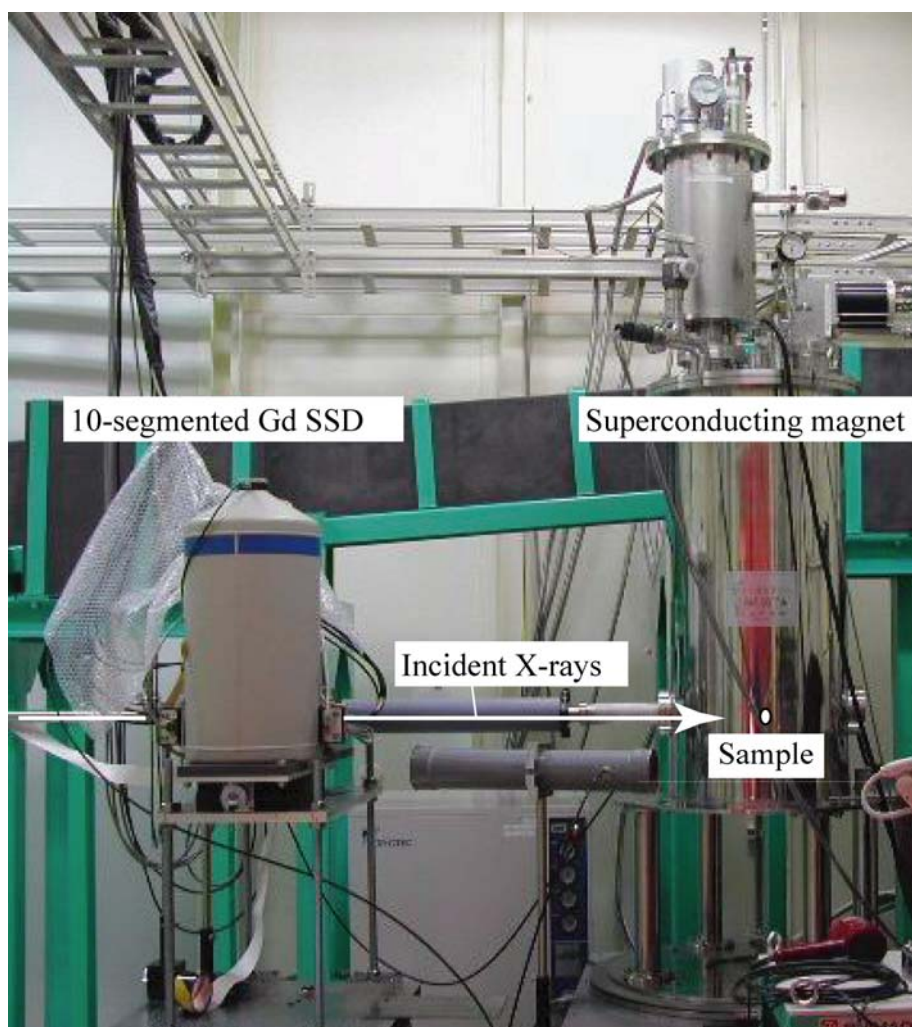


Figure 4.12 Experimental equipments in the station A of the beamline BL08W

The magnets are designed to be equipped with two different liquid He condensers (one has 3 W cooling power at 4.2 K for He gas recondensation and the other 12 W at 20 K for radiation shielding). The sample is cooled by another refrigerator (4.7 W at 20 K) at any temperature between room temperature and 10 K. The Ge solid-state detector system consists of 10-segmented Ge sensors, 10 preamplifiers, 10 amplifiers, 10 ADCs, 10 MCAs and one computer. The effective area of a Ge crystal is 100 mm². For the MCP measurement, a scattering angle is desirable to be as close to 180° as possible. The Gd crystals are therefore circularly arranged around the hole (11 mm in diameter) through which the incident x-rays are introduced to the sample. The diameter of the circle of the sensors is 42 mm. The distance between the detector and the sample is 1 m. A trigger signal to reverse the magnetic field direction is given from the computer synchronized with the change of the memory address of the data from the MCA's.

4.2.4 Beamline BL39XU at SPring8

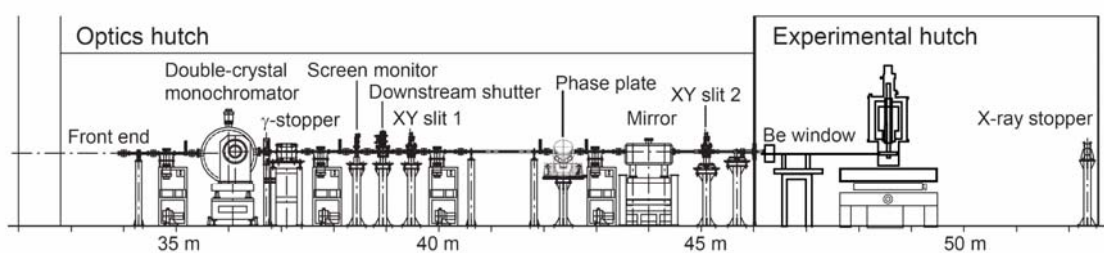
The BL39XU is an undulator beamline which is equipped with an in-vacuum type undulator and a rotated-inclined double-crystal monochromator. The combination of fundamental / third harmonics of undulator radiation with the Si 111 reflection of the monochromator covers an energy range from 5 to 37 keV. The photon flux onto a sample is maximized at every X-ray energy by synchronous tuning between the undulator gap and the monochromator angle.

A platinum-coated mirror of horizontal deflection is used to reduce the amount of higher harmonics to less than a factor of 10⁻⁴. The cutoff energy is adjustable from 8 to 20 keV with an appropriate glancing angle between 2 and 9 mrad. The mirror is mechanically bendable for providing a horizontally focused beam. A

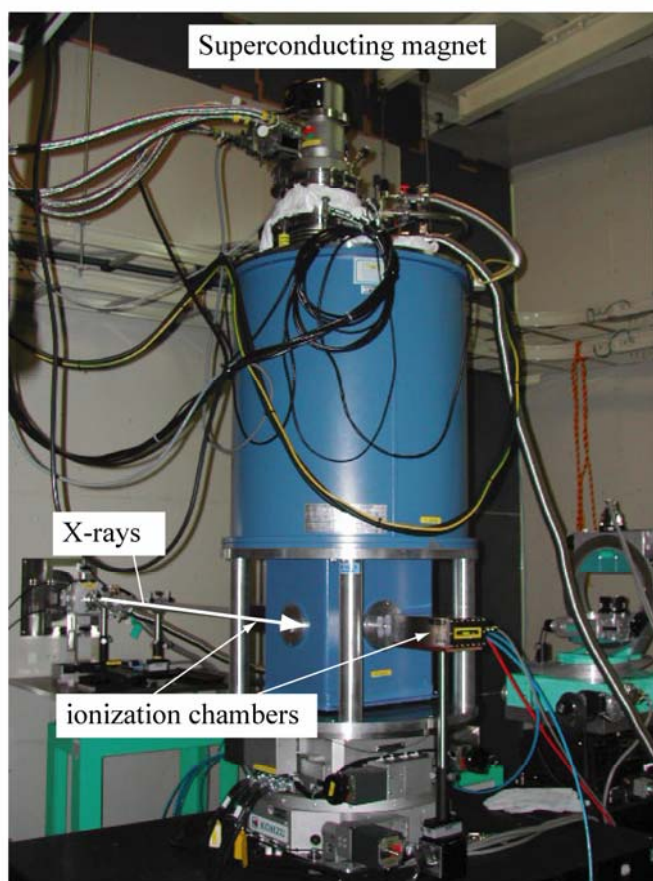
diamond X-ray phase retarder (XPR) is installed between the monochromator and the mirror. It functions as a quarterwaveplate with high efficiency. Crystals of various thicknesses (0.34, 0.45, 0.73, and 2.7 mm) are available.

The superconducting magnet (SCM) is designed for XMCD experiments under a magnetic field up to 100 kOe. The assembly of a variable temperature insert (VTI) allows measurements between 1.7 and 300 K. The split-type superconducting coils are equipped to generate a field in the horizontal direction. The diameter of the magnet clear bore is 54 mm. A sample is placed inside a 25 mm-diameter cylinder in the VTI. The SCM has X-ray transparent Be windows at both front and back (on the field axis) and on both sides (perpendicular to the field). The opening size of the front and rear windows is 10 mm in diameter, while the side windows are 20 mm in diameter. This design of the coils and the windows allows XMCD measurements either in transmission mode or in fluorescence mode as well as non-resonant magnetic diffraction experiments with a 90° degree scattering angle. The SCM is equipped with a liquid helium recondensing cooler which enables continuous operation of the SCM for more than 7 days with no additional coolant.

When the present work was carried out SCM was available for XMCD experiments but not for diffraction measurements because of a vibration problem. Sample vibrations are found to have amplitude of approximately ± 30 μm . This vibration is caused by the vibration of the recondensing cooler. Vibration of this magnitude results in a small degradation in the quality of XMCD measurements; the effect is negligible in most cases. However, this vibration will seriously influence data taken during diffraction measurements with a single crystalline sample.



(a)



(b)

Figure 4.13 (a) The lay-out of Beamline BX39U and (b) the superconducting magnet system

The optical system used for the XMCD measurements is shown in Figure 4.13. Undulator light linearly polarized in the orbital plane was monochromated by a Si(111) fixed-exit double-crystal monochromator. The phase retarder was a diamond (111) plate 0.5 mm thick and was in the Laue geometry with the $(2\bar{2}0)$ symmetric reflection plane tilted by 45° with respect to the polarization plane of the incoming beam. The piezo-driven oscillation stage was mounted on an $\omega - 2\theta$ rotation stage, which was used to adjust the Bragg condition of the retarder crystal. Fast switching of photon helicity was realized by flipping the phase retarder around the Bragg angle using the oscillation stage. The X-rays linearly polarized in the orbital plane were alternately converted to right circularly (RC) and left circularly (LC) at 40 Hz with a 50% duty ratio. The oscillation amplitude of the phase retarder was kept at 130 arcsecond while scanning the incident photon energy. During this operation the center of oscillation was adjusted by the rotation stage to satisfy the Bragg condition for the incident energy. The degree of circular polarization was estimated to be more than 90% from the polarization measurements previously performed with the phase retarder in a static operation.

4.3 Experimental Procedures

Fe/Al/Gd/Al magnetic multilayer films (MLFs) with different Al thickness were prepared by means of DC + RF magnetron sputtering. The IMC has been examined by measuring magnetic hysteresis and the temperature dependence of magnetization curves of the MLF's using SQUID. Under some specific conditions, applied field and temperature, magnetic Compton profiles (MCPs) of some of the MLFs were measured at beamline BL08W (station A) of SPring-8. The line-shape

analysis of experimental MCP's using MCPs of Fe/Al and Gd/Al MLFs is useful to evaluate the amounts of Fe-spin and Gd-spin in Fe/Al/Gd/Al MLFs. The orientation of Gd-spins in Gd layers in the MLF's were examined by means of X-ray magnetic circular dichroism (XMCD) at the Gd-L₃ edge.

4.3.1 Sample Preparation

Before describing the sample details, I would like to address here about the basic information about the materials which will be used in calculation of magnetization value. Table 4.1 shows the basic parameters of Fe, Gd, and Al.

Table 4.1 Basic parameters of the materials, Fe, Gd, and Al [Kittel, Ed. 7th].

Parameters	Fe	Gd	Al
1. Electron configuration	$[Ar]3d^64s^2$	$[Xe]4f^75d6s^2$	$[Ne]3s^23p$
2. Atomic number	26	64	13
Atomic mass	55.85	157.25	26.98
3. Bulk crystal's structure	bcc	hcp	fcc
Lattice constant, in Å	2.87	3.63, 5.78	4.05
4. Density in g cm ⁻³	7.87	7.89	2.70
Concentration in 10 ²² cm ⁻³	8.50	3.02	6.02
5. Curie temperature, in K	1043	292	-
6. Saturation magnetization M_s			
at Room temperature	1707	-	-
at 0 K	1740	2060	-
7. Effective magneton number			
At 0 K, per formula unit (μ_B)	2.22	7.63	-

The samples studied in this thesis were prepared by the DC+RF magnetron sputtering. The targets sources of Fe, Gd, and Al were employed. The purities of the targets were 99.999% for Al and 99.9% for Fe and Gd. Each of the sources and the substrate holder were equipped with individual computer-controlled mechanical shutters, which were actuated in accord with a deposition procedure. Depositing is suddenly started or stopped by switching the shutters (covering the target and the substrate) to open and close, respectively. These shutters are working under a computer controlled with the thickness detection system. The user interface at the PC console provides the option of working under the sequence which is programmed by user.

The samples were deposited under a pressure $\sim 5 \times 10^{-4}$ torr which was previously pumped down to the background pressure $\sim 2 \times 10^{-7}$ torr. High purity argon gas was employed at a pressure of ~ 360 torr (0.05 MPa). Rotating technique of the substrate was performed for homogenous deposition. The thickness of each layer was individually monitored as a shift of the oscillation frequency of a quartz single crystal. The discharge parameters and others sputtering conditions are listed in Table 4.2.

All of the samples are listed in Table 4.3. The magnetic multilayer films (MLFs) of Al/Fe/Al/Gd were deposited on either polyimide film substrate (POL) or polyethylene film substrate (PET). Polyimide film (Kapton® film in commercial name) was chosen to be the substrate because of its non-magnetic property and convenience of preparing the sample for SQUID. The thickness of Fe and Gd was fixed to be 20 and 40 Å, respectively, while the thickness of the Al spacer (R) was varied from 0 to 100 Å. Fe/Al MLF of $R = 200$ Å was made for comparison

with those of Fe/Al/Gd/Al MLFs. On the other hand, in order to reduce the Compton-scattering intensity from a substrate, the samples of $R = 5$ and 20 \AA MLFs for MCP measurements were prepared on $4\text{-}\mu\text{m}$ -thick PET-foils instead of $25\text{-}\mu\text{m}$ -thick polyimide films used for the magnetization measurements. In addition, Fe/Al and Gd/Al MLFs of $R = 5 \text{ \AA}$ were prepared.

Table 4.2 Sputtering conditions used in preparation of all the samples in this thesis.

Discharge Parameters	
Operating pressure	$\sim 5 \times 10^{-4}$ torr
Direct current (Dc)	
Discharge current (Fe, Gd, Al)	0.15 Amp
Discharge voltage (Fe, Gd, Al)	440 V, 220 V, 280 V
Deposition rates	
Fe	1
Gd	2
Al	0.5
Magnetic field	
Sputtering conditions	
Background pressure	$\sim 2 \times 10^{-7}$ torr
Substrate temperature	Room temperature
Cooling water rate	2 liters/min
Bombarding gas	Ar
Gaseous rate	
Fe – cathode	6.5 ccm
Gd – cathode	6.5 ccm
Al – cathode	10.0 ccm

Table 4.3 Series of the samples deposited either on a polyimide film (POL) and a polyethylene film (PET).

Magnetic multilayer films	Al thickness (RÅ)
1. POL/[Al(RÅ)/Gd(40Å)/Al(RÅ)/Fe(20Å)]×20/Al(RÅ)	0, 5, 7, 10, 20, 30, 100
2. POL/Al(20Å)/[Fe(20Å)/Al(RÅ)]×20/Al(20Å)	200
3. PET/[Al(RÅ)/Gd(40Å)/Al(RÅ)/Fe(20Å)]×100/Al(RÅ)	5, 10, 20
4. PET/[Al(RÅ)/Gd(40Å)]×100/Al(20Å)	5
5. PET/[Al(RÅ)/Fe(40Å)]×100/Al(5Å)	5

4.3.2 Magnetometry

Preparation of the SQUID sample is illustrated in Figure 4.14. MLF has a shape of circle (shaded circle in panel (a)), while the substrate is circle or square. The SQUID's sample was cut to have a size of approximately $3 \times 3 \text{ mm}^2$. Then it was fixed inside of a straw by using varnish. Near the bottom and the top of the straw were vented, as shown in Figures (b-d). Figure (e) shows an example of the SQUID's sample which is set into the sample rod.

Basic magnetic properties of each sample were investigated by measuring the hysteresis of magnetizations and temperature dependence of magnetizations. The magnetizations versus magnetic fields ($M(H)$) were measured at 5 K and 300 K; the applied magnetic field up to $\pm 50 \text{ kOe}$. An external field (H) was applied parallel to the sample plane and the total magnetizations (M) were measured

as a function of H in the direction of the applied field. The magnetizations versus temperatures ($M(T)$) were measured under the applied fields 100 Oe and 1 kOe. Only in some cases the $M(T)$ is measured at 25 kOe. For each $M(T)$ measurement, the sample was cooled down to 5 K without H . Then, the data were taken in DC-mode with increasing temperature up to 300 K. The result is denoted to be zero-field cool (ZFC) data. Then the sample was cooled down to 5 K with H left unchanged. Then the $M(T)$ data was measured with increasing temperature. The results are denoted to be field cool (FC).

The M-H of the varnish, without the sample, was measured. The result is shown in Figure 4.15. The magnetization (emu/g) of varnish is related to the external applied field by equation

$$M = 2.01861 \times 10^{-5} - 7.01431 \times 10^{-7} \times H$$

Majority of varnish mass is in the order of 10^{-3} g, so that the magnetization of the varnish is in the order of 10^{-8} at $H = 100$ Oe, and 10^{-5} at $H = 50$ kOe. These are very small as compared with that of the raw SQUID's data which is in the order of 10^{-2} . The magnetization curve of varnish was subtracted from the raw data. The raw data was normalized by the area of the sample. This sample area was manipulated from the picture which is taken together with a scale by optical microscope (see Figure 4.16).

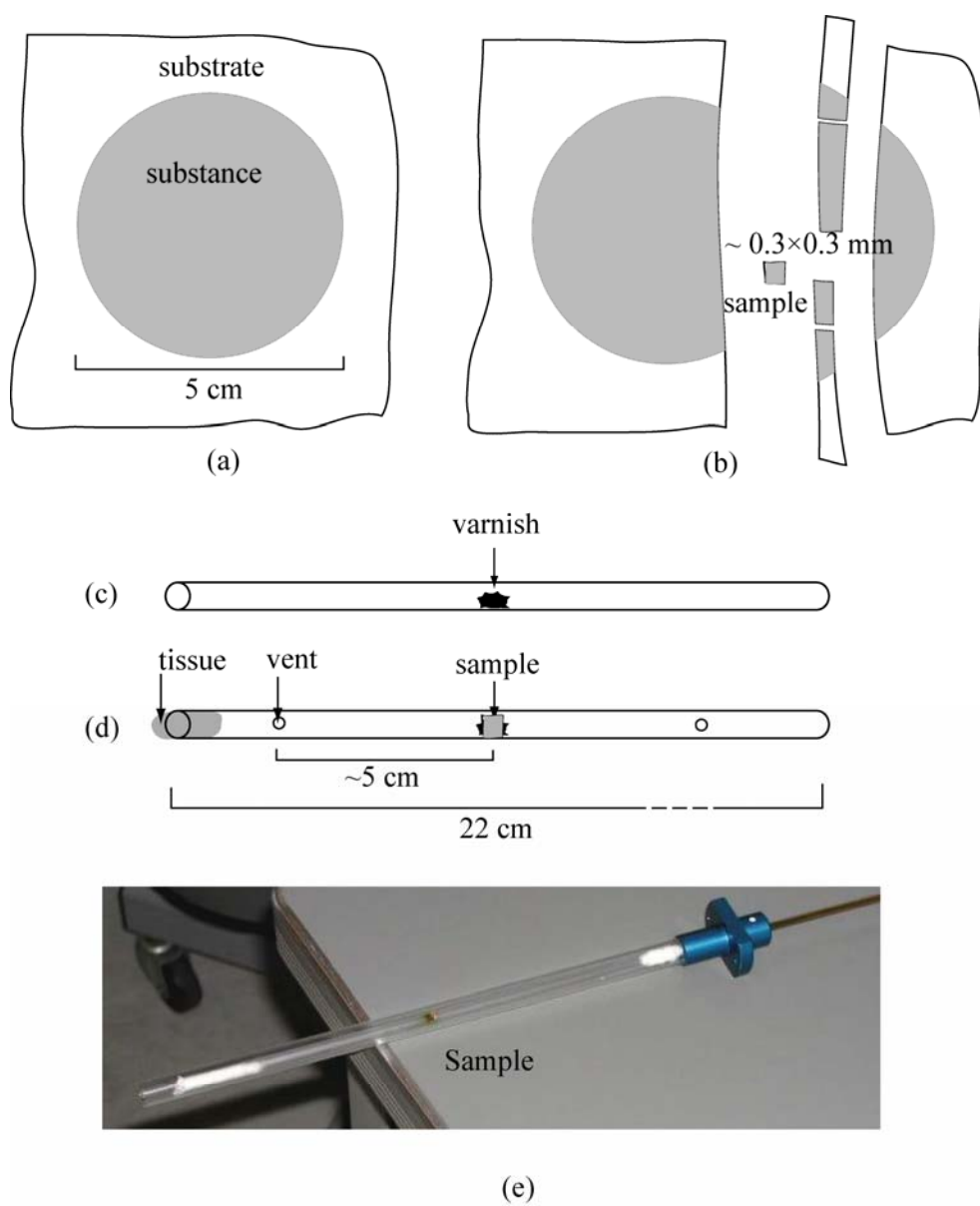


Figure 4.14 Sample set up for magnetization measurements using SQUID.

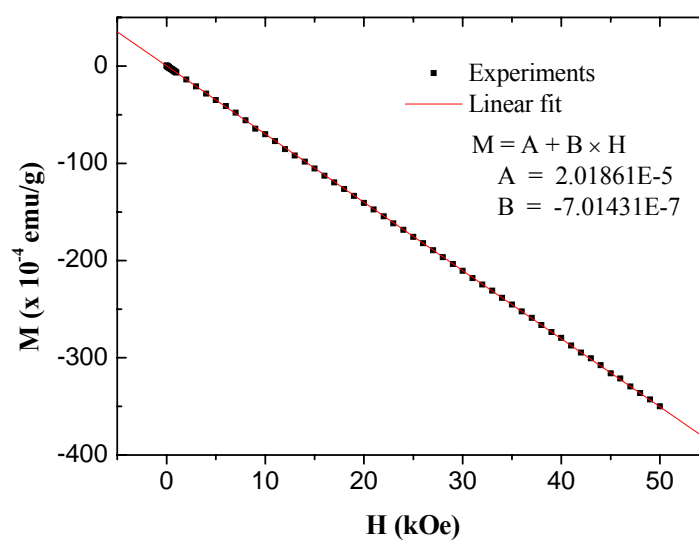


Figure 4.15 M-H curve of vanish

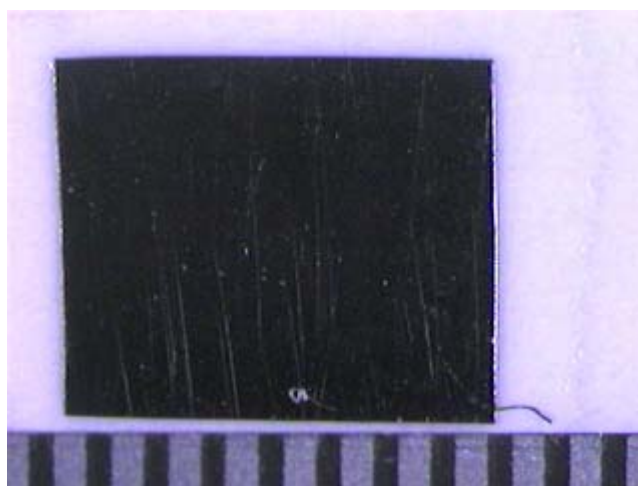


Figure 4.16 SQUID sample taken by an optical microscope. The scale resolution is 0.05 cm.

4.3.3 Magnetic Compton Profile (MCP)

Sample setting for the MCP measurements is illustrated in Figure 4.17. In order to increase the Compton-scattering intensity, a sample was cut as shown in Figure (b). These MLF tapes (10 mm in width) were rolled 12 times (panel (c)), pressed to a square shape of $10 \times 10 \text{ mm}^2$, and then fixed to a copper sample holder, seen in panel (d). When the sample was set in the chamber the sample surface is parallel to the direction of the incident X-rays and applied magnetic field (see panel (e)).

All MCP measurements were carried out on the beamline BL08W station A, SPring-8. The incident energy of the circularly polarized X-rays was selected to be 175-keV. The direction of the incident X-rays was parallel to the sample plane. The scattered X-rays with an angle of 178 degrees to the incident X-rays were detected. The size of the incident X-ray beam at the sample position is less than $0.6 \times 1.5 \text{ mm}^2$ (height \times width). Experimental parameters, R , T and H , have been selected to clarify the origins of the observed characteristics of M-T curves of $R = 5$ and 20. These experimental conditions are tabulated in Table 4.4. In addition, MCPs of Fe/Al and Gd/Al MLFs were measured at 300 K under 1 kOe and 10 K under 25 kOe, respectively for the line-shape analysis. The accumulation times for the sample of $R = 5$ were respectively 9.3, 7.2 and 6.7 hours at 10 K under 1 kOe, 300 K under 1 kOe, and 10 K under 25 kOe. Those for the sample of $R = 20$ were respectively 11 and 13.3 hours at 10 K under 1 kOe and 300 K under 1 kOe. The accumulation time of 15 hours was consumed for each of the samples of Fe/Al and Gd/Al MLFs.

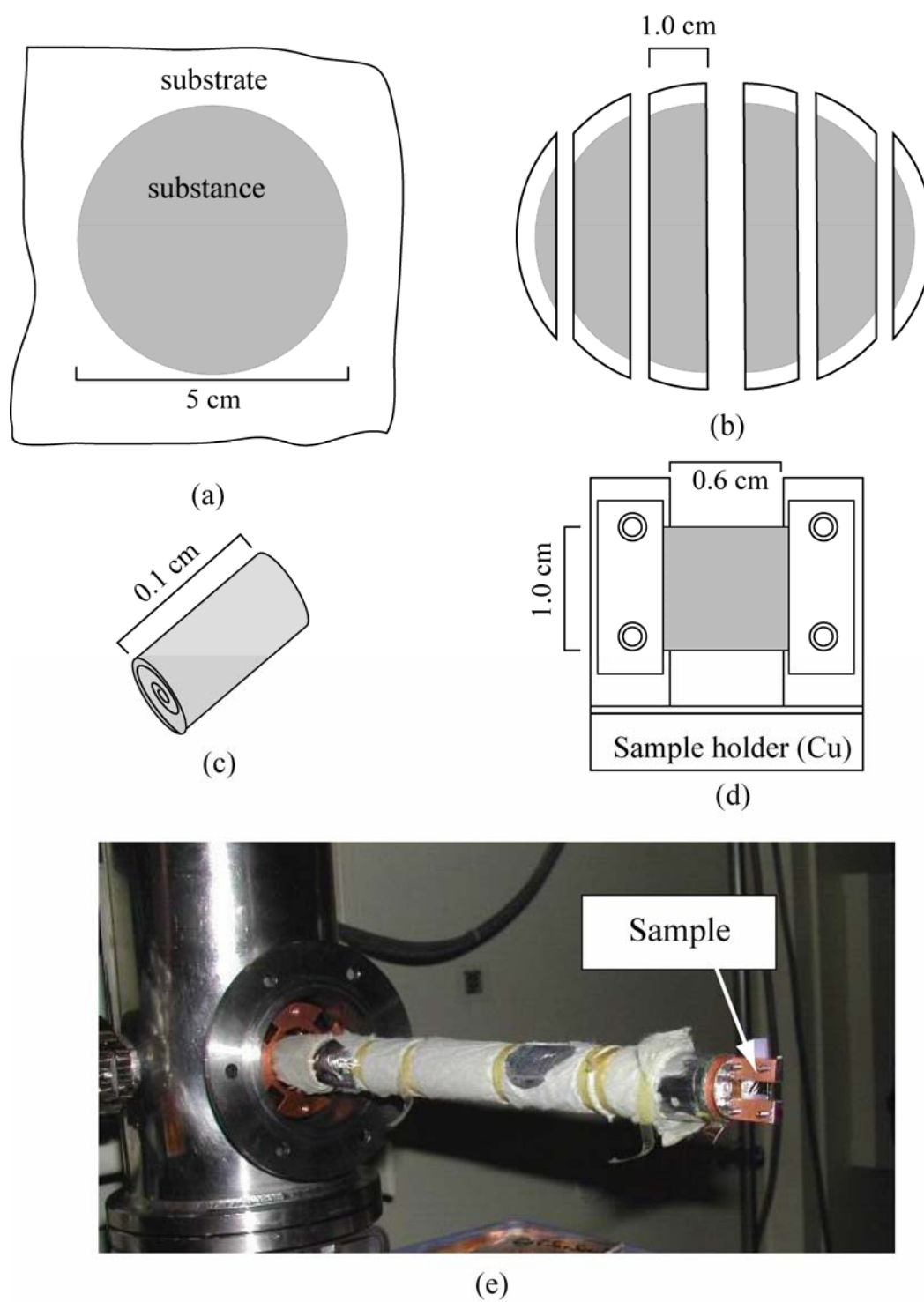


Figure 4.17 Preparation of MCP' sample

Table 4.4 Experimental conditions for MCP measurements.

MLFs	Exp. Conditions	
	T (K)	H (kOe)
PET/[Al(RÅ)/Gd(40Å)/Al(RÅ)/Fe(20Å)]×100/Al(RÅ)		
R = 5	10	1
	10	25
	300	1
R = 20	10	1
	300	1
PET/[Al(RÅ)/Gd(40Å)]×100/Al(20Å)	10	25
PET/[Al(RÅ)/Fe(40Å)]×100/Al(5Å)	300	1

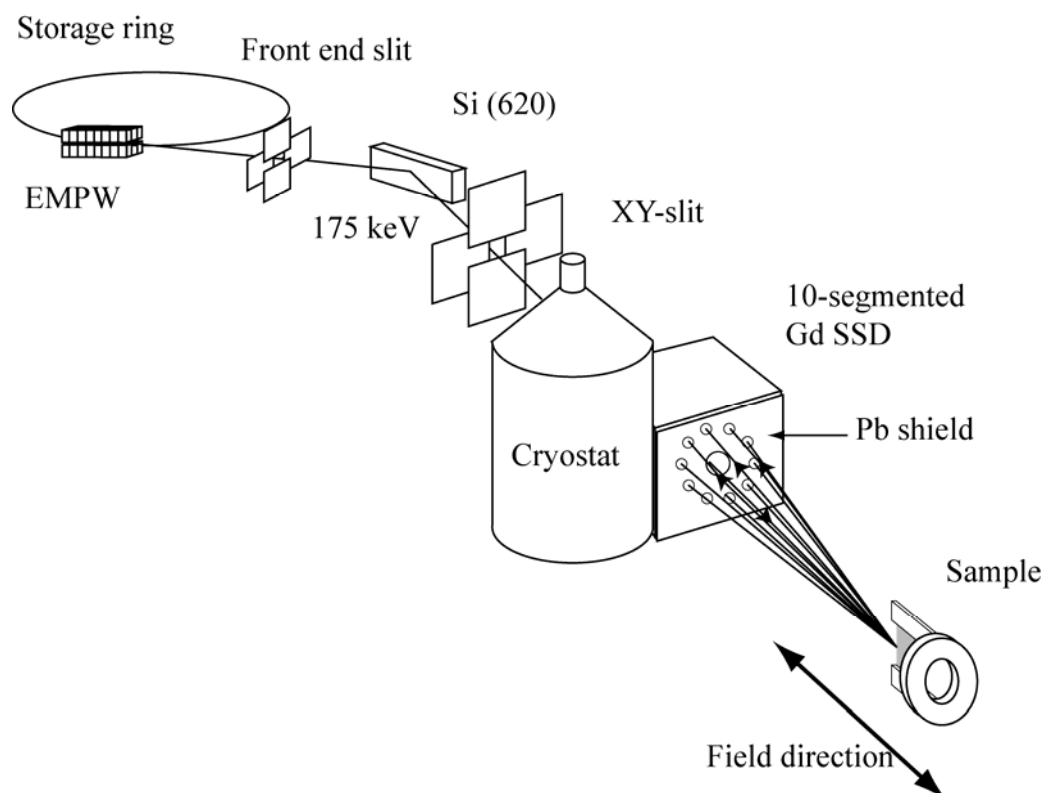


Figure 4.18 Experimental set up for MCP measurements.

4.3.4 X-ray Magnetic Circular Dichroism (XMCD)

The samples are prepared to have a length and a width of 10 and 5 mm, respectively, and five of the samples are stacked for the measurements, as shown in Figure 4.19. The samples and experimental conditions are listed in Table 4.5.

The XMCD measurements are made at beamline BL39XU of SPring-8. Incident X-rays have the energies of ~ 7.109 and of ~ 7.249 keV for measurements at Fe-K and Gd-L₃ edges, respectively. The hystereses of XMCD signal have been measured for the samples of $R = 0, 5$ (PET substrate), 10, and 100. A superconducting magnet including liquid helium cryostat has been employed. The direction of the applied field is parallel to that of the incident x-rays and the sample plane is fixed at $\sim 10^\circ$ away from the incident x-ray direction.

A diagram of the electric circuit used for phase-sensitive detection is shown in Figure 4.20. It consists of a logarithmic converter circuit and a lock-in amplifier. Voltage signals $V(I_0)$ and $V(I)$, which were proportional to the intensities of incident and transmitted beam, respectively. The logarithmic converter gave a voltage signal $V(\mu t)$ which corresponds to the absorption coefficient $\ln(I_0/I)$ via $V(I_0)$ and $V(I)$. The AC component of $V(\mu t)$ directly gave the XMCD, $\Delta\mu t$, and was measured through the lock-in amplifier referring to the frequency of the helicity switching, whereas the DC component gave the ordinary absorption coefficient, $\bar{\mu}t$, and was measured with the digital voltmeter.

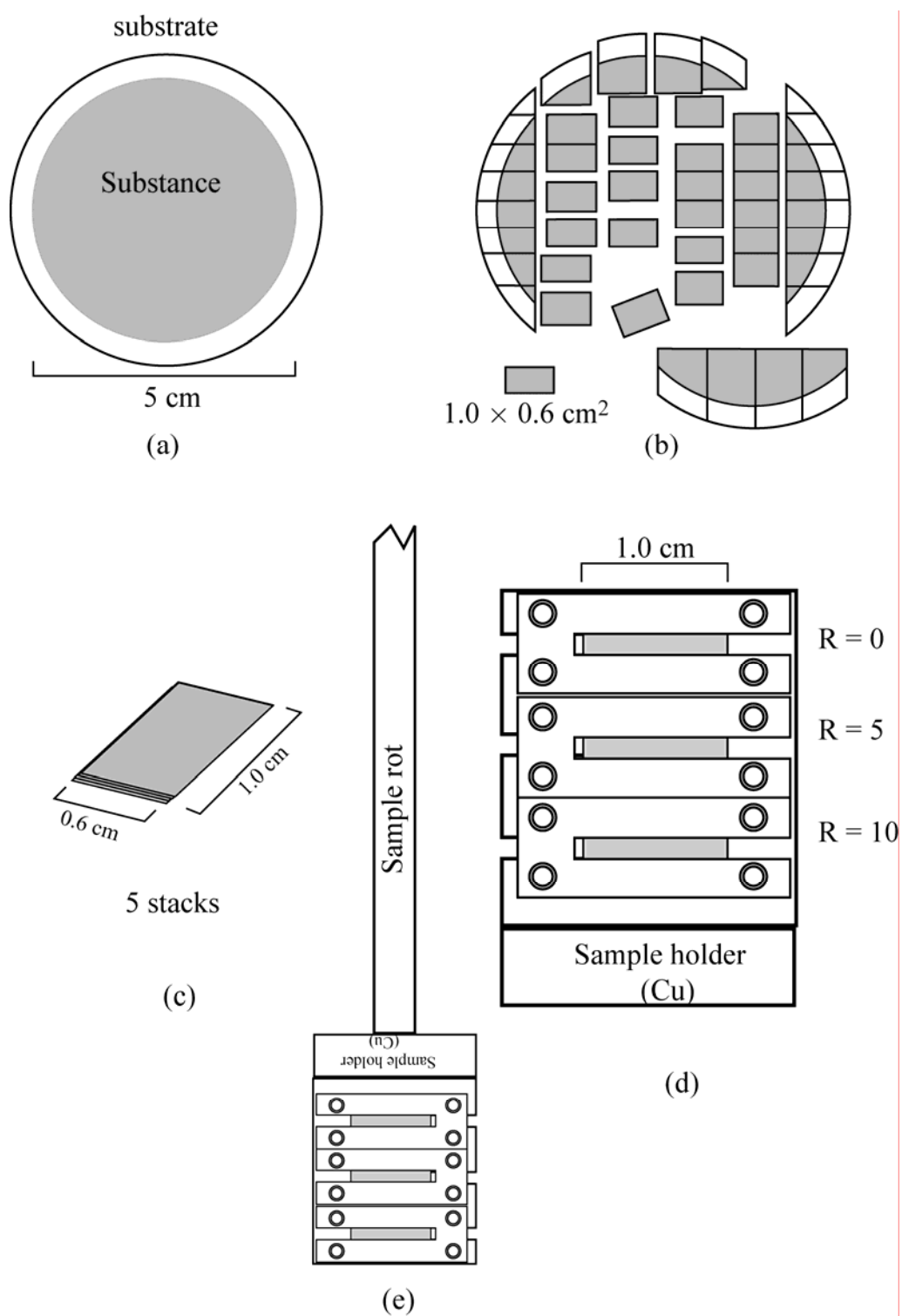


Figure 4.19 Sample preparation for XMCD measurements.

Table 4.5 List of XMCD's samples and of the experimental conditions.

[Al(RÅ)/Gd(40Å)/Al(RÅ)/Fe(20Å)]×20/Al(RÅ) MLFs	Exp. Conditions	
	T (K)	H (kOe)
R = 0 (POL film substrate)	160	Up to ±100
	280	
R = 5 (PET-foil substrate)	5	Up to ±100
	50	
	280	
R = 10 (POL film substrate)	5	Up to ±100
	50	
	280	
R = 100 (POL film substrate)	5	Up to ±100
	280	

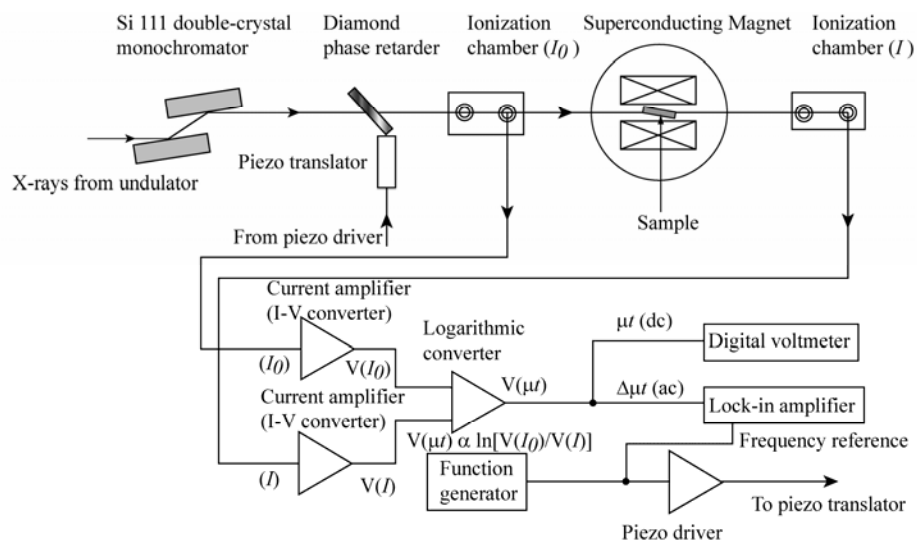


Figure 4.20 Schematic diagram of the electric circuit for the XMCD measurement and along with the diagram of X-ray beam.

CHAPTER V

EXPERIMENTAL RESULTS

5.1 Magnetization Curves

The samples are classified into two groups: one is characterized by a common substrate of the polyimide film (POL), and the other by the substrate of the polyethylene film (PET). The magnetization curves of the POL-substrate samples change greatly as the thickness of Al spacer is gradually increased. The results of magnetization measurement on the PET-substrate samples are used for analyzing the magnetic Compton profiles (MCPs).

5.1.1 Magnetization Curves of the Polyimide Film-Substrate Samples.

Figure 5.1(a) to (i) show the curves of magnetization versus applied magnetic field, $M(H)$, of the POL samples. Figure 5.1 (a) covers the magnetization at 5 K, and shows different features depending on the thickness, R , of the Al spacer. Figure 5.1 (b) to (h) show the magnetic hystereses in a low field region. The coercive field, H_c , abruptly increases when a 5-Å Al spacer is inserted. On the contrary, H_c decreases when R is increased from 5 to 30 Å. Small kinks pointed by arrows near H_c have been observed on the $M(H)$ curves of $R = 5, 7, \text{ and } 10$ (Figure 5.1 (c), (d), and (e), respectively), but not on the others.

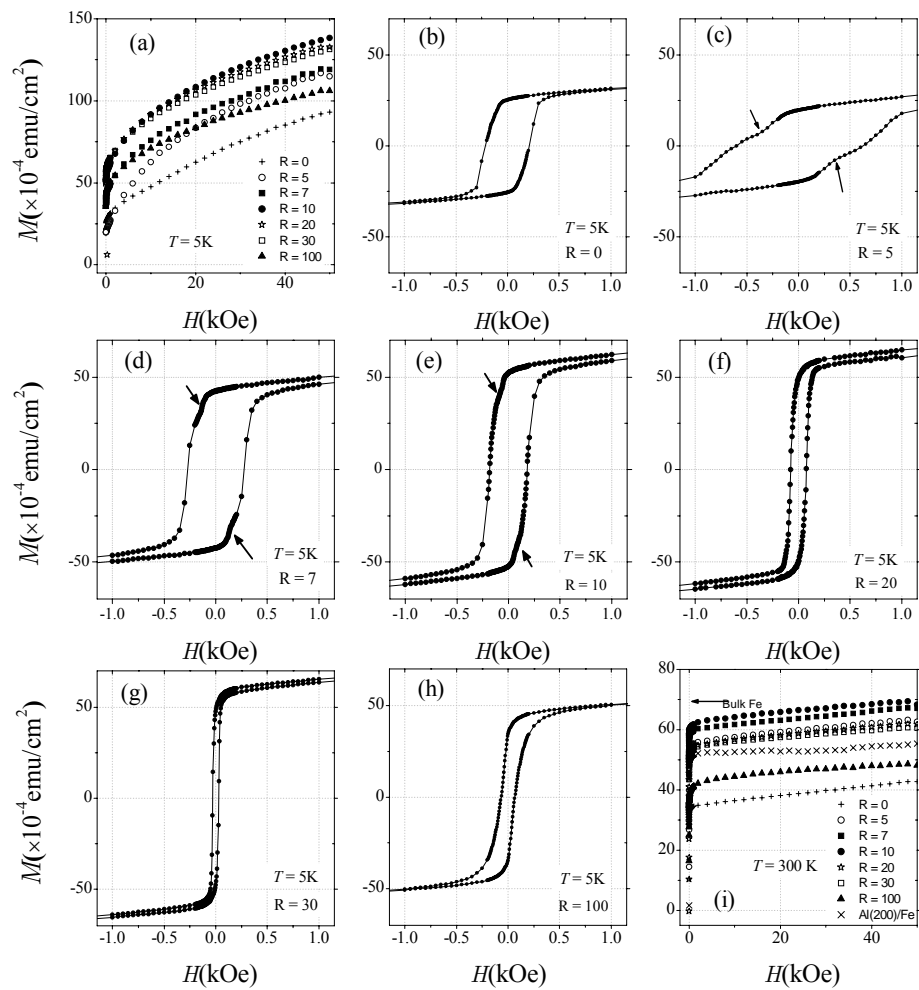


Figure 5.1 Magnetization curves of Al/Fe/Al/Gd MLFs on POL film; a) at 5 K up to 50 kOe, b) ~h) at 5K in a low field region, and i) at 300 K.

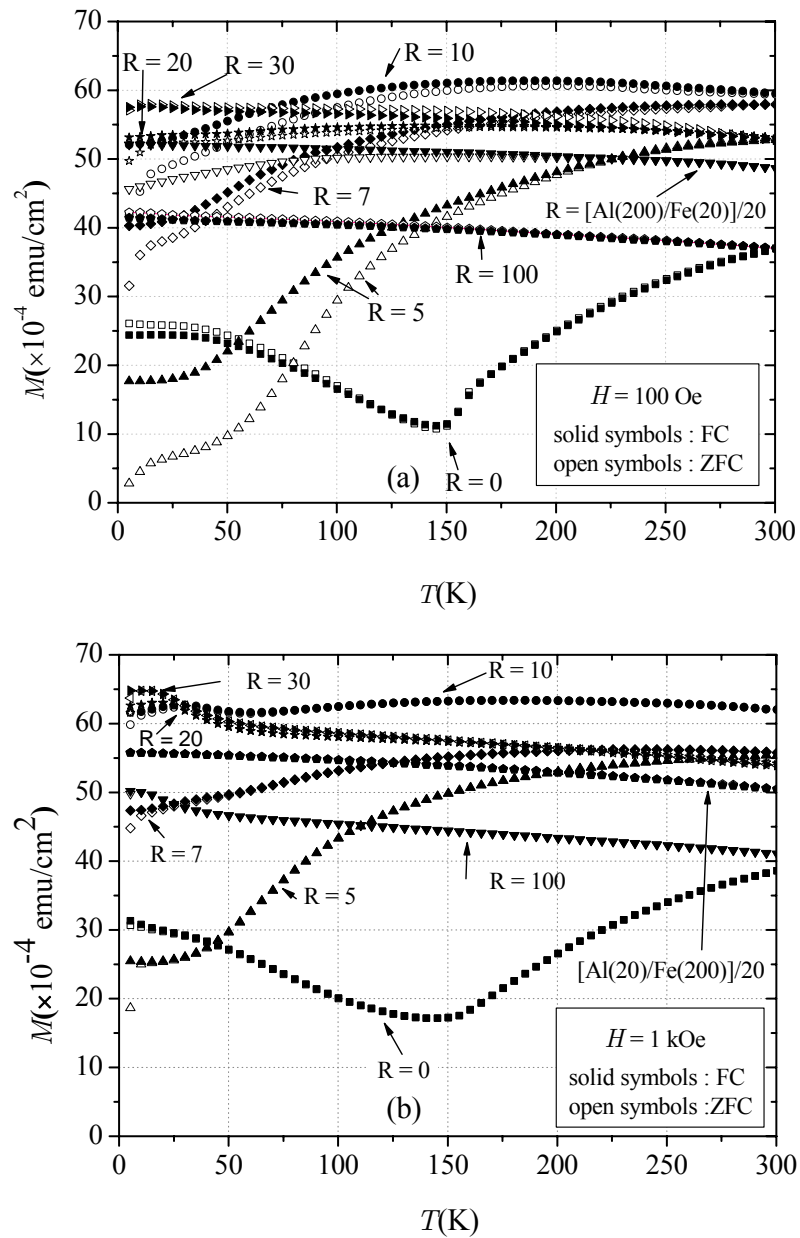


Figure 5.2 Temperature dependence of magnetization ($M(T)$ curves) of the Al/Fe/Al/Gd MLFs measured at (a) 0.1 kOe and (b) 1 kOe.

Figure 5.1(i) shows $M(H)$ curves at 300 K together with a curve of $[\text{Al}(200 \text{ \AA})/\text{Fe}(20 \text{ \AA})] \times 20/\text{Al}(20 \text{ \AA})$ which is denoted as Al(200)/Fe. All of the samples show monotonously increasing magnetization with increasing H except for the Al/Fe MLF, whose magnetization is rather constant in a high field region.

Figure 5.2(a) and (b) show $M(T)$ curves of the MLFs measured at $H = 0.1 \text{ kOe}$ and 1 kOe , respectively. The presence of the Al spacer induces quite different $M(T)$ curves to that of the Fe/Gd MLF ($R = 0$). The magnetization of Fe/Gd MLF decreases with increasing temperature until around 150 K and changes to increase. The minimum point of the magnetization in Figure 5.2(a) indicates a compensation temperature, T_{Comp} , which is not found in the present Fe-Al-Gd MLFs.

At $H = 0.1 \text{ kOe}$ (Figure 5.2(a)), a large difference between the ZFC- and the FC- curves was observed in the case of $R = 5$. The difference is much reduced when R is changed to 7. Moreover, It's almost disappear for $R = 30$ and 100. At $H = 1 \text{ kOe}$ (Figure 5.2(b)), no difference between the ZFC- and the FC-curves was observed for all the samples.

For $R = 5$, the magnetization slightly increases when the temperature is increased from 5 K to 50 K and then rapidly increases till 100 K, and after that slowly increases until 300 K. For $R = 7$, the magnetization is much larger than that for $R = 5$. It slowly increases when the temperature increases and is almost constant between 200 K and 300 K. The magnetization for $R = 10$ shows the largest value among all the samples above 100 K. The amounts of magnetization of $R = 20, 30,$ and 100 monotonously decrease with increasing temperature. For $R = 100$, although the tendency of $M(T)$ curve is similar to $R = 30$, the amount of magnetization is much

smaller than that of $R = 30$. The amount of magnetization of Al(200)/Fe MLF is smaller than those of $R = 10, 20$ and 30 , but larger than that of $R = 100$.

At $H = 1$ kOe (Figure 5.2 (b)), small humps were observed on the curves of $R = 10, 20$ and 30 around 30 K, 20 K and 15 K, respectively, but not on the others including $R = 0$. These humps were not observed at $H = 0.1$ kOe.

5.1.2 Magnetization Curves of the Polyethylene Film-Substrate Samples.

$M(H)$ curves of MLFs on PET film at 5 K up to 50 kOe are shown in Figure 5.3(a) to (e), and at 300 K in Figure 5.3(f). $M(H)$ curves of $R = 10$ and 20 at 5 K exceed that of Al(5)/Fe(20) MLF above 5 kOe, while $M(H)$ curve of $R = 5$ crosses Al(5)/Fe(20) line around 20 kOe. Contrary to bulk Gd, which is magnetically soft, the magnetization of Al(5)/Gd(40) MLF shows gradual increment, and does not saturate even at 50 kOe, indicating the presence of fairly strong magnetic anisotropy in Gd layers at 5 K. While at 300 K, $M(H)$ of Al(5)/Gd(40) MLF demonstrates that this MLF becomes paramagnetic.

Low field $M(H)$ curves of Al(5)/Gd(40) MLF are shown in Figure 5.3(b) and those of $R = 5, 10,$ and 20 are shown in Figs. (c), (d), and (e), respectively. We see that H_c of the Al/Gd MLF is comparable to that of $R = 5$ MLF. H_c decreases rapidly with increasing the thickness of Al spacer. The small kinks were observed for $R = 5$ and 10 , but not for $R = 20$. Even though the magnitude of magnetization of the PET-substrate samples is different from that of the POL-substrate sample, which could be ascribed to the slight differences in actual thickness of Al, Fe and Gd layers from the nominal thickness, the tendency of magnetization is similar to the POL-film samples with the same R .

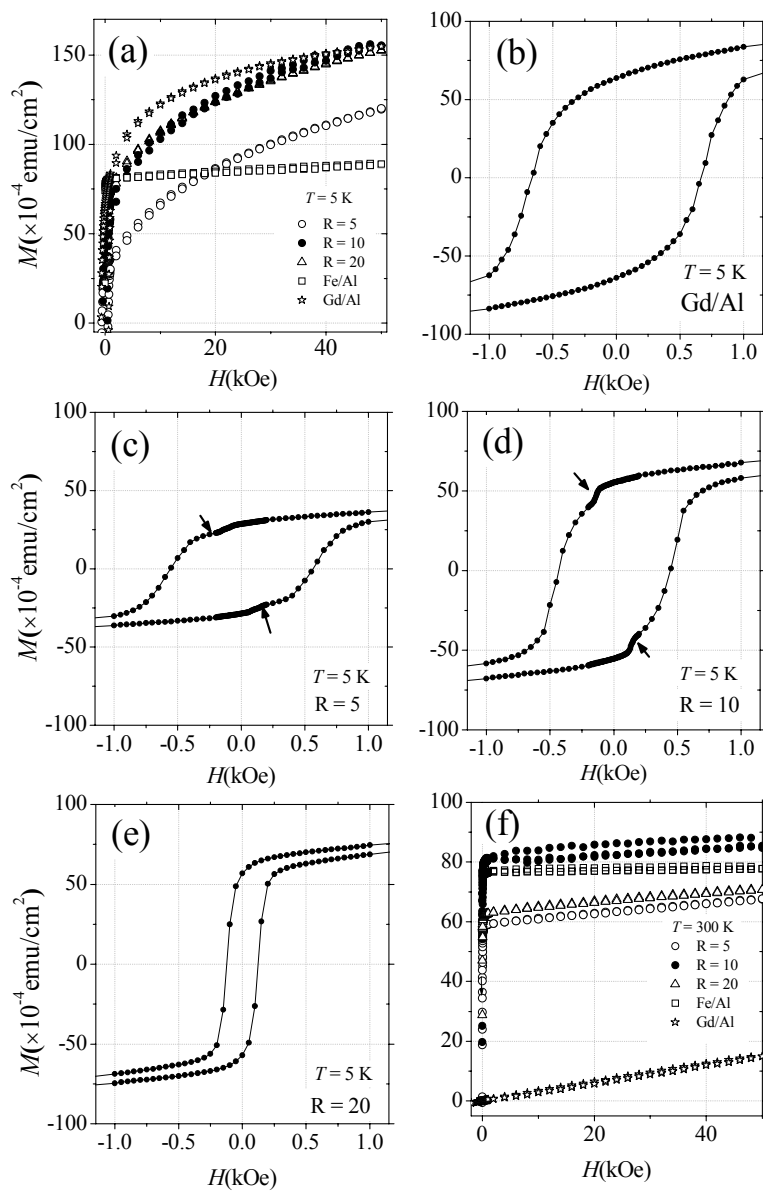


Figure 5.3 $M(H)$ curves of MLFs sputtered on PET substrates; (a) at 5K up to 50 kOe, (b)~(e) at 5 K in a low field region, and (f) at 300 K up to 50 kOe.

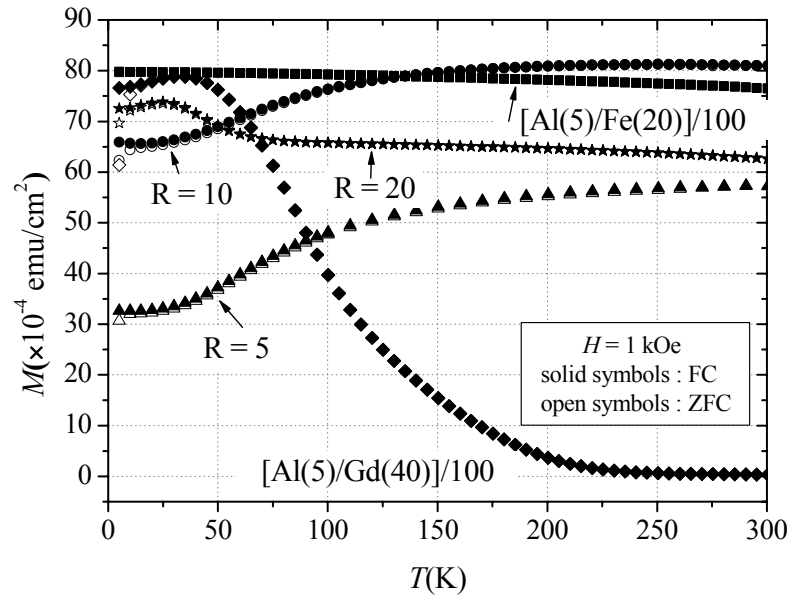


Figure 5.4 $M(T)$ curves at 1 kOe of MLFs sputtered on PET substrates.

Figure 5.4 shows $M(T)$ curves at 1 kOe. Unlike with an approximately flat curve of the Al(5)/Fe(20) MLF, the Al(5)/Gd(40) MLF significantly depends on T , and almost loses its magnetization above 230 K. The Al spacer between Fe and Gd layers induces quite different $M(T)$ curves from that of the Al/Fe and Al/Gd MLF's. When the thickness of Al spacer is increased from $R = 5$ to 10, like the cases of the POL-film samples, the magnetization increases significantly. At 1 kOe, we notice that the curve of $R = 20$ is accompanied by a small hump around 20 K, the same as the POL-film sample of $R = 20$.

Two unexpected features are found in the figure: First, the magnetization of Al(5)/Fe(20) MLF at 5 K exceeds the expected value of α -Fe(20 Å) MLF, 69×10^{-4} emu/cm². On the basis of this evidence, it is concluded that the Fe-layer thickness of Al(5)/Fe(20) MLF on PET film should be corrected to 23 Å, so that

its magnetization is consistent with that of α -Fe. Since the MLFs of Al(5)/Fe(20), R = 10 and 20 MLFs on PET film were prepared in the same sputtering condition, the thickness of these Fe-layers should be also corrected to 23 Å. A systematic error on the input parameter for the sputtering could be introduced during these sample preparations. No such discrepancy was found in the thickness of R = 5 MLF and Gd layers.

Second, the magnetization of R = 20 MLF is quite smaller than that of R = 10 MLF in spite of reexamined Fe-layer thickness of 23 Å. To examine this feature, a Mössbauer spectrum of R = 20 MLF at room temperature under 1-kOe external field (not shown in this thesis) was measured. The result has verified the presence of non- or para-magnetic component, the amount of which was about 20% of the normal ferromagnetic part. Some reports suggest the presence of paramagnetic intermixture of Fe and Al at the Al/Fe interface (Fonda and Traverse, 2004; Carbucicchio et al., 2000). It is, however, not clear whether the present para- or non-magnetic component exists in the interface, because the MLFs of R = 5 and 10 do not indicate such an amount of intermixture.

5.2 Magnetic Compton Profiles

The observed MCPs of R = 5 and 20 are shown in Figure 5.5 and Figure 5.6, respectively. The horizontal axis denotes the electron momentum in atomic units (a.u.): $1 \text{ a.u.} = mc/137.036 = 0.19928 \times 10^{-18} \text{ cm}\cdot\text{g}/\text{s}$, where m is the mass of electron and c is the velocity of light.

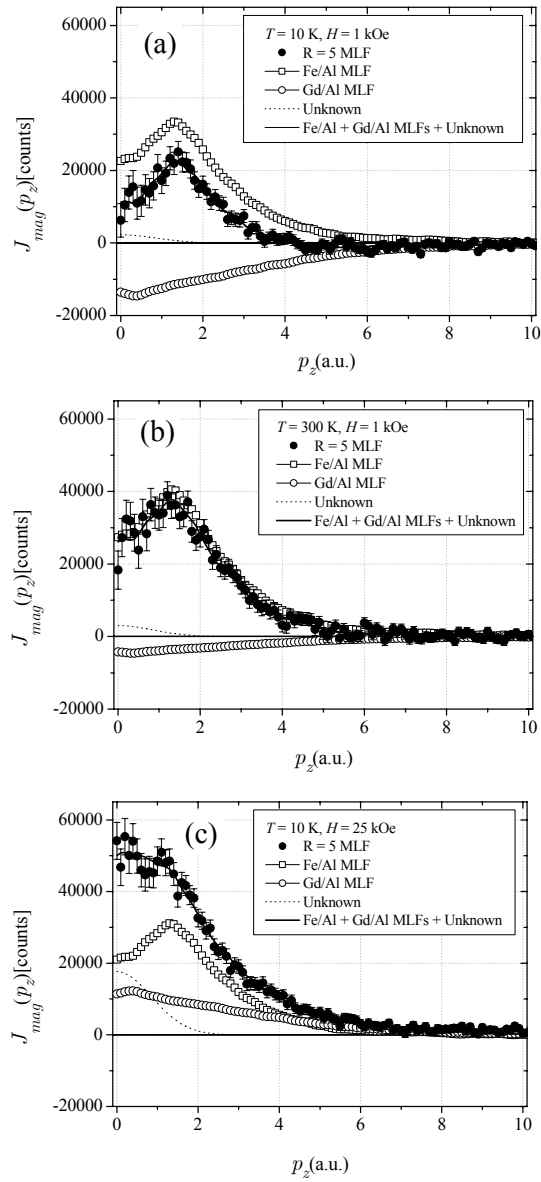


Figure 5.5 MCPs of the sample of $R = 5$ on PET foil substrate at (a) 10 K under 1 kOe, and (b) 300 K under 1 kOe.

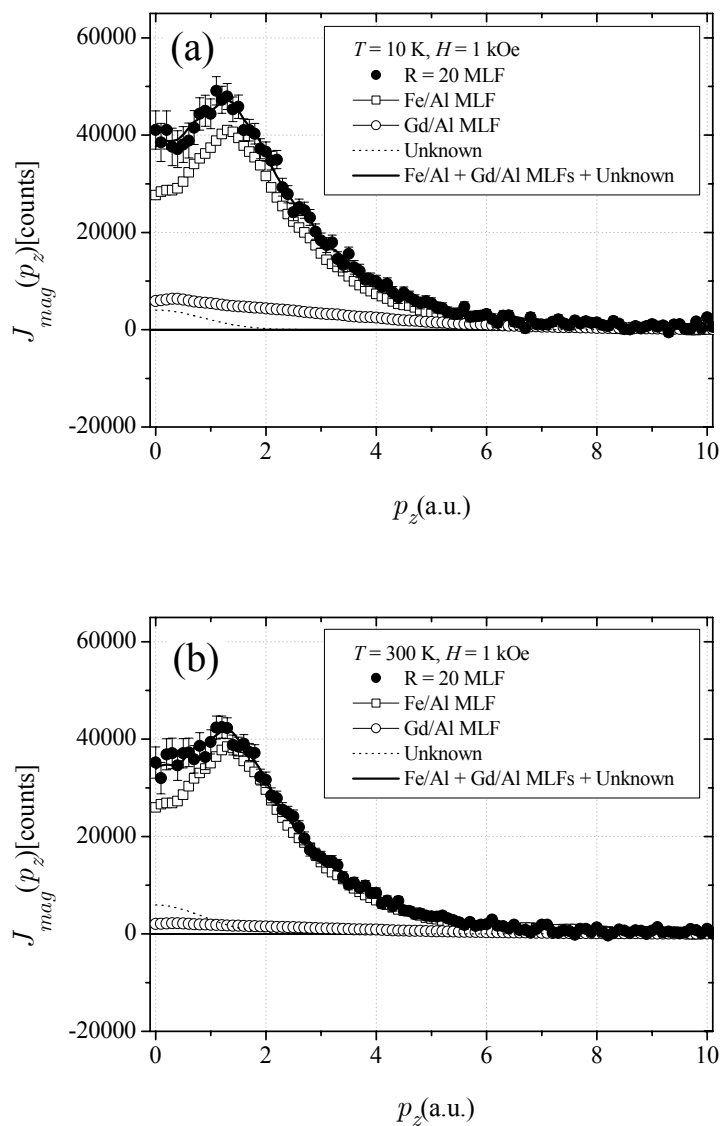


Figure 5.6 MCPs of the sample of R = 20 on PET foil substrate at (a) 10 K under 1 kOe, and (b) 300 K under 1 kOe.

The line-shape analysis was made on each MCP by a least-square fitting method using three components: experimental MCPs of Al/Fe MLF and Al/Gd one, and an assumed itinerant electron-like MCP with a Gaussian momentum distribution

in a low momentum region (denoted as 'unknown part'), alike that of itinerant electrons. The intensity of each MCP was scaled to the corresponding amount of the magnetization induced at the same temperature and magnetic field. The negative signs of the Gd MCP in Figure 5.5(a) and (b) mean that the Gd-spin direction is opposed to the direction of the total spin magnetization mainly induced by the Fe spins. At 10 K under 25 kOe (Figure 5.5(c)), both the Fe- and Gd-spin magnetizations are positive, and a low positive peak of an unknown profile was required to be introduced to attain a reasonable line-shape fitting. In the case of the sample of $R = 20$, the Gd component is positive in sign at 10 K (Figure 5.6(a)), and is relatively small at 300 K (Figure 5.6(b)).

5.3 Hysteresis of the XMCD Effect

Examples of X-ray magnetic circular dichroism (XMCD) and absorption spectra measured at the Fe K - and Gd L_3 edges are shown in Figure 5.7 (a) and (b), respectively. The ordinate indicates the magnitude of the observed XMCD effect. The spectra were measured on the sample of $R = 5$ (PET substrate) at $T = 50$ K and $H = 100$ kOe. The maximum peaks of the XMCD spectra at the Fe K - and Gd L_3 - edges were found at 7.1095 and 7.2445 keV, respectively, which are pointed by the arrows in the figures. The magnetic hysteresis loops of XMCD have been measured at these X-ray energies. Note that, at $H = 100$ kOe and $T = 50$ K, both the XMCD peaks of Fe K - and Gd L_3 edges show positive. These signs are the same as ferromagnetic bulk Fe and Gd samples. This means that the directions of Fe and Gd magnetic moments in the MLF are in the same direction of H .

The measurements of hysteresis loops of XMCD at the Gd- L_3 edge were successful, and the results are shown in this thesis. On the other hand, however, the

results of the measurements at the Fe- K edge were not included in this thesis, because of a poor signal to noise ratio caused by the following reason: As mentioned in the Chapter IV, the sample was fluctuated during the measurement by the vibration of the recondensing cooler. Since the XMCD signal at the Fe- K edge was weak, the hysteresis loops of XMCD at this edge were not good enough to show any useful information. One may think of the preparation of more numbers of stacks so as to increase the XMCD signal of the Fe- K edge. However, at the same time the transmittance of X-rays (measured in transmission mode) is decreased because of the absorption by Gd layers, resulting an insufficient signal to noise ratio.

Figure 5.8 shows the XMCD-hysteresis loops of the sample Fe/Gd MLF ($R = 0$) at 160 K and 280 K. In a low field region, the field dependence of the XMCD effect at 280 K is significantly different from that at 160 K, which is just above the compensation temperature of about 150 K.

Figure 5.9(a) shows the temperature dependence of hysteresis of XMCD effect on the sample of $R = 5$. The XMCD curve intersects with the abscissa at $H \sim 10$ kOe for 5 K, and ~ 20 kOe for 50 K. Figure 5.9(b) shows that H_c decreases rapidly with increasing the temperature. Although it is difficult to evaluate the absolute value of the Gd moments, the magnitude of the XMCD effect at 280 K is much reduced from that at 5 K.

Figure 5.10(a) and (b) show the temperature dependence of hysteresis curves of the sample of $R = 10$. The curve intersects with the abscissa at $H \sim 3$ kOe and $H \sim 5$ kOe when the temperature is 5 K and 50 K, respectively. In Figure 5.10(b), even though the XMCD signal is very noisy at 280 K, it can be deduced that the Gd layers in the sample of $R = 10$ at 280 K are not paramagnetic.

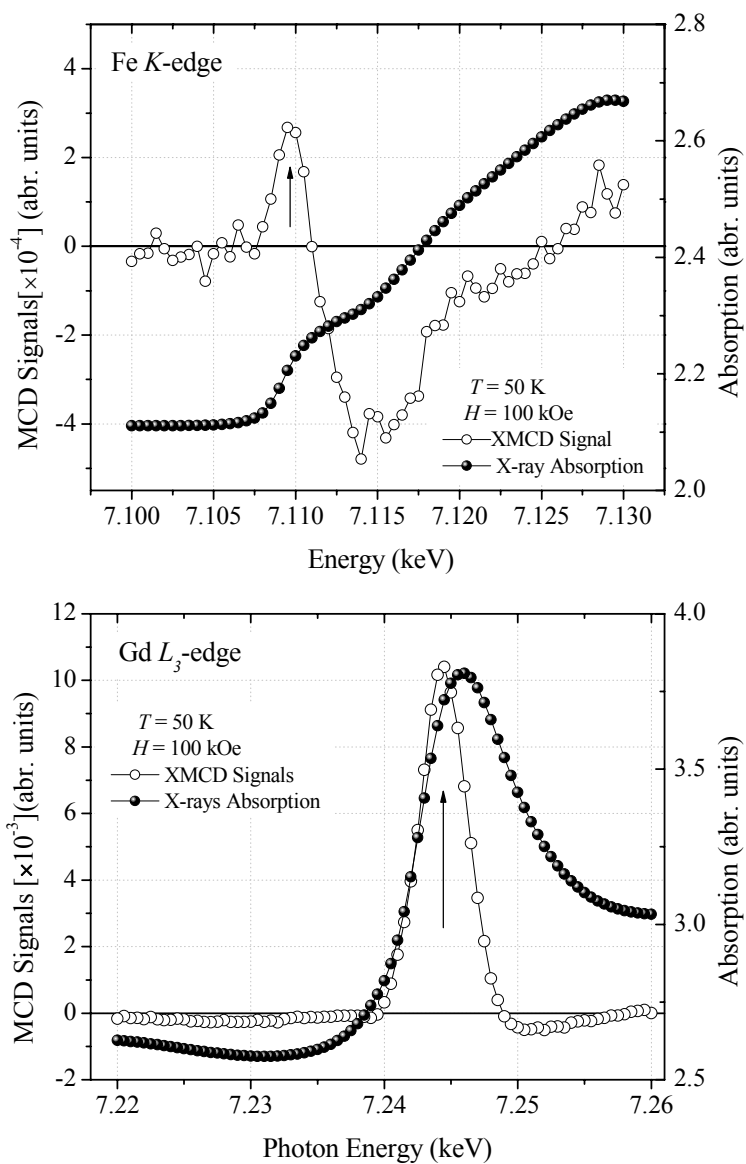


Figure 5.7 XMCD and absorption spectra measured at (a) the Fe K edge (7.111 keV) at room temperature and 100 kOe, and (b) the Gd L_3 edge (7.243 keV), measured at 50 K and 100 kOe.

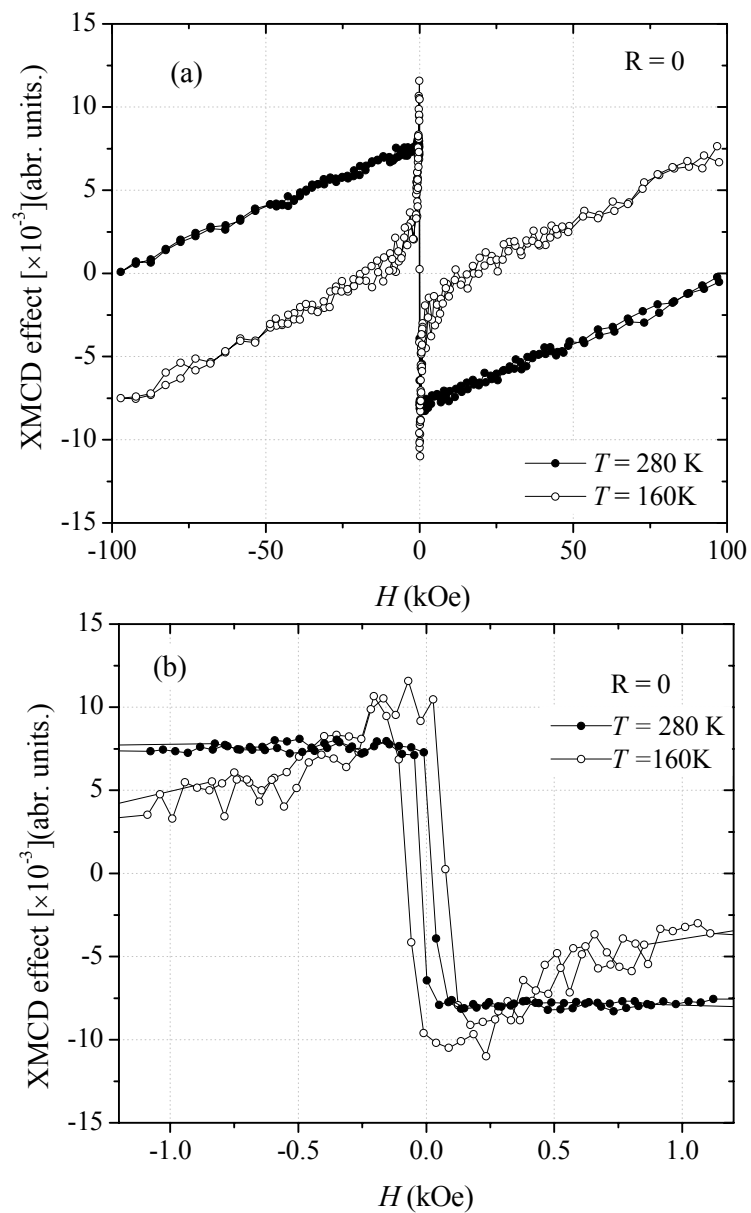


Figure 5.8 Hysteresis loop of XMCD effect of the sample $R = 0$ at 280 K (solid circle) and 160 K (open circle); (a) covers a high field region, (b) a low field region. The solid lines are just for eye guide.

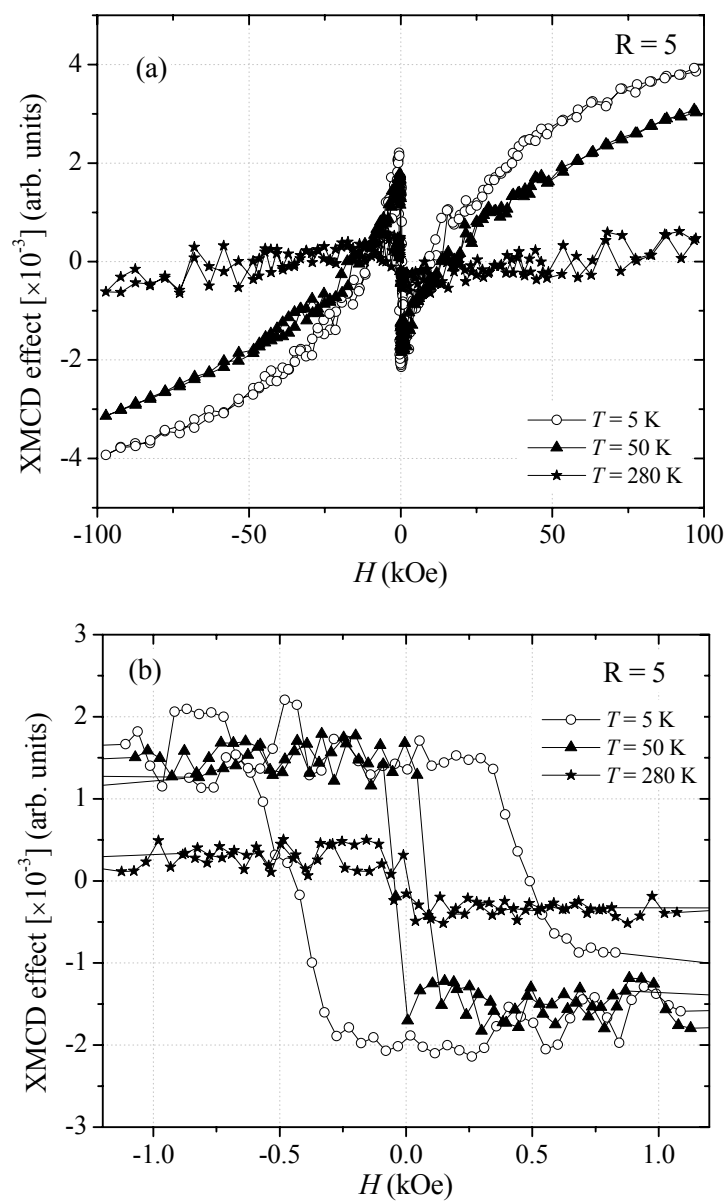


Figure 5.9 Magnetic hysteresis of XMCD effect of the sample of $R = 5$ at 5 K (open circles), 50 K (triangles), and 280 K (stars); (a) covers a high field region, (b) a low field region. The solid lines are just for eye guide.

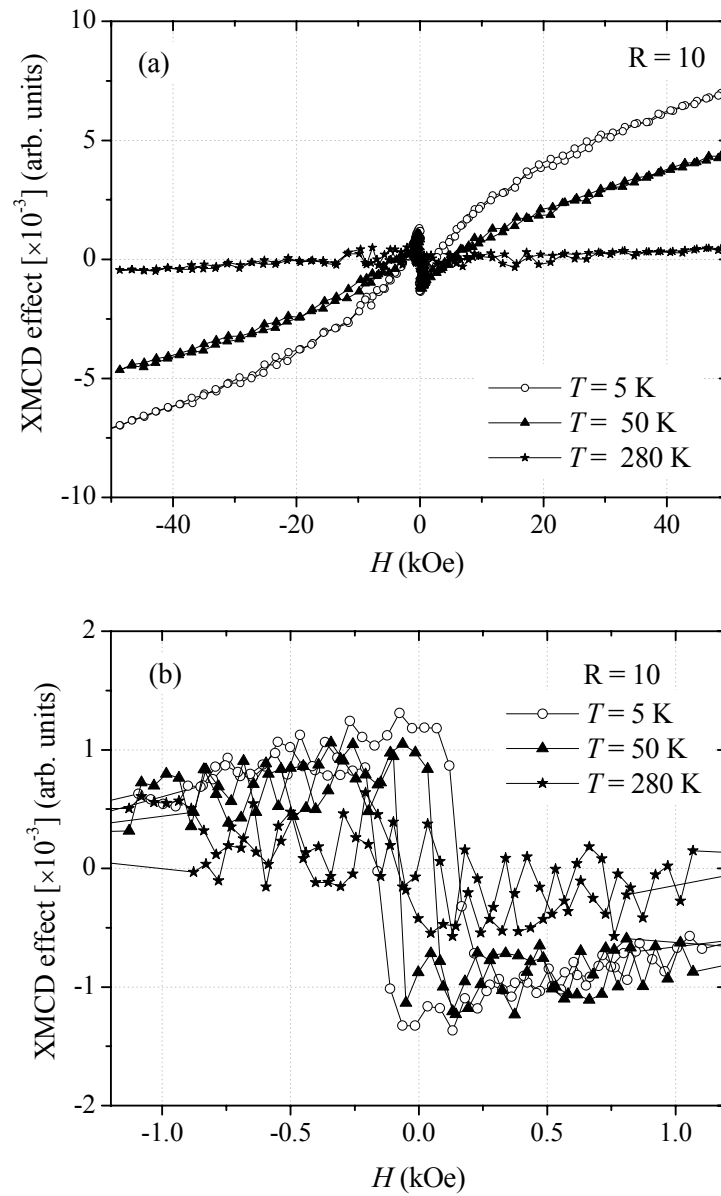


Figure 5.10 Magnetic hysteresis of XMCD effect of the sample of $R = 10$ at 5 K (open circles), 50 K (triangles), and 280 K (stars); (a) covers a high field region, (b) a low field region. The solid lines are just for eye guide.

Figure 5.11(a) and (b) show the XMCD effect for the sample of $R = 100$ at 5 and 280 K, respectively. This sample exhibits paramagnetic even at 5 K, and also 280 K. Accordingly, in a high field region, the magnitude of XMCD at 50 K is increased in comparison with that at 280 K.

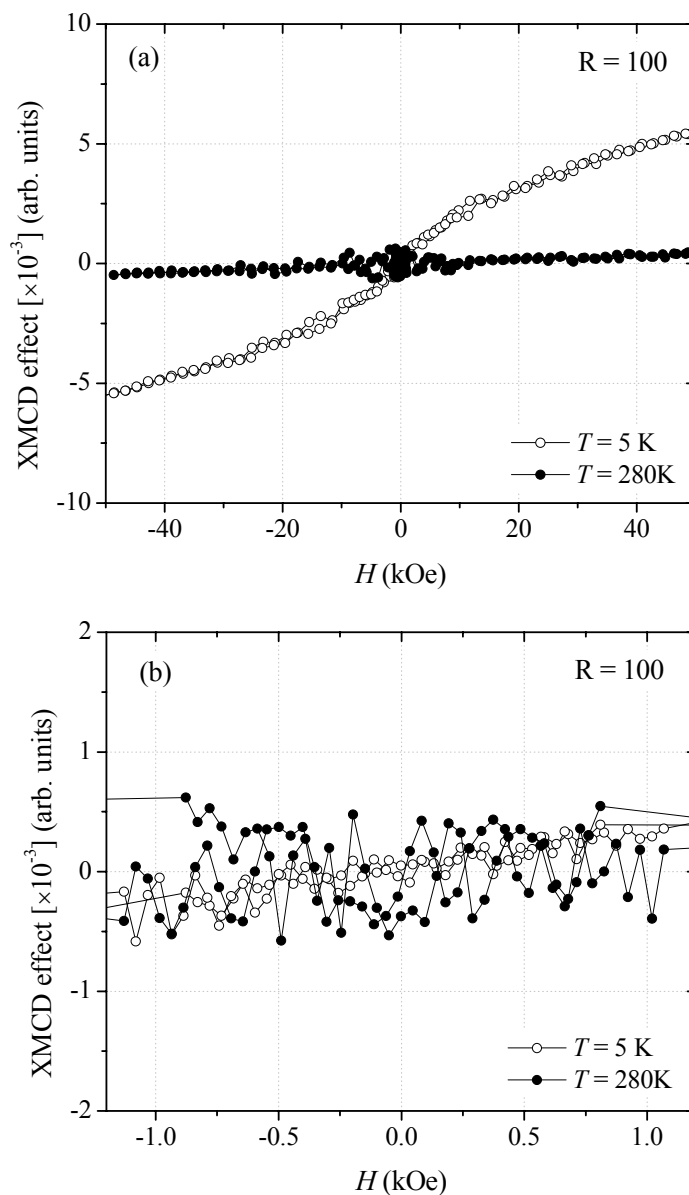


Figure 5.11 Magnetic hysteresis of XMCD effect of the sample of $R = 100$ at 5 K (open circles) and 280 K (solid circles); (a) covers a high field region, (b) a low field region. The solid lines are just for eye guide.

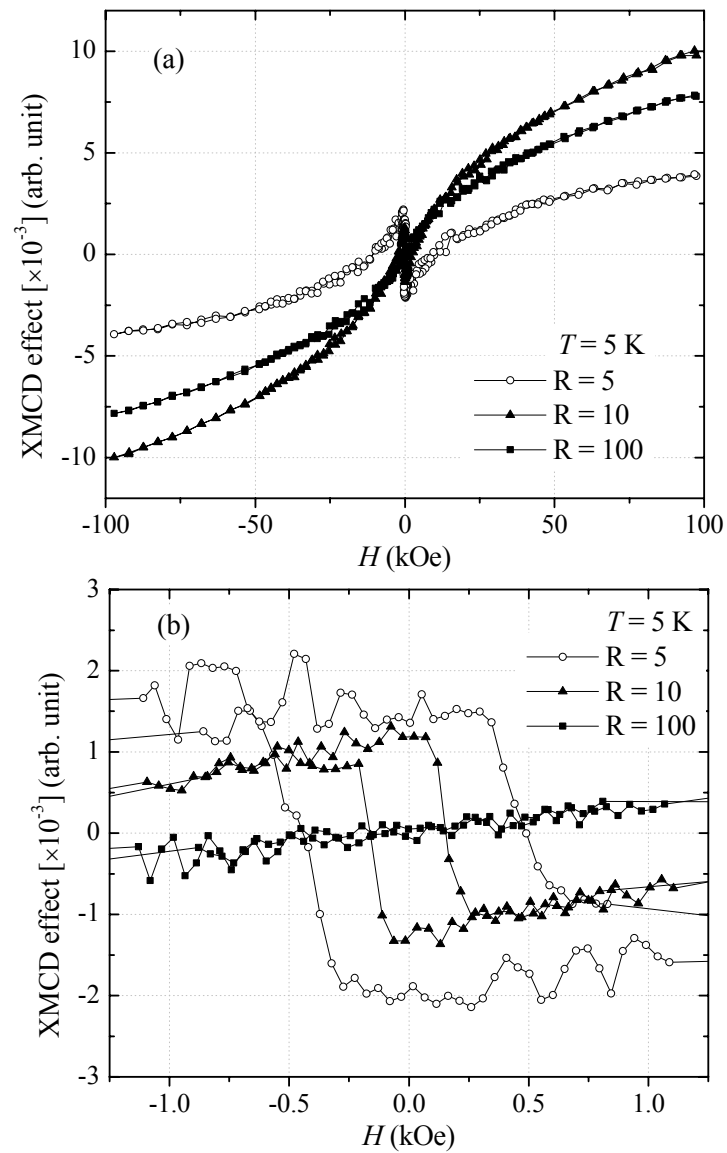


Figure 5.12 Magnetic hysteresis of XMCD effect at 5 K of the sample of $R = 5$ (open circles), $R = 10$ (triangles), and $R = 100$ (solid squares); (a) covers a high field region, (b) a low field region. The solid lines are just for eye guide.

The hysteresis loops of the XMCD effect at 5 K of the samples of $R = 5$, 10, and 100 are shown together in Figure 5.12(a) and (b). For the samples of $R = 5$ and 10, the sign of XMCD is opposite to that of the field in a low field region, as seen in Figure 5.12(b).

It is also shown in Figure 5.12(b) that H_c is notably decreased by increasing R , and disappears for $R = 100$. This evidence suggests that the magnitude of H_c is strongly influenced by the Gd-layer magnetization, because the disappearance of H_c for $R = 100$ is consistent with the paramagnetic behavior of Gd-layer at 5 K in the MLF of $R = 100$, as shown in Figure 5.11.

In summary, the experimental results obtained by SQUID, MCP, and XMCD techniques show phenomena which depend on the thickness of the Al spacer. The phenomena can be itemed as the following contents.

(1) The magnitudes of magnetization of MLFs at low temperature depend on the thickness of Al spacer. They increase considerably with increasing the thickness of Al as seen in $M(H)$ and $M(T)$ curves (Figure 5.1 and Figure 5.2, respectively).

(2) The magnetization of Al(5)/Gd(20) MLF, under $H = 1$ kOe, disappears at about 250 K, as shown in Figure 5.4.

(3) A compensation temperature (T_{Comp}) was observed for the Fe/Gd MLF, but not observed for the Al/Fe/Al/Gd MLFs, as seen in Figure 5.2.

(4) Small kinks were observed at low temperatures on the $M(T)$ curves of the samples of $R = 20$ and 30 under 1 kOe (Figure 5.2(b)).

(5) The coercive force (H_c) at 5 K decreases rapidly with increasing the thickness of Al from 5 to 30 Å. It also depends on the temperature, as shown in Figure 5.12(b).

(6) The line-shape analysis of MCP confirms the antiferromagnetic spin coupling between Fe and Gd layers, and demonstrates that both the spin magnetization are changed to positive by an external magnetic field.

(7) In the line-shape fitting of MCPs measured at 25 kOe, the introduction of an unknown profile was required in the cases of $R = 5$ and 20.

(8) The signs of XMCD signals at the Gd-L₃ edge have revealed the directional rotation of the Gd-layer magnetization with increasing an external magnetic field.

CHAPTER VI

DISCUSSION AND CONCLUSION

6.1 Discussion

The experimental data are discussed on the basis of the assumptions that the total magnetization of magnetic multilayer film (MLF) is mainly affected by (1) *intralayer* exchange coupling in Fe and Gd layers, (2) Zeeman interactions of Fe and Gd magnetic moments with an external field (H), (3) *interlayer* magnetic coupling (IMC) between Fe and Gd spins, and (4) magnetic anisotropy in Gd layers and the negligibly weak magnetic anisotropy in Fe layers. The discussion mainly aims to study the IMC in Al/Fe/Gd/Al MLFs.

6.1.1 IMC in Al/Fe/Al/Gd MLFs

The antiferromagnetic IMC between Fe and Gd layers across the Al spacer is directly determined by the analyses of MCPs and the hysteresis loops of the Gd-XMCD effect. According to the MCP analysis on the sample of $R = 5$ at 10 K and 1 kOe, the magnitude of the Fe-layer magnetization is larger than that of the negative Gd magnetization (see Figure 5.5(a)). Thus the Fe moments align along the direction of the external field, and the Gd moments in the opposite direction. This situation is observed as negative signs of the Gd-XMCD-effect on the samples of $R = 5$ and 10 at 5 K (see Figure 6.1(a) and (b)).

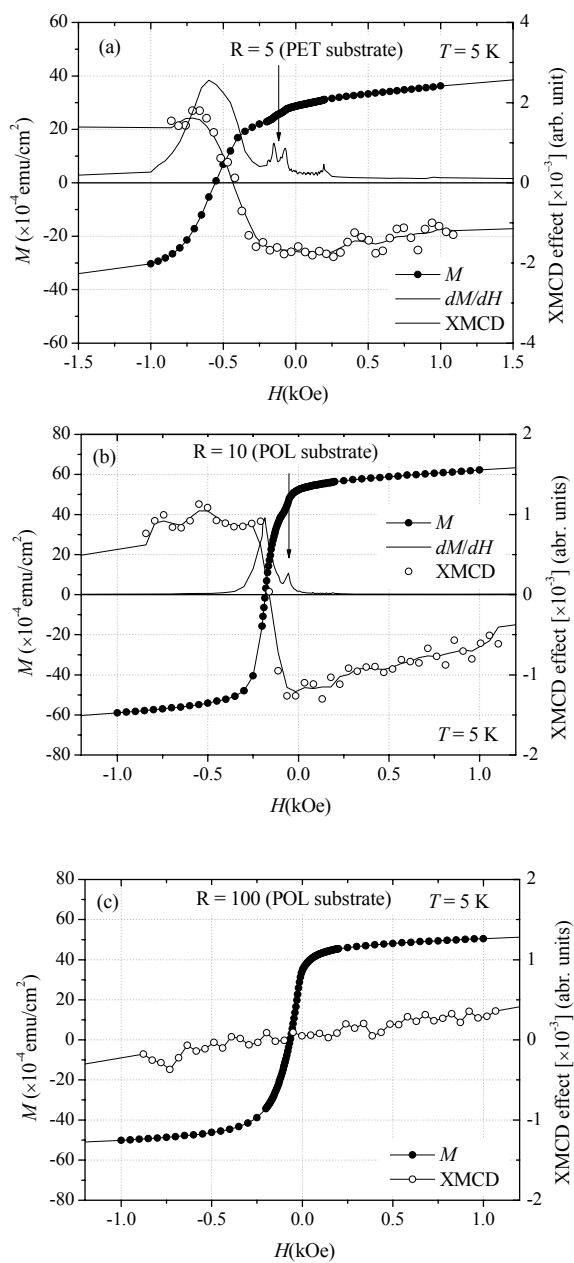


Figure 6.1 XMCD effects in a low field region at 5 K for $R = 5, 10,$ and $100,$ where H is decreased from 50 kOe to -50 kOe.

When the thickness of Al spacer is increased to 100 Å, the Gd-XMCD-effect curve shown in Figure 6.1(c) indicates paramagnetic behavior. It can be deduced that the IMC between Fe and Gd layers disappears when $R = 100$. The strength of IMC, therefore, depends on the thickness of Al spacer. The quantitative discussion on the R dependence of the IMC strength will be made in 6.1.2.

As shown in Figure 6.2, the a.f. IMC still exists even at 280 K in the samples of $R = 5$ and 10, which is clarified by the negative sign of the Gd-XMCD effect. It should be noted that the Gd-XMCD effect of the sample of $R = 10$ is still negative in sign at $H = 1$ kOe, while the Gd-MCP of the sample of $R = 20$ (Figure 5.1(b)) is positive in sign, indicating that the external field 1 kOe is enough to turn the Gd-spin direction to the field direction for $R = 20$, but cannot for $R = 10$. This means that the a. f. IMC in the sample of $R = 20$ is weaker than 1kOe, when it is expressed by an equivalent magnetic field.

6.1.2 Al-thickness Dependence of IMC Strength in Al/Fe/Al/Gd MLFs

On the basis of the $M(H)$ (Figure 5.1) and $M(T)$ curves (Figure 5.2), the effect of Al spacer on the strength of a.f. IMC between Fe and Gd layers can be discussed as follows: The increment of the magnitude of M with increasing the Al thickness implies the more reduction of the negative magnetization of Gd layers than the reduction of the positive magnetization of Fe ones. These reductions are results of the larger increment of a canted angle of Gd spins than Fe spins, which is made possible by the reduction of the strength of the IMC between Fe and Gd.

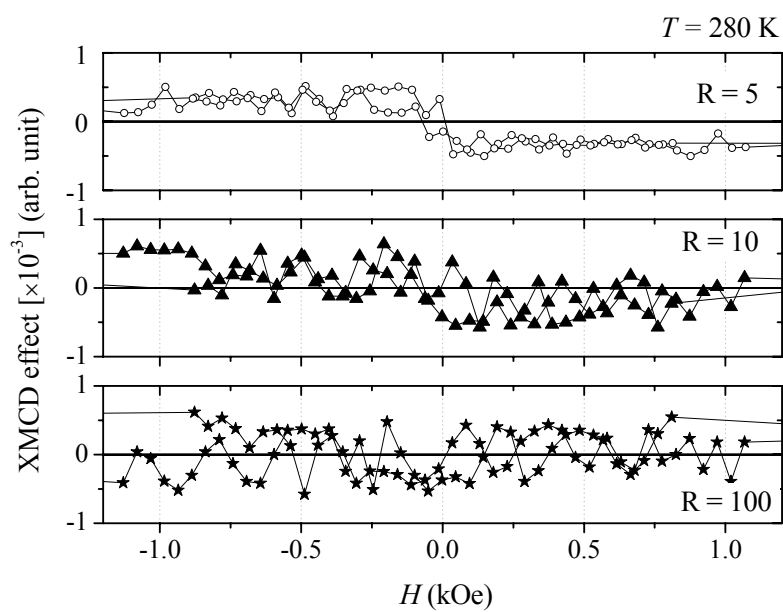


Figure 6.2 Hysteresis of Gd-XMCD effect of the samples of $R = 5$, 10, and 100 at 280 K.

The general description of $M(H)$ curve can be made by the presence of the magnetic anisotropy in Gd layers: the magnetic anisotropy in Fe layers is faint as has been found in Fe/Al MLF. Under external fields less than 500 Oe, the exchange coupling field between Fe and Gd layers is stronger than the external field. Then the Fe and Gd spins couple almost antiparallel, where the Fe magnetization is positive, and are polarized in the direction of the external field without making large canting angles. With the increment of external field, both the spins tend to cant away from the field direction, and the total magnetization gradually increases. When the external field is reversed its direction, the coupled spins remain its magnetization until the gain of the total Zeeman energy is enough to overcome the anisotropy energy of the Gd layer. Since the directions of anisotropy-axis may be distributed in the Gd layers, the coupled spins may gradually rotate to more stable directions, and the sign of the total magnetization changes to negative.

We notice, however, the steep changes of the magnetization at low fields, the kinks, which are clarified in their derivative curves shown in Figure 6.1(b), (c), and (d). We need another mechanism to explain the presence of the kink. If it is allowed to assume the spin-flip of an uppermost Fe layer at the external field corresponding to the kink position, the sudden reduction of the magnetization can be expected. The exchange coupling between the uppermost Fe layer and the beneath Gd layer is weaker than that of an inner Fe layer sandwiched by two neighbor Gd layers.

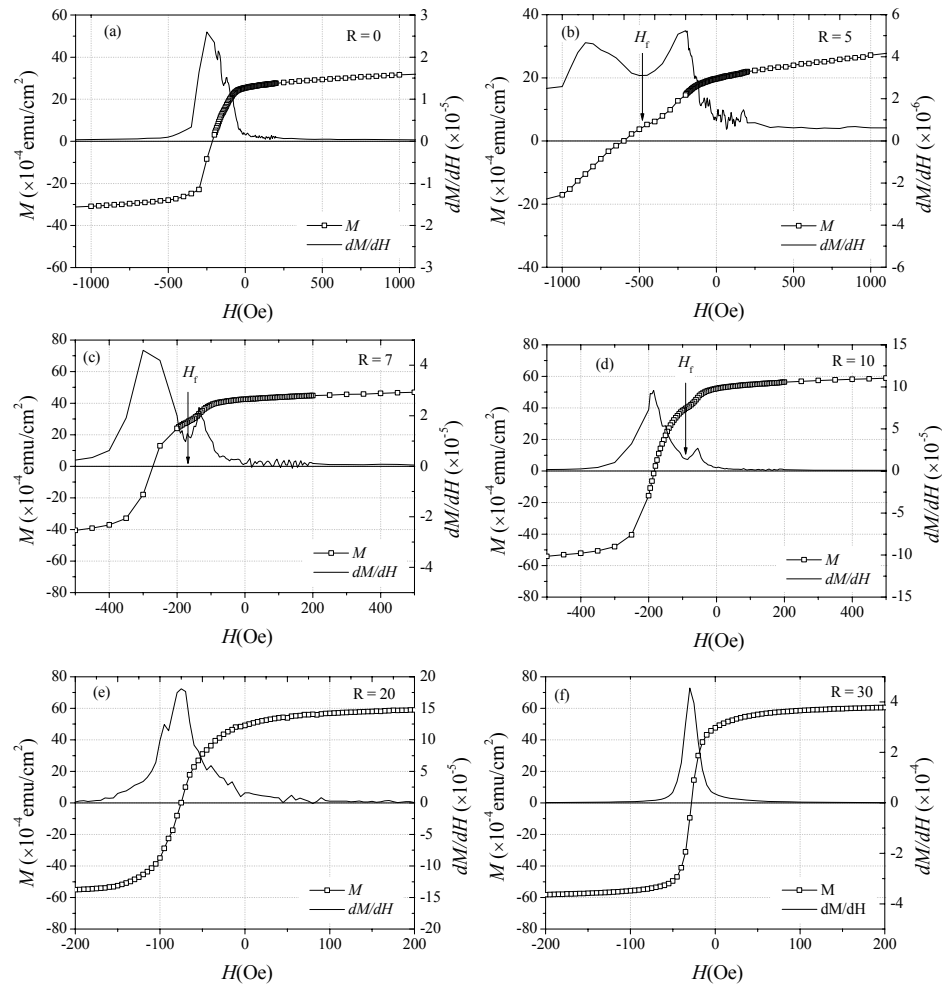


Figure 6.3 $M(H)$ at 5 K and its derivative curves for the samples of $R = 0$ to 30 sputtered on POL film. H_f denotes an external field at the saddle-point of the derivative peaks.

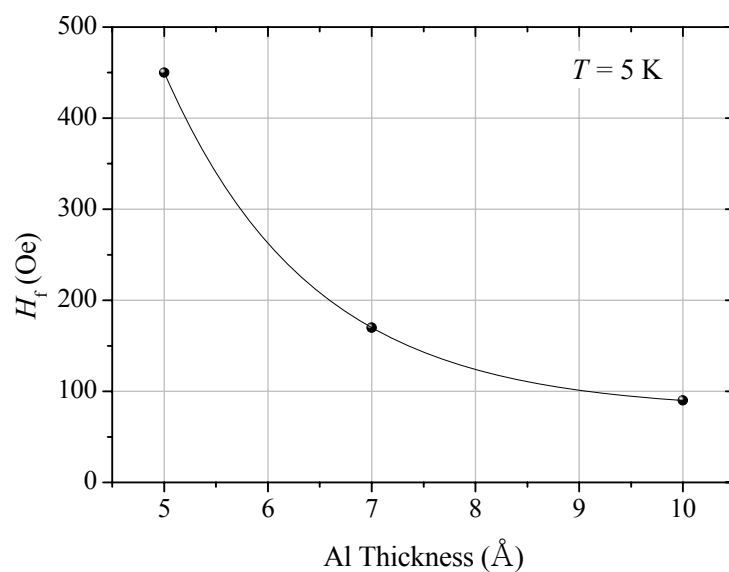


Figure 6.4 The end-point field of the kinks, H_f , versus the thickness of Al spacer at $T = 5$ K. The solid line shows a fit curve using an inverse 1st exponential function.

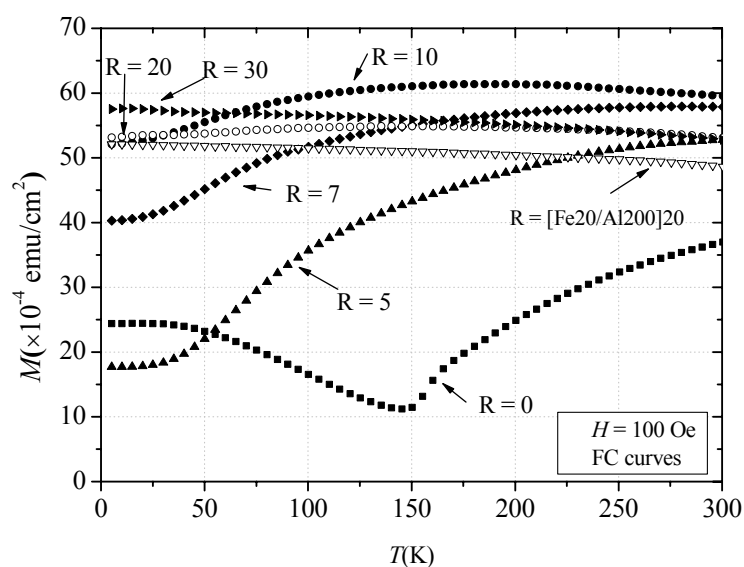


Figure 6.5 $M(T)$ curves of MLFs on POL substrate and Al(200)/Fe MLF measured under $H = 100$ Oe. The Al thickness is denoted by R in units of Å.

The uppermost Fe layer is therefore easier to be influenced by a low external field than the inside Fe layers, and is easily reversed its spin direction before the gradual rotation of the inside spins. Quantitatively the step of the observed kink is comparable to the change of the magnetization due to the spin-flip of a single Fe layer. Actually the kink has a width. This will reflect the inhomogeneous IMC between Fe and Gd layers. In the case of $R = 0$, the energy of IMC between Fe and Gd spins is stronger than the Zeeman energy of the uppermost Fe moment, and no kink was observed. While in the case of $R = 100$, the IMC disappears, and whole Fe and Gd magnetic moments behave independently, resulting no kinks.

The effect of R on the IMC between Fe and Gd can be quantitatively investigated from the change of a magnetic field, H_f , which makes the spin flip of the outermost Fe layer complete. They are pointed by arrows in Figure 6.3(b) to (d). A maximum exchange field between the uppermost Fe layer and the beneath Gd layer is considered to be equivalent to H_f . When the external field exceeds H_f , the inside Fe and Gd moments start to gradually rotate. By plotting H_f as a function of R , we obtain Figure 6.4. The curve indicates that the IMC strength more decreases when the Al thickness is reduced from 5 to 7 Å than from 7 to 10 Å. Empirically, the IMC strength is well expressed by an inverse exponential function of Al thickness.

The reduction of the strength of IMC is in good agreement with the change of $M(T)$ curves, as shown in Figure 6.5. To avoid the influence of a random spin-orientation or spin glass-like behavior in Gd layers, only the FC curves will be discussion here. At low temperatures the increment of the magnitude of M is larger when R is increased from 5 to 7 than when R is increased from 7 to 10. On the contrary, M for $R = 20$ has a lesser magnitude than that for $R = 10$. This is

inconsistent with the above explanation that the IMC decreases with increasing the Al thickness spacer, *i. e.*, the magnitude of M for $R = 20$ should be at least equal to or larger than that for $R=10$. The discrepancy of this feature has been solved by the presence of a paramagnetic component at least in Fe layers in the actual samples of $R \geq 20$. A Mössbauer spectrum of the $R = 20$ MLF at room temperature, not shown in this thesis, has elucidated the presence of non- or para-magnetic component, the amount of which was about 20% of the normal ferromagnetic part. It is, however, not clear whether the present non- or para-magnetic component exists in the interface, because the MLFs of $R = 5$ and 10 do not indicate such an amount of intermixture. The clarification of this phenomenon is out of the scope of this thesis.

For the sample of $R = 0$, the IMC strength can be estimated using $M(H)$ curves of Gd/Al MLF (Figure 6.6) in the following consideration. At 5 K the total magnetization is 26×10^{-4} emu/cm² under 100 Oe, where Fe and Gd spins are considered to be coupled antiparallel and Fe spins are fully polarized along the external field direction. This antiparallel coupling between Fe and Gd spins is indicated by the Gd-XMCD effect of the sample $R = 5$ at 5 K (Figure 6.1(a)), in which Fe layers are fully polarized along the direction of H ; since the IMC of $R = 0$ MLF is stronger and the external field is lower than that for the MCP measurement on $R = 5$ MLF, the Fe-layer magnetic moment at 5 K under 100 Oe can be considered to be fully polarized in the external field direction, that is, the Fe-layer magnetization is -69×10^{-4} emu/cm². Accordingly the magnetization of Gd layer is estimated to be 95×10^{-4} emu/cm². If it is allowed to assume that the same magnetization as the FC magnetization in $R = 0$ MLF at 10 K emerges on a hysteresis curve of Al(5)Gd(40) MLF at 5 K, which is magnetized up to 50 kOe, we can read from the curve of

Al(5)/Gd(40) MLF in Figure 6.6 that the same amount of magnetization is induced when H is 2.1 kOe. We can thus estimate an effective field from negatively polarized Fe layers on Gd layers to be -2.1 kOe. The evaluated magnitude of this effective field is reasonable, because it is larger than the twofold magnitudes of IMC shown in Figure 6.4 as H_f at 5 K, 0.45 kOe, 0.18 kOe and 0.095 kOe for $R = 5, 7$ and 10, respectively.

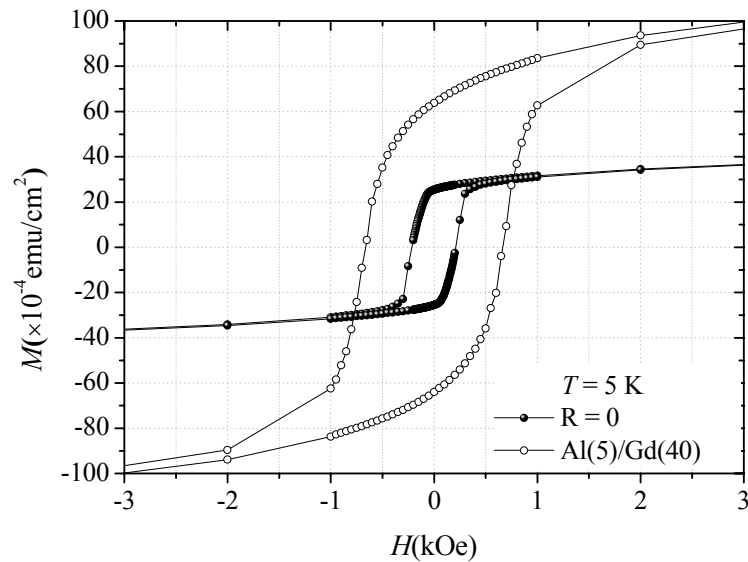


Figure 6.6 Hysteresis loops of magnetization of the samples $R = 0$ (POL substrate) and Al(20 Å)/Gd(40 Å) MLF (PET substrate) at 5 K.

6.1.3 Compensation Temperature

As mentioned in the above sections, the presence of Al spacer between Gd and Fe layers introduces the change of the magnitude of IMC between them, and varieties of the temperature dependence of magnetization can be explained by the

variation of IMC. At the same time the presence of Al spacer reduces the Curie temperature of Gd layer. This effect is observed as a shift of the compensation temperature of the present MLFs.

The $M(T)$ curves of Fe(20)/Gd(40) MLF ($R = 0$) shows a minimum of M around 150 K, as shown in Figure 6.5, *i.e.*, the system has T_{Comp} around 150 K, similar to that reported in Fe(33Å)/Gd(49Å) MLF (Morishita, 1985). Since the magnetization of Fe layers is not much changed by the temperature below 300 K, the presence of T_{Comp} means that, in the low temperature region, the magnetization of Gd layers is larger than that of Fe layers, and it becomes smaller than the Fe magnetization above 150 K due to the thermal effect. When $R = 5$, T_{Comp} approaches 0 K, which means the further reduction of the Gd magnetization due to the lower Curie temperature of Gd layer than that of $R = 0$.

It is worthwhile to explain the limited emergence of T_{Comp} only on the $M(T)$ curves for $R = 0$ and 5 MLFs. The disappearance of T_{Comp} in MLFs having thicker Al layers than 5 Å means the further reduction of the amount of Gd spontaneous magnetization, probably the reduction of a Curie temperature of a Gd layer, when it is sandwiched by thicker Al layers. As a result, the Gd magnetization cannot overcome the Fe magnetization. The reduction of Curie temperature of crystallized ultrathin Gd(0001)/W(110) films are reported when the thickness is less than 28 monolayers (about 90 Å), and a Curie temperature of 220 K was observed in the case of 9 monolayer film (Farle et al., 1993). Since the present 40-Å thick film of Gd is roughly in the similar thickness region, the reduction of Gd-layer magnetization in MLF can be ascribed to the thickness effect.

6.1.4 Coercive field (H_C) of Al/Fe/Al/Gd MLFs

Another phenomenon related with the thickness of Al is the coercive field, H_C . It decreases significantly from about 600 Oe for $R = 5$ to 75 Oe for $R = 20$, as plotted in Figure 6.7. This result is also explained by the change of the IMC strength that is controlled by the Al-layer thickness.

According to Figure 6.7 the Fe/Gd MLF ($R = 0$) has H_C of 213 Oe. This should be ascribed to the magnetic anisotropy in Gd layers, because H_C of Fe/Al MLF has been found to be less than 10 Oe. In the case of $R = 5$, H_C is larger than that of $R = 0$, indicating the increment of the magnetic anisotropy energy of Gd layers due to the contact of Gd layers to Al layers. This has been experimentally confirmed by a large H_C of Gd(40)/Al(5) MLF shown in Figure 5.3(b), which is almost the same to that of $R = 5$. The contact of Gd layer to Al layer seems to induce a certain change of crystal lattice structure of Gd layers.

As shown in Figure 6.7, H_C is reduced with increasing R from 5 to 10. It should be noted that the decrease of H_C in the hysteresis loop of Gd-XMCD effect shown in Figure 6.8. is the same as that of $M(H)$ curves between $R = 5$ and 10 shown in Figure 5.1(c) and (e). This is one of the clear evidences that H_C is induced by the Gd-layer magnetic anisotropy and not by the Fe-layer one. The reduction of H_C above $R = 5$ can be approximated by the following simple relation,

$$H_C = \frac{2K}{M_0}, \quad (3.15)$$

where K is the anisotropy constant of Gd layer, and M_0 is the remanent magnetization. This relation is known as a rough explanation of the relation between

H_C and M_0 of a simple ferromagnet. The inverse proportion of H_C to M_0 means that the larger the positive Zeeman energy which is induced by the reversed magnetic field, the smaller the coercive field. In other words, the large magnetic moment is easy to turn its direction beyond the anisotropy barrier, when the direction of the external field is reversed. Using the experimental values of K and M_0 , the anisotropy constant $K = 12 \text{ MOe}\cdot\text{emu}/\text{cm}^2$ at 5 K is obtained by a three-point least square fitting for $R = 5, 7$ and 10. Using the relation (3.15), the anisotropy constant for the $R = 0$ MLF is evaluated to be $4.5 \text{ MOe}\cdot\text{emu}/\text{cm}^2$.

The IMC becomes weak when R exceeds 10, and Fe and Gd magnetic moments behave independently. The hysteresis curve thus approaches to a simple sum of two magnetizations. In the present cases, the Gd magnetization is reduced, and the resultant H_C is almost determined by that of Fe layer, and becomes small as shown in Figure 6.7.

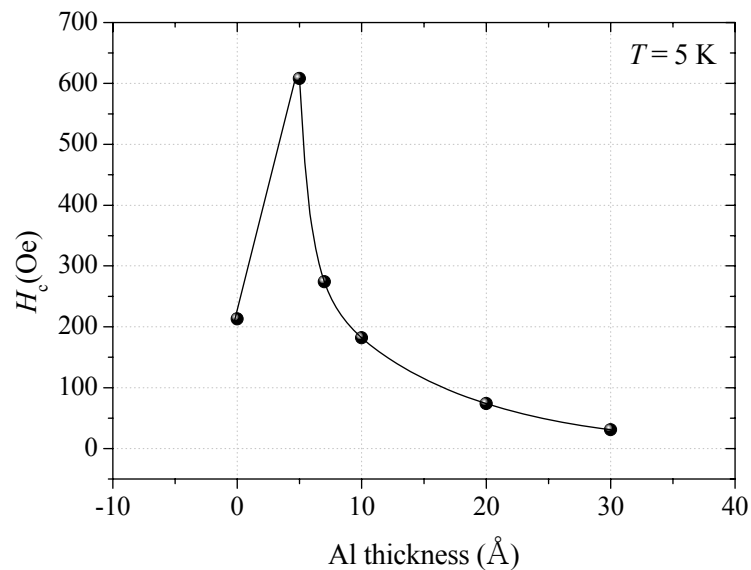


Figure 6.7 Coercive field (H_C) versus Al thickness. The solid line is just a simple eye guide.

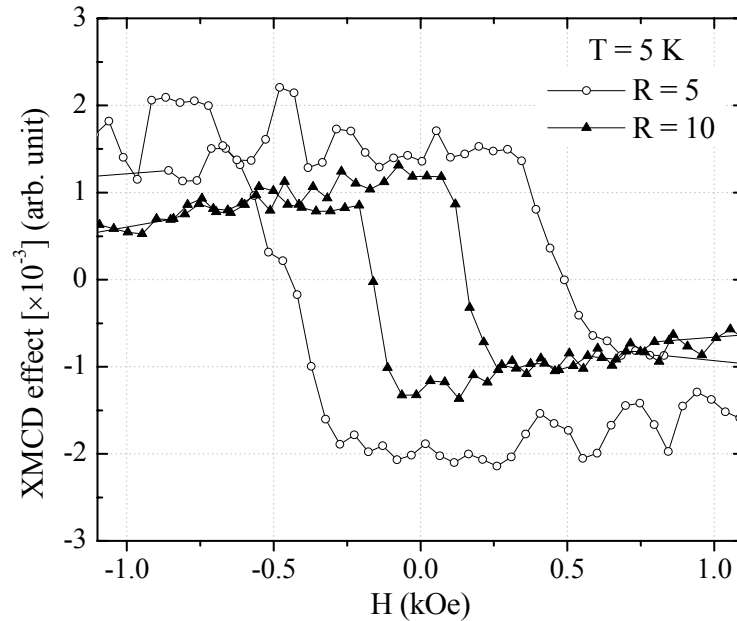


Figure 6.8 Hysteresis loops of Gd-XMCD at 5 K for the samples of $R = 5$ and 10 deposited on POL film.

6.1.5 Spin Moments Investigated by MCPs

The numerical results of the line-shape analysis on MCPs of the samples of $R = 5$ and 20 (shown in Figure 5.5 and Figure 5.6, respectively) are tabulated in Table 6.1.

The line-shape analysis on MCP of $R = 5$ at 10K and 1 kOe clarifies that IMC between Fe and Gd layers is antiferromagnetic, and a 25-kOe external field is enough to turn the Gd-spin magnetization into a positive value. The reduction of magnetization of $R = 5$ MLF toward low temperatures in Figure 5.4 is thus explained by the negative spin polarization of Gd layers, not by the reduction of Fe-layer magnetization. This explanation is confirmed by the gradual increase of the FC $M(T)$

curve of an additional Al(200)/Fe(20) MLF by lowering the temperature, in which IMC between Fe layers can be weaker than R = 5 MLF.

Table 6.1 Fe-spin, Gd-spin and unknown part magnetizations for R = 5 and 20 at the specified H and T . The samples were deposited on PET film.

Magnetization	R = 5		R = 20		
	(10^{-4}emu/cm^2)		(10^{-4}emu/cm^2)		
H	1 kOe		25 kOe	1 kOe	
T	10 K	300 K	10 K	10 K	300 K
total (SQUID)	31	57	85	72	64
Fe layer	68(7)	61(6)	52(7)	58(4)	55(2)
Gd layer	-38(8)	-6(5)	23(5)	12(4)	6(2)
unknown part	2(2)	2(2)	10(2)	2(1)	3(1)

If we try to quantitatively compare the magnetization of R = 5 at 1 kOe with Al(5)/Fe(20) in Figure 5.4, the $M(T)$ of the latter should be multiplied by 0.9 to equalize the thickness of Fe layer to that of R = 5 MLF. After that we find that $M(T)$ of R = 5 MLF at 300K is smaller than that of Al(5)/Fe(20) MLF. This is consistent with the presence of negative spin polarization of Gd layer determined by the MCP analysis. As shown in Figure 5.3(a), the $M(H)$ of R = 5 MLF at 5K exceeds the magnetization of Al(5)/Fe(20) at 25 kOe. This is also consistent with the results of MCP analysis, although it is at 10 K.

The MCP analysis on $R = 20$ shows the positive spin polarization of Gd spins at 10 and 300K. It is reasonable to conclude that the increment of Al-layer thickness from 5 to 20 Å much weakens a. f. IMC between Fe and Gd layers, and Gd spins cannot keep its negative polarization under a 1-kOe field. This positive spin polarization of Gd layers explains the hump on the $M(T)$ curve of $R = 20$ around 25 K in Figure 5.4, that is, Gd spins are in ferromagnetic ordered state below 50 K, and are forced to be positively polarized by the external 1-kOe field.

According to the MCP analysis on $R = 5$ MLF at 10K and 1 kOe, the Fe-layer magnetization, 68 emu/cm^2 , is comparable to that of α -Fe of 20 Å in thickness. This means that the Fe spins are almost parallel to the external field. Consequently, Gd spins, which are coupled to Fe spins by the anti-ferromagnetic IMC, are antiparallel to the external field. This is consistent with the indication from the XMCD effect in Figure 6.1(a).

When the external field is increased up to 25 kOe at 10 K, both Fe and Gd spins positively polarized, and the elucidated magnitudes of them by the MCP analysis are smaller than those at 1 kOe. This feature means that both the spins cant from the direction of the external field. At 300 K, the Fe layer keeps high magnetization. On the other hand, the Gd layer shows a little amount of negative magnetization of -6 emu/cm^2 , indicating the significant reduction of Gd spontaneous magnetization in the MLF of $R = 5$ at 300 K.

The MCP analysis suggests the presence of the unknown component, which is tentatively expressed by a Gaussian profile at a low momentum region. Contrary to relatively small their contributions in the whole cases, the unknown component shows a noticeable amount in the case of $R = 5$ at a low (10 K) and a high

magnetic field (25 kOe). Although its origin is not clear, this seems suggest the presence of a few paramagnetic components in MLF.

6.1.6 Al(5)/Fe(20) and Al(5)/Gd(40) MLFs

The attrition ratio of FC magnetization of Al(5)/Fe(20) MLF (see Figure 5.4) between 79.8×10^{-4} emu/cm² at 5 K and 76.5×10^{-4} emu/cm² at 300 K is larger than that of α -Fe. A Curie temperature of Fe layer in this MLF seems to be reduced, due to the weak interlayer exchange coupling between Fe layers. In fact, an additionally prepared Al(200)/Fe(20) MLF (see its $M(T)$ curve in Figure 6.4), in which the interlayer exchange interaction between Fe layers is more weakened, shows a larger ratio than Al(5)/Fe(20) MLF. These are consistent with a report on Curie-temperature reduction of a thin Fe layer (Sudhakar Rao et al., 2002).

$M(T)$ of Al(5)/Gd(40) MLF in Figure 5.4 shows that the magnitude of the magnetization of the MLF is almost zero above 250 K. This verifies that the Curie temperature of the Al(5)/Gd(40) MLF is lower than that of bulk Gd.

6.1.7 The Difference Between FC and ZFC Magnetization Curves

According to Figure 5.2(a), there is a distinct difference between ZFC- and FC-magnetization curves under $H = 100$ Oe in the case of $R = 5$, but not $R = 0$. This difference decreases when R is increased and almost disappears for $R = 30$ and 100. Under $H = 1$ kOe (Figure 5.2(b)), however, no difference were observed between ZFC- and FC-curves for all the samples. The difference between ZFC- and FC-magnetization curves can be taken place by the presence of the random anisotropic magnetic anisotropy in Gd layers. When Al-thickness is increased ($R > 5$), not only the IMC between Fe and Gd layers is weakened but a Curie temperature of the Gd layer is decreased. The Fe layers, which become a major part of magnetization,

are then easier to be magnetized by the external field of 100 Oe, and the difference between ZFC- and FC- magnetization curves of the samples with $R > 5$ is therefore reduced.

6.1.8 Fe- and Gd- Spin Orientation in Al/Fe/Al/Gd MLFs

The orientation of spin moments in the Gd layer (M_{Gd}) and that in the Fe layer (M_{Fe}) can be represented by combining the results of the hysteresis loop of Gd-XMCD effect and the numerical analysis of MCPs summarized in Table 6. Here we assume that Gd or Fe spins are ferromagnetically coupled in each layer. The variation in M_{Gd} with increasing H can be demonstrated by Gd-XMCD effect. In general, either kind of states can be induced in a low field region, one is the so called Gd-aligned state, where M_{Gd} is fully aligned parallel to the direction of H and antiparallel to M_{Fe} , and the other is the Fe-aligned state, where M_{Fe} and M_{Gd} are substituted in the Gd-aligned state, as shown in Figure 6.9 (a) and (b).

At 5 K without H , the spin orientation of Fe(20 Å)/Gd(40 Å) MLF is in the Gd-aligned state, while all of the present Al/Fe/Al/Gd MLFs are in the Fe-aligned state. When H is increased, Gd spins in Al/Fe/Al/Gd MLFs tend to rotate to decrease their Zeeman energy, associating with the increment of the a.f. IMC energy and the balancing rotation of Fe spins. The directions of M_{Gd} and M_{Fe} are then fixed in balance with them, and make angles to H , as shown in Figure 6.9(c).

In the case of $R = 5$, the Gd-XMCD effect intersects the abscissa at $H_1 = 8.5$ kOe, as shown in Figure 6.10(a), indicating that the direction of M_{Gd} is perpendicular to the H direction (see Figure 6.9(d)). This means that the total magnetic moment (M) is equal to the projection of M_{Fe} onto the field direction. Here

M is read from the $M(H)$ curve in Figure 6.10(a) to be 63×10^{-4} emu/cm². Since the magnitude of M_{Fe} is 69×10^{-4} emu/cm² (equal to that of alpha-Fe of 20 Å in thickness), which is consistent with the numerical analysis of MCPs (Table 6.1), the angle α between the directions of M_{Fe} and H is obtained as 24° . Similar calculation for $R = 10$ gives $\alpha = 10^\circ$ with $H_1 = 2.1$ kOe and $M = 68 \times 10^{-4}$ emu/cm² (see Figure 6.10(b)). The reduction of α with increasing R is one of the results of the attenuation of a. f. IMC between Fe and Gd layers, i.e., the more the a. f. IMC is reduced, the more the small angle α is effective to lower the Zeeman energy of Fe spins. Unfortunately, the values of H_1 at 280 K cannot be read from the hysteresis of the Gd-XMCD effect because of an insufficient signal to noise ratio.

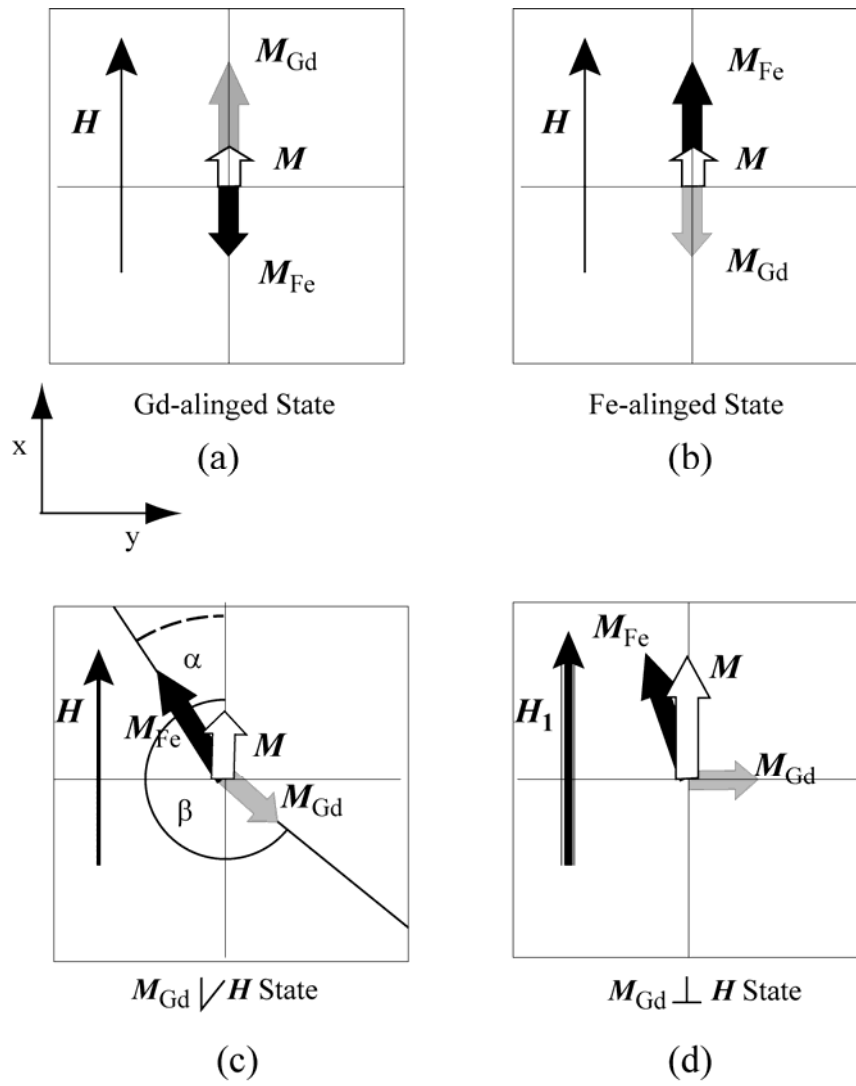


Figure 6.9 Fe-spin (M_{Fe}), Gd-spin (M_{Gd}), and total magnetic moments (M) in Al/Fe/Al/Gd MLFs.

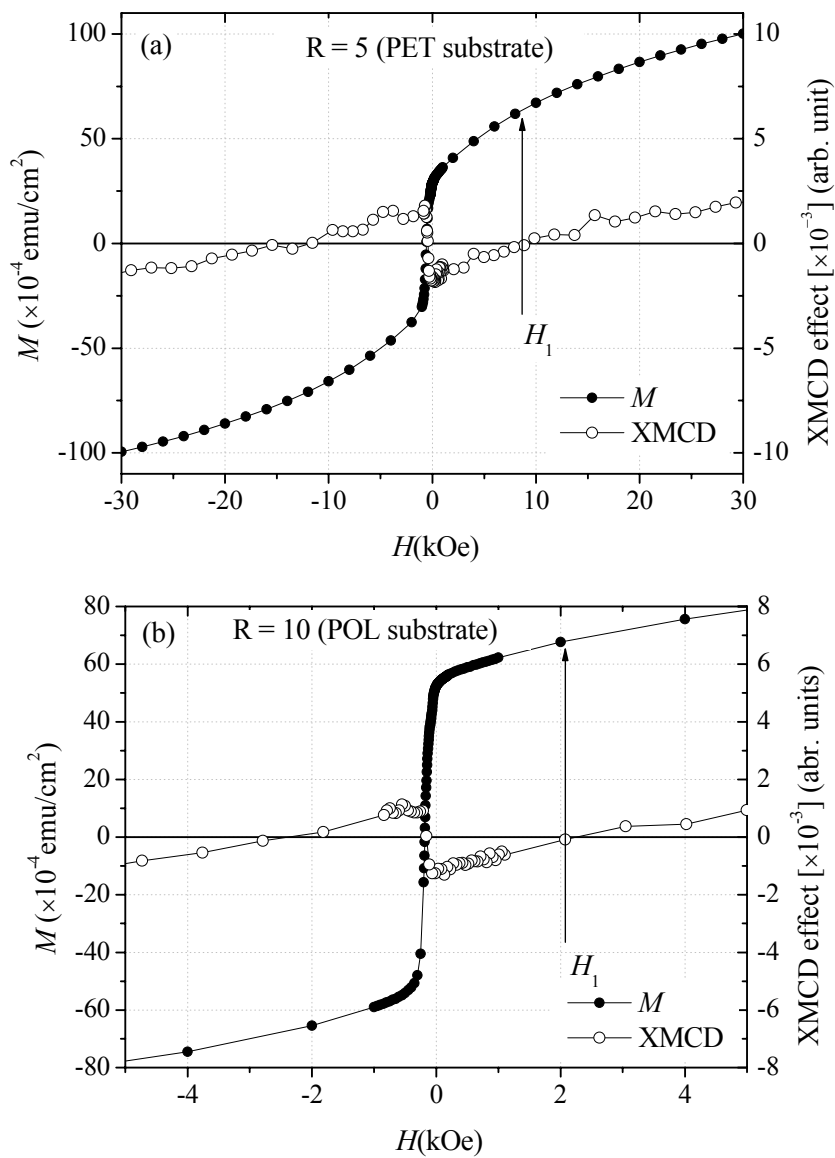


Figure 6.10 XMCD effect and total magnetization of the sample R = 5 and 10 measured at 5 K

6.2 Conclusion

The interlayer magnetic coupling (IMC) was experimentally investigated in multilayer films (MLFs) of $[\text{Al}(R\text{\AA})/\text{Gd}(40\text{\AA})/\text{Al}(R\text{\AA})/\text{Fe}(20\text{\AA})] \times N/\text{Al}(R\text{\AA})$, where $R = 0, 5, 7, 10, 20, 30$, and 100 as nominal thicknesses ($N = 100$ for $R = 5$ and 20 on polyethylene-film substrates, and $N = 20$ for $R = 0, 5, 7, 10, 20, 30$, and 100 on polyimide-film substrates), together with $[\text{Al}(5\text{\AA})/\text{Gd}(40\text{\AA})] \times 100$ and $[\text{Al}(5\text{\AA})/\text{Fe}(20\text{\AA})] \times 100$. Magnetization curves and temperature dependence of them were measured.

In addition to the bulk magnetization measurements, the synchrotron-radiation based methods, X-ray magnetic Compton-profile (MCP) method and X-ray magnetic circular dichroism (XMCD) method, have been successfully applied as for element selective techniques. MCP measurements were carried out for the samples of $R = 5$ and 20 . The results have led to the following conclusions. Magnetic hysteresis loops of XMCD effect were measured on the samples of $R = 0, 5, 10$, and 100 at the Gd L_3 -edge.

The magnetic field dependence of Fe- and Gd-spin orientations has been successfully investigated by this element selective method.

The whole experimental results, $M(H)$, $M(T)$, cohesive fields of the Gd-XMCD curves, canted angles of Fe and Gd magnetic moments, are reasonably explained by the attenuation of the IMC by the Al spacer. The following results are also mentioned:

(1) The IMC in Al/Fe/Al/Gd MLFs is antiferromagnetic coupling, the same as that in Fe(20 Å)/Gd(40 Å) MLF.

(2) The Al spacer is effective to control the magnitude of IMC between Fe(20Å) and Gd(40Å). They are evaluated as an effective magnetic field from Fe layers to be 2.1, 0.9, 0.36 and 0.19 kOe for $R = 0, 5, 7,$ and 10, respectively. Empirically, the magnitude of IMC is proportional to an inversed exponential function.

(3) The IMC disappears when the Al spacer is above 20 Å in thickness. Even at 5 K the sample of $R = 100$ behaves paramagnetic.

(4) The magnetization of Gd layers in Al/Gd/Al/Fe MLF is reinforced by IMC with neighboring Fe layers through Al spacer of 5 and 10 Å in thickness, but isolated from Fe-layer magnetization in the case of 20 Å.

(5) The observed attenuation of the magnetization of Fe(20Å)/Al(5Å) and Gd(40Å)/Al(5Å) MLF with increasing the temperature is consistent with the reported reduction of the Curie temperature due to the thickness effect.

(6) Notable change of coercive force is found to be inversely proportional to the remanence field, similar to the cases of common ferromagnetic material. The anisotropy constants are evaluated to be 4.5 MOe·emu/cm² for $R = 0,$ and approximately 12 MOe·emu/cm² for $R = 5, 7,$ and 10.

The present study shows that a combination of magnetization and MCP measurements is effective to determine individual spin moments in constituent magnetic layers of MLFs and spin coupling states between them. It also suggests that useful magnetic properties can be artificially obtained by means of magnetic MLF systems composed of [A/B/C] structure, with antiferromagnetically coupled A and C layers separated by a nonmagnetic B layer. Although only the thickness of B layer was altered in the present study, desirable magnetic properties can be created by selecting suitable combination of A, B and C layers.

Further investigation is required to clarify the origin of the reduction of Curie temperature and magnetically hard property of Gd layer prepared by a magnetron sputtering method.

REFERENCES

REFERENCES

- Allenspach, R., and Weber, W. (1998). Oscillatory magnetic properties. **IBM Journal of Research and Development** 42: 7-23
- Baibich, M. N., et al. (1988 November). Giant magnetoresistance of (001)Fe/(001)Cr magnetic superlattices. **Physical Review Letters** 61:2472-2475.
- Binasch, G., Grunberg, P., Saurenbach, F., and Zinn, W. Enhanced magnetoresistance in layered magnetic structures with antiferromagnetic interlayer exchange. **Physical Review B** 39:4828-4830
- Bruno, P. (1995). Theory of interlayer magnetic coupling. **Physical Review B** 52: 411-439.
- Bruno, P. (1999). Theory of interlayer exchange interactions in magnetic multilayers. **Journal of Physics Condensed Matter and an Institute of Physics Journal** 11: 9403-9419.
- Bruno, P. and Chappert, C. (1991). Oscillatory coupling between ferromagnetic layers separated by a nonmagnetic metal spacer. **Physical Review Letters** 67: 1602-1605.
- Bruno, P. and Chappert, C. (1992). Ruderman-Kittel theory of oscillatory interlayer exchange coupling. **Physical Review B** 46: 261-270.
- Camley, R. E. (1987). Surface spin reorientation in thin Gd films on Fe in an applied magnetic field. **Physical Review B** 35: 3608-3611.
- Camley, R. E. (1989). Properties of magnetic superlattices with antiferromagnetic interfacial coupling: magnetization, susceptibility, and compensation points.

- Physical Review B** 39: 12316-12319.
- Camley, R. E. and Stamps, R. L. (1993). Magnetic multilayers: spin configurations, excitations and giant magnetoresistance. **Journal of Physics Condensed Matter and an Institute of Physics Journal** 5: 3727-3786.
- Camley, R. E. and Tilley, D. R. (1988). Phase transitions in magnetic superlattices. **Physical Review B** 37: 3413-3421.
- Carbucicchio, M. et al. (2000). Size-dependent magnetic properties in Fe/Al multilayers. **Journal of Magnetism and Magnetic Materials** 215-216: 563-565.
- Chen, C. T., Sette, F., Ma, Y., and Modesti, S. (1990). Soft-x-ray magnetic circular dichroism at the $L_{2,3}$ edges of nickel. **Physical Review B** 42: 7262-7265.65
- Coehoorn, R. (1991). Period of oscillatory exchange interactions in Co/Cu and Fe/Cu multilayer systems. **Physical Review B** 44: 9331-9337.
- Cooper, J., Mijnen, P. E., Shiotani, N., Sakai, N., and Bansil, A. **X-ray Compton scattering**. New York: Oxford university
- Deaven, D. M., Rokhsar, D. S., and Johnson, M. (1991). Simple theory of exchange coupling in transition-metal magnetic multilayers. **Physical Review B** 44: 5977-5980.
- Deb, A., Hiraoka, N., Itou, M., Sakurai, Y., and Onodera, M., and Sakai, N. (2001). Spin-dependent electron momentum density in the Ni_2MnSn Heusler alloy. **Physical Review B** 63: 205115-1-10
- Demokritov, S. O. (1998). Biquadratic interlayer coupling in layered magnetic systems. **Journal of Physics D: Applied Physics** 31: 925-941.
- Demokritov, S., Wolf, J. A., and Grunberg, P. A. (1991). Evidence for oscillations in

the interlayer exchange coupling of Fe films across Cr films from spin waves and M(H) curves. **Europhysics Letters** 15: 881

du Tremolet de Lacheisserie, E., Gignoux, D., and Schlenker. (2002). **Magnetism II-materials & applications**. Norwell, Massachusetts, USA: Kluwer Academic Publisher.

Dufour, C., Cherifi, K., Marchal, G., and Mangin, Ph. (1993). Polarized neutron scattering from Gd/Fe multilayers: Twist phase and spin-flop scattering. **Physical Review B** 47: 14572-14575.

Edwards, D. M., Mathon, J., Muniz, R. B., and Phan, M. S. (1991). Oscillations of the exchange in magnetic multilayers as an analog of de Haas-van Alphen effect. **Physical Review Letters** 67: 493-496.

Erickson, R. P., Hathaway, K. B., and Cullen, J. R. (1993). Mechanism for non-Heisenberg-exchange coupling between ferromagnetic layers. **Physical Review B** 47: 2626-2635.

Farrow, R. F. C., Lee, C. H., and Parkin, S. S. P., (1990). Magnetic multilayer structure. **IBM Journal of Research and Development** 34: 903-915.

Fert, A., Grünberg, P., Berthélémy, A., Petroof, F., and Zinn, W. (1995). Layered magnetic structures: interlayer exchange coupling and giant magnetoresistance. **Journal of Magnetism and Magnetic Materials** 140-144: 1-8.

Fonda, E. and Traverse A. (2004). Evidence of intermixing at the Fe/Al interface in multilayers produced by metal vapor deposition at room temperature. **Journal of Magnetism and Magnetic Materials** 268: 292-297.

Fub, A., Demokritov, S., Grunberg, P., and Zinn, W. (1992). Short- and long period oscillations in the exchange coupling of Fe across epitaxially grown Al- and

- Au- interlayers. **Journal of Magnetism and Magnetic Materials** 103: L221-L227.
- Gradmann, U., and Muller, J. (1968). Flat ferromagnetic, epitaxial 48Ni/52Fe(111) films of Fe atomic layers. **Physica Status Solidi B Basic Research** 27: 313.
- Grunberg, P., Demokritov, S., Fuss, A., Vohl, M., and Wolf, J. A. Layered magnetic structures: Antiferromagnetic-type interlayer coupling and magnetoresistance due to antiparallel alignment. **Journal of Applied Physics** 69: 4789-4791.
- Grunberg, P., Schreiber, R., Pang, Y., Brodsky, M. B., and Sowers, H. (1986). Layered magnetic structures: Evidence for antiferromagnetic coupling of Fe layers across Cr interlayers. **Physical Review B** 57: 2442-2445.
- Gutierrez, C. J., Krebs, J. J., Filipkowski, M. E., and Prinz, G. A. (1992). Strong temperature dependence of the 90° coupling in Fe/Al/Fe(001) magnetic trilayers. **Journal of Magnetism and Magnetic Materials** 116: L305-L306.
- Haeiwa, T., Negoro, H., and Matsumoto, M. (1991). Soft-magnetic properties of compositionally modulated Fe/Al films. **Journal of Applied Physics** 69: 5346-5348.
- Herman, F., Sticht, J., and Schilfgaarde, M. V. (1991). Spin-polarized band structure of magnetically coupled multilayers. **Journal of Applied Physics** 69: 4783-4785.
- Himpsel, F. J., Jung, T. A., and Seider, P. F. (1998). Electronic states in magnetic nanostructures. **IBM Journal of Research and Development** 42: 33-41.
- Hosoito, N., Hashizume, H., and Ishimatsu, N. (2002). Magnetization curves of an Fe/Gd multilayer film calculated from Gd magnetization depth profiles determined by resonant x-ray magnetic scattering. **Journal of Physics:**

Condensation of Matter 14: 5289-5301.

Huai, Y. and Cochrane, R. W. (1992, September). Oscillatory magnetic coupling and magnetoresistance in Co/Re superlattices. **Journal of Applied Physics** 72(6): 2523-2525.

Ishimatsu, N. et al. (1999). Magnetic structure of Fe/Gd multilayers determined by resonant x-ray magnetic scattering. **Physical Review B** 60: 9596-9606.

Jones, B. A. (1998). Theory of exchange coupling in magnetic multilayers. **IBM Journal of Research and Development** 42: 25-31.

Kakutani, Y., Kubo, Y., Koizumi, A., Sakai, N., Ahuja, B. L., and Sharma, B. K. (2003). Magnetic Compton profiles of Fcc-Ni, Fcc-Fe₅₀Ni₅₀ and Hcp-Co. **Journal of the Physical Society of Japan** 72: 599-606.

Koizumi, A., Takagaki, M., Suzuki, M., Kawamura, N., and Sakai, N. (2000). Anomalous magnetic hysteresis of Gd and Fe moments in a Gd/Fe multilayer measured by hard x-ray magnetic circular dichroism. **Physical Review B** 61: 14909-14912.

Krompiewski, S., Krey, U., and Pirnay, J. (1993). Exchange coupling and magnetization in bcc-(001) Fe/Cu multilayers by a tight-binding LMTO-ASA method. **Journal of Magnetism and Magnetic Materials** 121: 238-241.

Lee, S. J., Abdul-Razzaq, W. (2000). The magnetic transition temperature due to the interlayer-coupling in magnetic/non-magnetic multilayer films. **Journal of the Physical Society of Japan** 69: 3040-3044.

LePage, J. G. and Camley, R. E. (1990). Surface phase transitions and spin-wave in semi-infinite magnetic superlattices with antiferromagnetic interfacial coupling. **Physical Review Letters** 65: 1152-1155.

- Majkrzak, et al. (1986). Observation of a magnetic antiphase domain structure with long-range order in a synthetic Gd-Y superlattice. **Physical Review Letters** 56:2700-2703.
- Majkrzak, et al. (1986). Observation of a magnetic antiphase domain structure with long-range order in a synthetic Gd-Y superlattice. **Physical Review Letters** 56:2700-2703.
- Mathon, J., Villeret, M., and Edwards, D. M. (1992). Exchange coupling in magnetic multilayers: effect of partial confinement of carriers. **Journal of Physics: Condensation of Matter** 4: 9873-9892.
- Mathon, J., Villeret, M., Muniz, R. B., d' Albuquerque e Castro, J., and Edwards, D. M. (1995). Quantum well theory of the exchange coupling in Co/Cu/Co(001). **Physical Review Letters** 74: 3696-3699.
- Mathon, J., Villeret, M., Umerski, A., Muniz, R. B., d' Albuquerque e Castro, J. (1997). Quantum-well theory of the exchange coupling in magnetic multilayer with application to Co/Cu/Co(001). **Physical Review B** 56:11797-11809.
- Meiklejohn, W. H. and Bean, C. P. (1957). New magnetic anisotropy. **Physical Review B: Condensed Matter** 105: 904.
- Meiklejohn, W. H. and Bean, C. P. (1956). New magnetic anisotropy. **Physical Review B: Condensed Matter** 102: 1413.
- Nagakubo, M., Yamamoto, T., and Naoe, M. (1988). Magnetic properties and structure of Fe/Al multilayered films prepared by ion-sputtering. **Journal of Applied Physics** 64: 5751-5753.
- Narnas, J. (1992). Coupling between two ferromagnetic films through a non-magnetic metallic layer. **Journal of Magnetism and Magnetic Materials** 111: L215-

L219.

Ortega, J. E. and Himpsel, F. J. (1992). Quantum well states as mediators of magnetic coupling in spurlattices. **Physical Review Letters** 69: 844-847.

Ortega, J. E., Himpsel, F. J., Mankey, G. J., and Willis, R. F. (1993). Quantum-well states and magnetic coupling between ferromagnets through a noble-metal layer. **Physical Review B** 47: 1540-1552.

Ounadjela, K., Muller, D., Dinia, A., Arbaoui, A., Panissod, P., and Suran, G. (1992, April) Perpendicular anisotropy and antiferromagnetic coupling in Co/Ru strained spuerlattices. **Physical Review B** 45: 7768-7771.

Parkin, S. S. P. (1991 December). Systemmatic variation of the strength and oscillation period of indirect magnetic exchange coupling through the 3d, 4d, and 5d transition metals. **Physical Review Letters** 67: 3598-3601.

Parkin, S. S. P., More, N., and Roche, K. P. (1990 May). Oscillations in exchange coupling and magnetoresistance in metallic spurlattice structrues: Co/Ru, Co/Cr, and Fe/Cr. **Physical Review Letters** 64: 2304-2308

Petroff, F., et al. (1991). Oscilatory interlayer exchange and magnetoresistance in Fe/Cu multilayers. **Physical Review B** 44 : 5355-5357

Ruderman, M. A., Kittel, C. Indirect exchange coupling of nuclear magnetic moments by conduction electrons. **Physical Review** 96: 99-102.

Ruhrig, M. et al. (1991). Domain observations on Fe-Cr-Fe layered structures: evidence for a biquadratic coupling effect. **Physica Status Solidi A Applied Research** 125: 635.

Sajieddine, M. et al. (1994). Experimental and theoretical spin configurations in Fe/Gd multilayers. **Physical Review B** 49: 8815-8820.

- Sakai, N. (1996). Magnetic Compton scattering and measurements of momentum distribution of magnetic electrons. **Journal of Applied Crystallography** 29: 81-99.
- Sakai, N., Koizumi, A., Miyamoto, N., and Tanaka, Y. Momentum-space magnetism Studied by magnetic Compton scattering. **AIP Conference Proceedings** 389: 399-411.
- Sakurai, Y. et al. (1995). High-resolution Compton scattering study of Li: asphericity of the Fermi surface and electron correlation effects. **Physical Review Letters** 74: 2252-2255.
- Salamon, M. B., Shantanu Sinha, Rhyne, J. J., Cunningham, J. E., Borchers, J., and Flynn, C. P., (1986, January)., Long-Rang incommensurate magnetic order in a Dy-Y multilayer. **Physical Review Letters** 56: 259-262.
- Schilfgaarde, M. van., Herman, F., Parkin, S. P. P., and Kudrnovsky, J. (1995). Theory of oscillatory exchange coupling in Fe/(V, Cr) and Fe/(Cr,Mn). **Physical Review Letters** 74: 4063-4067.
- Slonczewski, J. C. (1995). Overview of interlayer exchange theory. **Journal of Magnetism and Magnetic Materials** 150: 13-24.
- Stiles, M. D. (1999). Interlayer exchange coupling. **Journal of Magnetism and Magnetic Materials** 200: 322-337.
- Takagaki, M., Koizumi, A., Kawamura, N., Suzuki, M., and Sakai, N. (2003). Element-specified observation of surface-influenced magnetization process in Gd/Fe multilayer. **Journal of the Physical Society of Japan** 72: 245-248.
- Takanashi, K., Kamiguchi, Y., Fujimori, H., and Motokawa, M. (1992). Magnetization and magnetoresistance of Fe/Gd ferrimagnetic multilayer films. **Journal of**

the Physical Society of Japan 61: 3721-3731.

Unguris, J., Celotta, R. J., and Pierce, D. T. (1993). Oscillatory magnetic coupling in Fe/Ag/Fe(100) sandwich structures. **Journal of Magnetism and Magnetic Materials** 127: 205-213.

Unguris, J., Celotta, R. J., and Pierce, D. T. (1994). Oscillatory exchange coupling in Fe/Au/Fe(100). **Journal of Applied Physics** 75: 6437-6349

Vaezzadeh, M., George, B., and Marchal, G. (1994). Surface-induced transitions in Fe/Gd multilayers studied by magnetoresistance measurements. **Physical Review B** 50: 6113-6118.

Wang, J. F., Cui, F. Z., Wang, Y., and Fan, Yu-dian. (1990). Structure and magnetic properties of Fe/Al multilayers synthesized by planar magnetron sputtering. **Journal of Magnetism and Magnetic Materials** 89: 153-158.

Wu, Z., Suresh Babu, V., Seehra, M. S., and Abdul-Razzaq. (1992). Two magnetic-ordering temperatures in Fe/Al multilayered films. **Physical Review B** 45: 2285-2289.

Yafet, Y. (1987). Ruderman-Kittel-Kasuya-Yoshida range function of a one-dimensional free-electron gas. **Physical Review B** 36: 3948-3949.

APPENDICES

APPENDIX A

ELECTROMAGNETIC RADIATION

Light is electromagnetic radiation. Theoretically, it is given by solving the electromagnetic equations. In this section the solutions of the electromagnetic equations are presented. Light is quantized. Quantized light is particles being referred to photons. Maxwell's equations are expressed by

$$\mathit{div}\mathbf{D} = 4\pi\rho \quad (\text{Coulomb's law}) \quad (\text{A.1})$$

$$\mathit{div}\mathbf{B} = 0 \quad (\text{Absence of magnetic monopole}) \quad (\text{A.2})$$

$$\mathit{rot}\mathbf{E} = -\frac{1}{c} \frac{\partial \mathbf{B}}{\partial t} \quad (\text{Electromagnetic induction law}) \quad (\text{A.3})$$

$$\mathit{rot}\mathbf{H} = \frac{4\pi\mathbf{j}}{c} + \frac{1}{c} \frac{\partial \mathbf{D}}{\partial t} \quad (\text{Ampere's law}) \quad (\text{A.4})$$

Here, \mathbf{E} and \mathbf{H} are the electric field and the magnetic field in vacuum, respectively. \mathbf{D} and \mathbf{B} are the electric and magnetic field in a material, ρ the charge density and \mathbf{j} the current density. \mathbf{D} and \mathbf{B} are expressed using the materials constants as

$$\left. \begin{aligned} \mathbf{D} &= \varepsilon\mathbf{E} \\ &= (1 + 4\pi\alpha)\mathbf{E} \\ &= (\mathbf{E} + 4\pi\mathbf{P}) \end{aligned} \right\} \quad (\text{A.5})$$

$$\mathbf{P} = \alpha\mathbf{E} \quad (\text{A.6})$$

$$\mathbf{j} = \sigma\mathbf{E} \quad (\text{A.7})$$

$$\mathbf{B} = \mu\mathbf{H} \quad (\text{A.8})$$

The electric field vector, \mathbf{D} , in a material is called electric displacement vector and the magnetic field vector, \mathbf{B} , in the material is called the magnetization vector. \mathbf{P} is called the polarization vector. The equations given in (A.5) through (3.9) are those describing the relations of \mathbf{E} and \mathbf{H} with $\mathbf{D}, \mathbf{B}, \mathbf{P}$ and \mathbf{j} and quantities, ϵ, α, σ and μ are tensors. They are characteristic of materials. ϵ is referred to dielectric constant, α the polarizability, σ the conductivity and μ the permeability. In case of μ , relations similar to (A.5) are given by

$$\begin{aligned}\mu &= 1 + 4\pi\chi \\ \mathbf{M} &= \chi\mathbf{H}\end{aligned}\tag{A.9}$$

χ is called the susceptibility and the magnetic polarization, \mathbf{M} , is also referred to the magnetization in many cases.

The meanings of (A.1) through (A.4) are shown in parentheses. Ampere's law, (A.4), indicates that the magnetic field is formed by electric currents. There, we view $\partial\mathbf{D}/\partial t$ as the current. If the electric field varies with time, the field change is equivalent to the current. The quantity, $\partial\mathbf{D}/\partial t$, is called the displacement current. Suppose the static current \mathbf{j} equal zero. If the electric field changes with time, (A.4) tells us that the magnetic field exists there. (A.3) and (A.4) show that the electric field varying with time generates the magnetic field and magnetic field varying with time generates the electric field. (A.7) shows the Ohmic law.

(A.1) shows that the charge distribution generates the electric field and (A.2) shows that the static magnetic field cannot be produced if the magnetization does not exist in a material from the beginning. The origin of the magnetization is the electron spins and the existence of the electron spin was demonstrated by spectroscopy, namely by the analyses of atomic spectra.

The origin of tensors $\varepsilon, \alpha, \sigma, \mu$ and χ cannot be clarified by the Maxwell's equations. They are clarified by the electronic theory of solids, quantum mechanics, and the statistical mechanics. The constants of materials are investigated through analyses of their dependence on photon energy. Since the origins of the materials constants are known already, the contemporary researches are made by the measurements of spectra and results are used to analyze the electronic structure.

Now we solve Maxwell's equations to find the electromagnetic waves in vacuum. In vacuum, $\rho = 0, \alpha = 0, \chi = 0$, and $\sigma = 0$. Then $\varepsilon = 1$ and $\mu = 1$ from (A.5) through (A.9). Then, we have

$$\left. \begin{aligned} \text{rot}\mathbf{H} - \frac{1}{c} \frac{\partial \mathbf{E}}{\partial t} &= 0 \\ \text{rot}\mathbf{E} + \frac{1}{c} \frac{\partial \mathbf{H}}{\partial t} &= 0 \\ \text{div}\mathbf{E} &= 0 \end{aligned} \right\} \quad (\text{A.10})$$

as the electromagnetic equations in vacuum. We operate $\frac{1}{c} \frac{\partial}{\partial t}$ to the first equation and rot to the second equation. Then we have

$$\frac{1}{c} \frac{\partial}{\partial t} \text{rot}\mathbf{H} - \frac{1}{c^2} \frac{\partial^2 \mathbf{E}}{\partial t^2} = 0 \quad (\text{A.11})$$

$$\text{rot}(\text{rot}\mathbf{H}) + \frac{1}{c} \frac{\partial}{\partial t} \text{rot}\mathbf{H} = 0 \quad (\text{A.12})$$

Making [(A.11)-(A.12)], we have

$$-\text{rot}(\text{rot}\mathbf{H}) - \frac{1}{c^2} \frac{\partial^2 \mathbf{E}}{\partial t^2} = 0 \quad (\text{A.13})$$

From the formula of vector operation, we have

$$\text{rot}(\text{rot}\mathbf{E}) = \text{grad}(\text{div}\mathbf{E}) - \nabla^2 \mathbf{E}$$

$$= -\nabla^2 \mathbf{E} \quad (\because \text{(A.10)}) \quad (\text{A.14})$$

Here,

$$\nabla^2 \equiv \frac{\partial^2}{\partial x^2} + \frac{\partial^2}{\partial y^2} + \frac{\partial^2}{\partial z^2}$$

Then, we have

$$\frac{1}{c^2} \frac{\partial^2 \mathbf{E}}{\partial t^2} - \nabla^2 \mathbf{E} = 0 \quad (\text{A.15})$$

In a similar way, we operate *rot* to the first equation of (A.10) and $\frac{1}{c} \frac{\partial}{\partial t}$ to the

second equation. Manipulating the results in the similar way, we have

$$\frac{1}{c^2} \frac{\partial^2 \mathbf{H}}{\partial t^2} - \nabla^2 \mathbf{H} = 0 \quad (\text{A.16})$$

(A.15) and (A.16) have the same mathematical form. They have the form of a wave equation. They are often called the telegraphic equations. Since they have the same form, we formulate a equation that gives us the solutions, \mathbf{E} and \mathbf{H} , more generally. For the purpose to obtain the general equation, we introduce the vector potential, \mathbf{A} , defined as

$$\begin{aligned} \mathbf{E} &= -\frac{1}{c} \frac{\partial \mathbf{A}}{\partial t} \\ \mathbf{H} &= \text{rot} \mathbf{A} \end{aligned} \quad (\text{A.17})$$

Inserting (A.17) into the first equation of (A.10) and using (A.14), we have

$$\frac{1}{c^2} \frac{\partial^2 \mathbf{A}}{\partial t^2} - \nabla^2 \mathbf{A} = 0 \quad (\text{A.18})$$

In the calculation, the assumption is made that $\text{div} \mathbf{A} = 0$. Note that, because of the first equation of (A.14),

$$\begin{aligned} \text{div} \mathbf{E} &= -\frac{1}{c} \frac{\partial}{\partial t} \text{div} \mathbf{A} = 0 \\ \therefore \quad \text{div} \mathbf{A} &= 0 \end{aligned} \quad (\text{A.19})$$

A general solution of (A.18) is

$$\mathbf{A} = \mathbf{A}_0 f(\boldsymbol{\kappa} \cdot \mathbf{r} \pm \omega t) \quad (\text{A.20})$$

$$\boldsymbol{\kappa}^2 - \frac{1}{c} \omega^2 = 0 \quad (\text{A.21})$$

Here, $f(\xi)$ is an arbitrary function of ξ . If we insert (A.20) and (A.21) into (A.18), we find (A.20) together with (A.21) is the solution of (A.18). Since the form of the differential equation is the same, \mathbf{H} and \mathbf{E} have the same forms as (A.20) with (A.21). Thus, we can write the solutions of the telegraphic equations as

$$\left. \begin{aligned} \mathbf{A} &= \mathbf{A}_0^+ f_a(\boldsymbol{\kappa} \cdot \mathbf{r} + \omega t) + \mathbf{A}_0^- f_a(\boldsymbol{\kappa} \cdot \mathbf{r} - \omega t) \\ \mathbf{E} &= \mathbf{E}_0^+ f_a(\boldsymbol{\kappa} \cdot \mathbf{r} + \omega t) + \mathbf{E}_0^- f_a(\boldsymbol{\kappa} \cdot \mathbf{r} - \omega t) \\ \mathbf{H} &= \mathbf{H}_0^+ f_a(\boldsymbol{\kappa} \cdot \mathbf{r} + \omega t) + \mathbf{H}_0^- f_a(\boldsymbol{\kappa} \cdot \mathbf{r} - \omega t) \end{aligned} \right\} \quad (\text{A.22})$$

For simplicity, we take \mathbf{r} to be z and consider only $-\omega$ solution. If the phase of $f(\xi)$ at t_0 equals to be $\xi_0 = \xi(z_0, t_0) = \kappa z_0 - \omega t_0$, and at $t_0 + \Delta t$ this phase moves to

$$\xi_0 = \xi(z_0 + \Delta z, t_0 + \Delta t) = \kappa(z_0 + \Delta z) - \omega(t_0 + \Delta t)$$

we have

$$\kappa(z_0 + \Delta z) - \omega(t_0 + \Delta t) = \kappa z_0 - \omega t_0$$

Then we have

$$\frac{\Delta z}{\Delta t} = \frac{\omega}{\kappa}$$

At very small Δt , this gives the speed, v , of the movement of the same phase, and thus, of $f(\xi)$. Therefore,

$$v = \frac{\omega}{\kappa} \quad (\text{A.23})$$

From (A.21) and (A.23), we have

$$v = c$$

This means that c equals to the speed of light. In other words, the solution of Maxwell's equation presents that the electromagnetic wave is nothing but light.

The practical form of $f(\xi)$ is determined by solving the boundary condition problem. The mathematical treatment of this problem is found in many text books of the electromagnetic theory and optics. We do not come in this problem here. Instead, we consider this problem from phenomenological point of view. We postulate the solution $f(\xi)$ to be oscillatory functions. This is because the electromagnetic wave is generated the oscillation of electrons, more rigorously, by the electric dipole oscillation. Examples: Fluorescence, antenna, spark (experimentally by Herz), Krystron, magnetron, lasers, etc.

Since the solution is an oscillatory function, we can expand the solution, $f(\kappa \cdot \mathbf{r} \pm \omega t)$, in the Fourier series. In other words the solution is given by the superposition of harmonic waves. In order to see the nature of the solution, we consider only one piece of plane wave, as

$$\left. \begin{aligned} \mathbf{A} &= \mathbf{A}_0 \exp i(\kappa \cdot \mathbf{r} - \omega t) \\ \mathbf{E} &= \mathbf{E}_0 \exp i(\kappa \cdot \mathbf{r} - \omega t) \\ \mathbf{H} &= \mathbf{H}_0 \exp i(\kappa \cdot \mathbf{r} - \omega t) \end{aligned} \right\} \quad (\text{A.24})$$

Here, ω has the nature of the angular frequency. Then we have

$$\omega = 2\pi\nu = \frac{2\pi c}{\lambda} \quad (\text{A.25})$$

Here, ν is the oscillation frequency and λ is the wavelength. From (A.21) and (A.25), we have

$$\kappa = \frac{1}{c}\omega = \frac{2\pi}{\lambda} \quad (\text{A.26})$$

Thus κ is the wave number vector; it is directed toward the direction of the propagation of the wave. We have adopted the $-\omega$ wave. In this case, the wave propagates from $r < 0$ to $r > 0$. In case of the $+\omega$, the wave propagates from $r > 0$ to $r < 0$.

We insert the third equation of (A.24) into (A.3). Then we have

$$\text{rot}\mathbf{E} - \frac{i\omega B_0}{c} e^{i(\kappa \cdot \mathbf{r} - \omega t)} = 0 \quad (\text{A.27})$$

Here we used the third equation of (A.24) and (3.9) obtaining

$$\begin{aligned} \mathbf{B} &= \mu \mathbf{H}_0 \exp(\kappa \cdot \mathbf{r} - \omega t) \\ &= B_0 \exp(\kappa \cdot \mathbf{r} - \omega t) \end{aligned} \quad (\text{A.28})$$

From (A.27) and (3.9) we have

$$\text{rot}\mathbf{E} - \frac{i\omega\mu}{c} \mathbf{H} = 0 \quad (\text{A.29})$$

From (A.29) and the second equation of (A.17), we have

$$\text{rot}\mathbf{E} - \frac{i\omega\mu}{c} \text{rot}\mathbf{A} = 0 \quad (\text{A.30})$$

Selecting an appropriate gauge, we have

$$\mathbf{E} = \frac{i\omega\mu}{c} \mathbf{A} \quad (\text{A.31})$$

This is an important relation that shows $\mathbf{E} \parallel \mathbf{A}$.

Next, we come back to (A.24). We put

$$\tau = \kappa \cdot \mathbf{r} - \omega t \quad (\text{A.32})$$

Then the electromagnetic waves are written as

$$\left. \begin{aligned} \mathbf{A} &= \mathbf{A}_0 e^{i\tau} \\ \mathbf{E} &= \mathbf{E}_0 e^{i\tau} \\ \mathbf{H} &= \mathbf{H}_0 e^{i\tau} \end{aligned} \right\} \quad (\text{A.33})$$

Wave vector $\boldsymbol{\kappa}$ is written as

$$\boldsymbol{\kappa} = \kappa_x \mathbf{u}_x + \kappa_y \mathbf{u}_y + \kappa_z \mathbf{u}_z \quad (\text{A.34})$$

where $(\mathbf{u}_x, \mathbf{u}_y, \mathbf{u}_z)$ is a unit vector directing to the unit vector $(\mathbf{e}_x, \mathbf{e}_y, \mathbf{e}_z)$ of \mathbf{r} . Then, we have

$$\boldsymbol{\kappa} \cdot \mathbf{r} = \kappa_x x + \kappa_y y + \kappa_z z \quad (\text{A.35})$$

Therefore we have from (A.32) through (A.35)

$$\left. \begin{aligned} \frac{\partial}{\partial x} e^{i\tau} &= i\kappa_x e^{i\tau} \\ \frac{\partial}{\partial y} e^{i\tau} &= i\kappa_y e^{i\tau} \\ \frac{\partial}{\partial z} e^{i\tau} &= i\kappa_z e^{i\tau} \end{aligned} \right\} \quad (\text{A.36})$$

Thus, we have

$$\nabla e^{i\tau} = i\boldsymbol{\kappa} e^{i\tau} \quad (\text{A.37})$$

Also we have

$$\frac{\partial}{\partial t} e^{i\tau} = -i\omega e^{i\tau} \quad (\text{A.38})$$

Thus we can replace operation ∇ with $i\boldsymbol{\kappa}$ and operation $\partial/\partial t$ with $-i\omega$. Since rot is equal to $\nabla \times$ and div is equal to $\nabla \cdot$. Using these relations, we obtain from (A.1) through (3.9),

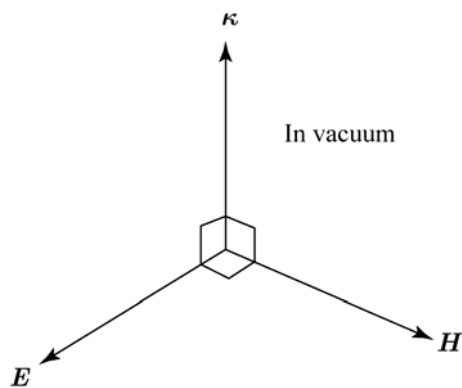
$$\left. \begin{aligned}
 \boldsymbol{\kappa} \times \mathbf{E} &= \mu\omega\mathbf{H} \\
 \boldsymbol{\kappa} \times \mathbf{H} &= -\varepsilon\omega\mathbf{E} \\
 \boldsymbol{\kappa} \cdot \mathbf{E} &= 0 \\
 \boldsymbol{\kappa} \cdot \mathbf{H} &= 0
 \end{aligned} \right\} \quad (\text{A.39})$$

$$\left. \begin{aligned}
 \boldsymbol{\kappa} \times \mathbf{E} &= \omega\mathbf{B} \\
 \boldsymbol{\kappa} \times \mathbf{H} &= -\omega\mathbf{D} \\
 \boldsymbol{\kappa} \cdot \mathbf{D} &= 0 \\
 \boldsymbol{\kappa} \cdot \mathbf{B} &= 0
 \end{aligned} \right\} \quad (\text{A.40})$$

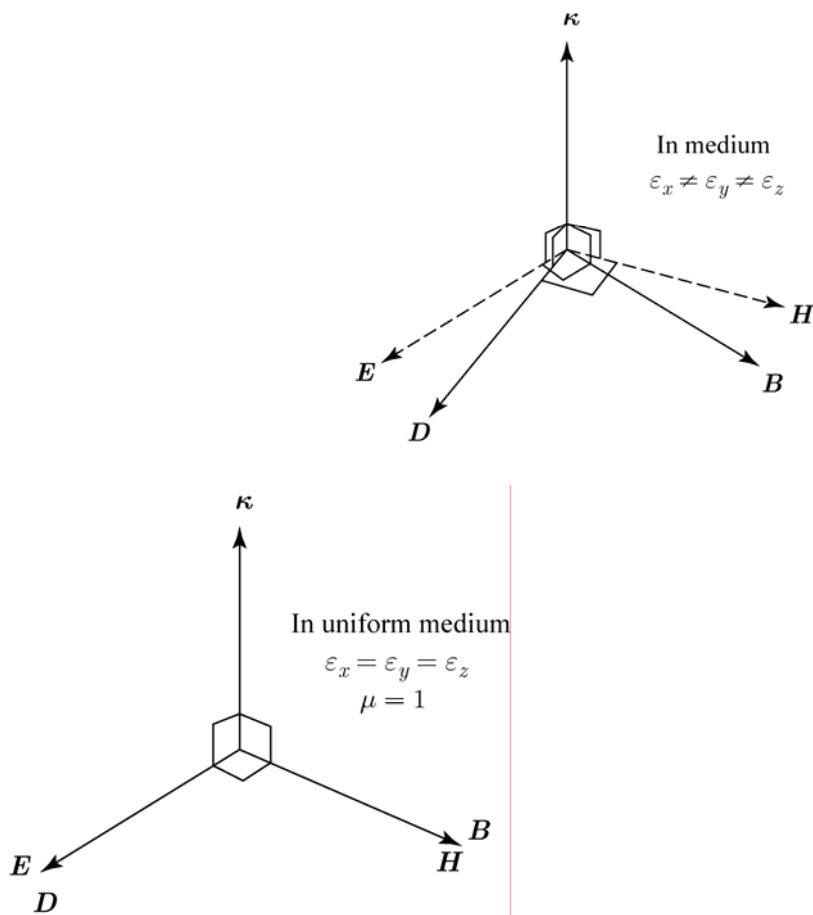
From (A.39) and (A.40) we conclude the following important nature of the electromagnetic wave:

$$1) \quad \left. \begin{aligned}
 \boldsymbol{\kappa} &\perp \mathbf{E} \\
 \boldsymbol{\kappa} &\perp \mathbf{H} \\
 \mathbf{H} &\perp \mathbf{E}
 \end{aligned} \right\} \quad (\text{A.41})$$

This means that the electromagnetic wave in vacuum is the transverse wave and the electric field is perpendicular to the magnetic field.



$$2) \quad \left. \begin{array}{l} \kappa \perp B \\ \kappa \perp D \\ B \perp E \\ D \perp H \end{array} \right\} \quad (\text{A.42})$$



In a transparent material, the electromagnetic wave formed by the B and D is the transverse wave. However B is not perpendicular to D .

APPENDIX B

QUANTIZATION OF ELECTROMAGNETIC FIELD

We consider equation (A.18), from first equation in (A.24) and (A.31) solution of the equation (A.18) may be written as

$$\mathbf{A}_k(\mathbf{r}, t) = \frac{c}{i\omega_k} \mathbf{E}_0 \exp[i(\mathbf{k} \cdot \mathbf{r} - \omega_k t)] \quad (\text{B.1})$$

Here \mathbf{k} denotes the wave vector number which is discussed already in (A.26), $k^2 = (\omega / c)^2$. If we have a number of waves of different ω in a large box with volume $V = XYZ$. Then the wave vector \mathbf{k} becomes discrete, and satisfies the condition

$$(k_x X, k_y Y, k_z Z) = 2\pi \times (\text{Integer}) \quad (\text{B.2})$$

Thus, the general form of the vector potential may be expressed by a superposition of \mathbf{A}_k , namely

$$\mathbf{A}(\mathbf{r}, t) = c \sqrt{\frac{2\pi}{\omega V}} \sum_{k,s} \{ e_{k,s} A_{k,s} \exp[i(\mathbf{k} \cdot \mathbf{r} - \omega_k t)] + e_{k,s}^+ A_{k,s}^+ \exp[-i(\mathbf{k} \cdot \mathbf{r} - \omega_{k,s} t)] \} \quad (\text{B.3})$$

Here $e_{k,s}$ ($s = 1, 2$) denotes real polarization vector that satisfy the equations

$$\begin{aligned} \mathbf{e}_{k,s} \cdot \mathbf{k} &= 0, & \mathbf{e}_{k,1} \cdot \mathbf{e}_{k,2} &= 0, \\ \mathbf{e}_{k,1} \cdot \mathbf{e}_{k,1} &= 1 \end{aligned} \quad (\text{B.4})$$

and the $A_{k,s}$ are complex constants that are proportional to the amplitudes of the wave vector potential. Since we shall deal with real quantities, we assume that

$$A_{k,s}^* = A_{k,s}^+ \quad (\text{B.5})$$

Since the time-independent Hamiltonian is equal to the total energy in material system. Then, we should expect to obtain a Hamiltonian for the radiation field by computing the total energy E in material, namely,

$$E = \frac{1}{8\pi} \int (E^2 + H^2) dV \quad (\text{B.6})$$

Computing E and H from (A.17) using (B.3), and use the notation $rot\mathbf{A} \equiv \nabla \times \mathbf{A}$,

$$E = \frac{1}{8\pi} \int \left[\left| \frac{1}{c} \frac{\partial \mathbf{A}}{\partial t} \right|^2 + |\nabla \times \mathbf{A}|^2 \right] dV$$

$$E = \frac{1}{8\pi} \int \left[\left(\frac{1}{c} \frac{\partial \mathbf{A}}{\partial t} \right)^* \cdot \left(\frac{1}{c} \frac{\partial \mathbf{A}}{\partial t} \right) + (\nabla \times \mathbf{A})^* \cdot (\nabla \times \mathbf{A}) \right] dV$$

Because

$$\begin{aligned} (\nabla \times \mathbf{A}) \cdot (\nabla \times \mathbf{B}) &= \nabla \cdot [\mathbf{A} \times (\nabla \times \mathbf{B})] + \mathbf{A} \cdot [\nabla \times (\nabla \times \mathbf{B})] \\ &= \nabla \cdot [\mathbf{A} \times (\nabla \times \mathbf{B})] + \mathbf{A} \cdot [\nabla(\nabla \cdot \mathbf{B}) - \nabla^2 \mathbf{B}] \end{aligned}$$

$$\therefore E = \frac{1}{8\pi} \int \left[\left(\frac{1}{c} \frac{\partial \mathbf{A}}{\partial t} \right)^* \cdot \left(\frac{1}{c} \frac{\partial \mathbf{A}}{\partial t} \right) + \mathbf{A}^* \cdot [\nabla(\nabla \cdot \mathbf{A})] - \mathbf{A}^* \cdot [\nabla^2 \mathbf{A}] \right] dV \quad (\text{B.7})$$

The second term of equation (B.7) can be rewritten in the surface integral (Gauss's dispersion formula) and disappears at the surface. Thus, we obtain

$$E = \frac{1}{8\pi} \int \left[\left(\frac{1}{c} \frac{\partial \mathbf{A}}{\partial t} \right)^* \cdot \left(\frac{1}{c} \frac{\partial \mathbf{A}}{\partial t} \right) - \mathbf{A}^* \cdot \left[\frac{1}{c^2} \frac{\partial^2 \mathbf{A}}{\partial t^2} \right] \right] dV$$

$\therefore k^2 = (\omega/c)^2$ Thus, the energy may be written in the form

$$E = \sum_{k,s} \omega_{k,s} a_{k,s} a_{k,s}^* \quad (\text{B.8})$$

where

$$\left. \begin{aligned} a_{\mathbf{k},s} &= A_{\mathbf{k},s} e^{-i\omega_{\mathbf{k},s}t} \\ a_{\mathbf{k},s}^* &= A_{\mathbf{k},s}^* e^{i\omega_{\mathbf{k},s}t} \end{aligned} \right\} \quad (\text{B.9})$$

If we now regard $a_{\mathbf{k},s}$ and $ia_{\mathbf{k},s}$ as conjugate variables and (B.8) as the Hamiltonian of the system, we find that the Hamiltonian equations are

$$\left. \begin{aligned} \dot{a}_{\mathbf{k},s} &= \frac{\partial H}{\partial ia_{\mathbf{k},s}} = -i\omega_{\mathbf{k},s} a_{\mathbf{k},s} \\ \dot{a}_{\mathbf{k},s}^* &= \frac{\partial H}{\partial a_{\mathbf{k},s}} = i\omega_{\mathbf{k},s} a_{\mathbf{k},s}^* \end{aligned} \right\} \quad (\text{B.10})$$

The solution of (B.10) lead to the time dependence expressed by (B.9). Hence, (B.8) actually is the Hamiltonian function of the system.

Up to this point, the derivation is within a framework of semi-classical member. To present the energy in equation (B.8) in quantum mechanical presentation, the following new variables are introduced.

$$Q_\lambda = \frac{1}{\sqrt{2\omega_\lambda}}(a_\lambda + a_\lambda^*), \quad P_\lambda = \dot{Q}_\lambda = \frac{\omega_\lambda}{i\sqrt{2\omega_\lambda}}(a_\lambda - a_\lambda^*) \quad (\text{B.11})$$

$$\text{or} \quad a_\lambda = \frac{1}{\sqrt{2\omega_\lambda}}(\omega_\lambda Q + iP_\lambda), \quad a_\lambda^* = \frac{1}{\sqrt{2\omega_\lambda}}(\omega_\lambda Q - iP_\lambda) \quad (\text{B.12})$$

Substituting into (B.8), we obtain

$$H = \sum_\lambda E_\lambda = \frac{1}{2} \sum_\lambda (P_\lambda^2 + \omega_\lambda^2 Q_\lambda^2) \quad (\text{B.13})$$

Here λ denotes \mathbf{k}, s . Equation (B.13) is the same as for a system of harmonic oscillators. This means that a radiation field is equivalent to a system of harmonic oscillators. We use (B.13) to shift to quantum mechanical representation. By transforming (a_λ, a_λ^*) to annihilation and creation operators $\hbar(\hat{a}, \hat{a}^+)$ through the relation (B.11) and (B.12), the hamiltonian becomes

$$H = \sum_{\lambda} \frac{\hbar\omega}{2} [\hat{a}^+ \hat{a} + \hat{a} \hat{a}^+] \quad (\text{B.14})$$

From $[\hat{a}, \hat{a}^+] = 1$, we obtain

$$H = \sum_{\lambda} \hbar\omega \left[\hat{a}^+ \hat{a} + \frac{1}{2} \right] \quad (\text{B.15})$$

This is a simple harmonics Hamiltonian in quantum mechanics. The wave vector potential in equation (B.3) can be written in the general form as

$$\mathbf{A}(\mathbf{r}, t) = c \sqrt{\frac{\hbar}{V}} \sum_{\mathbf{k}, s} \frac{1}{\sqrt{\omega_{\lambda}}} \left\{ \mathbf{e}_{\mathbf{k}, s} \hat{a}_{\mathbf{k}, s} \exp[i(\mathbf{k} \cdot \mathbf{r})] + \mathbf{e}_{\mathbf{k}, s}^+ \hat{a}_{\mathbf{k}, s}^+ \exp[-i(\mathbf{k} \cdot \mathbf{r})] \right\} \quad (\text{B.16})$$

$$\mathbf{A}(\mathbf{r}, t) = \sum_{\mathbf{k}, s} \left[\hat{a}_{\mathbf{k}, s} \mathbf{A}_{\mathbf{k}, s} + \hat{a}_{\mathbf{k}, s}^+ \mathbf{A}_{\mathbf{k}, s}^{\dagger} \right] \quad (\text{B.17})$$

$$\mathbf{A}_{\lambda} = c \sqrt{\frac{\hbar}{V}} \sum_{\mathbf{k}, s} \sqrt{\frac{1}{\omega_{\mathbf{k}, s}}} \left\{ \mathbf{e}_{\mathbf{k}, s} \exp[i(\mathbf{k}_{\mathbf{k}, s} \cdot \mathbf{r})] \right\} \quad (\text{B.18})$$

where the symbols \mathbf{e}, \mathbf{k} denote the unit electric field vector (vector of polarization) and the wave vector, respectively.

APPENDIX C

HAMILTONIAN OF ELECTRON INTERACTING WITH ELECTROMAGNETIC FIELD

Interaction between electromagnetic field (photon) and electron can be derived in classical consideration. The relativistic mechanical equation of a charged particle in electric field \mathbf{E} and magnetic flux density \mathbf{B} is

$$\frac{d}{dt} \left\{ \frac{m\mathbf{v}}{\sqrt{1 - (v/c)^2}} \right\} = e \left(\mathbf{E} + \frac{1}{c} [\mathbf{v} \times \mathbf{B}] \right) \quad (\text{C.1})$$

The right hand side denotes a Lorentz force. This equation can be obtained from the following Hamiltonian; the proof is given below.

$$H = \sqrt{\left(\mathbf{p} - \frac{e}{c} \mathbf{A} \right)^2 c^2 + m_0^2 c^4} + e\phi \quad (\text{C.2})$$

[Proof of Equation (C.2)]

Hermitian satisfy the following relations.

$$\frac{d\mathbf{r}}{dt} = \frac{\partial H}{\partial \mathbf{p}}, \quad \frac{d\mathbf{p}}{dt} = -\frac{\partial H}{\partial \mathbf{r}} \quad (\text{C.3})$$

$$\begin{aligned} \therefore \frac{d\mathbf{r}}{dt} &= \frac{\left(\mathbf{p} - \frac{e}{c} \mathbf{A} \right)^2 c^2}{\sqrt{\left(\mathbf{p} - \frac{e}{c} \mathbf{A} \right)^2 c^2 + m_0^2 c^4}} \\ &\equiv \mathbf{v} \end{aligned} \quad (\text{C.4})$$

$$\begin{aligned} \therefore \quad \mathbf{p} - \frac{e}{c} \mathbf{A} &= \frac{m_0 c}{\sqrt{(1 - (\mathbf{v}/c)^2)}} \mathbf{v} \\ \mathbf{p} &= \frac{m_0 c}{\sqrt{(1 - (\mathbf{v}/c)^2)}} \mathbf{v} + \frac{e}{c} \mathbf{A} \end{aligned} \quad (\text{C.5})$$

The first term of the right hand side of equation (C.5) is a kinetic momentum of the charge particle. That means \mathbf{p} is a total momentum of the system, and $(e/c)\mathbf{A}$ is a momentum induced by the electromagnetic field. Using a relation

$$\begin{aligned} \frac{d\mathbf{A}}{dt} &= \frac{\partial \mathbf{A}}{\partial t} + \frac{\partial \mathbf{A}}{\partial x} \frac{\partial x}{\partial t} + \frac{\partial \mathbf{A}}{\partial y} \frac{\partial y}{\partial t} + \frac{\partial \mathbf{A}}{\partial z} \frac{\partial z}{\partial t} \\ &= \frac{\partial \mathbf{A}}{\partial t} + \left(v_x \frac{\partial}{\partial x} + v_y \frac{\partial}{\partial y} + v_z \frac{\partial}{\partial z} \right) \mathbf{A} \\ &= \frac{\partial \mathbf{A}}{\partial t} + \{(\mathbf{v} \cdot \nabla) \mathbf{A}\} \end{aligned}$$

and equation (C.5),

$$\frac{d\mathbf{p}}{dt} = \frac{d}{dt} \left(\frac{m_0 c}{\sqrt{(1 - (\mathbf{v}/c)^2)}} \mathbf{v} \right) + \frac{e}{c} \frac{d\mathbf{A}}{dt} + \frac{e}{c} \{(\mathbf{v} \cdot \nabla) \mathbf{A}\} \quad (\text{C.6})$$

From equation (C.3)

$$\frac{\partial \text{H}}{\partial \mathbf{r}} \equiv \nabla \text{H} = \frac{1}{2} \frac{c^2}{\sqrt{\left(\mathbf{p} - \frac{e}{c} \mathbf{A} \right)^2 c^2 + m_0^2 c^4}} \nabla \left\{ \left(\mathbf{p} - \frac{e}{c} \mathbf{A} \right) \cdot \left(\mathbf{p} - \frac{e}{c} \mathbf{A} \right) \right\} + e \nabla \phi$$

By using (C.4), we obtain

$$\frac{\partial \text{H}}{\partial \mathbf{r}} = \frac{1}{2} \frac{\sqrt{\left(\mathbf{p} - \frac{e}{c} \mathbf{A} \right)^2 c^2 + m_0^2 c^4}}{c^2} \nabla \{ \mathbf{v} \cdot \mathbf{v} \} + e \nabla \phi \quad (\text{C.7})$$

By applying a formula

$$\begin{aligned} \nabla(\mathbf{A} \cdot \mathbf{B}) &= (\mathbf{B} \cdot \nabla) \mathbf{A} + (\mathbf{A} \cdot \nabla) \mathbf{B} + \mathbf{B} \times (\nabla \times \mathbf{A}) + \mathbf{A} \times (\nabla \times \mathbf{B}) \\ \nabla(\mathbf{A} \cdot \mathbf{A}) &= 2[(\mathbf{A} \cdot \nabla) \mathbf{A} + \mathbf{A} \times (\nabla \times \mathbf{A})] \end{aligned} \quad (\text{C.8})$$

,we obtain

$$\begin{aligned}\frac{\partial H}{\partial \mathbf{r}} &= \frac{\sqrt{\left(\mathbf{p} - \frac{e}{c} \mathbf{A}\right)^2 c^2 + m_0^2 c^4}}{c^2} [(\mathbf{v} \cdot \nabla) \mathbf{v} + \mathbf{v} \times (\nabla \times \mathbf{v})] + e \nabla \phi \\ &= (\mathbf{v} \cdot \nabla) \left(\mathbf{p} - \frac{e}{c} \mathbf{A}\right) + \mathbf{v} \times \left(\nabla \times \left(\mathbf{p} - \frac{e}{c} \mathbf{A}\right)\right) + e \nabla \phi \\ \frac{\partial H}{\partial \mathbf{r}} &= -\frac{e}{c} [(\mathbf{v} \cdot \nabla) \mathbf{A}] + \mathbf{v} \times (\nabla \times \mathbf{A}) + e \nabla \phi\end{aligned}\quad (\text{C.9})$$

From (C.3), (C.6)-(C.9), we obtain

$$\begin{aligned}\frac{d}{dt} \left(\frac{m_0 c}{\sqrt{1 - (\mathbf{v}/c)^2}} \mathbf{v} \right) &= -\frac{e}{c} \frac{d\mathbf{A}}{dt} - e \nabla \phi + \frac{e}{c} [\mathbf{v} \times (\nabla \times \mathbf{A})] \\ &= e \left[-\frac{1}{c} \frac{d\mathbf{A}}{dt} - \nabla \phi \right] + \frac{e}{c} [\mathbf{v} \times (\nabla \times \mathbf{A})] \\ &= e \mathbf{E} + \frac{e}{c} [\mathbf{v} \times \mathbf{B}] \quad Q.E.D.\end{aligned}$$

This equation is identical to equation (C.1), meaning that the Hamiltonian ((C.2)) is correct. The relativistic correction to the Hamiltonian is

$$H = m_0 c^2 \left(1 + \frac{\left(\mathbf{p} - \frac{e}{c} \mathbf{A}\right)^2}{2m_0^2 c^2} - \frac{\left(\mathbf{p} - \frac{e}{c} \mathbf{A}\right)^4}{8m_0^2 c^2} + \dots \right) + e\phi \quad (\text{C.10})$$

So that within a framework of non-relativistic approximation, we obtain

$$H = \frac{1}{2m_0} \left(\mathbf{p} - \frac{e}{c} \mathbf{A}\right)^2 + m_0 c^2 + e\phi \quad (\text{C.11})$$

$$H = \frac{1}{2m_0} \mathbf{p}^2 + m_0 c^2 + e\phi - \frac{e}{2m_0 c} [\mathbf{p} \cdot \mathbf{A} + \mathbf{A} \cdot \mathbf{p}] + \frac{1}{2m_0} \left(\frac{e}{c}\right)^2 \mathbf{A}^2 \quad (\text{C.12})$$

$$H = \frac{1}{2m_0} \mathbf{p}^2 + m_0 c^2 + e\phi + H_1 + H_2 \quad (\text{C.13})$$

where

$$H_1 = -\frac{e}{2m_0c}(\mathbf{p} \cdot \mathbf{A} + \mathbf{A} \cdot \mathbf{p}) = \frac{i\hbar e}{2m_0c}(\nabla \cdot \mathbf{A} + \mathbf{A} \cdot \nabla) \quad (\text{C.14})$$

$$H_2 = \frac{1}{2m_0} \left(\frac{e}{c}\right)^2 \mathbf{A}^2 \quad (\text{C.15})$$

Equation (C.13) shows the total Hamiltonian of the system. The interaction between the electron and photon are expressed by H_1 and H_2 .

APPENDIX D

EXPECTED COMPTON PROFILE FOR FREE ELECTRON

The wave vectors of electrons in a crystal are defined as

$$\left. \begin{aligned}
 \mathbf{k} &= \mathbf{k}(k_x, k_y, k_z) \\
 k_x &= \frac{2\pi}{N_x a_x} n_x \\
 k_y &= \frac{2\pi}{N_y a_y} n_y \\
 k_z &= \frac{2\pi}{N_z a_z} n_z \\
 n_x, n_y, n_z &: \text{interger}
 \end{aligned} \right\} \quad (\text{D.1})$$

Here a_α ($\alpha = x, y, z$) is the inter atomic distances and N_α is the number of atoms in the crystal along the α line. We find that one allowed \mathbf{k} is in the unit $\Delta n_x \Delta n_y \Delta n_z$ that is equal to unity. Let the number of states (number of \mathbf{k} vector) in the space $d\mathbf{k}^3 = dk_x dk_y dk_z$ be $\Delta N(k)$. Obviously ΔN is proportional to $d\mathbf{k}^3$, as

$$dN = A d\mathbf{k}^3 \quad (\text{D.2})$$

Here A is the proportionality constant. From (D.1) we have

$$\begin{aligned}
d\mathbf{k}^3 &= dk_x dk_y dk_z = \frac{8\pi^3}{N_x N_y N_z a_x a_y a_z} dn_x dn_y dn_z \\
&= \frac{8\pi^3}{L_x L_y L_z} dn_x dn_y dn_z \\
&= \frac{8\pi^3}{V} dn_x dn_y dn_z
\end{aligned}$$

$$d\mathbf{k}^3 = \frac{8\pi^3}{V} dn_x dn_y dn_z \quad (\text{D.3})$$

Here L_x , L_y and L_z are the lengths of the crystal and V is the volume of the crystal.

Obviously, since $dN = dn_x dn_y dn_z$, we have

$$dN = \frac{V}{8\pi^3} d\mathbf{k}^3 \quad (\text{D.4})$$

Thus, we can convert the summation over \mathbf{k} to the integration as,

$$\sum_{\mathbf{k}} \rightarrow \frac{V}{8\pi^3} d\mathbf{k}^3 \quad (\text{D.5})$$

Equation (1.13) and the argument leading to this, we have

$$\begin{aligned}
N(p_z) &= \frac{V}{8\pi^3} \cdot \pi p_z^2 \tan^2 \theta_F dp_z \\
&= a p_z^2 dp_z
\end{aligned} \quad (\text{D.6})$$

Here,

$$a = \frac{V}{8\pi^2} \tan^2 \theta_F \quad (\text{D.7})$$

Then we have for the intensity to be observed as

$$\begin{aligned}
N_{obs} &= \sigma N(p_z) \\
&= a\sigma p_z^2 dp_z
\end{aligned} \quad (\text{D.8})$$

Thus, the Compton profile is an upward parabola.

APPENDIX E

ANGULAR MOMENTUM

The angular momentum is treated mathematically as the irreducible representation of the rotational group. By means of this treatment, all the physical nature of the angular momentum is mathematically is described quite generally and completely.

Suppose that there are many electrons and each electron is in the central field potential, $V(r_k)$. The angular momentum of an electron is defined as

$$\mathbf{l}_k = \mathbf{r}_k \times \mathbf{p}_k \quad (\text{E.1})$$

We define the total angular momentum of all electrons as

$$\mathbf{L} = \sum_k \mathbf{l}_k \quad (\text{E.2})$$

In the system in which the central field approximation is valid, the Hamiltonian,

$$\left. \begin{aligned} \mathbf{H} &= \sum_k h_k \\ h_k &= -\frac{\hbar^2}{2m} \nabla_k^2 + V(r_k) \end{aligned} \right\} \quad (\text{E.3})$$

In $V(r_k)$, the electron-electron interaction $\sum_{i>k} \frac{e^2}{r_{ik}}$ is averaged and renormalized. This

is the central field approximation. As a result, the hamiltonian, h , of each electron has the partial dependent only on r and is spherically symmetric. The solution in the spherical coordinate, (r, θ, ϕ) , is given by

$$\psi(r, \theta, \phi) = \hat{N}R_{nl}(r)Y_{lm}(\theta, \phi) \quad (\text{E.4})$$

In this section, however, we see the nature of the angular momentum more physically only on the basis of quantum mechanics. For brevity, suffix k is dropped out. Here, $Y_{lm}(\theta, \phi)$ is the spherical harmonic function and \hat{N} is the normalization constant. Although $R_{nl}(r)$ is determined by $V(r)$, $Y_{lm}(\theta, \phi)$ has its own characteristics. For example,

$$\mathbf{l}^2 Y_{lm}(\theta, \phi) = \hbar^2 l(l+1) Y_{lm}(\theta, \phi) \quad (\text{E.5})$$

$$l_z Y_{lm}(\theta, \phi) = \hbar m Y_{lm}(\theta, \phi) \quad (\text{E.6})$$

We should remark that $\mathbf{l} = (\hbar/i)\nabla$. The proof of (E.5) and (E.6) are in many standard text books of quantum mechanics. Since the solution $\psi(r, \theta, \phi)$ (E.4) is variable-separable between r and (θ, ϕ) , (E.3) through (E.6) show

$$\begin{aligned} [\mathbf{l}^2, h] &= [\mathbf{l}^2 h - h \mathbf{l}^2] = 0 \\ [l_z, h] &= [l_z h - h l_z] = 0 \end{aligned} \quad (\text{E.7})$$

From (E.2), (E.3), and (E.7), we have

$$\begin{aligned} \sum_k [\mathbf{l}_k^2, h_k] &= [\mathbf{L}^2, H] = 0 \\ \sum_k [l_{z,k}, h_k] &= [L_z, H] = 0 \end{aligned} \quad (\text{E.8})$$

These indicate that \mathbf{L}^2 and L_z commute the Hamiltonian. In other words, the eigenfunctions which diagonalizes the hamiltonian also diagonalizes \mathbf{L}^2 and L_z .

From the definition, (E.1), of the angular momentum, we can proof the following commutation relation:

$$\left. \begin{aligned} l_y l_z - l_z l_y &= i\hbar l_x \\ l_z l_x - l_x l_z &= i\hbar l_y \\ l_x l_y - l_y l_x &= i\hbar l_z \end{aligned} \right\} \quad (\text{E.9})$$

Therefore we have

$$\left. \begin{aligned} l_{y,k} l_{z,j} - l_{z,j} l_{y,k} &= i\hbar l_{x,k} \delta_{k,j} \\ l_{z,k} l_{x,j} - l_{x,j} l_{z,k} &= i\hbar l_{y,k} \delta_{k,j} \\ l_{x,k} l_{y,j} - l_{y,j} l_{x,k} &= i\hbar l_{z,k} \delta_{k,j} \end{aligned} \right\} \quad (\text{E.10})$$

From the first equation of (E.10), we see

$$\begin{aligned} L_y L_z - L_z L_y &= \sum_{k,j} (l_{y,k} l_{z,j} - l_{z,j} l_{y,k}) \\ &= \sum_{k,j} i\hbar l_{x,k} \delta_{k,j} \\ &= \sum_k i\hbar l_{x,k} \\ &= i\hbar L_x \end{aligned} \quad (\text{E.11})$$

Similar commutation relations are held for all components, L_x , L_y , and L_z . Therefore

we write

$$\left. \begin{aligned} L_y L_z - L_z L_y &= i\hbar L_x \\ L_z L_x - L_x L_z &= i\hbar L_y \\ L_x L_y - L_y L_x &= i\hbar L_z \end{aligned} \right\} \quad (\text{E.12})$$

The relations, (E.10), show that all of L_x, L_y, L_z cannot be diagonalized with H and

define the orbital angular momenta through the commutation relation as

$$\left. \begin{aligned} J_y J_z - J_z J_y &= i\hbar J_x \\ J_z J_x - J_x J_z &= i\hbar J_y \\ J_x J_y - J_y J_x &= i\hbar J_z \end{aligned} \right\} \quad (\text{E.13})$$

As the eigenvector assigning the eigen state of the system, we define $|M\rangle$ as

$$J |M\rangle = \hbar M |M\rangle \quad (\text{E.14})$$

Here, we see that we employ the matrix formalism of quantum mechanics. We select the eigen states with which the z component of \mathbf{J} is diagonalized.

Instead of J_x and J_y , we use J_+ and J_- defined as

$$\left. \begin{aligned} J_+ &= J_x + iJ_y \\ J_- &= J_x - iJ_y \end{aligned} \right\} \quad (\text{E.15})$$

Using J_+ , J_- and the commutation relations, (E.12), we obtain the new commutation relations as

$$\left. \begin{aligned} J_+J_z - J_zJ_+ &= -\hbar J_+ \\ J_-J_z - J_zJ_- &= -\hbar J_- \\ J_+J_- - J_-J_+ &= 2\hbar J_z \end{aligned} \right\} \quad (\text{E.16})$$

We operate $|M\rangle$ on the first equation of (E.16).

$$J_+J_z|M\rangle - J_zJ_+|M\rangle = -\hbar J_+|M\rangle$$

From (E.14) we have

$$J_+\hbar M|M\rangle - J_zJ_+|M\rangle = -\hbar J_+|M\rangle$$

Therefore

$$J_z(J_+|M\rangle) = \hbar(M+1)(J_+|M\rangle) \quad (\text{E.17})$$

Similarly we operate $|M\rangle$ on the second equation of commutation relation (E.16) and have

$$J_z(J_-|M\rangle) = \hbar(M-1)(J_-|M\rangle) \quad (\text{E.18})$$

Relations (E.17) and (E.18) indicate that both $J_+|M\rangle$ and $J_-|M\rangle$ are the eigen vectors of J_z . J_{\pm} is the operators to change $|M\rangle$ to $|M \pm 1\rangle$ as seen below. From (E.14), we have

$$J_z |M \pm 1\rangle = \hbar(M \pm 1) |M \pm 1\rangle \quad (\text{E.19})$$

If we compare this with (E.17) we have

$$J_+ |M\rangle = \alpha |M + 1\rangle \quad (\text{E.20})$$

In a similar way, from (E.19) and (E.18), we have

$$J_- |M\rangle = \beta |M - 1\rangle \quad (\text{E.21})$$

(E.17), (E.18), (E.20), and (E.21) show that there are a group of eigen values generated by J_+ and J_- and differing by 1. So, rewriting α and β , we can write

(E.20) and (E.21) as

$$\left. \begin{aligned} J_+ |M - 1\rangle &= c_M |M\rangle \\ J_- |M\rangle &= d_M |M - 1\rangle \end{aligned} \right\} \quad (\text{E.22})$$

Suppose the maximum value of the eigenvalues is J . Then $J_+ |M\rangle$ cannot exist and

$$\left. \begin{aligned} c_{M+1} &= 0 \\ M &= J, J - 1, J - 2, \dots \end{aligned} \right\} \quad (\text{E.23})$$

From the third equation of the commutation relations, (E.16), and (E.22) we have

$$c_M d_M - c_{M+1} d_{M+1} = 2\hbar^2 M \quad (\text{E.24})$$

Also from (E.23) we have

$$\langle M - 1 | J_- | M \rangle = d_M \quad (\text{E.25})$$

Therefore,

$$\begin{aligned} d_M^* &= \langle M - 1 | J_- | M \rangle^* \\ &= \langle M | J_-^* | M - 1 \rangle \\ &= \langle M | J_+ | M - 1 \rangle \\ &= c_M \end{aligned}$$

Therefore

$$d_M^* = c_M \quad (\text{E.26})$$

Here we have used the following relations:

$$\begin{aligned} J_-^* &= (J_x - iJ_y)^* \\ &= J_x^* + iJ_y^* \\ &= J_x + iJ_y \\ &= J_+ \end{aligned} \quad (\text{E.27})$$

Note that J_x and J_y are hermitian. Inserting (E.26) into (E.24), we have

$$|c_M|^2 - |c_{M+1}|^2 = 2\hbar^2 M \quad (\text{E.28})$$

Therefore we have

$$\begin{aligned} |c_M|^2 &= 2\hbar^2 \sum_{M=M}^J \hat{M} \\ &= 2\hbar^2 \frac{1}{2} (M+J)(J-M+1) \\ &= \hbar^2 (M+J)(J-M+1) \end{aligned}$$

Thus we have

$$c_M = \hbar \sqrt{(M+J)(J-M+1)} \cdot e^{i\theta} \quad (\text{E.29})$$

We select the phase factor to be unity ($\theta = 0$). From (E.27) and (E.24), we also have

$$|d_M|^2 - |d_{M+1}|^2 = 2\hbar^2 M \quad (\text{E.30})$$

Thus we obtain the same result as (E.29) for d_M in case of $\theta = 0$. Therefore we have

$$c_M = d_M \quad (\text{E.31})$$

Suppose the minimum value of M to be M_0 . Then, we have

$$J_- |M_0\rangle = 0 \quad (\text{E.32})$$

From (E.29), (E.31), and (E.32), we have

$$J_- |M_0\rangle = \hbar\sqrt{(J + M_0)(J_0 - M + 1)} |M_0 - 1\rangle = 0$$

Therefore we have

$$M_0 = -J \quad (\text{E.33})$$

From (E.23) and (E.24), we see that M takes values from J to $-J$ with an interval of an unity. The number of terms is $2J + 1$. The number of terms is an integer. Thus, we have

$$2J + 1 = \text{integer}$$

Thus,

$$J = \text{integer}$$

or half integer. (integer multiple of $1/2$)

Next, we have from (E.13) and (E.15)

$$\begin{aligned} J_+ J_- &= J_x^2 + J_y^2 + \hbar J_z \\ &= J^2 - J_z^2 + \hbar J_z \end{aligned}$$

Therefore we have

$$\mathbf{J}^2 = J_+ J_- - \hbar J_z + J_z^2$$

Thus we have from (E.22), (E.29) and (E.31)

$$\begin{aligned} \mathbf{J}^2 |M\rangle &= J_+ J_- |M\rangle - \hbar J_z |M\rangle + J_z J_z |M\rangle \\ &= [(J + M)(J - M + 1) - M + M^2] \hbar^2 |M\rangle \\ &= \hbar^2 J(J + 1) |M\rangle \end{aligned} \quad (\text{E.34})$$

We write $|JM\rangle$ in place of $|M\rangle$ given above and summarize the results obtained above

$$\begin{aligned} \mathbf{J}^2 |J, M\rangle &= \hbar^2 J(J + 1) |J, M\rangle \\ J_z |J, M\rangle &= \hbar M |J, M\rangle \\ J_+ |J, M - 1\rangle &= \hbar\sqrt{(J + M)(J - M + 1)} |J, M\rangle \\ J_- |J, M\rangle &= \hbar\sqrt{(J + M)(J - M + 1)} |J, M - 1\rangle \end{aligned} \quad (\text{E.35})$$

Here, J is either an integer or a half integer.

In actual cases, we have to deal with the spin-orbit coupling. In such cases, we have to sum two angular momenta. We will discuss this problem below.

Let us define an angular momentum \mathbf{J} composed of two angular momenta, \mathbf{J}_1 and \mathbf{J}_2 , as

$$\mathbf{J} = \mathbf{J}_1 + \mathbf{J}_2 \quad (\text{E.36})$$

Suppose that the eigenvector $|JM\rangle$ of \mathbf{J} is formed as

$$|JM\rangle = \sum_{M_1, M_2} \langle J_1 M_1, J_2 M_2 | JM \rangle |J_1 M_1\rangle |J_2 M_2\rangle \quad (\text{E.37})$$

Here, $|J_1, M_1\rangle$ and $|J_2, M_2\rangle$ are the eigenvectors of \mathbf{J}_1 and \mathbf{J}_2 , respectively. All pairs of quantum numbers, (J, M) , (J_1, M_1) , and (J_2, M_2) satisfy the conditions given by (E.35). $\langle J_1 M_1, J_2 M_2 | JM \rangle$ is a coefficient to be decided using (E.35). Coefficient $\langle J_1 M_1, J_2 M_2 | JM \rangle$ is referred to as Wigner coefficient or Clebsch-Gordon coefficient and are generally obtained by the use of the group theory. This part of the theory is out of scope in the present thesis.

From (E.36), J_z is given by

$$J_z = J_{z1} + J_{z2} \quad (\text{E.38})$$

Therefore we have from (E.36) and (E.38)

$$J_z |JM\rangle = \sum_{M_1, M_2} \langle J_1 M_1, J_2 M_2 | JM \rangle J_z |J_1 M_1\rangle |J_2 M_2\rangle \quad (\text{E.39})$$

$$\begin{aligned} J_z |J_1 M_1\rangle |J_2 M_2\rangle &= (J_{z1} + J_{z2}) |J_1 M_1\rangle |J_2 M_2\rangle \\ &= \hbar(M_1 + M_2) |J_1 M_1\rangle |J_2 M_2\rangle \end{aligned} \quad (\text{E.40})$$

This indicates that $|J_1 M_1\rangle |J_2 M_2\rangle$ is the eigen vector of J_z . We define M as

$$M = M_1 + M_2 \quad (\text{E.41})$$

We insert (E.41) and (E.40) into (E.39) and have

$$\begin{aligned}
 J_z |JM\rangle &= \hbar \sum_{M_1, M_2} \langle J_1 M_1, J_2, M_2 | JM \rangle (M_1 + M_2) |J_1 M_1\rangle |J_2 M_2\rangle \\
 &= \hbar \sum_{M_1, M_2} \langle J_1 M_1, J_2, M_2 | JM \rangle M |J_1 M_1\rangle |J_2 M_2\rangle \\
 &= \hbar M \sum_{M_1, M_2} \langle J_1 M_1, J_2, M_2 | JM \rangle |J_1 M_1\rangle |J_2 M_2\rangle \\
 &= \hbar M |JM\rangle
 \end{aligned} \tag{E.42}$$

Therefore, M defined as the sum of M_1 and M_2 in (E.41) is eigenvalue of J_z .

Through the discussion leading to (E.35), the quantum number J of the eigen vector $|JM\rangle$ is equal to the maximum number of M . In the same way J_1 , is the maximum number of M_1 , and J_2 the maximum number of M_2 . Form (E.41), we see

$$\text{Maximum } M = \text{Maximum } M_1 + \text{Maximum } M_2$$

Thus, we have

$$J = J_1 + J_2 \tag{E.43}$$

The only one eigen vector having the maximum number M is possible to occur.

$$\text{It is } |J_1 + J_2, J_1 + J_2\rangle = |J_1 J_1\rangle |J_2 J_2\rangle \tag{E.44}$$

In $|JM\rangle$, we assign the good quantum number as M . J is the maximum number of M . If M is changed, the orbital quantum number can be different from J , although J_1 and J_2 are maximum number of M_1 , and M_2 . In other words, the value of J corresponding to the first equation of (E.35) corresponding to the value of M which is not necessary equal to $J_1 + J_2$. The various combination of M_1 , and M_2 produce various combinations of M , M_1 and M_2 which satisfy (E.40). There are two eigen vectors operator \mathbf{J} for $M = J - 1$. One of them is from J given by (E.43). In this

case, $M = J_1 + J_2 - 1$. The other is $J = J_1 + J_2 - 1$ and $M = J_1 + J_2 - 1$. The eigenvalue corresponding to $|JM\rangle$ are

$$|J_1 + J_2, J_1 + J_2 - 1\rangle \text{ and } |J_1 + J_2 - 1, J_1 + J_2 - 1\rangle$$

The parent vectors corresponding to $|J_1 M_1\rangle$ and $|J_2 M_2\rangle$ are

$$|J_1, J_1 - 1\rangle |J_2, J_2\rangle \text{ and } |J_1, J_1\rangle |J_2, J_2 - 1\rangle$$

In a similar way there are three $|JM\rangle$ for $M = J - 2 = J_1 + J_2 - 2$.

$$|J_1 + J_2, J_1 + J_2 - 2\rangle |J_1 + J_2 - 1, J_1 + J_2 - 2\rangle |J_1 + J_2 - 2, J_1 + J_2 - 2\rangle$$

The parent vectors are

$$|J_1, J_1 - 2\rangle |J_2, J_2\rangle, |J_1, J_1 - 1\rangle |J_2, J_2 - 1\rangle, |J_1, J_1\rangle |J_2, J_2 - 2\rangle$$

The situation that the number of parent vectors $|J_1 M_1\rangle |J_2 M_2\rangle$ increases by 1 as M decreases by 1 continues in the range

$$|J_1 - J_2| \leq M \leq J_1 + J_2 \quad (\text{E.45})$$

Let us assume $J_1 > J_2$. This does not violate generality. The parent vectors for $M = J_1 - J_2$ are

$$|J_1, J_1 - 2J_2\rangle |J_2, J_2\rangle, |J_1, J_1 - 2J_2 + 1\rangle |J_2, J_2 - 1\rangle, |J_1, J_1 - 2J_2 + 2\rangle |J_2, J_2 - 2\rangle \dots \dots \dots, |J_1, J_1\rangle |J_2, -J_2\rangle$$

The total number of the parent vectors is $2J_2 - 1$. For $M = J_1 - J_2 - 1$, the parents are

$$|J_1, J_1 - 2J_2 - 1\rangle |J_2, J_2\rangle, |J_1, J_1 - 2J_2\rangle |J_2, J_2 - 1\rangle, |J_1, J_1 - 2J_2 + 1\rangle |J_2, J_2 - 2\rangle \dots \dots \dots, |J_1, J_1 - 1\rangle |J_2, -J_2\rangle$$

The number of parent vectors is also $2J_2 - 1$ and the same as that for $M = J_1 - J_2$.

This means the $J = J_1 - J_2 - 1$ does not occur. Thus, possible \hat{J} values are

$$\hat{J} = J_1 + J_2, \quad J_1 + J_2 - 1, \quad J_1 + J_2 - 2, \dots, J_1 - J_2 + 1, J_1 - J_2$$

This indicates the possible number of \hat{J} are $2J_2 + 1$. The number of independent eigen vectors is calculated as

$$\begin{aligned} \sum_{\hat{J}=J_1-J_2}^{J_1+J_2} (2\hat{J} + 1) &= (J_1 + J_2)(J_1 + J_2 + 1) - (J_1 - J_2)(J_1 - J_2 - 1) + 2J_2 + 1 \\ &= (2J_1 + 1)(2J_2 + 1) \end{aligned} \quad (\text{E.46})$$

This number equals the total number of parent vectors as should be expected. The situation described above is depicted in Figure Appendix 1 for $J_1 = 3$ and $J_2 = 2$.

As mentioned just below (E.34), M, M_1 and M_2 take the values

$$\left. \begin{aligned} M &= J, J - 1, J - 2, \dots, -J + 1, -J \\ M_1 &= J_1, J_1 - 1, J_1 - 2, \dots, J_1 + 1, -J_1 \\ M_2 &= J_2, J_2 - 1, J_2 - 2, \dots, J_2 + 1, -J_2 \end{aligned} \right\} \quad (\text{E.47})$$

For maximum M , the eigen vector is given by (E.44).

$$|J_1 + J_2, J_1 + J_2\rangle = |J_1, J_1\rangle |J_2, J_2\rangle \quad (\text{E.44})$$

We operate $J_- = J_{1-} + J_{2-}$ on (E.44) using (E.35)

$$\begin{aligned} J_- |J_1 + J_2, J_1 + J_2\rangle &= (J_{1-} + J_{2-}) |J_1, J_1\rangle |J_2, J_2\rangle \\ \hbar\sqrt{2(J_1 + J_2)} |J_1 + J_2, J_1 + J_2 - 1\rangle &= \hbar\sqrt{2J_2} |J_1, J_1\rangle |J_2, J_2 - 1\rangle \\ &\quad + \hbar\sqrt{2J_1} |J_1, J_1 - 1\rangle |J_2, J_2\rangle \end{aligned}$$

\therefore

$$|J_1 + J_2, J_1 + J_2 - 1\rangle = \sqrt{\frac{J_2}{J_1 + J_2}} |J_1, J_1\rangle |J_2, J_2 - 1\rangle + \sqrt{\frac{J_1}{J_1 + J_2}} |J_1, J_1 - 1\rangle |J_2, J_2\rangle \quad (\text{E.48})$$

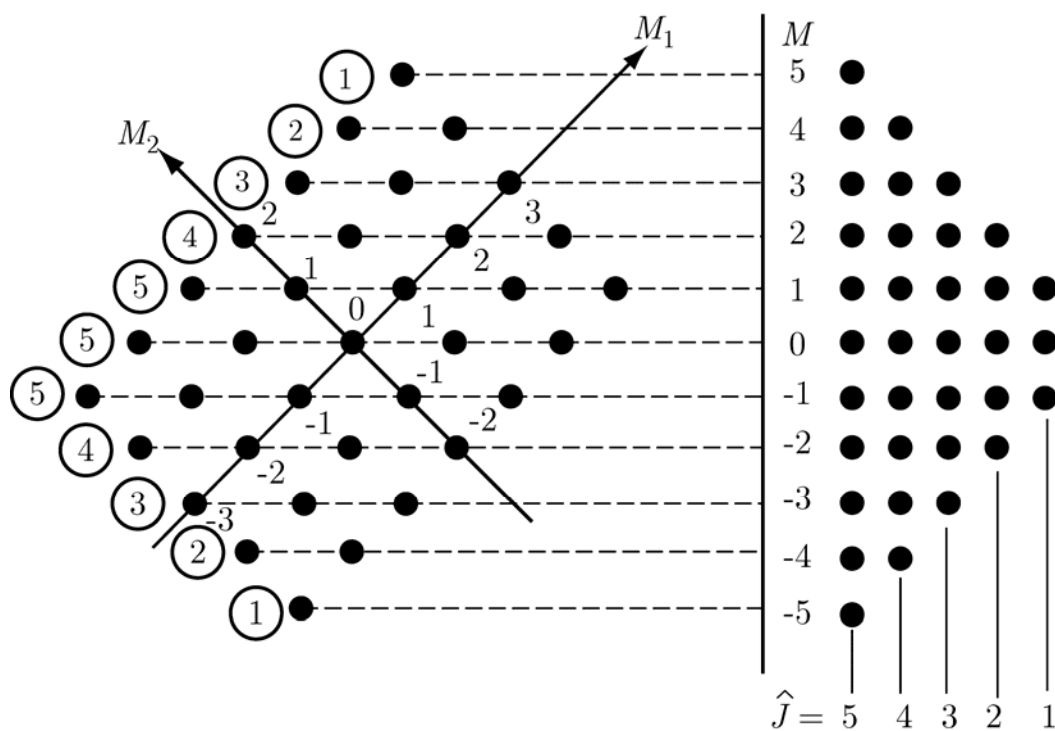


Figure Appendix 1 Number of eigen vectors $|\hat{J}M\rangle$ (number in circles) and \hat{J} and M formed by M_1 and M_2 . $J_1 = 3$ and $J_2 = 2$. Note $-J \leq M \leq J$, $-J_1 \leq M_1 \leq J_1$, $-J_2 \leq M_2 \leq J_2$, $M = M_1 + M_2$.

If we find the linear combination of $|J_1, J_1\rangle|J_2, J_2 - 1\rangle$ and $|J_1, J_1 - 1\rangle|J_2, J_2\rangle$ which is orthogonal to (E.48), it is the eigen vector, $|J_1 + J_2 - 1\rangle|J_1 + J_2 - 1\rangle$. For doing this we define $|\psi\rangle$ as

$$\left. \begin{aligned} |\psi\rangle &\equiv A|J_1, J_1\rangle + B|J_2, J_2 - 1\rangle \\ \langle J_1 + J_2, J_1 + J_2 - 1|\psi\rangle &= 0 \\ \langle\psi|\psi\rangle &= 1 \end{aligned} \right\} \quad (\text{E.49})$$

These result in simultaneous equations:

$$\left. \begin{aligned} s_1 A + s_2 B &= 0 \\ A^2 + B^2 &= 1 \end{aligned} \right\} \quad (\text{E.50})$$

The solution gives us

$$\begin{aligned} |\psi\rangle &= |J_1 + J_2 - 1, J_1 + J_2 - 1\rangle \\ &= \sqrt{\frac{J_1}{J_1 + J_2}} |J_1, J_1\rangle|J_2, J_2 - 1\rangle - \sqrt{\frac{J_1}{J_1 + J_2}} |J_1, J_1 - 1\rangle|J_2, J_2\rangle \end{aligned} \quad (\text{E.51})$$

The fact that $|\psi\rangle$ is equal to eigen vector $|J_1 + J_2 - 1, J_1 + J_2 - 1\rangle$ can be proved by making $J_+ |J_1 + J_2 - 1, J_1 + J_2 - 1\rangle = 0$. If we apply J_- to (E.48) and (E.51), we obtain $|J_1 + J_2, J_1 + J_2 - 2\rangle$, $|J_1 + J_2 - 1, J_1 + J_2 - 2\rangle$. If make the linear combination of $|J_1 M_1, J_2 M_2\rangle$ ($M_1 + M_2 = J_1 + J_2 - 2$) so that it is orthogonal to $|J_1 + J_2, J_1 + J_2 - 2\rangle$ and $|J_1 + J_2 - 1, J_1 + J_2 - 2\rangle$, we obtain $|J_1 + J_2 - 2, J_1 + J_2 - 2\rangle$, The result is

$$\begin{aligned}
|J_1 + J_2 - 2, J_1 + J_2 - 2\rangle = & \frac{1}{\sqrt{(J_1 + J_2 + 1)(2J_1 + 2J_2 - 1)}} \\
& \times \left[\begin{aligned} & \sqrt{J_1(2J_1 - 1)} |J_1, J_1\rangle |J_2, J_2 - 2\rangle \\ & - \sqrt{(2J_1 - 1)(2J_2 - 1)} |J_1, J_1 - 1\rangle |J_2, J_2 - 1\rangle \\ & + \sqrt{J_2(2J_2 - 1)} |J_1, J_1 - 2\rangle |J_2, J_2\rangle \end{aligned} \right] \quad (E.52)
\end{aligned}$$

We can show

$$J_+ |J_1 + J_2 - 2, J_1 + J_2 - 2\rangle = 0 \quad (E.53)$$

This proves that (E.52) is eigen vector.

The coefficients of the linear combinations shown above are the Wigner coefficients. In case of orbital angular moments, they are quantized so that they are eigen vectors of the hamiltonian with the crystal field in many cases. In such cases, the coefficients corresponding to the Wigner coefficients are referred to as the Clebsch-Gordon coefficients. Therefore, the name of the Wigner coefficients is used only for the spin vectors in many cases. The general formula of the Clebsch-Gordon coefficient and the Wigner coefficient are found in a standard text book dealing with the problem.

In the text, we deal with the Zeeman effect. It is stated there that the energy levels of atoms in a magnetic field, H , is given by (1.105) as

$$\left. \begin{aligned} \langle W \rangle &= \hbar\omega_L Mg \\ \hbar\omega_L &= \frac{\mu_B H}{\hbar} \end{aligned} \right\} \quad (1.105)$$

and Lande's g factor as

$$g = 1 + \frac{2J(J+1) + S(S+1) - L(L+1)}{2J(J+1)} \quad (1.106)$$

In what follows, we consider the abnormal Zeeman effect to show the formalism of Lande's g -factor.

First we consider the LS coupling

$$\mathbf{J} = \mathbf{L} + \mathbf{S} \quad (\text{E.54})$$

A very important assumption here to make is that L can be a good quantum number. In a many electron system, the total orbital angular momentum cannot be the constant of motion. Therefore L cannot be a quantum number to design the state of the system. However, we assume that the total angular momentum is the constant of motion satisfying the commutation relation with hamiltonian \hat{H} . Also we assume that total spin S can be a good quantum number of the system. This is the case, if the central field approximation is valid. If the spin-orbit interaction is strong, this is not the case. However, in many cases, the spin-orbit interaction is weak and it is treated as the perturbation. Thus in the ground state without the perturbation can be treated by the central field approximation.

If the spin-orbit interaction is strong, the orbital angular momentum and the spin angular momentum couple to form the total angular momentum of the single electron, j . Then the total angular momenta of different electrons couple to make total angular momentum of the atom. This coupling scheme is called the $j - j$ coupling and important in the inner shell excitation. If the spin-orbit interaction is weak, the strong electrostatic interaction align electron spins and the total S is formed. Then LS coupling results in. This is the case which is observed in the valence shell spectra.

First we take the direction of \mathbf{J} as the z axis in the state without the magnetic field. From the nature summarized in (E.35),

$$\left. \begin{aligned} \frac{d\mathbf{J}^2}{dt} &= \frac{1}{i\hbar} [\mathbf{J}^2, \hat{H}] = 0 \\ \frac{d\mathbf{J}_z}{dt} &= \frac{1}{i\hbar} [\mathbf{J}_z, \hat{H}] = 0 \end{aligned} \right\} \quad (\text{E.55})$$

Thus \mathbf{J}^2 and \mathbf{J}_z are the constants of motion. In the same way, $\mathbf{L}^2, L_z, \mathbf{S}^2$ and S_z are constants of motion. Since we take the z axis along the direction of \mathbf{J} , we can say that \mathbf{L} and \mathbf{S} are making precession around \mathbf{J} . This is shown in Figure Appendix 2

When a magnetic field is applied and we take the z axis toward the magnetic field \mathbf{H} , (E.55) shows that \mathbf{J} makes precession around the field direction as shown in Figure Appendix 2. In the text we show that the magnetic moment, $\boldsymbol{\mu}$, associated with the angular momentum, \mathbf{J} , is given by (1.94) as

$$\boldsymbol{\mu} = \gamma \mathbf{J} \quad (\text{1.94})$$

$$\begin{aligned} \boldsymbol{\mu} &= -\frac{e\hbar}{2mc} \mathbf{J} \\ &= -\mu_B \mathbf{J} \end{aligned} \quad (\text{E.56})$$

Here, μ_B is the Bohr magneton.

In case of the magnetic moment associated with the electron spin, it is different from (E.56) and given by

$$\boldsymbol{\mu} = -2\mu_B \mathbf{S} \quad (\text{E.57})$$

This is the intrinsic nature of the electron and proved by Dirac's quantum electrodynamics. The total magnetic moment, $\boldsymbol{\mu}$, is given by

$$\boldsymbol{\mu} = \boldsymbol{\mu}_L \cdot \cos \theta_s + \boldsymbol{\mu}_S \sin \theta_s \quad (\text{E.58})$$

Here θ_L and θ_S are the angles between \mathbf{L} and \mathbf{J} and that between \mathbf{S} and \mathbf{J} . From (E.57) and (E.58) we have

$$\boldsymbol{\mu} = -\mu_B \mathbf{L} \cos \theta_L - 2\mu_B \mathbf{S} \cos \theta_S \quad (\text{E.59})$$

(E.59) suggests that (E.56) is not valid for the total magnetic moment, since the contribution of the spin is not similar to that of the orbital angular momentum; the Bohr magneton is practically double. Thus we put, instead of (E.56),

$$\boldsymbol{\mu} = -g\mu_B\mathbf{J} \quad (\text{E.60})$$

The precession of $\boldsymbol{\mu}$ around the magnetic field is depicted in Figure Appendix 2.

(E.59) is rewritten as

$$\boldsymbol{\mu} = -\mu_B\mathbf{L}\frac{(\mathbf{L}\cdot\mathbf{J})}{|\mathbf{S}||\mathbf{J}|} - 2\mu_B\mathbf{S}\frac{(\mathbf{S}\cdot\mathbf{J})}{|\mathbf{S}||\mathbf{J}|} \quad (\text{E.61})$$

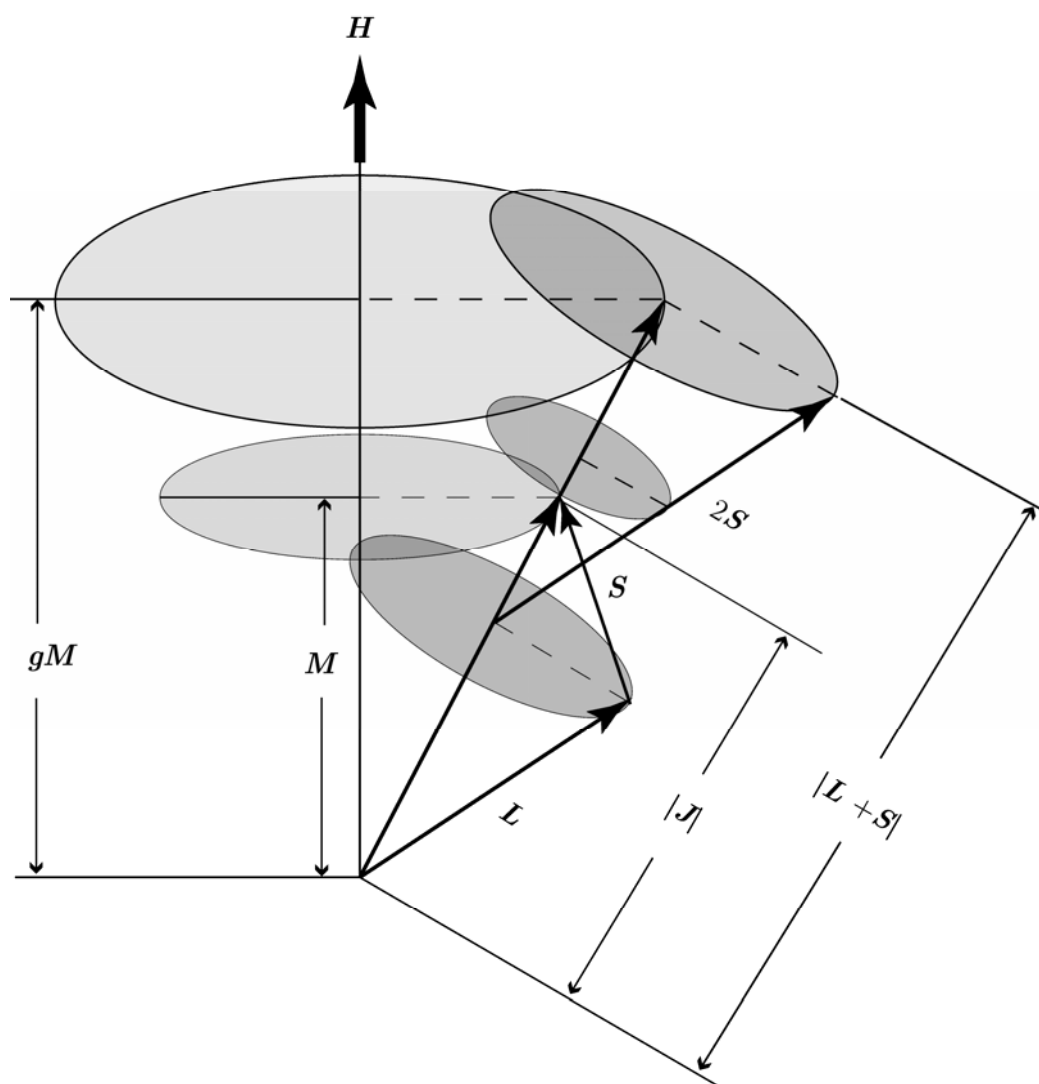


Figure Appendix 2 Angular momentum consideration of the Zeeman effect. The LS coupling is assumed to occur.

From (E.60) and (E.61), we have

$$g\mathbf{J} = \mathbf{L} \frac{(\mathbf{L} \cdot \mathbf{J})}{|\mathbf{S}||\mathbf{J}|} + \mathbf{S} \cdot \frac{(\mathbf{S} \cdot \mathbf{J})}{|\mathbf{S}||\mathbf{J}|} \quad (\text{E.62})$$

On the other hand we have

$$\left. \begin{aligned} \mathbf{S}^2 &= \mathbf{L}^2 + \mathbf{J}^2 - 2(\mathbf{L} \cdot \mathbf{J}) \\ \mathbf{L}^2 &= \mathbf{S}^2 + \mathbf{J}^2 - 2(\mathbf{S} \cdot \mathbf{J}) \end{aligned} \right\} \quad (\text{E.63})$$

From (E.54), (E.62) and (E.63) we have

$$g = 1 + \frac{2J(J+1) + S(S+1) - L(L+1)}{2J(J+1)} \quad (\text{1.106})$$

A more quantum mechanical explanation is complicated. From the general properties of the angular momentum, we have (see Condon-Shortley p. 63 and p. 69)

$$\left. \begin{aligned} \langle JM | T_z | JM \rangle &= M \langle J | T | J \rangle \\ \langle J_1 J_2 J | T | J_1 J_2 J \rangle &= \langle J_1 J_2 | T | J_1 J_2 \rangle \frac{R(J)}{2J(J+1)} \\ R(J) &= J(J+1) - J_1(J_1+1) + J_2(J_2+1) \end{aligned} \right\} \quad (\text{E.64})$$

From these formulae, we have

$$\left. \begin{aligned} \langle JM | L_z | JM \rangle &= \frac{\hbar M}{2J(J+1)} [J(J+1) + L(L+1) - S(S+1)] \\ \langle JM | S_z | JM \rangle &= \frac{\hbar M}{2J(J+1)} [J(J+1) + S(S+1) - L(L+1)] \end{aligned} \right\} \quad (\text{E.65})$$

The level energy to cause the Zeeman effect is

$$W = \frac{\mu_B H}{\hbar} (L_z + 2S_z) \quad (\text{E.66})$$

From (E.65) and (E.66), we have

$$\begin{aligned}
\langle W \rangle &= \langle JM | W | JM \rangle \\
&= \mu_B H \frac{M}{2J(J+1)} \left[\frac{J(J+1) + L(L+1) - S(S+1)}{+2J(J+1) + 2S(S+1) - 2L(L+1)} \right] \quad (\text{E.67}) \\
&= \left[1 + \frac{J(J+1) - L(L+1) + S(S+1)}{2J(J+1)} \right] \mu_B H M
\end{aligned}$$

From (1.99), (1.100) and (E.67), we see

$$g = 1 + \frac{2J(J+1) + S(S+1) - L(L+1)}{2J(J+1)} \quad (1.106)$$

CURRICULUM VITAE

FIRST NAME: RITTHIKRAI

LAST NAME: CHAI-NGAM

GENDER: Male

NATIONALITY: Thai

DATE OF BIRTH: March 2, 1976

PLACE OF BIRTH: Roi-Ed

EDUCATION BACKGROUND:

- B.Sc. (2nd Hons.) in major Physics March 9, 1998. Faculty of Science, Sri Nakharinwirot University, Thailand.
- Master of Science (Physics), May 21, 2001. Suranaree University of Technology, Thailand.

WORK EXPERIENCE:

- A teacher in physics at Mahasarakham University Demonstration School, Amphur Muang, Mahasarakham, Thailand, 1999.

PUBLICATIONS:

- R. Chai-Ngam, Nobuhiko Sakai, Akihisa Koizumi, Hisao Kobayashi and Takehiko Ishii. Experimental study on interlayer magnetic coupling in sputtered Al/Fe/Al/Gd magnetic multilayer films I. **Journal of the Physical Society of Japan** 74: 1843 – 1848.